Membrane Disruption Mechanisms of Antimicrobial Peptides and Their Combinations with Antibiotics: An Insight from Experimental Studies and MD Simulations

A Thesis Submitted to The University of Manchester
For the Degree of Doctor of Philosophy
In the Faculty of Science and Engineering

Mingrui Liao
Department of Physics and Astronomy
2022

List of content

Membrane Disruption Mechanisms of Antimicrobial Peptides and Their Combinations with Antibiotics: An Insight from Experimental Studies and MD Simulations 1

Abstract 8

Declaration 10

Copyright statement 11

Acknowledgements 12

List of publications 14

Chapter 1 Introduction 17

- **1. Scientific background and motivation** 17
  - **1.1 Bacterial cell walls and biomembranes** 18
  - **1.2 Novel antimicrobial peptides/polymers and their action mechanisms with bacteria** 19
  - **1.3 Environmental responsive AMPs and their applications** 21
  - **1.4 Effects of drug combinations against pathogenic bacteria** 22
  - **1.5 The synergic mechanisms of combinatorial therapy** 24
- **2. Outline of the thesis** 25

Chapter 2 Intramembrane Nanoaggregates of Antimicrobial Peptides Play a Vital Role in Bacterial Killing 31

- **Abstract** 32
- **1. Introduction** 33
- **2. Results and discussions** 35
  - **2.1 Antibacterial efficacy and biocompatibility evaluation** 35
  - **2.2 Bacterial dynamic killing and membrane disruptions by AMPs** 36
  - **2.3 Membrane-lytic binding of AMPs** 39
  - **2.4 Penetration of single AMP through membranes via PMF** 45
  - **2.5 Neutron reflectivity for different AMP binding to the DPPG monolayer** 48
  - **2.6 AMP intramembrane aggregation varied with peptide to lipid ratio** 50
  - **2.7 The mode of action for IM disruption** 53
- **3. Conclusions** 57
- **4. Experimental section** 58
- **Acknowledgements** 58

Conflict of interest 58

5. **References** 58

Supporting Information 61

1. **Chemical Reagents and Physicochemical Properties of AMPs** 62

2. **Experiment Methods** 63

2.1 Atomic force microscopy (AFM) and surface physical activity 63

2.2 Small angle neutron scattering (SANS) 63

2.3 Haemolytic activity and MTT assays 64

2.4 Antimicrobial efficacy and bacterial dynamic killing 65

2.5 Bacterial membrane permeability and depolarization and live/dead staining assays 65

2.6 BODIPY™-TR-cadaverine (BC) displacement by AMPs' LPS binding 66

2.7 Fluorescence leakage from SUVs 66

2.8 Zeta-potential and Raman spectra of SUVs after AMP binding 67

2.9 Neutron reflection (NR) of AMP binding to spread lipid monolayers 68

2.10 Simulation models and methods 69

3. **Molecular Parameters in Neutron Experiments** 70

4. **Force Field of MD Simulations and PMF Method** 70

5. **Beads Mapping in CG Models, Adsorption of Peptides at the Air/Liquid Interface and Aggregating in Solution** 72

6. **SANS Fitting Parameters of AMP Self-assembly in Solution** 76

7. **Antimicrobial and Biocompatibility Assays** 77

8. **AFM of Pure Liposome and Raman Spectroscopy of Liposomes with and without AMPs** 78

9. **SANS Fitting Model of SUV with AMPs and NR Fitting Model of AMPs' Binding with Lipid Monolayer** 83

10. **AMPs' Binding Behaviours onto DPPG Bilayers with P/L Changing, and Dye Leakage of AMPs Attacking Pure POPG SUVs.** 86

11. **References** 90

Chapter 3 From Cell Wall to Cytoplasmic Membrane: Multiple Actions of Antimicrobial Peptides against Gram-positive Bacteria 92

Abstract 93

6. **Introduction** 94

7. Experiment methods 96

2.1 Antimicrobial Evaluations of AMPs 96

2.2 Evaluations of Dynamic Bacterial Killing 97

2.3 BODIPY™-TR-cadaverine (BC) Displacement of LTA in both Cell Free and Cell Systems 97

2.4 Cytoplasmic Membrane Depolarization, AMP's Binding to Anionic Lipid and Laurdan-based Membrane Fluidity Measurements 98

2.5 Scanning Electron Microscopy (SEM) of Bacterial Cell Morphology 99

2.6 Circular Dichroism Spectra and Zeta Potential Measurements 99

2.7 SUV Leakage 100

2.8 SANS of Lipid SUVs with AMP binding 100

2.9 CG-MD Simulation of Cytoplasmatic Membrane Interacting with AMPs 101

2.10 Neutron Reflection (NR) of Lipid Monolayers Interacting with AMPs 102

8. Results and discussions 102

3.1 Antimicrobial Activity of AMPs and Membrane Targeting Actions 102

3.2 AMP Binding with LTA in Cell Wall 104

3.3 Effects of AMPs on Cytoplasmic Membrane: Structural Basis to Depolarization and Leakage 107

3.4 AMP Binding on Anionic Lipids and Effects on Membrane Fluidity 111

3.5 MD Simulation of POPG/CL Membrane Binding with AMP 113

3.6 NR Study of AMP Binding with DPPG Monolayer 117

9. Conclusion 121

Author Information 122

Conflicts of Interest 122

Acknowledges 122

10. References 123

Sopporting Information 128

1. Bacterial strains and materials 129

2. Fluorescence spectroscopy 129

3. SANS Fitting Model of LTA/POPC and PVCL2/POPG SUVs with AMPs 132

4. NR Fitting Model of AMPs' Binding with DPPG Monolayers 136

5. References 139

Chapter 4 Antimicrobial Synergy of Lipopeptides Paired with Conventional Antibiotics 140

Abstract 141

1. Introduction 142

2. Experiment methods 145

2.1 Circular dichroism 145

2.2 Surface physical activities of lipopeptides and their binding behaviour on the liquid lipid monolayer 145

2.3 Fluorescence spectroscopy assay, SUV leakage and Raman spectroscopy 146

2.4 2D NMR NOESY 147

2.5 Atomic force microscopy (AFM) and small angle neutron scattering (SANS) 147

2.6 Antibacterial assays 148

2.7 Dynamic antimicrobial action, bacterial live/dead staining 149

2.8 NPN uptake, membrane depolarization and TC uptake 149

2.9 Hemolytic activity and MTT assays 150

2.10 Neutron reflection (NR) 151

2.11 Atomistic molecular dynamics (MD) simulations 151

3. Results and discussions 152

3.1 Antimicrobial activity 153

3.2 Synergism of binary lipopeptide-antibiotic mixtures 154

3.3 Biocompatibility and dynamic killing of binary mixtures 156

3.4 Bacterial membrane targeting and action mechanism of lipopeptide 160

3.5 Insight into the co-assembly between lipopeptide and MC 166

3.6 NR determination of binding of binary antimicrobial mixture onto DPPG monolayer 168

3.7 MD simulations of interactions between membrane and drug pair 170

4. Conclusions 174

Associated Content 175

Author information 175

Conflicts of interest 175

Acknowledgements 175

5. References 176

Supporting information 182

1. Bacterial strains and materials 183

2. Key physical parameters used in neutron experiments 183

3. Molecular information of lipopeptides and antibiotics, and their antimicrobial and biocompatible assays 184

4. AMPs' structure and physical activity 187

5. Kinetic leakage fraction of POPC/LPS SUVs with lipopeptides 189

6. PG micelles with lipopeptides in SANS fit models 190

7. Raman spectrum of POPC/POPG with lipopeptides 191

8. Lipopeptide self-assembly and co-assembly with MC in SANS fit models 192

9. NOESY spectrum and Fluorescence assays of C_8GIK-MC complex 193

10. Parameters in NR monolayer fit models 195

11. MD simulation of MC with POPG/PVCL2 membrane 197

12. References 198

Chapter 5 Combination of pH-responsive AMP hydrogel and conventional antibiotic against Gram-negative bacteria 199

Abstract 200

1. Introduction 202

2. Experiment methods 204

2.1 Minimum Inhibitory Concentrations (MICs), Dynamic Killing and Drug Combination Evaluations 204

2.2 Cell Biocompatibility Assays 205

2.3 Evaluation of NPN Uptake and Cytoplasmic Membrane Depolarization Effects 206

2.4 BODIPY-TR-cadaverine (BC) Displacement from LPS in Cell-free and Cell Systems 207

2.5 NAO Assays and Leakage of SUVs 207

2.6 Circular Dichroism (CD) Spectroscopy, Thioflavin T (ThT) Titration and Atomic Force Microscopy (AFM) 209

2.7 MD Simulations 209

2.8 SANS of Peptide Self-assembly and Lipid SUVs with AMPs 210

2.9 Fluorescence Spectra of AMP-MC Drug Pair Interaction 211

- **3. Results and discussions** 211
  - **3.1 Self-assembly of pH-responsive Peptides** 211
  - **3.2 Antimicrobial Activities of Peptides** 217
  - **3.3 Cytocompatibility of Peptides** 219
  - **3.4 FICI Determination of Drug Combination and Mode of Membrane Disruption** 220
  - **3.5 BC Displacement, NAO Assays, Leakage and SANS of SUVs after AMP Binding** 224
- **4. Conclusions** 229
- **Associated content** 231
- **Author information** 231
- **Conflicts of interest** 231
- **Acknowledgements** 231
- **5. References** 232

Supporting information 236

- **1. Bacterial strains and materials** 237
- **2. Peptides' structural information** 237
- **3. Fitting models and parameters in SANS measurements** 238
- **4. References** 245

Chapter 6 Conclusions and future work 246

- **1. Conclusions** 246
- **2. Future work** 248
- **3. References** 250

Abstract

Mingrui Liao

The University of Manchester

Doctor of Philosophy

2022

Membrane Disruption Mechanisms of Antimicrobial Peptides and Their Combinations with Antibiotics: An Insight from Experimental Studies and MD Simulations

Antimicrobial peptides (AMPs) offer great potential in the fight against multi-drug resistant (MDR) microbes via the mode of membrane targeting. However, the potency and selectivity of AMPs must be substantially improved. By combining experiments and molecular dynamics (MD) simulations, this thesis work focuses on exploring how representative cationic AMPs interact with the bacterial outer and inner membranes. Antimicrobial efficacy, dynamic killing, neutron reflection (NR) and small angle neutron scattering (SANS) together with MD simulations have been used to investigate the membrane-lytic actions of four AMPs, G(IIKK)$_3$I-NH$_2$ (G$_3$), G(IIKK)$_4$I-NH$_2$ (G$_4$), previously-studied GLLDLLKLLLKAAG-NH$_2$ (LDKA, biomimetic) and GIGAVLKVLTTGLPALISWIKRKR-NH$_2$ (Melittin, natural). Distinctly different intramembrane nanoaggregates were formed when the four AMPs were bound to the inner and outer membranes. G$_3$ and G$_4$ formed smaller but further inserted intramembrane nanoaggregates into bacterial membranes which were well correlated to their greater antimicrobial efficacy and faster dynamic killing.

Substitutions of hydrophobic or cationic amino acids in G$_3$ (also denoted as GIK) led to AMPs of G(WWKK)$_3$W-NH$_2$ (GWK), G(FFKK)$_3$F-NH$_2$ (GFK), and G(IIRR)$_3$I-NH$_2$ (GIR), with varying antimicrobial activities. Electronic microscopy imaging and fluorescence assays revealed structural disruptions by AMP binding to bacterial cell walls, anionic lipoteichoic acids (LTA) and cytoplasmic membrane. GWK and GIR can rigidify the cytoplasmic membrane and decrease the diffusive efficiency of the anionic lipid membrane more significantly than GIK and GFK, associated with intramembrane peptide nanoaggregates.

Synergistic combination of an antibiotic and an aiding agent provides an important but largely unexploited option to ‘repurpose’ existing biomaterial’s space while addressing issues of potency, spectrum, toxicity and drug-resistance. Antibiotic tetracycline/minocycline (TC/MC) combined with the broad-spectrum antimicrobial lipopeptides (C_8GIK and C_8GIR) has been shown to improve the efficiency of membrane targeting and intramembrane accumulation. Binary antibiotic-lipopeptide combinations displayed synergistic effects against both Gram-positive and Gram-negative bacterial strains including 3 MDR strains, featured by fast time-killing and high TC/MC uptake.

Finally, GIIKDIIKDIIKDI and GIIKKIIDDIIKKI (denoted as 3D and 2D, respectively), designed by selective substitutions of cationic residues of Lys (K) in the extensively studied peptide G(IIKK)$_3$I with anionic residue Asp (D), interacted differently with the inner and outer membranes of Gram-negative bacteria in a pH-responsive manner. Different antimicrobial efficacies of 2D and 3D were underlined by the interplay between their ability to bind to the outer membrane lipid LPS (lipopolysaccharide), outer membrane permeability change and inner membrane depolarization and leakage. This thesis study has thus provided useful data to present AMPs as a promising alternative to combat antimicrobial resistance. Rational structural design together with intramembrane structural analysis offers an effective route for optimizing AMP performance.

Declaration

The author hereby declares that no portion of the work referred to in the thesis has been submitted in support of an application for another degree or qualification of this or any other university or other institute of learning.

Copyright statement

i. The author of this thesis (including any appendices and/or schedules to this thesis) owns certain copyright or related rights in it (the "Copyright") and s/he has given The University of Manchester certain rights to use such Copyright, including for administrative purposes.

ii. Copies of this thesis, either in full or in extracts and whether in hard or electronic copy, may be made only in accordance with the Copyright, Designs and Patents Act 1988 (as amended) and regulations issued under it or, where appropriate, in accordance with licensing agreements which the University has from time to time. This page must form part of any such copies made.

iii. The ownership of certain Copyright, patents, designs, trademarks and other intellectual property (the "Intellectual Property") and any reproductions of copyright works in the thesis, for example graphs and Tables ("Reproductions"), which may be described in this thesis, may not be owned by the author and may be owned by third parties. Such Intellectual Property and Reproductions cannot and must not be made available for use without the prior written permission of the owner(s) of the relevant Intellectual Property and/or Reproductions.

iv. Further information on the conditions under which disclosure, publication and commercialisation of this thesis, the Copyright and any Intellectual Property and/ or Reproductions described in it may take place is available in the University IP Policy (see http://documents.manchester.ac.uk/DocuInfo.aspx?DocID=24420), in any relevant Thesis restriction declarations deposited in the University Library, The University Library's regulations (see http://www.library.manchester.ac.uk/about/regulations/) and in The University's policy on Presentation of Theses

Acknowledgements

I would like to thank my supervisors, Prof. Jian Lu, Dr. Thomas Waigh, Dr. Jichen Li and Prof. Andrew Mcbain, for their advice and guidance during my PhD study. Four years have been away in a moment, there are love, joy and sadness in our study and live, we became more mature in mind in this period.

I would like to say thank you to my deeply loved parents for their selfless support, they are ordinary but great and undertake too much behind me for their son. I cannot focus on my research and continuously make progress without their encouragements. I am also grateful to everyone in Jian's group: Dr. Zongyi Li, Dr. Haoning Gong, Dr. Xuzhi Hu, Lin Zhang, Dr. Ke Fa, Dr. Huayang Liu, Dr. Sean Ruane, Dr. Jessica Carter, Dr. Jing Zhang, Dr. Daniela Ciumac, Peter Hollowell, Dr. Laura Fox, Kangcheng Sheng, Tianhao Ge, Zeyuan Zhuang, Ke Ding, Anna Stephens, Zihan Huang and Jamie Fearnley. I would like to sincerely thank Zongyi, Xuzhi and Haoning for their help with the related experiments and inspiring discussions, and Ziwei Wang for her input with the AFM and Raman spectroscopy experiments. I acknowledge Dr. Yao Chen for his assistance with the neutron diffraction experiments at the ILL. I would appreciate all the local scientists from the ISIS neutron facility for their great input on our neutron experiments and follow-up experiments: Dr. Mario Campana, Dr. Luke Clifton, Dr. John Webster, Dr. Kun Ma, Dr. Peixun Li, Dr. Stephen King, Dr. Gregory Smith. I would be not successful with the neutron experiments without their assistance. Meanwhile, I would be sincerely grateful to the local scientists at the ILL neutron facility Dr. Armando Maestro, Dr. Richard Campbell, Dr. Giovanna Fragneto, Dr. Philipp Gutfreund, Dr. Isabelle Grillo, Dr. Ralf Schweins and Dr. Bruno Deme for their great support with the neutron reflectivity, small angle neutron scattering and neutron diffraction experiments. The collaboration with Prof. Jian Zhou, Dr. Xuebo Quan, Dr. Shengjiang Yang, Dr. Zheng Chen from South China University of Technology is greatly acknowledged.

Finally, I am grateful for the funding support from the joint PhD program of the

University of Manchester and the China Scholarship Council (CSC201806150001), and the computing resource from the Computational Shared Facility 3 (CSF3) at the University of Manchester.

List of publications

Papers

1. ***Liao, M.***; Quan, X.; Gong, H.; Hu, X.; Ke, F.; Li, Z.; Liu, H.; Lu, J.R. *et al.*, Intramembrane Nanoaggregates of Antimicrobial Peptides Play a Vital Role in Bacterial Killing. *Small* **2022**. (**Accepted paper**)
2. ***Liao, M.***; Gong, H.; Hu, X.; Ke, F.; Li, Z.; Liu, H.; Lu, J.R. *et al.*, Antimicrobial Synergy of Lipopeptides Paired with Conventional Antibiotics. **2022**. (**Submitted Manuscript**)
3. ***Liao, M.***; Gong, H.; Hu, X.; Ke, F.; Li, Z.; Liu, H.; Lu, J.R. et al., AMPs' Damage on Both Cell Wall and Cytoplasmic Membrane Linked to Their Antimicrobial Activity against Gram-positive Bacteria. **2022** (**Submitted Manuscript**)
4. ***Liao, M.***; Gong, H.; Hu, X.; Lu, J.R., Combination of pH-responsive AMPs and Conventional Antibiotic in Treatment of Gram-negative Bacteria. **2022** (**Submitted Manuscript**)
5. ***Liao, M.***; Chen, Y.; Quan, X.; Gong, H.; Hu, X.; Ke, F.; Li, Z.; Liu, H.; Lu, J.R. *et al.*, Positively-charged and Aromatic Residues in Alpha-Helix AMPs and Their Effects on Bacterial Membrane Disruption. **2022** (**Ready for Submission**)
6. Gong, H.; Hu, X.; Fa, K.; ***Liao, M.***; Liu, H.; Fragneto, G.; Campana, M.; Lu, J.R., How do Antimicrobial Peptides Disrupt the Lipopolysaccharide Membrane Leaflet of Gram-Negative Bacteria? *Journal of Colloid and Interface Science*. **2022 (Submitted Manuscript)**
7. Hu, X., Carter J., Ge, T., ***Liao, M.***, Stephens, A., Mclnnes, E., Padia, F., Lu, J.R. *et al.*, Impacts of Chain and Head Lengths of Nonionic Alkyl Ethoxylate Surfactants on Cytotoxicity to Human Corneal and Skin Cells in Agri-spraying Processes. *Journal of Colloid and Interface Science* **2022**, 628, 162-173.
8. Fa, K.; Liu, H.; Gong, H.; Zhang, L.; ***Liao, M.***; Hu, X.; Ma, K.; Li, P.; Lu, J.R. *et al.*, In-membrane Nanostructuring of Cationic Amphiphiles Affects Their Antimicrobial Efficacy and Cytotoxicity: A Comparison Study between a De Novo Antimicrobial Lipopeptide and Traditional Biocides. *Langmuir* **2022**, 38 (21), 6623-6637.
9. Hu, X., Gong, H., Liu, H., Wang, X., Wang, W., ***Liao, M.***, Li, Z., Ma, K., Li, P., Rogers, S., Schweins, R., Liu, X., Padia, F., Bell, G., Lu, J.R. *et al.*, Contrasting Impacts of Mixed Nonionic Surfactant Micelles on Plant Growth in the Delivery of Fungicide and Herbicide. *Journal of Colloid and Interface Science* **2022**, 618, 78-87.
10. Zhang, J.; Gong, H.; ***Liao, M.***; Li Z.; Lu, J.R. *et al.*, High Antifungal Activity and High Selectivity of Designed Short Peptides. *Journal of Colloid and Interface Science* **2022**, 608, 193-206.

11. Chen, Y.; ***Liao, M.***; Ma, K.; Wang, Z.; Lu, J.R.; Li, P. *et al.*, Implications of Surfactant Hydrophobic Chain Architecture on the Surfactant-Model Skin Lipid Interaction. *Journal of Colloid and Interface Science* **2022**, 608, 405-415.

12. Liu, H.; Fa, K.; Hu, X.; Li, Z.; Ma, K.; ***Liao, M.***; Zhang, L.; Schweins, R.; Thomas, R. K.; Lu J. R., How do Chain Lengths of Acyl-L-carnitines Affect Their Surface Adsorption and Solution Aggregation? *Journal of Colloid and Interface Science* **2022**, 609, 491-502.

13. Gong, H.; Hu, X.; **Liao, M.**; Fa, K.; Clifton, L.; Sani, M.; King, S.; Maestro, A.; Separovic, F.; Waigh, T.; Xu, H.; McBain, A.; Lu, J., Structural Disruptions of the Outer Membranes of Gram-Negative Bacteria by Rationally Designed Amphiphilic Antimicrobial Peptides. *ACS Applied Materials & Interfaces* **2021**, 13, 16062-16074.

14. ***Liao, M.***, Liu, H., Wang, X., Hu, X., Brenan, K., Mecha, J.; Lu, J.R. *et al.*, A Technical Review of Face Mask Wearing in Preventing Respiratory COVID-19 Transmission. *Current Opinion in Colloid & Interface Science* **2021**, 101407. (**Invited review**)

15. Liu, H.; Hu, X.; Li, Z.; Fa, K.; Gong, H.; Ma, K.; ***Liao, M.***; Li, P.; Websterb, J.; Petkov, J.; Thomas, K. R.; Lu J., Surface Adsorption and Solution Aggregation of a Novel Lauroyl-l-carnitine Surfactant. *Journal of Colloid and Interface Science* **2021**, 591, 106-114.

16. Hu, X.; Gong, H.; Hollowell, P.; ***Liao, M.***; Raune, S.; Liu, H.; Lu, J.R. *et al.*, What Happens When Pesticides are Solubilised in Binary Ionic/Zwitterionic-Nonionic Mixed Micelles? *Journal of Colloid and Interface Science* **2021**, 586, 190-199.

17. Chen, Z.; ***Liao, M.***; Zhang L.; Zhou J., Molecular Simulations on the Hydration and Underwater Oleophobicity of Zwitterionic Self-assembled Monolayers. *AIChE Journal* **2021**, 67, e17103.

18. Gong, H.; Sani, M.; Hu, X.; Fa, K.; Hart, William J.; ***Liao, M.***; Hollowell, P.; Carter, J.; Lu, J. *et al.*, How do Self-Assembling Antimicrobial Lipopeptides Kill Bacteria? *ACS Applied Materials & Interfaces* **2020**, 12, 50, 55675-55687.

19. Gong, H.*; ***Liao, M.****; Hu, X.; Ke, F.; Phanphak, S.; Ciumac, D.; Hollowell, P.; Lu, J.R. *et al.*, Aggregated Amphiphilic Antimicrobial Peptides Embedded in Bacterial Membranes. *ACS Applied Materials & Interfaces* **2020,** 12, 40, 44420-44432. (*** Co-first author**)

20. Hu, X.; Pambou, E.; Gong, H.; ***Liao, M.***; Hollowell, P.; Liu, H.; Lu, J.R. *et al.*, How Does Substrate Hydrophobicity Affect the Morphological Features of Reconstituted Wax Films and Their Interactions with Nonionic Surfactant and Pesticide? *Journal of Colloid and Interface Science* **2020**, 575, 245-253.

21. Hu, X.; ***Liao, M.***; Gong, H.; Zhang, L.; Cox, H.; Waigh, T.A.; Lu, J.R., Recent Advances in Short Peptide Self-assembly: from Rational Design to Novel

Applications. *Current Opinion in Colloid & Interface Science* **2020**, 45, 1-13.

Chapter 1 Introduction

1. Scientific background and motivation

Most antimicrobial peptides (AMPs) are cationic and can bind to negatively charged lipid membranes. With the permeability change of bacterial membrane by cationic AMP binding, peptides' influx can affect a variety of intracellular mechanisms, including inhibition of many biochemical reactions such as DNA replication, protein synthesis, enzymatic activities and cell-wall biosynthesis.[1] Despite decades of intensive study, it is hard to identify a clear mechanism between AMP's membrane activity and killing effects. With more and more efficient computing tools developed for the screening of AMPs, a deeper and more precise understanding of AMPs' effects on membrane targets can improve the efficiency of screening new antibacterial agents.[2-5]

Most experimental studies of AMPs' bactericidal effects have focused on *in vitro* planktonic cultures and well-established membrane bilayer models.[6] These assays reveal a variety of specific biophysical and biochemical phenomena, but cannot provide direct evidence for peptides' membrane activity associated with their antimicrobial effects. For example, fluorescent methods can identify the permeability change of the outer membrane (OM) and the depolarization of the cytoplasmic membrane (CM), record the real-time dye uptake/leakage from the membranes, monitor dissipation of the proton motive force (PMF) and many additional effects.[7] Some specific fluorescence probes can label lipid molecules such as lipopolysaccharides (LPS) and lipoteichoic acids (LTA), to measure peptides' affinity with lipid molecules on the molecular level. However, fluorescent indicators are incapable of explaining the binding behaviors and structural changes after AMP interacting with lipid molecules.[8, 9] On the other hand, some studies employed simulation-guided method to screen more effective peptides. This approach has provided a good application of simulation tools but should be more combined with experimental work.[5, 10] Neutron reflectometry (NR) and small angle neutron scattering (SANS) would be good tools to provide structural information on AMPs' interacting with diverse membrane types, and in good complement with fluorescence assays. Molecular dynamics (MD) simulations are widely used in studying peptides' interaction with membrane models and can directly present phenomena that cannot be observed in corresponding experimental work.

1.1 Bacterial cell walls and biomembranes

Gram-positive bacteria are different from Gram-negative bacteria in many aspects including components of cell walls, membrane symmetricity, and charged lipid components/ratios in cytoplasmic membranes. (**Figure 1**) The cell wall of Gram-positive bacteria can provide sufficient mechanical support to the cellular matrix and improve the cell adaptability to the changes of osmotic pressure from the outer environment. As a main origin of net negative charges, polyanionic macromolecules wall teichoic acids (WTA, with 30 ~ 40 repeating units) and acidic polysaccharides are covalently linked to the cell wall or the cytoplasmic membrane. While lipoteichoic acids (LTA) are based on poly (glycerol phosphate) chains and penetrate the wall network, but are not covalently linked to the cell wall.[11] Gram-negative bacteria lack a thick cell wall and have an asymmetrical outer membrane bearing lipopolysaccharides (LPS, outer leaflet) and phospholipids (inner leaflet). LPS imparts strongly negative charges to the cell surface. The presence of negatively charged lipids such as phosphatidylglycerol (PG), phosphatidylserine (PS), or cardiolipin (CL) in microbial cell membrane, make the outer surface appealing to cationic molecules such as AMPs.[12] Both outer membrane of Gram-negative bacteria and thick cell wall of Gram-positive bacteria play important roles in supporting cell morphology and improving resistance to environmental changes. Due to the negatively-charged property of cell wall or outer membrane, whose barrier functions should be considered in case of AMP attacking bacterial cells, such as reducing peptides' efficiency of cytoplasmic membrane penetration and delaying peptides' intracellular interaction mechanisms.

Other than the various lipids and polyanionic molecules composed of the membrane, a large amount of proteins cover about 30 % of the membrane area.[13, 14] Lipid domains together with proteins and lipid types associated with membrane proteins are of important implications in many cellular processes such as signal transduction and membrane fusion. Overall, lipids influence proteins mutually and shape the signal transduction of membrane proteins.[15]

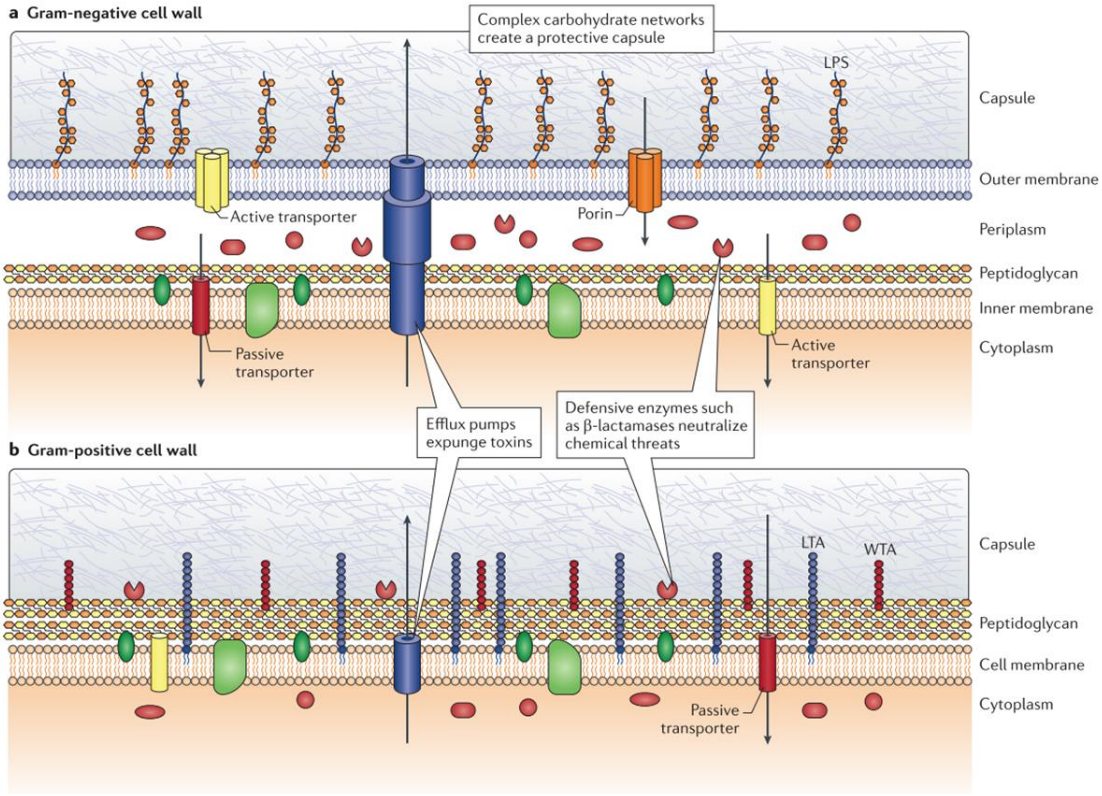

Figure 1. Schematic diagram of Gram-negative and Gram-positive cell walls.[16] Many components in the membrane associated with the cell walls limit the ability of antibiotic penetration and AMPs' membrane disruption, such as efflux pumps and defensive enzymes, thick coating of carbohydrate capsule, polyanionic lipopolysaccharide (LPS), lipoteichoic acid (LTA) and wall teichoic acid (WTA). Peripheral membrane proteins and enzymes are colored in green and dark red, respectively.

1.2 Novel antimicrobial peptides/polymers and their action mechanisms with bacteria

Natural antimicrobial peptides (AMPs) so far are of great amount, and are categorized via their diverse secondary structures and linear or nonlinear molecular structures. AMPs are usually with sequence length ranging from 10 to 40 amino acids and rich in positively-charged residues like Lys (K) and Arg (R), and also contain substantial proportion of hydrophobic residues like Ile (I), Leu (L), Phe (F) and Trp (W).[17] The above peptide composition give the ability of the molecules to fold into an amphiphilic structure, hydrophobic and cationic amino acids are spatially organized in separate patches upon binding onto biomembranes.[18, 19] As a salient feature, AMPs' amphiphilicity is helpful in their interaction with the biological membranes, and plays important role in ranging from membrane permeability change to interaction with cytoplasmic molecules.[20]

Other than the typical action modes between AMP and biological membrane, they are barrel-stave, carpet and toroidal models[21], Rathinakumar and co-workers[22, 23] proposed that peptides' antimicrobial activities related to their membrane targeting were not dependent on specific peptide sequences or secondary structures (such as beta-strand, alpha-helix, or both of beta-strand and alpha-helix), "interfacial activity" of peptide should attract more attention, namely AMPs partition into the membrane and reorganize the membrane structure continuously. They pointed out that after peptide's binding onto membrane, the dynamic procedure of peptide self-assembly onto membrane and following cell penetration or pore-formation are critical to cause potent membrane-destabilization.

High level of protease within chronic wounds would cleavage AMPs constituting natural amino acids into nonfunctional residue segments. For example, protease containing wound fluids from diabetic foot ulcers can degrade host defense peptide LL-37 and lower its therapeutic efficacy.[24] To overcome peptide proteolysis in antimicrobial treatment *in vivo*, D-amino acids were introduced into natural peptides to substitute L-amino acids, while the peptides still kept antimicrobial potency and exhibited ideal protease-resistance.[25] It was reported that AMPs composed of beta-amino acids with good resistance to enzymatic proteolysis had been designed.[26, 27] Meanwhile, staple peptides were also constructed and exhibited improved metabolic stabilities compared to linear short peptides.[28-30] On the other hand, the introduction of both L- and D-amino acids into linear or cyclic peptides can also be used to regulate peptide's selectivity and antimicrobial potency.[31, 32]

Similar to AMPs, antimicrobial polymers mimic the structural features of host defense peptides (HDPs) and play important roles in more extensive antimicrobial scenes based on polymers' salient modifiable advantages.[12] In terms of antimicrobial mechanisms of polymers, even though they lack defined sequence, molecular weight and secondary conformation, they exert effects on permeability change of both outer and inner membranes in a similar manner to HDPs. Other than their effective binding with anionic lipids such as LPS and PG in membrane, it has been shown that those antimicrobial polymers displayed good affinity to peptidoglycan matrices and LTAs.[33, 34]

Amphiphilic AMPs are well-known for their sequence properties (such as secondary conformation and net charge) and potent antimicrobial activities, the fact of AMPs' self-assembly was neglected. Other than above peptide's membrane action linked to their antimicrobial activities, peptides' self-assembly has been considered to be an important property, and is highly related to their membrane behaviors. Overall, the diverse effects of peptide self-assembly includes peptides' bioactivities, action modes, cell toxicity and releasing efficiency.[35]

1.3 Environmental responsive AMPs and their applications

With the challenges from the complex microenvironments for the AMPs *in vivo*, different strategies for AMP's design and loading/releasing were employed to establish bio-responsive AMP systems. AMPs involving the protonation of histidine and aspartic acid residues exhibit high pH-dependent antimicrobial activity. In most cases, these AMPs are of good antimicrobial activity against microbes in presence of low pH condition, such acidic pH environment is generally found on the skin or at the initial phase of acute wound.[36, 37] Some pH-dependent AMPs have been developed for medical implications and shown good performances in clinical trials, including human cathelicidin LL-37.[38, 39]

Meanwhile, efforts have been made for designing AMP loading/releasing systems (such as antimicrobial hydrogels) aiming for a more precise and controllable release in the implications of wound-healing. To make use of the acidic microenvironment (pH ~5.5) in the infected chronic wounds, Wang *et al*. designed a pH-switchable AMP hydrogel showing broad-spectrum antimicrobial activity only under acidic condition and eradicating methicillin-resistant *Staphylococcus aureus* (MRSA) biofilm. It should be worth mentioning that acidic pH environment destabilized the nanofiber network of hydrogel and achieved the continuous peptide release.[40] For the situation of rich hydrolase in wound environments, peptides' property of enzymatic biodegradation can be suitable for the loading and controlled release of an AMP. A short peptide crosslinker was co-synthesized with a polymer scaffold to obtain the capacity of both drug loading (such as AMPs and antibiotics) and being cleaved by matrix metalloproteinase 8 (MMP-8).[41] The controllable release of AMPs can be achieved after AMPs loaded into such hydrogel scaffolds and used in chronic wound environment. Some systematic studies of bio-responsive hydrogels to be utilized and achieving on-demand AMP release in application of the wound treatments had been reviewed by Ulijn and Niazi *et al*.[42, 43]

1.4 Effects of drug combinations against pathogenic bacteria

Drug combinations in treatment of pathogenic bacteria can result in 4 different forms of interactions: synergism, additivity, antagonism and even suppression (**Figure 2**).[44] The effect of two combined drugs is stronger, equal, and weaker than that of the individual drug in the equivalent dose, respectively. Antagonism, when a drug hinders the effect of another drug, was reported early in the history of antibiotic implication as a warning against indeterminate treatment. Suppression is a subclass of antagonism in which the combined treatment effect is weaker than that of at least one of the drugs alone. The suppressive effect reported by Chait *et al*.[45] is a differential selection that can be inverted in a hyper-antagonistic class of drug combinations.

The "chequerboard" experiment is one of the most well-known and in simple forms for determination of fractional inhibitory concentration index (FICI), in which a two-dimensional array of serial concentrations of test compounds is used as the basis to evaluate that paired agents can exert inhibitory effects of different modes. FICI determination and time-killing pharmacodynamics (PD) experiments are two mainly popular methodologies accounted for antimicrobial interaction assessments.[46] FICI is defined as follow:

$$FICI = FICI_A + FICI_B \qquad \text{Equation (1)}$$

where $FICI_A$ is the ratio of MIC of drug A in combination and MIC of drug A alone, while $FICI_B$ is the same meaning of drug B. The FICI was interpreted as follows: synergy ($FICI \leq 0.5$), additive ($0.5 < FICI \leq 1$), indifference ($1 < FICI \leq 2$) and antagonism ($FICI > 2$). While in one editorial on the Journal of Antimicrobial Chemotherapy in 2003, it was insisted as a standard that authors submitting papers containing FICI data restricted themselves to interpretations of “synergy” ($FICI \leqslant 0.5$), “antagonism” ($FICI > 4.0$) and “no interaction” ($FICI > 0.5\text{-}4.0$).[46]

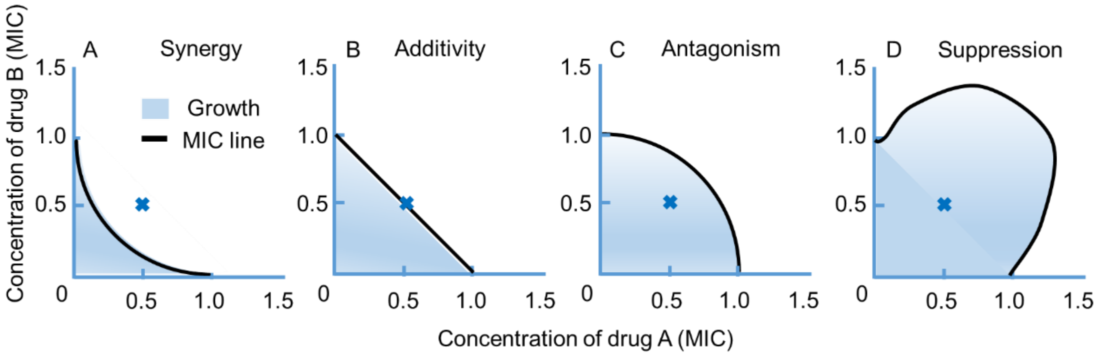

Figure 2. Four typical effects of drug pairs in treatment of microbes. (A) Area below minimal inhibitory concentration (MIC) line signifies synergy; (B) linear line signifies additive effect; (C&D) areas above linear MIC lines signify antagonism and even suppression. The drug concentrations marked by ✖ allow bacterial growth in the antagonistic case (FICI = 1) but not in the synergistic case (FICI << 1).

The advantage of synergistic drug combinations would lower drug toxicity and reduce side effects by high doses of single components. Drug pairs provide an additional treatment choice in some specific situations such as overcoming antibiotic resistance and effective concentration of single drug cannot be accumulated. Extensive studies now focus on designing new AMPs with less toxicity and applying AMPs in synergy studies due to their different targets compared to most conventional antibiotics. For example, Otvos *et al*. reported that AMP at sublethal concentration could impair the activity of drug-resistance related proteins and fully recover the activity of complementary antibiotic.[47] The different modes of action indicated the distinguished cell viability in AMPs killing bacteria, through general membrane interaction, from newly found intracellular targets or modulation of the host immunoregulation.[48]

Other than the synergy between AMPs and antibiotics, synergetic effects between AMPs would explain the presence of so many homologous AMPs in each specie, together with the need of wider antimicrobial spectrum and the inhibition of drug-resistance. In the study of the membrane disruption by natural AMPs piscidin 1 and 3 derivatized from the vertebrates, Hayden and colleagues found their complementary effects in antimicrobial activity based on the fact that piscidin 1 was more disruptive to bacteria membrane, while piscidin 3 bound stronger with DNA after membrane penetration.[49, 50] The synergy effects between AMP magainin II and synthetic derivative PGLa were supported by the evidence that a specific peptide complex formed upon their binding onto bacterial membrane model improved the rate of membrane pore formation in contrast to the single component.[51, 52]

1.5 The synergic mechanisms of combinatorial therapy

For drug combinations showing synergistic effects, the cellular interaction targets of two drugs should be different and have no conflicts. Bacteriostatic antibiotics with drug-target interactions, and their respective direct effects, are generally well-characterized. In contrast, bactericidal antibiotics with diverse targets (cell wall, outer membrane and intracellular targets) have been hypothesized to kill bacteria, in part by inducing production of damaging reactive species.

It is paramount to explore the rationale of agent combination to increase potency and efficacy through their combinatorial effects. Ankomah *et al*.[53] performed a series of work related to antimicrobial chemotherapy of drug combination to evaluate the pharmacodynamics, population and evolutionary dynamics by a combination of mathematical models and *in vitro* experiments. Time killing experiments with single and pairs of antibiotics are used to estimate the parameters and evaluate the fit of Hill-function-based pharmacodynamics models.[53] Compared to accurate estimating methods for synergistic drug pairs against bacteria, it is more important to explore universal combination routines and make “old drug” spring to life as drug combination. To make full use of current known drug targets especially resistance related targets, screening drug pairs targeting differently will greatly reduce the cost and alleviate the pressure in aimlessly exploring new combinations. Tan *et al.*[54] achieved the synergistic bioactivity of both agents affecting two interdependent cellular processes required for cell growth as well as the targeted inactivation of the resistance mechanism.

2. Outline of the thesis

In this PhD project, both coarse-graining and atomistic MD simulations were used to investigate peptides/lipopeptides’ self-assembly and aggregating behaviors in bulk solution, and peptides’ interaction including binding, insertion and self-assembly upon exposure to different lipid membranes. Computing simulations directly present the phenomena of peptide-membrane interaction process and their final equilibrated states, but experimental work is important and complementary to them. SANS has been employed to investigate peptides’ self-assembly behaviors in complement to other measurements like atomic force microscopy (AFM), and their action modes with membrane mimicry liposomes and the continuous effects on liposome size and morphology. NR is the main technique to study the specific binding of peptide onto Langmuir monolayer at the air/water interface, and provide details on the amount of peptide adsorption and structural changes of monolayers. Meanwhile, to reveal the relationship between peptides’ membrane behaviors and antimicrobial performances, different mechanisms at different levels should be unraveled through many commonly used techniques, such as fluorescence labeling and imaging, scanning electron microscope (SEM), circular dichroism (CD), Raman spectroscopy, and various biological assays. Here this part will outline the thesis structure and topics we studied. Methodologies and experimental details are given in the corresponding chapters

(**Chapter 2-5**).

In brief, we were trying to use the tools to bridge our understanding of the relation between peptides' membrane activity and antimicrobial potency, which would be significant for design of more effective AMPs. Four representative AMPs ($G(IIKK)_3I$/G_3; $G(IIKK)_4I$/G_4; GIGAVLKVLTTGLPALISWIKRKR/Melittin; GLLDLLKLLLKAAG/LDKA) was selected to study peptides' behaviors in the solution and their relation to membrane activities, and the role of peptides' interaction with both outer and inner membranes in their antimicrobial activities against Gram-negative bacteria. In this procedure, both experimental work and computing simulations were employed, it was found that NR would be in good complement with MD simulations.

On the other hand, drug combinations based on our designed peptides and conventional antibiotics were designed to study the mechanism of synergy effects in treatment of Gram-negative bacteria strains, and the intermolecular interaction of drug pairs in procedure of membrane binding. The formula of drug pairs would be of important role in clinical applications to share the advantages and avoid the disadvantages of multiple components. Furthermore, the pH-responsive antimicrobial peptides were designed for the application in the specific environments and of combining with conventional antibiotic. Furthermore, the self-assembly and antimicrobial mechanisms of pH-responsive peptide were studied, $G(IIKD)_3I$ (3D) showed a typical change of secondary conformation dependent on pH conditions under monomer/oligomer states. The pH conditions can adjust the charged states of peptide and regulate peptide's interaction with both outer and inner membranes including membrane leakage and depolarization, and hence showed selectively antimicrobial activity against both sensitive and drug-resistant Gram-negative strains.

In comparison to the treatment of Gram-negative bacteria, Gram-positive bacteria also widely threaten the healthcare system especially from the infectious influence of methicillin-resistant *S. aureus* (MRSA). To explore the mechanism of fast bacterial killing by AMPs, four different AMPs were designed by the substitution of cationic K (Lys) in pristine G(IIKK)$_3$I (GIK) with polar residue R (Arg) to be G(IIRR)$_3$I (GIR), or the substitution of hydrophobic I (Ile) with aromatic F (Phe)/W (Trp) to be G(FFKK)$_3$F (GFK) or G(WWKK)$_3$W (GWK). To explore peptides' membrane targeting modes linked their differential bacterial killing effects, peptides' interactions with LTA in cell wall and cytoplasmic membrane were studied via SEM, fluorescent assays, SANS, NR and MD simulations. It was found that other than the peptides' effects on membrane leakage and depolarization, their effects on membrane fluidity by intramembrane nanoaggregates would be important to cause membrane dysfunction and continuous death of bacteria cell.

References

[1] Hurdle JG, O'Neill AJ, Chopra I, Lee RE. Targeting bacterial membrane function: an underexploited mechanism for treating persistent infections. Nature Reviews Microbiology 2010;9:62-75.
[2] Yoshida M, Hinkley T, Tsuda S, Abul-Haija YM, McBurney RT, Kulikov V, et al. Using Evolutionary Algorithms and Machine Learning to Explore Sequence Space for the Discovery of Antimicrobial Peptides. Chem 2018;4:533-43.
[3] Lee EY, Lee MW, Fulan BM, Ferguson AL, Wong GCL. What can machine learning do for antimicrobial peptides, and what can antimicrobial peptides do for machine learning? Interface focus 2017;7:20160153.
[4] Söylemez ÜG, Yousef M, Kesmen Z, Büyükkiraz ME, Bakir-Gungor B. Prediction of Linear Cationic Antimicrobial Peptides Active against Gram-Negative and Gram-Positive Bacteria Based on Machine Learning Models. Applied Sciences 2022;12:3631.
[5] Chen CH, Starr CG, Troendle E, Wiedman G, Wimley WC, Ulmschneider JP, et al. Simulation-Guided Rational de Novo Design of a Small Pore-Forming Antimicrobial Peptide. Journal of the American Chemical Society 2019;141:4839-48.
[6] Ciumac D, Gong H, Hu X, Lu JR. Membrane targeting cationic antimicrobial peptides. Journal of colloid and interface science 2019;537:163-85.
[7] Zhu Y, Mohapatra S, Weisshaar JC. Rigidification of the Escherichia coli cytoplasm by the human antimicrobial peptide LL-37 revealed by superresolution fluorescence microscopy. Proceedings of the National Academy of Sciences 2019;116:1017-26.
[8] Parasassi T, Gratton E. Membrane lipid domains and dynamics as detected by Laurdan fluorescence. Journal of Fluorescence 1995;5:59-69.
[9] Swain J, Khoury ME, Flament A, Dezanet C, Briée F, Smissen PVD, et al. Antimicrobial activity of amphiphilic neamine derivatives: Understanding the mechanism of action on Gram-positive bacteria. BBA - Biomembranes 2019;1861:182998.

[10] Chen CHS, Charles G. Guha, Shantanu Wimley, William C. Ulmschneider, Martin B. Ulmschneider, Jakob P. Tuning of a Membrane-Perforating Antimicrobial Peptide to Selectively Target Membranes of Different Lipid Composition. The Journal of membrane biology 2021;254:75-96.
[11] Poxton IR. Teichoic Acids, Lipoteichoic Acids and Other Secondary Cell Wall and Membrane Polysaccharides of Gram-Positive Bacteria. 2015:91-103.
[12] Ganewatta MS, Tang C. Controlling Macromolecular Structures towards Effective Antimicrobial Polymers. Polymer 2015;63:A1-A29.
[13] Harayama T, Riezman H. Understanding the diversity of membrane lipid composition. Nature reviews Molecular cell biology 2018;19:281-96.
[14] van Meer G, Voelker DR, Feigenson GW. Membrane lipids: where they are and how they behave. Nature reviews Molecular cell biology 2008;9:112-24.
[15] Marrink SJ, Corradi V, Souza PCT, Ingólfsson HI, Tieleman DP, Sansom MSP. Computational Modeling of Realistic Cell Membranes. Chemical Reviews 2019;119:6184-226.
[16] Ruben Tommasi DGB, Grant K. Walkup, John I. Manchester and Alita A. Miller. ESKAPEing the labyrinth of antibacterial discovery. Nature Reviews Drug Discovery 2015;14:529-42.
[17] Epand RM, Vogel HJ. Diversity of antimicrobial peptides and their mechanisms of action. Biochimica et Biophysica Acta (BBA) - Biomembranes 1999;1462:11-28.
[18] Zasloff M. Antimicrobial Peptides of Multicellular Organisms. Nature 2002;415:389-95.
[19] Hancock RE, Sahl HG. Antimicrobial and host-defense peptides as new anti-infective therapeutic strategies. Nat Biotechnol 2006;24:1551-7.
[20] Castelletto V, Edwards-Gayle CJC, Hamley IW, Barrett G, Seitsonen J, Ruokolainen J. Peptide-stabilized emulsions and gels from an arginine-rich surfactant-like peptide with antimicrobial activity. ACS applied materials & interfaces 2019;11:9893-903.
[21] Brogden KA. Antimicrobial peptides: pore formers or metabolic inhibitors in bacteria? Nature Reviews Microbiology 2005;3:238-50.
[22] Rathinakumar R, Wimley WC. Biomolecular Engineering by Combinatorial Design and High-throughput Screening: Small, Soluble Peptides that Permeabilize Membranes. Journal of the American Chemical Society 2008;130:9849–58.
[23] Ramesh Rathinakumar WFW, William C. Wimley. Broad-spectrum antimicrobial peptides by rational combinatorial design and high-throughput screening: the importance of interfacial activity. Journal of the American Chemical Society 2009;131:7609-17.
[24] McCrudden MTC, McLean DTF, Zhou M, Shaw J, Linden GJ, Irwin CR, et al. The Host Defence Peptide LL-37 is Susceptible to Proteolytic Degradation by Wound Fluid Isolated from Foot Ulcers of Diabetic Patients. International Journal of Peptide Research and Therapeutics 2014;20:457-64.
[25] Maloy WL, Kari UP. Structure–activity studies on magainins and other host defense peptides. Biopolymers 1995;37:105-22.
[26] Porter EA, Wang X, Lee H-S, Weisblum B, Gellman SH. Non-haemolytic β-

amino-acid oligomers. Nature 2000;404:565-.

[27] Hamuro Y, Schneider JP, DeGrado WF. De Novo Design of Antibacterial β-Peptides. Journal of the American Chemical Society 1999;121:12200-1.

[28] Dinh TTT, Kim D-H, Luong HX, Lee B-J, Kim Y-W. Antimicrobial activity of doubly-stapled alanine/lysine-based peptides. Bioorganic & Medicinal Chemistry Letters 2015;25:4016-9.

[29] Li X, Chen S, Zhang WD, Hu HG. Stapled Helical Peptides Bearing Different Anchoring Residues. Chem Rev 2020;120:10079-144.

[30] Sabale PM, Imiolek M, Raia P, Barluenga S, Winssinger N. Suprastapled Peptides: Hybridization-Enhanced Peptide Ligation and Enforced alpha-Helical Conformation for Affinity Selection of Combinatorial Libraries. Journal of the American Chemical Society 2021;143:18932-40.

[31] Fernandez-Lopez S, Kim H-S, Choi EC, Delgado M, Granja JR, Khasanov A, et al. Antibacterial agents based on the cyclic d,l-α-peptide architecture. Nature 2001;412:452-5.

[32] Oren Z, Shai Y. Cyclization of a Cytolytic Amphipathic α-Helical Peptide and Its Diastereomer: Effect on Structure, Interaction with Model Membranes, and Biological Function. Biochemistry 2000;39:6103-14.

[33] Lienkamp K, Kumar KN, Som A, Nusslein K, Tew GN. "Doubly selective" antimicrobial polymers: how do they differentiate between bacteria? Chemistry – A European Journal 2009;15:11710-4.

[34] Epand RF, Mowery BP, Lee SE, Stahl SS, Lehrer RI, Gellman SH, et al. Dual Mechanism of Bacterial Lethality for a Cationic Sequence-Random Copolymer that Mimics Host-Defense Antimicrobial Peptides. Journal of Molecular Biology 2008;379:38-50.

[35] Tian X, Sun F, Zhou XR, Luo SZ, Chen L. Role of peptide self-assembly in antimicrobial peptides. Journal of Peptide Science 2015;21:530-9.

[36] Jones EM, Cochrane CA, Percival SL. The Effect of pH on the Extracellular Matrix and Biofilms. Advances in wound care 2015;4:431-9.

[37] Schneider LA, Korber A, Grabbe S, Dissemond J. Influence of pH on wound-healing: a new perspective for wound-therapy? Archives of dermatological research 2007;298:413-20.

[38] Malik E, Dennison SR, Harris F, Phoenix DA. pH Dependent Antimicrobial Peptides and Proteins, Their Mechanisms of Action and Potential as Therapeutic Agents. Pharmaceuticals 2016;9.

[39] Gontsarik M, Yaghmur A, Ren Q, Maniura-Weber K, Salentinig S. From structure to function: pH-switchable antimicrobial nano-self assemblies. ACS applied materials & interfaces 2019;11:2821-9.

[40] Wang J, Chen XY, Zhao Y, Yang Y, Wang W, Wu C, et al. pH-Switchable Antimicrobial Nanofiber Networks of Hydrogel Eradicate Biofilm and Rescue Stalled Healing in Chronic Wounds. ACS nano 2019;13:11686-97.

[41] Guo J, Sun H, Lei W, Tang Y, Hong S, Yang H, et al. MMP-8-Responsive Polyethylene Glycol Hydrogel for Intraoral Drug Delivery. Journal of dental research 2019;98:564-71.

[42] Niazi M, Alizadeh E, Zarebkohan A, Seidi K, Ayoubi-Joshaghani MH, Azizi M, et al. Advanced Bioresponsive Multitasking Hydrogels in the New Era of Biomedicine. Advanced Functional Materials 2021:2104123.

[43] Ulijn RV, Bibi N, Jayawarna V, Thornton PD, Todd SJ, Mart RJ, et al. Bioresponsive hydrogels. Materials Today 2007;10:40-8.

[44] Yeh PJ, Hegreness MJ, Aiden AP, Kishony R. Drug interactions and the evolution of antibiotic resistance. Nature Reviews Microbiology 2009;7:460-6.

[45] Chait R, Craney A, Kishony R. Antibiotic interactions that select against resistance. Nature 2007;446:668-71.

[46] Odds FC. Synergy, antagonism, and what the chequerboard puts between them. J Antimicrob Chemother 2003;52:1.

[47] Otvos L, de Olivier Inacio V, Wade JD, Cudic P. Prior Antibacterial Peptide-Mediated Inhibition of Protein Folding in Bacteria Mutes Resistance Enzymes. Antimicrobial agents and chemotherapy 2006;50:3146-9.

[48] Cassone M, Otvos Jr L. Synergy among antibacterial peptides and between peptides and small-molecule antibiotics. Expert Review of Anti-infective Therapy 2010;8:703-16.

[49] Perrin BS, Jr., Fu R, Cotten ML, Pastor RW. Simulations of Membrane-Disrupting Peptides II: AMP Piscidin 1 Favors Surface Defects over Pores. Biophysical journal 2016;111:1258-66.

[50] Hayden RM, Goldberg GK, Ferguson BM, Schoeneck MW, Libardo MD, Mayeux SE, et al. Complementary Effects of Host Defense Peptides Piscidin 1 and Piscidin 3 on DNA and Lipid Membranes: Biophysical Insights into Contrasting Biological Activities. The journal of physical chemistry B 2015;119:15235-46.

[51] Westerhoff HV, Zasloff M, Rosner JL, Hendler RW, De Waal A, Vaz Gomes A, et al. Functional synergism of the magainins PGLa and magainin-2 in Escherichia coli, tumor cells and liposomes. Eur J Biochem 1995;228:257-64.

[52] Katsumi Matsuzaki YM, Ken-ya Akada, Osamu Murase, Shuji Yoneyama, Michael Zasloff, and Koichiro Miyajima. Mechanism of Synergism between Antimicrobial Peptides Magainin 2 and PGLa. Biochemistry 1998;37:15144-53.

[53] Ankomah P, Levin BR. Two-drug antimicrobial chemotherapy: a mathematical model and experiments with Mycobacterium marinum. PLoS pathogens 2012;8:e1002487.

[54] Tan C, Therien A, Lu J, Lee SH, Caron A, Gill C, et al. Restoring Methicillin-Resistant Staphylococcus aureus Susceptibility to beta-Lactam Antibiotics. Science translational medicine 2012;4:126ra35.

Chapter 2 Intramembrane Nanoaggregates of Antimicrobial Peptides Play a Vital Role in Bacterial Killing

Mingrui Liao,[1#] Haoning Gong,[1] Xuebo Quan,[2] Ziwei Wang,[3] Xuzhi Hu,[1] Zheng Chen,[2] Zongyi Li,[1] Huayang Liu,[1] Lin Zhang,[1] Andrew J. McBain,[4] Thomas A. Waigh,[1] Jian Zhou,[2] and Jian Ren Lu[1,*]

[1]Biological Physics Laboratory, Department of Physics and Astronomy, School of Natural Science, The University of Manchester, Oxford Road, Manchester M13 9PL, UK.

[2]School of Chemistry and Chemical Engineering, Guangdong Provincial Key Laboratory for Green Chemical Product Technology, South China University of Technology, Guangzhou 510640, China.

[3]National Graphene Institute, The University of Manchester, Oxford Road, Manchester M13 9PL, UK.

[4]Division of Pharmacy and Optometry, School of Health Sciences, Faculty of Biology, Medicine and Health, The University of Manchester, Oxford Road, Manchester M13 9PL, UK.

[#]To whom as PhD candidate should be responsible to all the experiments.
*To whom all correspondence should be made: J.lu@manchester.ac.uk

Abstract

Recent developments in antimicrobial peptides (AMPs) have focused on the rational design of short sequences with less than 20 amino acids due to their relatively low synthesis costs and ease correlation of the structure-function relationship. However, gaps remain in our understanding of how short cationic AMPs interact with the bacterial outer and inner membranes to affect their antimicrobial efficacy and dynamic killing. We have examined the membrane-lytic actions of two designed AMPs, G(IIKK)$_3$I-NH$_2$ (G$_3$) and G(IIKK)$_4$I-NH$_2$ (G$_4$), and previously-studied GLLDLLKLLLKAAG-NH$_2$ (LDKA, biomimetic) and GIGAVLKVLTTGLPALISWIKRKR-NH$_2$ (Melittin, natural) as controls. The mechanistic processes of membrane damage and disruption strength of the four AMPs were characterized by molecular dynamics simulations and experimental measurements including neutron reflection and scattering. The results from the combined studies are characterized by distinctly different intramembrane nanoaggregates formed upon AMP-specific binding, reflecting clear influences of AMP sequence and charge and inner and outer membranes. G$_3$ and G$_4$ displayed different nanoaggregation with the outer and inner membranes, and the smaller sizes and further extent of insertion of the intramembrane nanoaggregates into bacterial membranes correlate well to their greater antimicrobial efficacy and faster dynamic killing. This work demonstrates the crucial roles of intramembrane nanoaggregates in optimising antimicrobial efficacy and dynamic killing.

Keywords: Antimicrobial peptides, nanoaggregates, sefl-assembly, lipid membrane, AMP design, intrammbrane aggregation, antimicrobial efficiency, bionanomaterials

1. Introduction

Since the discovery of penicillin, many antibiotics have been developed to protect humans and animals from infection. Antibiotics exert their antibacterial action by inhibiting the functions of biological pathways. A major drawback is however the development of resistance due to the pharmacological specificity of the antibiotics.[1-3] Commonly used antibiotics such as ampicillin, tetracycline and polymyxin B (PmB) are often associated with resistance, reducing their efficacy in clinical applications.[4-5] There is, therefore, an urgent need to develop more effective antimicrobial agents, particularly with efficacy against multidrug-resistant (MDR) pathogens.

Many natural cationic antimicrobial peptides (AMPs) have been discovered from the innate immune systems of humans, animals and plants.[1-3] Unlike most antibiotics, AMPs kill pathogens by binding to their membranes through physical interactions. Secondary conformational changes often occur after membrane association, making AMPs more effective at disrupting membrane structures and killing microorganisms by eliciting the leakage of internal contents.[6] Some 3000 natural cationic AMPs have been reported, with large variations in size, stability, potency and toxicity.[7] Because of the huge differences in sequence, length, source, side effects and toxicity, it has been difficult to understand how sequences directly affect the structure and function of AMPs. From the development of AMPs for medical applications, the long native sequences that may involve other biological functions can complicate their potential uses as therapeutics. Further issues with long sequences lie in their vulnerability to enzymatic degradation, cost of synthesis, purification and control of their secondary structures in product formulation.[8]

Natural AMPs that have been extensively studied include Melittin from bee venom, Maginin-2 frog skin and Cathelicidin LL-37 from human tissues.[9-11] These natural AMPs and their mimetics such as Pexiganan have shown a wide range of efficacy against both Gram-positive and Gram-negative bacteria.[12-15] Rational designed AMPs aim to shorten the sequences, whilst optimizing their functional performance against clinical pathogens, such as Gram-negative *Escherichia coli* and *Pseudomonas* *aeruginosa*, and Gram-positive *Streptococcus aureus, Streptococcus pyogenes* and *Enterococcus faecalis* and several antibiotic-resistant strains such as vancomycin-resistant *S. aureus*.[16] Malmsten *et al.*[17-18] have designed C-terminal end-tagging AMPs with W and F residues based on the proline-arginine-leucine-rich repeat protein (PRELP). They observed increased antimicrobial potency from the peptides with end sequences of GRRPRPRPRP and RRPRPRPRP against Gram-positive *S. aureus* and Gram-negative *P. aeruginosa* clinical isolates, with similar performance also observed in the presence of human plasma and blood. Other cationic peptides such as Aremicin and its isoform have also been explored for their membrane permeabilization effects.[19-21]

Although it is widely hypothesized that AMPs permeate bacterial membranes by carpet-like or toroidal-pore modes of action forming transmembrane nanopores,[14] there is still a lack of understanding of dynamic binding processes and morphological structures. Furthermore, the exact processes of membrane disruptions from different AMPs may differ. It is therefore difficult to understand the mechanisms that underlie different antimicrobial efficacy, dynamic efficiency and cytotoxicity. Investigating how AMP molecules interact with bacterial membranes and the associated antimicrobial performance may inform the design of new AMPs by minimizing the cytotoxicity to host cells whilst maximizing their actions against pathogens.

Because membrane binding and subsequent interaction are key to understanding AMP-membrane interactive processes and controlling antimicrobial efficacy and efficiency, previous studies by Clifton *et al.*[22], Paracini *et al.*[23], Gong et al.[21] and others[24-27] have explored the development of asymmetric outer membrane (OM) and symmetric inner membrane (IM) models to facilitate experimental measurements and molecular dynamics (MD) simulations. Studies by Clifton *et al.*[22] and Paracini *et al.*[23] show how PmB, one of the few antibiotics which act directly on Gram-negative bacterial membranes, interacts with OM and IM membrane models, linking different membrane interactions to the rate-limiting steps of antimicrobial activity.

The current work aims to compare the behaviour of two of our designed short AMPs with the widely studied natural and biomimetic ones. By comparing the differential action modes targeting the OM and IM of Gram-negative bacteria, we explore the relationship between specific intramembrane aggregating behaviour of AMPs, their antimicrobial activity and dynamic killing efficiency. The combination of MD simulations and experimental measurements including neutron reflection and scattering offers crucial insights into the dynamic membrane-lytic processes and main structural characteristics of intramembrane nanoaggregates formed upon AMP binding. These nanostructures and their extent of insertion into bacterial membrane models provide vital evidence for direct correlation to their antimicrobial efficacy and dynamic killing.

2. Results and discussions

2.1 Antibacterial efficacy and biocompatibility evaluation

AMPs kill bacteria by binding to bacterial membranes and causing structural disruptons. Minimum inhibition concentration (MIC) is a good indicator of the antibacterial efficacy of an AMP. MIC values measured for the range of bacteria selected are shown in **Table S4**. G_3, G_4 and Melittin show MICs below 10 μM, whilst the MICs of LDKA are well above 10 μM against the two *E. coli* strains. In contrast, tetracycline and minocycline also show low MICs, consistent with their high potency. Based on the MIC values, both the designed AMPs and traditional antibiotics can inhibit bacterial growth against both Gram-positive and Gram-negative bacterial strains. In contrast, the high MICs against resistant MRSA and ESBL-*E. coli* for ampicillin are consistent with the expected antibiotic resistance. With MICs below 10 μM, G_3 and G_4 are the most potent of the tested antimicrobials against pathogenic and drug-resistant bacterial strains. Conversely, MICs of LDKA against antibiotic-resistant strains are higher than its MICs against the non-resistant bacterial strains. Whilst these results reveal the impact of different bacterial membranes in normal and resistant strains, they also point to the effects of sequence-specific influences of AMPs.

An important property of an AMP is its selective responses to pathogenic bacteria and mammalian host cells. In this regard, haemolysis was assessed over the AMP concentrations considerably above the ranges used for antimicrobial studies, with tetracycline and minocycline used as controls. **Figure S5A** shows the fastest rising haemolysis profile of Melittin over the low concentration range, with EC_{50} (50% haemolysis) being reached at just 6 μM, consistent with its high cytotoxicity. In contrast, G_3 has low haemolytic activity, with its haemolysis profile close to those of the two antibiotics up to 100 μM. The haemolysis profile of G_4 is also very low below 10 μM, but it starts to deviate from 10 to 100 μM, with faster rising over the higher concentration range. On the other hand, LDKA shows a steady rise of haemolysis, even over the low concentration range around 10 μM and reaches EC_{50} around 300 μM. (**Table S4**) These concentration-dependent haemolysis profiles thus reveal different membrane interactions of the AMP molecules once exposed to hRBCs.

The biocompatibility of AMPs was further assessed by exposing them to human adult skin cells (HDFa) and mouse embryo fibroblast cells (3T3), with the results shown in **Figures S5B&C**. Cell viability of 3T3 is lower than that of HDFa, but the data together show the highest biocompatibility from G_3, followed by LDKA, G_4 and Melittin; consistent with the expected high toxicity of Melittin.

2.2 Bacterial dynamic killing and membrane disruptions by AMPs

The dynamic killing experiment assesses the efficiency of an AMP at killing bacteria under a short time of exposure. The percentage of bacterial killing was quantified when bacteria were exposed to a given AMP at 2×MIC under different exposure times, followed by re-culturing overnight and counting the viable CFU (colony-forming units). As shown in **Figures 1A&B**, all AMPs can kill both *E. coli* strains to achieve 1000 times reduction (the log3 reduction) within 2~3 h. In contrast, it would require 6 h or longer for tetracycline to achieve comparable killing effects. In fact, G_3 and G_4 can achieve the log3 reduction within 30 min and are thus of higher bactericidal efficiency than LDKA and Melittin, even though Melittin shows attractive MICs. These differences must arise from how each AMP disrupts the bacterial membrane in different ways.

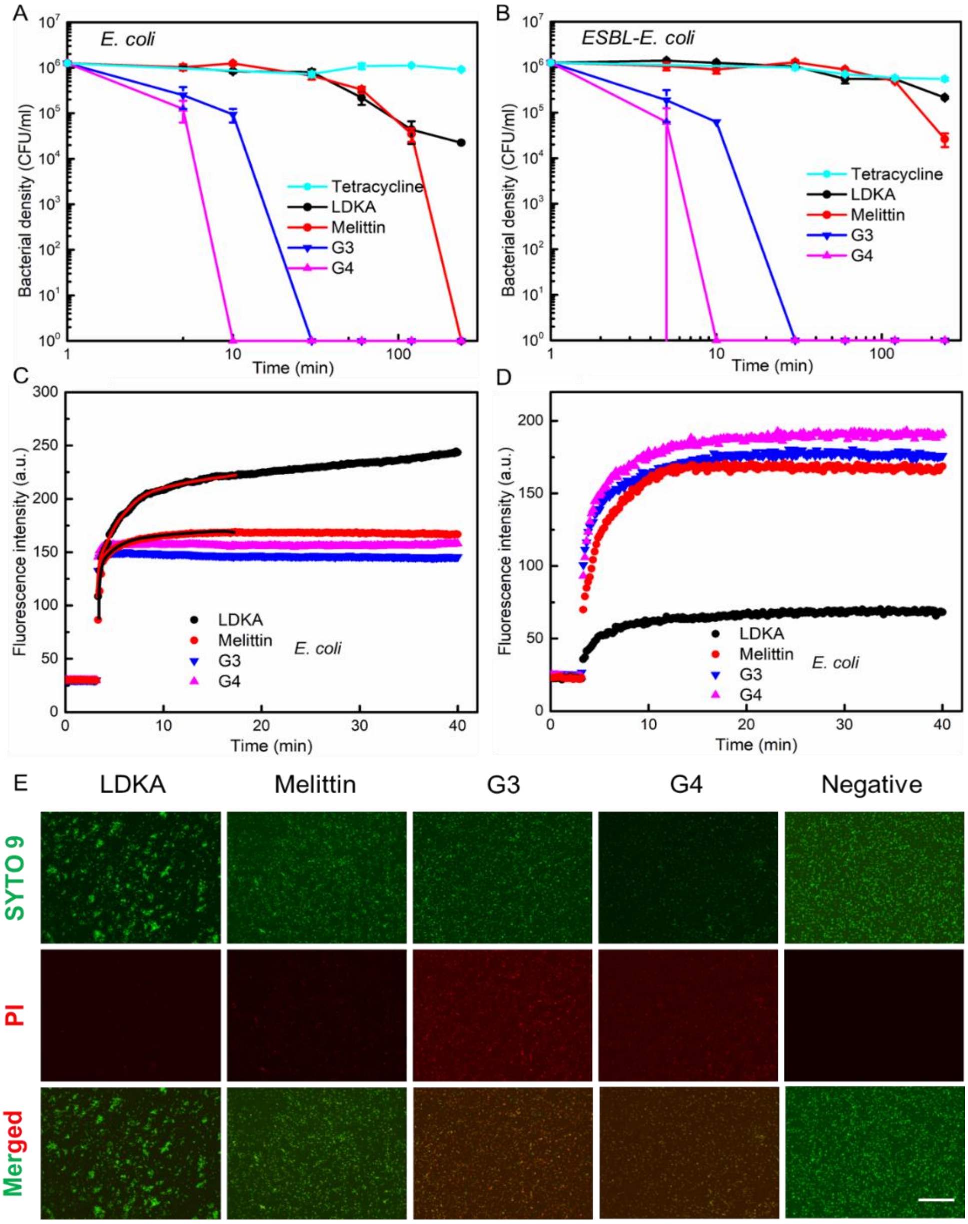

Figure 1. Dynamic killing performance of AMPs and antibiotics (at the concentrations of 2×MIC) against (A) Gram-negative *E. coli* and (B) ESBL-*E. coli*, plotted as bacterial density versus time. Fluorescence intensity is shown as a function of time for (C) permeability of outer membrane detected by fluorescent probe NPN and (D) cytoplasmic membrane depolarization by AMPs at 10 × MIC concentration for *E. coli* ATCC 25922 probed by a cationic dye DiSC$_3$(5). (E) Fluorescence microscopy images after SYTO 9/PI staining taken from *E. coli* (> 10^8 CFU/mL) after exposure to AMPs

(at 8 × MIC) for 3 h. Scale bar, 50 μm.

Dynamic killing profiles (**Figures 1A&B)** were measured at bacterial densities of 10^6 CFU/mL. As the dynamic killing process occurred very fast, it was difficult to visualize the different actions of the AMPs with bacterial membranes. To facilitate the direct observations of live/dead states of bacteria, Gram-negative *E. coli* cells were stained with SYTO 9 and propidium iodide (PI) after being incubated with AMPs at 10^8 CFU/ml (**Figure 1E**). The cell density employed in SYTO 9/PI staining was to enhance the total membrane surface area following the work by McGoverin *et al.*[28] AMP concentrations must also be adjusted to achieve the dynamic killing of bacteria that can be measured via fluorescence imaging. Fluorescence images taken from SYTO 9 staining show clear green spots in the bacterial samples, indicating that bacteria were distributed uniformly (data not shown). After exposure to AMPs for 3 h, however, different green intensities and spot sizes were observed (top row images in **Figure 1E**), indicating different levels of live bacteria under different physical states. Changes in red intensity were also observed after exposure to PI (middle row images in **Figure 1E**). Exposure of both G_3 and G_4 to *E. coli* led to a very strong red colour and hence high antimicrobial potency, while little red colour was detected from Melittin and LDKA, indicating high cell viability and low antimicrobial potency under similar treatments. When LDKA was added to *E. coli*, bacterial clusters occurred. Clustering might have worked to keep some bacteria alive. These observations reveal that G_3 and G_4 not only kill bacteria under lower MICs but also impose faster and more effective antibacterial actions than Melittin and LDKA.

To elucidate how the four AMPs kill bacteria, antimicrobial activity studies were carried out to explore whether AMPs killed bacterial cells by permeabilizing their OM, by depolarizing their cytoplasmic IM, or by a combination of both actions. Fluorescent probe NPN [1-(N-phenylamino) naphthalene] was used to assess whether AMPs were able to permeabilize the OM of *E. coli* and drug-resistant ESBL-*E. coli*. NPN is hydrophobic. It exhibits weak fluorescence emission in an aqueous environment but a strong signal when it permeates the bacterial OM that is damaged by AMP. **Figures**

1C&S4A show that the probe interacts with the lipidic environment of permeable OM once exposed to all four AMPs. LDKA achieved the strongest fluorescence intensity after the first 10 min exposure and the progressive increase in fluorescence intensity indicates that LDKA molecules binding onto the OM facilitated continuous permeability increase for NPN. In contrast, G_3 and G_4 can also change the membrane permeability quickly which reaches the equilibrium state within the first 5-10 min. Melitttin flows a similar trend but shows higher equilibrium fluorescence intensity, indicating its stronger ability to cause greater OM leakage and NPN permeation.

3,3'-dipropylthiacarbocyanine iodide ($DiSC_3(5)$) dye was used as a sensitive cationic indicator of membrane depolarization targeting the IM of *E. coli* and ESBL-*E. coli*, with the time-dependent changes shown in **Figure 1D&S4B**. The results indicate that all four AMPs can cause the IM depolarization of Gram-negative bacteria, but the degree of membrane disruption follows the order of $G_4 > G_3 \approx$ Melittin > LDKA, at the concentration of 10 × MIC. The highest fluorescence intensity from G_4 matches its fastest dynamic killing as shown in **Figure 1A**. The lowest fluorescence intensity from LDKA may result from its relatively low cationic net charge or the low transfer of LDKA to the inner membrane. These observations from bacterial systems promote further studies exploring how the AMPs interact with OM and IM via model membrane systems.

2.3 Membrane-lytic binding of AMPs

2.3.1 Secondary structural changes

The secondary structural conformations of the four AMPs in Tris buffer (pH = 7.4) and micellar solutions of sodium dodecyl sulphate (SDS, 25 mM, pH = 7.4) were compared. SDS micelles simulate an environment of negatively-charged microbial membranes. When changed from Tris buffer solution to SDS micellar solution, G_3 and G_4 transformed from non-ordered to α-helical conformations, evident from the characteristic double minima at ~208 and 222 nm (**Figures S6A&B**). Increase in the number of repeat units of IIKK enhances the helical propensity, evident from the lower mean residue ellipticity values of G_4 between 208 and 222 nm than those of G_3. In contrast, LDKA and Melittin already adopted distinct α-helical structures in the same buffer and they retained almost the same secondary structure in SDS micelles, showing that their formation of the α-helix configuration did not require interaction with the negatively charged micellar surface. LDKA and Melittin possess both positively and negatively charged amino acids which can self-promote the adoption of α-helix conformation and nanoaggregation through intermolecular electrostatic interaction.

2.3.2 Zeta potential changes and leakage from IM models

Zeta potential changes (**Figure S6C**) were measured by titrating AMP solutions into 30% negatively charged DMPG SUVs. With the addition of cationic AMPs, the Zeta potential of the SUVs increased, indicating AMP binding and the process was driven by electrostatic interaction. The surface Zeta potential of the 30% DMPG SUVs was measured to be -22.4 ± 1.5 mV. Upon the addition of 10 μM cationic LDKA, which matched the concentration for 100% SUV leakage (**Figure S6C**), the net surface Zeta potential of the SUV remained negative. For G_3, G_4 and Melittin, the Zeta potentials passed zero and became positive. LDKA has a net positive charge of 2 and is of low net charge density compared to the other 3 AMPs. The slight negative surface potential of the SUV after LDKA binding may simply result from the low net charges of LDKA or its deep penetration into the lipid bilayer.

Figure S6D shows the rise of the percentage of fluorescence leakage (5(6)-carboxyfluorescein, CF) from the SUVs as a function of AMP concentration. The SUVs are comprised of POPG and POPC (molar ratio = 3 : 7), providing another mimicry of the charged IM of Gram-negative bacteria. G_3, G_4 and Melittin show similar leakage profiles against AMP concentration, while the conventional antibiotics tetracycline and minocycline have no detectable influence on SUV leakage, indicating a different pathway of membrane permeation. Melittin is more hydrophobic than G_3, but G_4 is more cationic. Despite the distinct differences in their hydrophobicity associated with cationicity and structural features, the concentration-dependent membrane binding capability does not appear significantly different. The concentration of G_3 to achieve

50% membrane leakage (L_{50}) is just over 1 µM while the L_{50} values of G_4 and Melittin are between 0.5-0.8 µM. At the concentrations causing 100% membrane leakage (L_{100}), their concentration gaps become wider; while L_{100} for G_3 is more than 10 µM, the values for G_4 and Melittin are less than 3 µM, showing their more potent membrane-lytic actions. In contrast, LDKA is more hydrophobic and less cationic, but its L_{100} is comparable to G_4 and Melittin. The rather high level of leakage from the inner membrane in contrast to the data shown in **Figure 1D** indicates that it might be difficult for LDKA to penetrate through the OM.

2.3.3 Interactions with OM and IM

Further AMP-membrane interactive processes were evaluated by studying their interactions with LPS from *E. coli* using the BODIPY™-TR-cadaverine (BC) displacement assay. BC is amphiphilic, can bind to the lipid A region of LPS and undergo a fluorescence self-quenching. The binding of other exogenous compounds on LPS can then be monitored by following the displacement of the BC probe from its binding to LPS as indicated by increased fluorescence intensity.

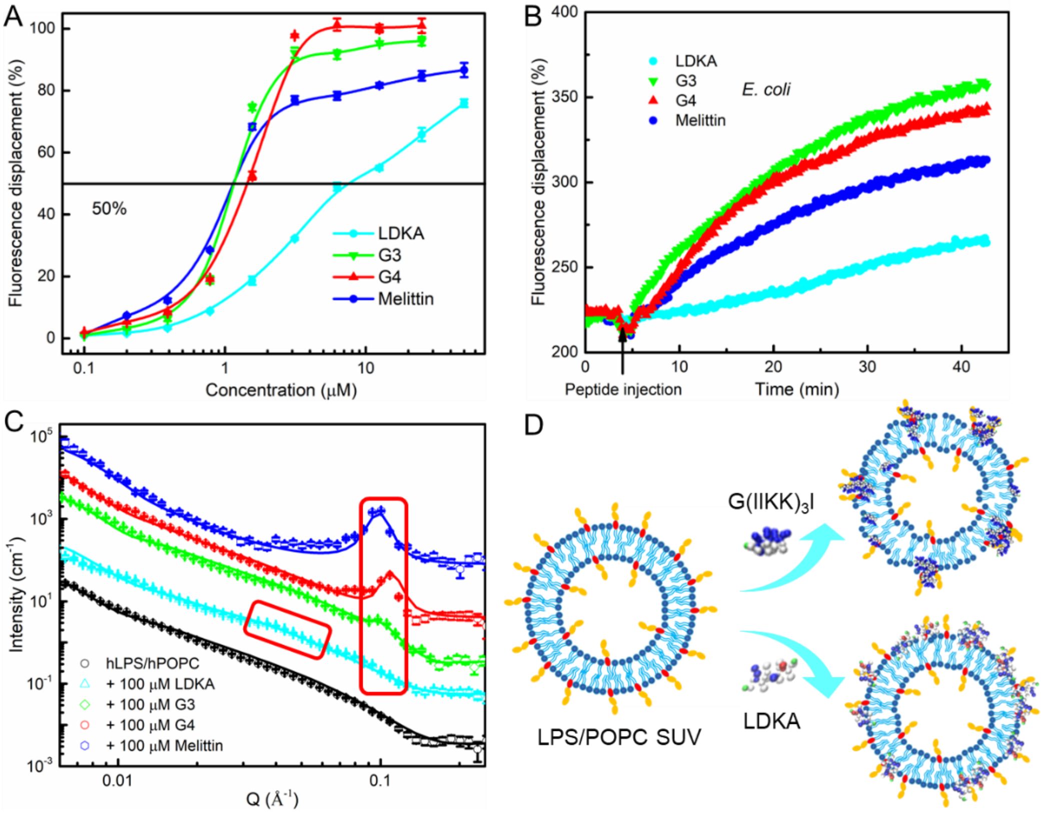

Figure 2. LPS displacement in cell-free and cell systems. (A) Fluorescence assays of BODIPY™-TR-cadaverine (BC) (5 µM) indicated rising BC fluorescence from cell-free LPS (dispersed at 20 µg/mL) with increasing AMP concentration; (B) dynamic BC fluorescence changes to indicate AMP binding to the LPS of *E. coli* (ATCC 25922) at the fixed concentration of 50 µM AMP. (C) SANS profiles of LPS/POPC SUVs (1 mM) in D_2O interacting with 100 µM G_3, G_4, LDKA and Melittin, plotted as a function of momentum transfer (Q). The continuous lines denote the best SUV model fits with the structural parameters listed in **Table S6.** (D) The schematic illustrations to depict intramembrane aggregates after AMP binding.

Figure 2A showed the displacement of the BC probe in the cell free-LPS with increasing AMP concentration. Displacement of BC from the cell free-LPS was observed from all four AMPs. The difference between them must arise from their different binding ability to LPS. The concentration of the 50% BC displacement for the AMPs followed the order of $G_3 \approx$ Melittin (1 µM) < G_4 (1.5 µM) < LDKA (7 µM), with Melittin showing an intermediate behavior of LPS binding.

To explore if the above LPS binding difference can also occur from bacteria, the same BC displacement assay was applied to *E. coli*. The steady rise of BC fluorescence shown in **Figure 2B** indicates the release of the BC probes with time, consistent with the gradual AMP binding to the OM of *E. coli*. Interestingly, the same trend of the BC displacement was observed, again in the ranking of $G_3 \approx G_4$ > Melittin > LDKA. These observations are consistent with the NPN uptake as shown in **Figure 1C**, indicating that LDKA and Melittin cannot be selective enough in LPS binding compared to G_3 and G_4.

To unravel the structural features of AMP binding to the OM characterized by the LPS component, SANS measurements of AMPs interacting with the LPS/POPC SUVs were carried out (**Figure 2C**). The LPS/POPC SUVs alone adopted a typical spherical structure. Upon binding of G_3/G_4/Melittin, the overall SUV nanostructures changed substantially. The most distinct structural change was the transformation of the single bilayer into periodic multi-bilayer stacks, supported by the broad peaks in their corresponding SANS profiles. In contrast, the similar shape in the profiles of SUVs with and without LDKA indicates no obvious size or structural changes upon LDKA binding. Thus, the occurrence of the broad peaks from the other three AMPs marks membrane fusion and the formation of AMP-LPS multi-layered stacks. The different binding and aggregating behaviors between LDKA and G_3 are schematically illustrated in **Figure 2D**.

The polydispersity index (PDI) of the bilayer thickness increased greatly from 0 to 0.3 or 0.4 after binding of SUVs with G_4 or Melittin, indicating non-uniform bilayer thickness as a result of the specific formation of LPS-AMP aggregates inserted into the membrane. The broad peaks have characteristic Q-positions at 0.1 (G_3), 0.11 (G_4) and 0.098 (Melittin) Å^{-1}, indicating the repeating bilayer unit thicknesses around 60 Å (=2π/Q), with the size for Melittin being the largest. The broad peak intensity or the full width at the half-maximum (FWHM) is relevant to the number of repeating units in stacks. These bilayer stacks were formed upon attack of the SUVs by the AMPs, and the order of the peak intensity follows: Melittin > G_4 > G_3 > LDKA, indicating that Melittin binding led to the stacks containing most bilayer repeats, followed by G_4.

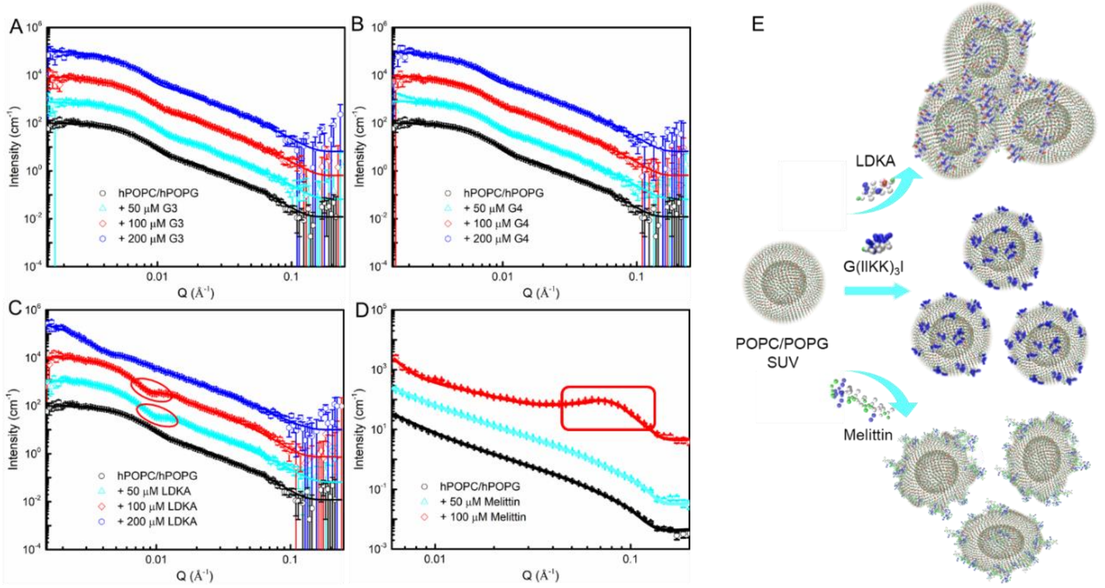

Figure 3. SANS profiles of POPG/POPC SUVs (1 mM) in D_2O interacting with (A) G_3, (B) G_4, (C) LDKA and (D) Melittin, plotted as a function of momentum transfer (Q). (E) Schematic illustrations to depict intramembrane aggregates after G_3, LDKA and Melittin binding. The SANS intensity profiles are shifted vertically for better

visualization from bottom to top. The continuous lines denote the best SUV model fits with the structural parameters listed in **Table S7&S7-1**. AMPs and vesicles interacted at 20 °C for 1 h before SANS measurements.

To unravel the morphological impact of the interaction of AMP binding to the IM, AFM imaging was first undertaken on the DMPC/DMPG bilayer formed on silicon wafer via topographic scanning at the air/solid interface (**Figures S6E and S7)** using the tapping mode. The supported lipid bilayer was formed by incubating DMPC/DMPG SUVs with silicon wafer and AFM imaging was undertaken before and after the exposure of the supported bilayer to AMPs at an approximate P/L ratio of 1:100.

The bilayer membrane formed was very uniform (**Figure S7**). After AMP binding, however, topographic distortions occurred (**Figure S6E**). Membranes exposed to LDKA and Melittin were rougher and possessed larger and more disrupted areas than those exposed to G_3/G_4. The heights of the humps induced by Melittin and LDKA are about 2 nm, compared to less than 1 nm from G_3/G_4 binding. These local morphological disorders from AMP-lipid nanostructures differ from the roughness associated with periodic waves in the lipid bilayer alone.

SANS was then utilized to unravel the structural impact of binding of the AMPs onto the inner bacterial membrane model by exposing hydrogenated AMPs to hydrogenated POPG/POPC SUVs in D_2O (**Figure 3A-D**). SANS runs from the SUVs in D_2O before interacting with AMPs were first made, and the main parameters obtained from the model fitting are listed in **Table S7**. All SANS profiles can be modelled as a sphere with a single lipid bilayer encapsulation. The POPG/POPC vesicles can be represented with a radius of 180 ± 10 Å from the best fits to the SANS profiles. The bilayer was fitted with a head layer of 7 ± 1 Å and a middle acyl layer of 27 ± 2 Å, leading to a total bilayer thickness of 41 ± 3 Å.

The binding of G_3 and G_4 over the low concentration range caused little change in the SUV radius or bilayer thickness, but an increase in G_3 and G_4 concentration led to the slight thickening of the outer head layer and changes in its scattering length density

(SLD), indicating the increase in AMP binding. Upon G_4 binding at 200 μM, there was a clear peptide layer protruding on top of the mixed outer head layer, a total of 18 ± 4 Å. At this concentration of G_4, a 4-layer SUV model must be used, with the structure and composition of the other two layers showing less changes from the lower concentrations. Upon binding of LDKA, however, the size of SUVs increased greatly from a radius of 180 ± 10 Å to 270 ± 10 Å at the LDKA concentration of 50 μM. An increase in LDKA concentration led to a further increase in the radius of SUVs. At the LDKA concentration of 200 μM, the spherical structure of the SUVs was kept, but its radius expanded to 460 ± 25 Å. This together with a radial polydispersity index of 0.6 ± 0.1 indicates the fusion of the individual SUVs induced by LDKA-bilayer stacks formed, evident from the broad SANS feature around 0.01 A^{-1} and the sharp increasing intensity in the lowest Q region. The large change in vesicular organization caused by LDKA binding is very different from the impact of other AMPs but is broadly consistent with the different surface Zeta potential changes of SUVs upon AMP binding as shown in **Figure S6C**.

In contrast, the binding of Melittin to the POPC/POPG SUVs also led to very noticeable changes in SANS profile against its concentration. At 100 μM of Melittin, the broad peak around 0.08 $Å^{-1}$ as shown in **Figure 3D** indicates multiple AMP-bilayer stacks associated with intensive membrane fusion induced by Melittin. The best-fit parameters upon Melittin binding at 50 and 100 μM are given in **Table S7-1**.

Moreover, the effects of AMP's membrane-binding on hydrophobic membrane cores were also explored via Raman spectroscopy. The results revealed changes of membrane packing density and orderness, thus providing alternative support to the changes of chemical environments associated with different AMP binding and intramembrane aggregation. (See **Figure S8** and **Table S5**)

2.4 Penetration of single AMP through membranes via PMF

To understand the energetic cost associated with the penetration of AMP through a bacterial membrane, potentials of the mean force (PMFs) were calculated from umbrella sampling simulations (CHARMM with a Hoover thermostat). The binding energy between a single AMP and the bacterial membrane model (POPG/POPC, 3/7, mol/mol) and the energy barrier of the AMP to penetrate into the membrane were calculated. The PMFs of an AMP adsorbed on the membrane surface are plotted as a function of the centre-of-mass (COM) separation distance between AMP and lipid membrane.[29] The PMF profiles of AMPs pulled from the bulk solution ($z = 5$ nm) to the lipid bilayer centre ($z = 0$ nm) were calculated to assess the membrane binding and penetration ability of the four AMPs, with the details of the steered molecular dynamics (SMD) simulations given in Section SI3.[30]

As shown in **Figure 4A**, all PMF curves first decrease with the approach of AMPs to the membrane surface, and a local free energy minimum is reached on the outer leaflet surface of the membrane (~1.75 nm). This indicates that the adsorption of the four AMPs on the membrane surface is energetically favourable and can happen spontaneously. The favourable membrane binding of AMPs is mainly driven by the strong electrostatic interaction between cationic AMPs and the anionic membrane interface. The adsorption energy of AMPs on the lipid membrane follows the order: Melittin (-133.3 kJ/mol) < G_4 (-119.4 kJ/mol) < G_3 (-103.4 kJ/mol) < LDKA (-58.4 kJ/mol), where a more negative value denotes a stronger binding ability. This order mainly relates to their relative amphiphilic balance, governed by the interplay between hydrophobic and electrostatic interactions between these AMPs and the lipid membrane model. Because of the charges and hydrophilic properties of these AMPs, however, their further insertion into the hydrophobic membrane core is entropically unfavored. This is reflected by the sharp increase of PMF profiles when AMPs were pulled from the membrane surface to the membrane core. Therefore, each AMP must overcome a large energy barrier to undertake membrane penetration, consistent with the previous simulation studies.[31]

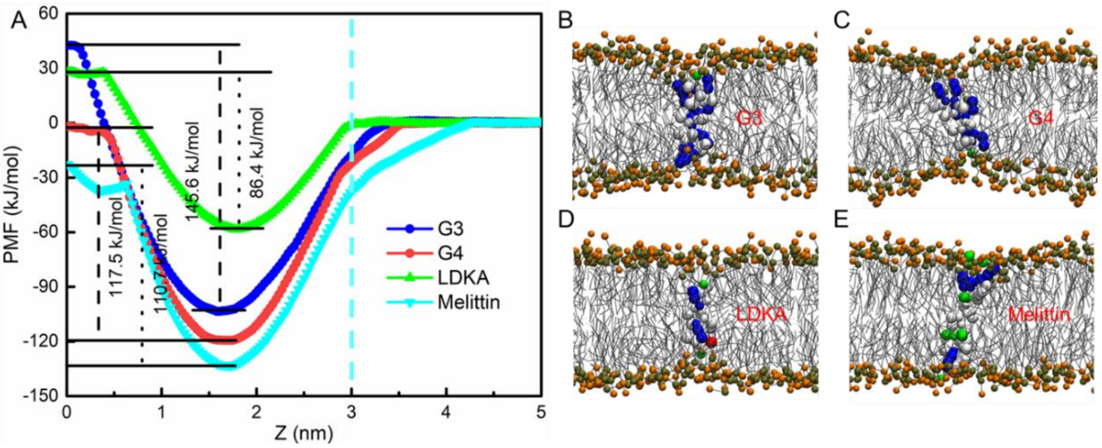

Figure 4. (A) Free-energy profiles of AMPs (PMFs) penetrating the membrane (POPC/POPG, 7/3, mol/mol) as a function of the distance (z) between the centre-of-mass (COM) of the lipid bilayer and the AMP. The dot-dashed sky-blue line marks the membrane surface, averaged from the COM location of head groups of the outer leaflet. The shadow area marks the local free energy minima of AMPs adsorbed onto the membrane. (B-E) Final equilibrated configurations of G_3, G_4, LDKA and Melittin are located in the membrane core.

The energy barriers of the AMPs shown in **Figure 4** differ, as indicated by the black dashed lines. As LDKA carries only +2 charges, the electrostatic interaction with the outer membrane surface is not as strong as that of the other three AMPs. Besides, its size is the smallest. Thus, the smallest energy barrier (86.4 kJ/mol) must be overcome for LDKA to enter the membrane. From the atomistic MD simulation of LDKA inserting into the model bacterial membrane of DMPG/DMPC (3/7, mol/mol) under 70 ºC, Chen *et al.*[32] showed that LDKAs flipped between surface-bound and transmembrane states and that their aggregates can cross the hydrophobic core of the membrane in stable low free-energy structures. The energy barrier associated with the insertion of a single LDKA into the bilayer prohibits this process from occurring spontaneously. Apart from intramembrane LDKA assembly, the mutual burial of LDKAs' hydrophilic charged groups helps LDKA aggregates penetrate through the bilayer. The rich hydrophilic cationic residues in G_3 and G_4 also prohibit them from penetrating through the membrane in the monomer state. On the other hand, the more hydrophobic residues on G_4 make it easier to approach the hydrophobic part of the bilayer than G_3, which reflects the G_4's smaller energy barrier (117.5 kJ/mol) for penetrating the outer leaflet than that of G_3 (145.6 kJ/mol). In contrast, the size of Melittin is the biggest with more hydrophobic amino acid residues than G_3 and G_4, but it has fewer charges (+ 6e for Melittin, +7e for G_3 and +9e for G_4). Its energy barrier (110.7 kJ/mol) is smaller than G_3 and G_4 (146 kJ/mol and 117.5 kJ/mol). **Figure 4B-E** shows the final equilibrated configurations of these AMPs located in the membrane core, with all AMPs being inserted vertically and their charged residues interacting with the lipid head groups on both sides of the lipid membrane. These configurations can reduce the unfavorable contacts between hydrophilic AMPs and hydrophobic membrane cores to minimize the total system's free energies.

2.5 Neutron reflectivity for different AMP binding to the DPPG monolayer

Spread lipid monolayer is a useful model to mimic the lipid membrane leaflet of bacteria. It was used to facilitate NR measurements to determine how AMP bound to the lipid membrane leaflet and caused structural disruptions. The spread DPPG monolayer worked as a charged bacterial membrane leaflet and the interfacial structural changes were highlighted through H/D substitutions. Thus, changes in the thickness and area per molecule of DPPG can be obtained from the deuterated DPPG (dDPPG) monolayer spread on the surface of null reflecting water (NRW, containing 8.1vol% D_2O). The extent of the mixing of the head group of DPPG with water can be obtained from parallel runs of hydrogenated (hDPPG) and dDPPG monolayer in D_2O. As AMPs are hydrogenated, the use of dDPPG in D_2O offers the largest contrast to highlight the amount and distribution of AMP. **Figure 5A** shows the reflectivity profiles measured under this contrast upon binding of Melittin, LDKA, G_3 and G_4, with that measured before AMP binding as control. The interfacial structure in terms of the relative locations between lipid monolayer, AMP and water are schematically shown in **Figure 5B**, where the relative change of SLD across the interface is marked by the intensity of the SLD bar. AMP binding to the hydrogenated lipid head group region under the aqueous subphase is highlighted by the expanded lipid head layer with low SLD (**Figure 5C**).

Figure 5D shows the volume fraction distributions of the acyl chain, head group and water across the interface for the DPPG monolayer at 28 mN/m before AMP binding. The thickness of the acyl chain layer is 18 Å and that of the head region is 10 Å. The head region is fully immersed in water. In the plots of the volume fraction distributions, a roughness of 2 Å was applied to smooth the sharp interfaces. The binding of Melittin to the DPPG monolayer led to the dissolution of 20 ± 2% of the interfacial lipid, consistent with significant membrane damage and massive peptide binding as depicted in **Figure 5E**. Whilst Melittin is fully associated with the entire lipid monolayer based on the model fit, there is also a Melittin layer of 29 ± 3 Å thick underneath the lipid head region with a volume fraction of 0.55 ± 0.05. LDKA has the weakest membrane-lytic activity among the four AMPs studied (**Figure 5F**), with only 5 ± 1% of the DPPG lipid removed. The amount of LDKA molecules inserted into the DPPG membrane was low, with the volume fractions of 0.05 ± 0.01 and 0.08 ± 0.01 in the lipid tail and head layers, respectively. LDKA formed an additional 21 ± 2 Å layer underneath the lipid head layer, with a volume fraction of 0.39 ± 0.04, suggesting strong aggregation underneath the lipid membrane but low penetration capability. In contrast, G_3 and G_4 have a strong membrane penetrating capability but relatively weak outer surface aggregation (**Figures 5G&H**), evident from much thinner adsorbed layers underneath the lipid head layer. The peptide layer (layer 3) for G_3 is thinner and less dense than that formed from G_4, consistent with G_3's lower hydrophobicity.

Figure 5I shows the amount of AMP insertion and adsorption across the DPPG tail layer (layer 1) and head layer (layer 2), and underneath the head (layer 3), in $\mu M/m^2$ and mg/m^2. All AMPs can bind into the entire lipid tail and head layers and they all form an adsorbed layer underneath the head group layer as well. LDKA is the smallest, displaying the lowest amount of insertion into the tail and head layers, but its adsorption is almost the highest together with Melittin in $\mu M/m^2$, consistent with their highest hydrophobicity. In contrast, Melittin has the highest molecular weight, and its surface adsorbed amount in mg/m^2 is also the highest. On the other hand, G_3 and G_4 show even distributions across the DPPG membrane leaflet. More detailed best-fit parameters from NR data analysis are given in **Table S8.**

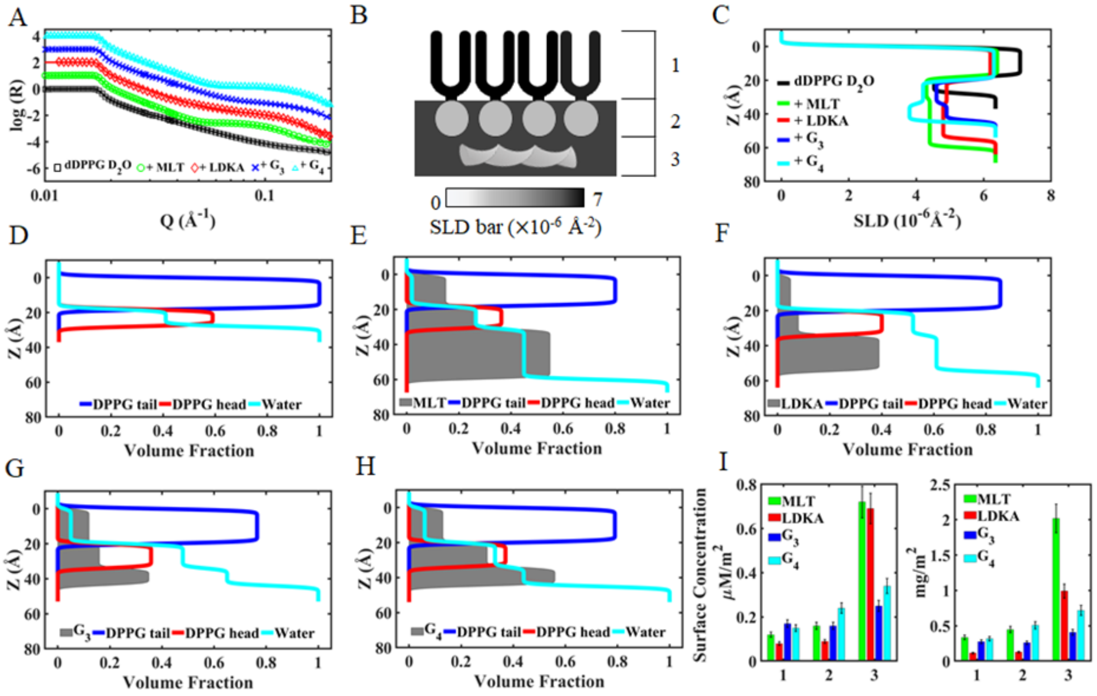

Figure 5. NR data and best model fits acquired from the initial DPPG monolayer and subsequent interactions with the four AMPs. (A) NR profiles plotted as the reflectivity (log *R*) as a function of momentum transfer (Q), are shifted vertically from bottom to top by multiplying factors of $\times 10^0$, $\times 10^1$, $\times 10^2$, $\times 10^3$, $\times 10^4$, respectively for improved visibility. (B) A cartoon illustrating the deuterated DPPG (d_{62}-DPPG) monolayer on the D_2O substrate, with interactions of hydrogenated peptides. Layers 1, 2, 3 represent the DPPG tail, DPPG head and adsorbed peptide layers underneath the lipid head layer, respectively. (C) SLD distributions as a function of perpendicular distance (*z*) from the best model fits to NR profiles. (D-H) Volume fraction distributions of AMPs (grey regions), lipids tails (blue lines), lipid heads (red lines), and D_2O (cyan lines) across the z-axis for (D) DPPG, and in presence of (E) Melittin 1 μM, (F) LDKA 10 μM, (G) G_3 3 μM, and (H) G_4 3 μM. (I) Surface concentrations of the 4 AMPs adsorbed in the 3 representative layers in units of μM/m^2 (left) and mg/m^2 (right).

2.6 AMP intramembrane aggregation varied with peptide to lipid ratio

Based on the different binding behaviour of AMPs on the DPPG monolayer from the NR study, MD systems containing different numbers of AMP were set up to explore the relationship between peptide number and intramembrane peptide aggregation behaviour (**Figure S9**). With the increase in AMP number, AMPs displayed different intramembrane aggregation by forming oligomers. The formation of peptide nanoaggregates occurred when the ratio of peptide to lipid (P/L) was at 1 : 22 for G_3 and 1 : 29 for G_4, Melittin and LDKA, mimicking the effects of increasing bulk AMP concentrations.

MD simulations have revealed that Melittin becomes integrated into the DPPG bilayer with the helical axis parallel to the bilayer and the hydrophobic inner surface becomes penetrated shallowly in the apolar portion of the membrane. This mode of action is consistent with what was previously proposed by Terwilliger *et al.*[33] The membrane-bound configuration in CG-MD simulations is well supported by CD and NMR studies from the micelle-bound Melittin.[34] Stable nanopores can be formed only above the critical P/L ratio of 1 : 22 within the timescale of microsecond MD simulations. Through X-ray diffraction, Lee *et al.* have revealed that the initial states for transient and stable pores caused by Melittin on negatively-charged DOPG/DOPC membrane (molar ratio = 3 : 7) were different, suggesting different binding mechanisms at low and high AMP concentrations.[35] Furthermore, the lipid structure of the pore is highly influenced by the formation of Melittin oligomers, and the peptide concentration is clearly an important factor.

As an AMP with strong self-assembly propensity, the state of the LDKA oligomers changes from dimer to cluster upon binding to the DPPG bilayer when the AMP number increases from 6 to 24. Increasing the LDKA number from 24 to 48, larger sizes of the LDKA aggregate are formed. In contrast, G_3 tends to be in the monomer state when the AMP number is less than 18. However, the typical oligomer state of both G_3 and G_4 is a tetramer. G_4 can form denser aggregates than G_3 at higher P/L ratios.

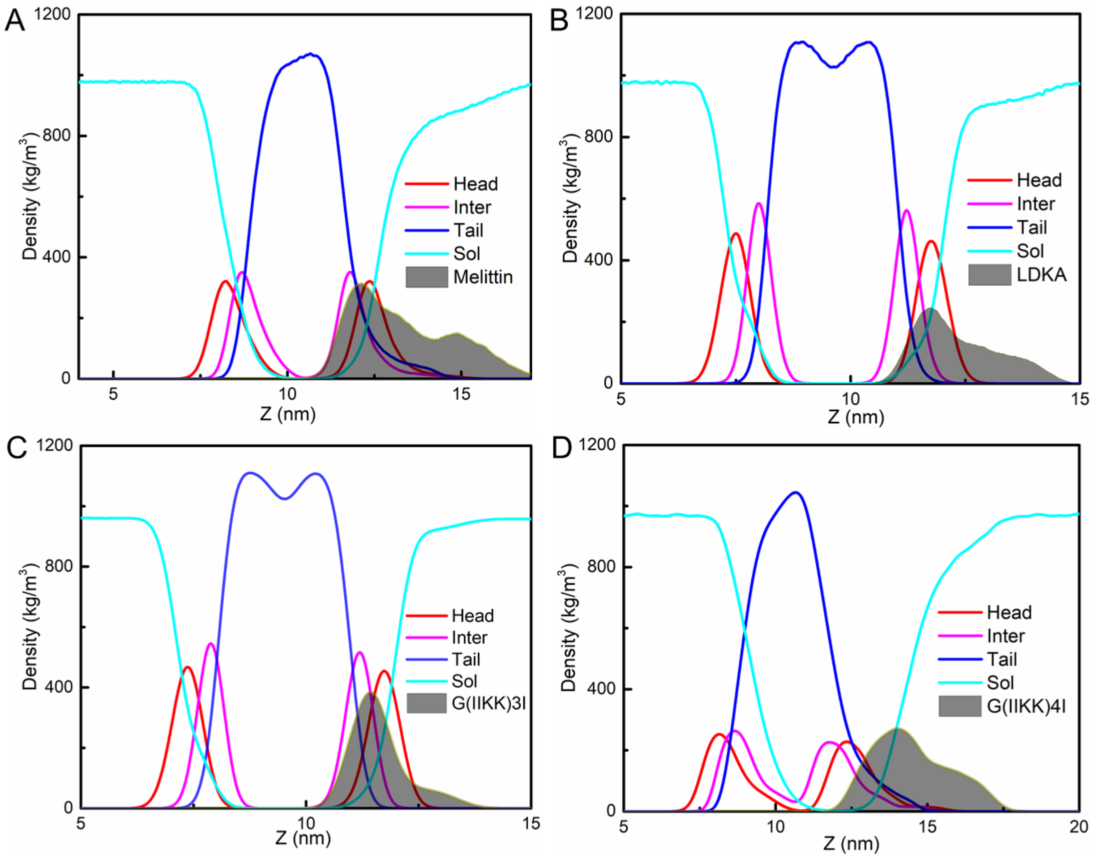

Figure 6. Mass density cross-section profiles as a function of perpendicular distance (z) of lipid, water and AMP (A) Melittin, (B) LDKA, (C-D) G_3/G_4 upon DPPG bilayers when peptide/lipid (P/L) ratio is 1 : 22 after MD simulation time of 1 μs. The light blue curves and areas filled with the grey shadow represent distributions of water molecules and peptides, respectively. The red, pink and blue curves stand for distributions of the head, inter linker and tail groups in DPPG bilayers.

Figure 6 shows the distribution of the four AMPs across the DPPG bilayer, plotted in the form of density profiles of the tail layer, head layer, the glycerol linker (Inter), AMP and water across the interface. AMP binding affects chain and head distributions of the lipid leaflet as shown in **Figure 5** from NR. Binding from all four AMPs leads to their insertion into the tail layer, evident from the overlaps between the tail distribution and AMP distribution, but the hydrophobic Melittin and G_4 showed a larger amount of AMP insertion into the membrane leaflet and bound underneath the lipid head layer (**Figure 6A&D**), consistent with their strong membrane disruptions and also shown in **Figure S10** as the side-view. G_3 displays a more even peptide distribution across the 3 different interfacial layers, with the least amount of the adsorbed layer underneath the head group layer. AMP insertion may promote the hydration of the tail layer, and this is evident from their overlaps with water distributions from all four AMPs.

A close inspection of the AMP distributions shown in the shaded areas in **Figures 5 E-H** with those in **Figure 6** reveals their different distribution shapes across the DPPG membrane leaflet due to different models adopted, but the overall amounts for each AMP are very close. As indicated previously, the association of Melittin into the interface results in the largest adsorbed amount, but its interfacial binding also spans the largest distance, consistently revealed in both NR and MD. The distribution is featured by a large peak arising from the insertion of Melittin into the DPPG leaflet and the outer shoulder associated with the adsorption of Melittin underneath the DPPG head layer. These features are common to the distributions of all other three AMPs. However, the actual shape of the G_3 distribution is characterized by the dominant peak arising from its penetration into the lipid membrane and a small shoulder indicating a smaller fraction of the adsorbed G_3 under the head region. This difference reveals that G_3 is more effective at penetrating the lipid membrane whilst Melittin forms a dominant layer underneath the head group layer.

One of the consequential impacts of different AMP interactions is their average intramembrane orientations. Chen *et al.*[36] have examined Melittin's orientations in a supported DPPG bilayer through different spectroscopy technologies. They found that the population of Melittin molecules perpendicular (about 100°) and parallel (about 6°) to the bilayer surface was 0.26 and 0.74, respectively. The state of being projected parallel to the surface is consistent with the characteristic surfactant-like amphiphilicity of Melittin. Whilst such spectroscopic studies are yet unavailable for the other three AMPs, small LDKA and G_3 molecules must adopt similar orientations to permeate the inner membrane by balancing various interactions, as evident from MD simulations.

2.7 The mode of action for IM disruption

When the P/L ratio onto the DPPG bilayer was further increased from N = 24 to N = 36

(Melittin) and 48 (LDKA, G_3 and G_4), more extensive membrane disruptions occurred during MD simulation times of microsecond, reflecting more closely what happened in the bacterial membranes as observed from the experiments. From MD simulations shown in **Figure 7**, the processes of AMP-lipid bilayer interaction can be roughly divided into three stages: AMP adsorption onto the lipid bilayer, intramembrane self-assembly or aggregation and formation of peptide-lipid nanostructures. The time-wise division is consistent with the modified "carpet model" of peptide pore formation proposed by Rathinakumar *et al.*[37], depicting the self-assembly of AMPs into the lipid bilayer surface at the early stage of membrane disruption. Through vesicular leakage assays of probe molecules with different sizes, a "pore state" on the lipid bilayer must have occurred, but such pores might not be simple water-filled transmembrane pores. Our combined experimental and MD studies suggest that these pores are complex and transient and that the scaffold nanostructures consist of peptides, lipids, water and ions.

Most AMPs approach the DPPG bilayer within 200 ns while some of them remain in bulk solution. As time goes on, both LDKA and G_4 start to form the "lipid humps" along with the peptide aggregates induced by the exposure to the lipid surface. G_4 can then roll up a piece of the DPPG membrane and contact its hydrophobic core, while G_3 locates around the head and glycerol parts of the DPPG bilayer at this stage, and the difference is reflected in the larger membrane curvature and bilayer thickness change caused by G_4 binding (**Figures 7C&D**). These features are broadly consistent with the larger size and greater hydrophobicity of G_4 and its potency in causing cell lysis and death.

During microsecond MD simulations, Melittin can occupy space in the DPPG head group layer, but does not extend to the centre of the bilayer easily (**Figure 7A**). Instead, Melittin molecules form a relatively thick layer underneath the DPPG head group layer due to the combined effects of electrostatic and intra-oligomer interactions. Such a thick peptide adsorbed layer onto the DPPG bilayer may work to suppress the disruption to the membrane. This statement can be supported by the MD results of different P/L ratios (N = 24 and 36) in the Melittin-DPPG system (**Figures S10** and **7A**), where membrane disruption at N = 24 is much more obvious than that observed at the higher P/L ratio. However, G_4 formed its thick adsorption layer in the DPPG bilayer at early times. Then, the thick G_4 templating disappears gradually upon the formation of the G_4-DPPG “humps”. Some lipid head groups around the G_4 nanoaggregates can move on to the centre of the lipid bilayer along with the hydrophilic outer surface of the G_4 oligomers, which effectively reduced the bilayer thickness nearby.[38]

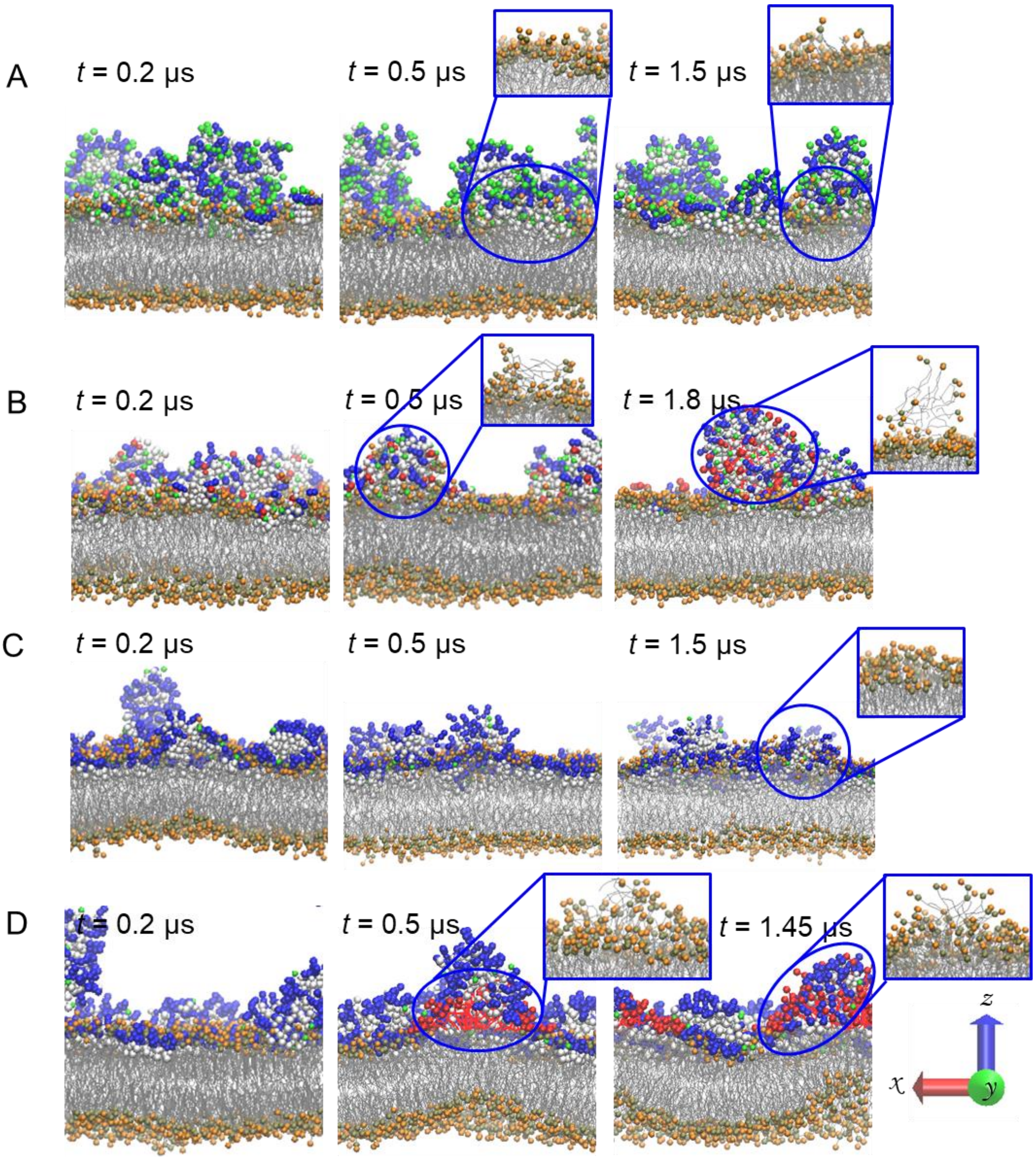

Figure 7. Side view of AMPs’ intermolecular interaction with DPPG bilayers at changing simulation times when peptide numbers are (A) N = 36 (Melittin) and (B-D) N = 48 (LDKA, G_3 and G_4). The inset graphs show the enlarged features inside the corresponding side views, and AMPs are ignored here to highlight lipid molecular

restructuring caused by AMP aggregation.

From the experimental observations of the leakage of SUVs, each AMP concentration corresponding to L_{50} of the POPG SUVs is higher than the corresponding one from 30% POPG SUVs. (**Figures S7D&S11**) The differences are especially notable for G_3 and G_4, showing the impact of the net membrane charge density. In a similar study of AMP-induced LUV leakage, Manzini *et al.*[39] also reported that cecropin-Melittin hybrid BP100 (an AMP of rich positively charged residues) showed higher leakage efficiency of LUVs with lower PG/PC molar ratios. The shapes of the kinetic curves in **Figure S11** are different with increasing peptide concentration, but the leakage fraction as defined in equ (6) of G_3 and G_4 at ~ 10 μM is much lower than LDKA and Melittin, consistent with the proposed changes in their membrane disruption mechanisms.

With increasing peptide concentration, suppression of SUV leakage occurs in Melittin above the concentration of 20 μM in 100% POPG SUVs, but not in 30% POPG SUVs. Following the work of Bogaart *et al.* on Melittin's mechanism of pore formation on zwitterionic and anionic liposomes, Melittin can induce the complete leakage of the single component DOPC. As the binding of Melittin molecules was weak, some of them can move to the freshly added DOPC liposomes and cause leakage.[40] In contrast, Melittin must be irreversibly bound to the POPG SUV surface, which prevented further Melittin molecules from forming pores. This oversaturation phenomenon only occurred in 100% POPG SUVs. As charge density goes down, e.g., in POPG/POPC (3:7) SUVs, no suppression to leakage occurred with increasing Melittin concentration.

From the simulation results shown in **Figure 7B**, LDKA nanofibers have a greater tendency to cluster onto the DPPG lipid bilayer than G_3 and G_4 and can even draw the lipid molecules out from the DPPG bilayer. Such action may arise from alternating positively and negatively charged residues on the surface of LDKA nanofibers, even though an LDKA molecule has less positive charges than G_3 and G_4.[41] However, apart from the entrapped lipid aggregates, other regions of the DPPG bilayer are not affected greatly and still well-preserved. In the G_4-lipid bilayer system (**Figure 7D**), the interfacial activity of G_4 causes intramembrane aggregation to form heterogeneous nanostructures of G_4 and lipid molecules in the form of "humps", causing local bilayer thinning and large membrane curvature change. These phenomena are consistent with experimental observations, showing stronger G_4 antimicrobial efficiency than that of LDKA. These different membrane disruptions from G_3, G_4, LDKA and Melittin affect their nanopore forming capabilities on the membrane and bacterial killing power from membrane leakage.

3. Conclusions

Through the combination of experiments and CG-MD simulations, the relationship between the self-assembly of AMPs and their ability to cause effective disruptions of different model membranes was examined. AMP's effects on both permeability of OM and depolarization of IM play important roles in the rapid killing of bacteria. The formation of the nanoaggregates on bacterial OM has a major impact on the efficiency of OM permeability and the level of AMPs that is available to attack bacterial IM. CG-MD simulations offer the benefit of linking the molecular structures to membrane-lytic binding processes, providing useful insights into the effects of AMP nanostructures on antimicrobial actions. Following previous studies on Melittin and MD simulations on cationic LDKA oligomers by Chen *et al.*[32], this work has revealed that LDKA clusters can be prevented from approaching bacterial IM by bacterial OM. Once reaching bacterial IM, LDKA can disrupt the IM integrity by forming AMP-lipid nanoaggregates and creating membrane defects. In contrast, the other three AMPs can more easily change the permeability of bacterial OM and cause more effective IM disruptions. Melittin tends to form a thick adsorbed layer and roll into large nanoaggregates on the lipid bilayer with increasing P/L ratio or concentration, whilst G_3 and G_4 form smaller aggregates which are more effective at becoming inserted into the charged membranes. This work shows that the "carpet model" is not the most efficient way to form nanopores and cause leakage. Potent antimicrobial activities must be associated with the intramembrane nanoaggregation as a more effective mode of action. Transitions to ordered amphiphatic structures based on their α-helical structures made G_3 and G_4 highly selective to bacterial membranes. MD simulations and experimental studies of membrane binding processes have thus offered valuable insights into the AMP-lipid nanoaggregates and their insertion into bacterial membrane. The ability to screen how a new AMP disrupts bacterial membrane via intramembrane nanoaggregation provides an important link between AMP design and their antimicrobial performance, crucial to AMP’s future development toward clinical applications.

4. Experimental section

Details of antimicrobial efficacy and bacterial dynamic killing of AMPs, haemolytic activity and cell MTT assays (materials, instruments and cell line), AFM images of lipid bilayer before and after binding with AMPs, surface physical activities of AMPs, SANS and NR experiment details, bacterial membrane permeability and depolarization and live/dead staining assays, CD measurements, liposome preparation and fluorescence leakage experiments, Zeta-potential and Raman spectra of SUVs, simulation models and methods, can be found in the **Supporting Information**.

Acknowledgements

We acknowledge PhD studentship support from the University of Manchester (UoM) to H.G. and X.H., UoM-CSC (China Scholarship Council) joint PhD programme funding to M.L., H.G., Z.W. and L.Z., a research grant from Syngenta to X.H. and funding from the National Natural Science Foundation of China (No. 21908066) to X.Q. We thank Rehana Sung and Derren Heyes for their assistance in the running of HPLC and CD. We acknowledge the beam times awarded from the ISIS Neutron Facility (RB 1920459 & 1920496) and the ILL Neutron Facility (DOI: 10.5291/ILL-DATA.9-13-730) and technical assistance from Mario Campana and Armando Maestro. Access to the Shared Computation Facility (SCF) at UoM is also gratefully acknowledged.

Conflict of interest

The authors declare no conflict of interest.

5. References

[1](a) Anthony; Hu Coates, Yanmin; Bax, Richard; Page, Clive, *Nature Reviews Drug Discovery* **2002**, *1*, 895-910; (b) David M. Livermore, Martin Blaser, Otto Carrs, et al., *Journal of Antimicrobial Chemotherapy* **2011**, *66*, 1941-1944; (c) Silver L. L., *Clinical Microbiology Reviews* **2011**, *24*, 71-109.

[2](a) Piddock Laura J. V., *Nature Reviews Microbiology* **2006**, *4*, 629-636; (b) Wright Gerard D., *Advanced Drug Delivery Reviews* **2005**, *57*, 1451-1470.

[3]Kem A. Sochacki, Kenneth J. Barns, Robert Bucki, et al., *Proceedings of the National Academy of Sciences of the United States of America* **2011**, *108*, E77-81.

[4]Guangshun Wang, Xia Li, Zhe Wang, *Nucleic Acids Research* **2009**, *37*, D933-937.

[5]Powers J. P., Hancock R. E., *Peptides* **2003**, *24*, 1681-1691.

[6](a) Allen J. Duplantier, Monique L. van Hoek, *Frontiers in Immunology* **2013**, *4*, 143; (b) Y. Zhu, S. Mohapatra, J. C. Weisshaar, *Proceedings of the National Academy of Sciences* **2019**, *116*, 1017-1026; (c) Brogden Kim A., *Nature Reviews Microbiology* **2005**, *3*, 238-250.

[7](a)Tomas Ganz, *Science* **1999**, *286*, 420-421; (b) De Yang, Arya Biragyn, David M. Hoover, et al., *Annual Review of Immunology* **2004**, *22*, 181-215; (c) Daniela Ciumac, Haoning Gong, Xuzhi Hu, et al., *Journal of Colloid and Interface Science* **2019**, *537*, 163-185.

[8]Michael Zasloff, *Nature* **2002**, *415*, 389-395.

[9](a) Neyrolles Olivier, Malmsten Martin, Kasetty Gopinath, et al., *PLoS ONE* **2011**, *6*, e16400; (b) Martin Malmsten, Mina Davoudi, Artur Schmidtchen, *Matrix Biology* **2006**, *25*, 294-300.

[10](a) Xuzhi Hu, Mingrui Liao, Haoning Gong, et al., *Current Opinion in Colloid & Interface Science* **2020**, *45*, 1-13; (b) Haoning Gong, Marc-Antoine Sani, Xuzhi Hu, et al., *ACS Applied Materials & Interfaces* **2020**, *12*, 55675-55687 ; (c) Haoning Gong, Mingrui Liao, Xuzhi Hu, et al., *ACS Applied Materials & Interfaces* **2020**, *12*, 44420-44432.

[11](a) L. A. Clifton, S. A. Holt, A. V. Hughes, et al., *Angew Chem Int Ed Engl* **2015**, *54*, 11952-11955; (b) N. Paracini, L. A. Clifton, M. W. A. Skoda, et al., *Proceedings of the National Academy of Sciences* **2018**, *115*, E7587-E7594.

[12]Berglund N. A., Piggot T. J., Jefferies D., et al., *PLoS Computational Biology* **2015**, *11*, e1004180.

[13]C. McGoverin, J. Robertson, Y. Jonmohamadi, et al., *Frontiers in Microbiology* **2020**, *11*, 545419.

[14]Xuebo Quan, Daohui Zhao, Libo Li, et al., *Langmuir* **2017**, *33*, 14480-14489.

[15]Barry Isralewitz, Mu Gao, Klaus Schulten, *Current Opinion in Structural Biology* **2001**, *11*, 224-230.

[16]Xuebo Quan, Delin Sun, Jian Zhou, *Physical Chemistry Chemical Physics* **2019**, *21*, 10300-10310.

[17]Charles H. Chen, Charles G. Starr, Evan Troendle, et al., *Journal of the American Chemical Society* **2019**, *141*, 4839-4848.

[18]Terwilliger Thomas, Weissman Larry, Eisenberg D., *Biophysical Journal* **1982**, *37*, 353-361.

[19]Jürgen Lauterwein, Chris Bösch, Larry R. Brown, et al., *Biochimica et Biophysica*

Acta (BBA) - Biomembranes **1979**, *556*, 244-264.

[20] Ming-Tao Leea, Tzu-Lin Sun, Wei-Chin Hung, et al., *Proceedings of the National Academy of Sciences* **2013**, *110*, 14243-14248.

[21] Xiaoyun Chen, Jie Wang, Andrew P. Boughton, et al., *Journal of the American Chemical Society* **2007**, *129*, 1420-1427.

[22] Ramesh Rathinakumar, William C. Wimley, *Journal of the American Chemical Society* **2008**, *130*, 9849–9858.

[23] Chen Song, Bert L. de Groot, Mark S. P. Sansom, *Biophysical Journal* **2019**, *116*, 1658-1666.

[24] Mariana C. Manzini, Katia R. Perez, Karin A. Riske, et al., *Biochimica et Biophysica Acta (BBA) - Biomembranes* **2014**, *1838*, 1985-1999.

[25] Geertvan den Bogaart, Jeanette Velásquez Guzmán, Jacek T. Mika, et al., *Journal of Biological Chemistry* **2008**, *283*, 33854-33857.

[26] Manzo Giorgia, Ferguson Philip M., Gustilo V. Benjamin, et al., *Scientific Reports* **2019**, *9*, 1385.

Supporting Information

Intramembrane Nanoaggregates of Antimicrobial Peptides Play a Vital Role in Bacterial Killing

Mingrui Liao,[1#] Haoning Gong,[1] Xuebo Quan,[2] Ziwei Wang,[3] Xuzhi Hu,[1] Zheng Chen,[2] Zongyi Li,[1] Huayang Liu,[1] Lin Zhang,[1] Andrew J. McBain,[4] Thomas A. Waigh,[1] Jian Zhou,[2] and Jian Ren Lu[1,*]

[1]Biological Physics Laboratory, Department of Physics and Astronomy, School of Natural Science, The University of Manchester, Oxford Road, Manchester M13 9PL, UK.

[2]School of Chemistry and Chemical Engineering, Guangdong Provincial Key Laboratory for Green Chemical Product Technology, South China University of Technology, Guangzhou 510640, China.

[3]National Graphene Institute, The University of Manchester, Oxford Road, Manchester M13 9PL, UK.

[4]Division of Pharmacy and Optometry, School of Health Sciences, Faculty of Biology, Medicine and Health, The University of Manchester, Oxford Road, Manchester M13 9PL, UK.

[#]To whom as PhD candidate should be responsible to all the experiments.
*To whom all correspondence should be made: J.lu@manchester.ac.uk

1. Chemical Reagents and Physicochemical Properties of AMPs

Hydrogenated and deuterated phospholipids, 1,2-dipalmitoyl-sn-glycero-3-[phosphor-rac-(3-lysyl(1-glycerol))] (sodium salt) (DPPG), 1,2-dipalmitoyl-d62-sn-glycero-3-[phosphor-rac-(1-glycerol)] (sodium salt) (d_{62}DPPG), 1,2-dipalmitoyl-sn-glycero-3-phosphocholine (DPPC), 1-palmitoyl-2-oleoyl-sn-glycero-3-phospho-(1'-rac-glycerol) (sodium salt) (POPG), 1-palmitoyl-2-oleoyl-sn-glycero-3-phosphocholine (POPC) and cholesterol were purchased from Avanti Polar Lipids (Alabaster, AL). Peptides were obtained from TopPeptide Bio Co Ltd. (Shanghai, China) and Ind-Chem Co Ltd. (Nanjing, China). They were synthesized using standard Fmoc solid-phase synthesis and purified using the rp-HPLC method with purities over 98%.[1] All the other chemicals were purchased from Sigma-Aldrich Co unless otherwise stated, all materials were used without further purification unless otherwise stated.

Table S1. Molecular structures of antimicrobial peptides (AMPs) with their basic properties.

Peptide denotation	Sequence	Theoretical M_w/g·mol^{-1}	Measured M_w/g·mol^{-1}	Charge/e	Retention time/min
G_3	G(IIKK)$_3$I	1636.2	1637.2	+7	18.2
G_4	G(IIKK)$_4$I	2118.9	2119.6	+9	15.2
LDKA	GLLDLLKLLLKAAG	1437.8	1438.9	+2	24.6
Melittin	GIGAVLKVLTTGLPALISWIKRKR	2846.5	2848.7	+6	22.3

The sequences of the designed antimicrobial peptides, their denotations, molecular weights, charges and retention times are provided in **Table S1**. The molecular weights of the synthetic peptides were verified using SELDI-TOF MS, and agreement between the theoretical and measured molecular weights confirmed that the peptides had been synthesized to the desired specifications. The hydrophobicity of a peptide can be evaluated through its measured retention time in PBS buffer solution. Melittin and LDKA are much more hydrophobic than G_3 and G_4.

2. Experiment Methods

2.1 Atomic force microscopy (AFM) and surface physical activity

AFM measurements of AMP nanoaggregates were performed on a MultiMode Nanoscope system (Digital Instruments, Santa Barbara, CA). Tapping mode images were captured using TESP-V2 silicon probes (Bruker, Germany) with a nominal spring constant of 40 N/m. For sample preparation, solutions of 10-20 μL were deposited onto a freshly cleaved mica surface for physical adsorption for ~2 min. Then, the sample was dried under a nitrogen stream.[2] The images of AMP induced membrane aggregates were obtained on a BRUKER Icon atomic force microscopy (AFM) equipped with a force modulation setup and high-resolution optical viewing system. The operation was in PeakForce Quantitative Nanoscale Mechanical (QNM) mode to obtain surface morphology. Data were collected using a Bruker Scanasyst-fluid+ AFM probe with a spring constant of 0.7 N/m, operating at a peakforce setpoint of 3 nN. All the images were analyzed using the NanoScope software (version 1.9).

Physical properties of the peptides determine their ability to adsorb at the air/water interface and reduce surface energy. They were determined by measuring their surface pressure changes (π in mN m^{-1}) at the air/water interface using a Du Noüy ring method supplied with the Krüss K11 tensiometer. 15 mL of the peptide stock solution at different concentrations was added into the glass dish and typically a maximum of 1 h was required for the surface tension to equilibrate. Equilibrium surface tensions were determined until the standard deviation of 10 successive runs was less than 0.1 mN/m.

2.2 Small angle neutron scattering (SANS)

Measurements were performed on the SANS2D and LARMOR instruments at the ISIS Pulsed Neutron Source, STFC Rutherford Appleton Laboratory, Didcot, UK. The samples of AMPs mixed with two different SUVs (LPS/POPC, mol/mol, 1/9; POPG/POPC, mol/mol, 7/3) separately in Tris NaCl D_2O buffer were studied in 2 mm path-length quartz cells (Hellma GmbH, Type 120) and SANS profiles measured at

20 °C. Raw SANS data were reduced using the Mantid framework and corrected following the standard procedures for the instrument.[3] Least-squares fitting analysis to a flexible cylinder/lamellar model with the SasView software version 5.0 was used to interpret the reduced data.

2.3 Haemolytic activity and MTT assays

Evaluation of peptide toxicity against mammalian cells was carried out on fresh hRBCs (human red blood cells) bought from Rockland Immunochemical Inc. (Limerick, US). hRBCs were diluted 25× with PBS to obtain a 4% (v/v) suspension for testing hemolytic activity. Twofold serial dilutions of AMPs were performed with PBS to give solutions with final concentrations ranging from 0 to 2000 μM. 100 μL of peptide solution was mixed with an equal volume of hRBC suspension before incubation at 37 °C for 2 h. Subsequently, the mixtures were centrifuged at 1500 *g* for 5 min and 100 μL of the supernatant was transferred to each well of 96-well plate. The extent of haemoglobin release was assessed by spectrophotometric measurements at 576 nm by the Varioskan LUX microplate reader (Thermo Scientific, USA). Untreated hRBCs and those treated with 1% Triton X-100 served as negative and positive controls, respectively. Data are expressed as mean ± standard deviation for two independent experiments performed in duplicate. The fraction of haemolysis was calculated using the following equation:

$$Haemolysis\ (\%) = \frac{(OD_{576nm}\ of\ treated\ sample - OD_{576nm}\ of\ negative\ control)}{(OD_{576nm}\ of\ positive\ sample - OD_{576nm}\ of\ negative\ control)} \quad (1)$$

Human dermal fibroblast cell (HDFa adult, ATCC PCS-201-012) and 3T3 cell (Embryo Fibroblast, Mus musculus, ATCC CRL-1658) tests were performed to assess the toxicity of AMPs. The cells were pre-seeded in a 96-well plate at a concentration of 1× 10^5 cells and experienced 24 h at 37.5 °C incubation. To each well was added 100 μL of AMP solutions following 2-fold dilutions of AMPs. The 96-well plate was incubated for 24 h. MTT solution at 10 μL per well (5 mg/mL) was then added to each well and the well plate was incubated for another 4 h. The supernatant was discarded, and 150 μL dimethyl sulfoxide (DMSO) was added to each well to dissolve the formazan crystals. The optical density was read at 570 nm on a Varioskan LUX microplate reader (Thermo Scientific, USA). Wells without cells were used as blanks and wells without peptides were taken as negative controls.

$$Cell\ viability\ (\%) = \frac{(OD_{570nm}\ of\ treated\ sample - OD_{570nm}\ of\ blank\ control)}{(OD_{570nm}\ of\ negative\ sample - OD_{570nm}\ of\ blank\ control)}$$

(2)

2.4 Antimicrobial efficacy and bacterial dynamic killing

The antimicrobial activity of the peptides and antibiotics was firstly studied against a panel of clinically relevant Gram-positive and Gram-negative bacteria. Antimicrobial efficacy was assessed by the same MIC (minimum inhibition concentration) assay as used in the previous work.[4] For dynamic killing, Gram-negative bacteria were treated with AMPs and antibiotics at twice the MIC. After various contact times (0 min, 5 min, 10 min, 30 min, 1 h, 2 h and 4 h) with different AMPs and controls, the bacterial samples were serially diluted and spread onto independent plates (MHB in full Agar). Untreated bacteria in PBS buffer solution served as a negative control. Colony-forming units (CFU) were counted after 18~24 h incubation at 37 ºC. The experiment was repeated twice under the same conditions.

2.5 Bacterial membrane permeability and depolarization and live/dead staining assays

E. coli ATCC25922 and ESBL- *E. coli* at log-phase were washed with HEPES buffer (5 mM HEPES + 20 mM glucose, pH 7.4) and diluted to ~10^7 CFU/ml. The cell suspensions were incubated with 5 μM NPN (for characterization of outer membrane permeability) and 2 μM DiSC3(5) (for characterization of inner membrane depolarization) for 1 h, respectively, at 37 ºC in a dark environment. After the fluorescence intensity was measured with a plate reader (NPN: λ_{ex}= 350 nm, λ_{em}= 420 nm; DISC3(5): λ_{ex}= 622 nm, λ_{em}= 670 nm) from each sample, AMP was then added, followed by further measurements of fluorescence intensity.

A similar method was used to collect and wash log-phase *E. coli* for live/dead staining assays. The bacteria at ~10^8 CFU/ml were then treated with and without AMPs for 3 hr. The cells were subsequently incubated with 2 μM SYTO 9 and 1 μM PI for 30 min in the dark, to make both live and dead cells fully stained. 40 μL suspension of the stained bacteria was dropped onto a glass slide, followed by covering the drop with a coverslip and imaging via fluorescence microscopy.

2.6 BODIPY™-TR-cadaverine (BC) displacement by AMPs' LPS binding

Binding to the lipid A region of LPS was determined using the BC displacement assay in both cell free and cell systems, in which the probe bound to LPS is self-quenched but fluoresces when released in solution. All the assays were performed in 96-well plates, and fluorescence was measured on a microplate reader as mentioned before using excitation and emission wavelengths of 580 nm and 620 nm, respectively. Probe displacement induced by Polymycin B (PmB) was used as positive control while the LPS-BC mixture without selected compounds was used as negative control.

The final concentrations of BC and LPS for cell-free measurements were diluted to 5 μM and 10 μg/ml in Tris buffer (150 mM NaCl, 10 mM Tris, pH 7.4). AMPs in Tris buffer and the LPS-probe mixture were added to the 96-well plate. The plate was kept for 1h in the dark at room temperature for equilibration. For assays performed on *E. coli* (ATCC 25922), desired concentrations of BC and freshly grown Gram-negative bacteria (final $OD_{600nm} \approx 0.1$) were mixed and kept for 30 min until equilibration. After that, selected AMPs (final concentration 50 μM) and mixtures of BC (final concentration 5 μM) and bacterial cells were added to the plate and recorded for 1 h.

2.7 Fluorescence leakage from SUVs

The membrane disruptive activity of the AMPs was quantitatively determined by the fractional leakage of SUV encapsulating self-quenching 5(6)-carboxyfluorescein (CF).[5] Dry lipid films (POPC/POPG, mol/mol, 7/3; 100% POPG) were prepared in advance and dissolved in 40 mM CF solution (Tris-HCl buffer, pH 7.4), followed by an extrusion process.[4, 6] CF loaded SUVs were passed through a Sephadex G50 gel to remove external fluorescein that was not encapsulated. Aliquots of 100 μl CF loaded SUVs (0.1 mg/ml) interacted with 100 μl of peptide solutions at various concentrations for 20 min, then the emission spectra of leaked fluorescein was measured using the same microplate reader as used in the cell culturing (Varioskan LUX) at $\lambda_{\text{emission}}$= 520 nm using $\lambda_{\text{excitation}}$ = 490 nm. Tris-HCl buffer and 0.2 % Triton X-100 solution were used as the negative control and positive control to interact with CF loaded SUVs to introduce 0% and 100% leakage, respectively. The leakage of CF was calculated from the following equation:

$$Leakage\, fraction\ (\%) = \frac{(I_p - I_0)}{(I_t - I_0)} \times 100 \qquad (3)$$

where I_0 is the initial fluorescence intensity before AMP addition, I_p is the fluorescence after peptide addition, and I_t is the fluorescence after Triton X-100 addition. All experiments were performed at 20 ± 1°C.

2.8 Zeta-potential and Raman spectra of SUVs after AMP binding

The membrane potential change upon cationic AMP binding to SUVs was characterized on the ZEN3600 Nano-ZS equipment (Malvern Instruments, Worcestershire, U.K.) at room temperature. The lipid vesicles (DMPC/DMPG, 7/3, mol/mol) were prepared using the same approach as described previously, without CF loading. A mixture of 10 μM AMP and 0.1 mg/ml SUVs was injected into a disposable capillary cell with model number DTS1060C. After an equilibrating time of 120 s, triplicate measurements were employed for each sample to calculate the errors. All Zeta potential measurements were performed in Tris-HCl buffer (10 mM Tris, 154 mM NaCl, pH 7.4) at 20 ± 1 °C.

Raman spectra were recorded using a HORIBA micro-Raman spectrometer equipped with an optical microscope. Samples were focused through a 100× lens and irradiated by 532 nm laser (2.33 eV). Data was collected using 1200 lines/mm grating with a spectral resolution of 2.71 cm^{-1}. Laser power was kept between 1 mW and 8 mW, and the integration time was 60 s. Spectra were collected and analysed in LabSpec 6 software.

2.9 Neutron reflection (NR) of AMP binding to spread lipid monolayers

Spread lipid monolayers were formed at the air/water interface using a purpose-built Langmuir trough to facilitate NR measurements.[7] In brief, a Langmuir trough (Nima Technology) with a surface area of 12.5 cm × 15 cm was filled with 70 mL of D_2O buffer (10 mM phosphate buffer, 137 mM NaCl, pH/pD = 7.4), followed by the addition of deuterated di-palmitic phophorylcholine (d_{62}-DPPG, dissolved in chloroform/methanol = 9/1, v/v) with the surface pressure controlled at 28 mN/m. Thereafter, hydrogenated AMPs were injected underneath the DPPG monolayers with the final bulk concentrations of 1 μM for Melittin and 3 μM for LDKA, G_3, and G_4. The lipid monolayers with and without the interaction of AMPs were also measured by NR for comparison.

NR experiments were performed using the FIGARO reflectometer at the ILL Neutron Source (Grenoble, France), and the SURF reflectometer at the ISIS Pulsed Neutron Source (Didcot, UK) as previously stated,[7] and NR data were analysed using a Motofit package.[8] In brief, the interfacial region was represented by i parallel slab layers, each characterized by thickness (τ_i) and scattering length density (SLD, ρ_i). The roughness across all interfaces was fixed at 1 Å. The interfacial structure was then used to calculate the reflectivity from the optical matrix formulism and then directly fitted to the measured NR profiles. Thereafter, volume fractions (φ) of different components distributed across the z-axis were derived from the SLD distributions measured under different isotopic contrasts. The volume fractions and SLDs in each layer must follow:

$$\sum_{i=0}^{n} \rho_i = 1 \text{ and } \sum_{i=0}^{n} \rho_i \varphi_i = \rho_{fit} \qquad (4)\&(5)$$

where n denotes the number of components. The surface concentration of a component in a layer was calculated using $\frac{\tau\varphi}{VN_A}$ (μM/m^2) and $\frac{\tau\varphi M}{VN_A}$ (mg/m^2), where V is the theoretical molecular volume, N_A is the Avogadro's number, and M is the molecular mass. The calculated SLDs, molecular masses, and molecular volumes of different components are given in **Table S2**.

2.10 Simulation models and methods

Lipid Bilayer and Peptide System. The CG structures of DPPG/DPPC and cationic AMPs are illustrated in **Figure S1**. All the MD simulations were completed in GROMACS with the MARTINI force field, with details given in Sections S3 and S4 of the Support Information (**SI3** and **SI4)**. In the systems containing cationic AMPs, counter ions are also included to provide charge neutrality. The initial size of the systems is 12.62×12.62×32.0 nm^3 in x, y and z directions (each leaflet of the bilayer containing 264 lipid molecules) and under periodic boundary conditions. The ratio of peptide and lipid (P/L) in the above peptide-bilayer systems is 1:22. When the ratio is doubled as 1:11, the initial box size would be 12.62×12.62×36.0 nm^3 for the peptide-DPPG bilayer system. The size in the z direction enables the simulation to be started with an appropriate initial distance between the peptides and the bilayer and thus reduces the possible influence of the initial states on the final simulation results. Before examining the interactions between the AMPs and lipid bilayers, we simulated the single lipid bilayer for a sufficiently long time (100 *ns*) to obtain a well-initialized lipid bilayer. Visualization of MD trajectories and simulation results was realized via the visual molecular dynamics (VMD) program.[9]

Peptide Aggregation in Bulk Solution. To study the self-assembly of different AMPs in bulk solution through MD simulation, peptide numbers in each simulation system were fixed and solvated with 100 mM NaCl solution. According to the peptide's secondary conformation in neutral solution, G_3 & G_4 were set up with random coil structures; LDKA and Melittin were kept in α-helical conformation. Similarly, the peptide-solution systems also employed periodic boundary conditions as in the peptide-lipid bilayer system. Each AMP-solution system experiences an MD simulation time of a microsecond after energy minimization and pre-equilibration.

3. Molecular Parameters in Neutron Experiments

Table S2. SLDs of lipids and peptides used in neutron data analysis.

Components		SLD (10^{-6} Å^{-2})	Molecular Mass	Molecular Volume
PBS Buffer		6.35	/	/
dDPPG[a]	Head	3.27	299	283
	Tail	7.08	484	865
Melittin[b]		2.87	2847	3697
LDKA[b]		2.16	1438	1962
G_3[b]		2.23	1636	2289
G_4[b]		2.24	2119	2966

[a] SLDs, molecular masses, and volumes of the deuterated DPPG were given in our previous publications.[4, 10]

[b] SLDs, molecular masses, and volumes of hydrogenated peptides in D_2O were calculated using an online SLD calculator (http://psldc.isis.rl.ac.uk/Psldc/).

4. Force Field of MD Simulations and PMF Method

Molecular dynamics (MD) simulations were carried out at a coarse-grained (CG) molecular level using the MARTINI force field.[11] The standard cut-offs for the MARTINI force field were used for non-bonded interactions; a cut-off of 1.1 nm was used for van der Waals (vdW) interactions, and the Coulomb potential was shifted to zero between 0 and 1.1 nm with a relative dielectric constant of 15 to account for non-polarizable water. The time step used was 20 fs and the neighbour list was updated every 10 steps. Initially, a CG DPPG bilayer containing 528 lipids was built using CHARMM-GUI[12] at 310 K and 1 atm. All peptide 3D structure models were set up by Avogadro software firstly to generate peptides' topologies, and the Martinize (v.2.6) script was used. The peptide structures were also used for secondary structure assignment, employing the Define Secondary Structure of Proteins (DSSP) program.[13] All simulations were run by the Gromacs 4.5.4 package,[14] and every simulation system initially experienced energy minimization for removing close molecular contacts. Thereafter, MD runs for the peptide-DPPG bilayer system were carried out in the constant-*NPT* ensemble at ~ 310 K using the Berendsen (equilibration run) and Nosé-Hoover (production run) thermostats with a time constant of 2 ps, representing physiological temperature as successfully employed previously in the MARTINI model, with pressure bath of 1 bar controlled by Berendsen (equilibration run) and Parrinello-Rahman barostat (production run) with time constants of 6 and 12 ps, respectively.[15] The compressibility of the systems was set at 3 × 10^{-4} bar^{-1} in both lateral and normal directions to ensure a tensionless lipid bilayer. While in the peptide-solution system, there is no pressure loaded on water box after an equilibration run.

The adsorption energy (U_{tot}) is comprised of a van der Waals (vdW) interaction energy (U_{vdW}) and electrostatic interaction energy (U_{ele}):

$$U_{\mathrm{tot}} = U_{\mathrm{ele}} + U_{\mathrm{vdW}} \tag{6}$$

In the original MARTINI force field, the vdW interaction energy is calculated by the Lennard-Jones potential model:

$$U_{\mathrm{vdW}} = 4\varepsilon_{ij}\left[\left(\frac{\sigma_{ij}}{r}\right)^{12} - \left(\frac{\sigma_{ij}}{r}\right)^{6}\right] \tag{7}$$

where r is the distance between the particle i and j, ε_{ij} is the depth of the potential well and σ_{ij} is the finite distance at which the inter-particle potential is zero.

Electrostatic interactions between charged groups were calculated via a shifted Coulombic potential energy function:

$$U_{\mathrm{ele}} = \frac{q_i q_j}{4\pi\varepsilon_0\varepsilon_1 r} \tag{8}$$

where r is the distance between the charge centre of particle i and j, q_i and q_j are the net charges of particles i and j, ε_0 is the value of the absolute dielectric permittivity of classical vacuum and ε_1 is the dielectric constant (varying from different systems, here it was set at 1.3 in our system) in MARTINI simulation.

To construct a series of initial configurations of AMP distancing from the bilayer, AMPs were dragged from the outside bulk solution into the lipid membrane along the z-axis (perpendicular to the membrane) by applying a pull force of 1000 kJ mol^{-1} nm^2, and the pull rate was kept at 0.01 nm ps^{-1}. Total 51 windows with a 0.1 nm step size were generated as starting points for the following umbrella sampling simulations. For each window, a biased harmonic potential with a force constant of 1000 kJ mol^{-1} nm^2 was adopted to make the AMP restrained within the sampling window. Each window was simulated for 400 ns. The first 200 ns of each run were discarded and the remaining 200 ns was chosen for data collection and analysis. The results of all the windows were integrated and the PMF profile was then derived with the weighted histogram analysis method (WHAM).[16]

5. Beads Mapping in CG Models, Adsorption of Peptides at the Air/Liquid Interface and Aggregating in Solution

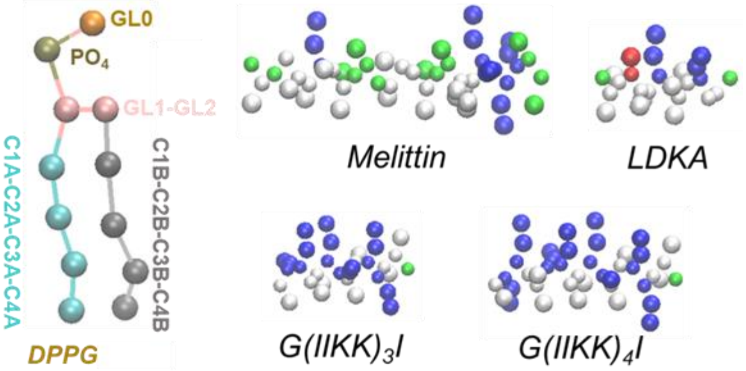

Figure S1. Schematic molecular structures of MARTINI CG DPPG lipid molecules and peptides: melittin, LDKA, G(IIKK)$_n$I-NH_2 (n = 3 and 4, denoted as G_3 and G_4). Orange and brown beads represent the head group PO_4 and GL0 of DPPG, and the same bead colouring corresponding to the head groups of DPPG was employed in the other graphs unless otherwise specified. Blue, red, white and green beads are amino acids with positively charged, negatively charged, hydrophobic and polar uncharged side chains, respectively.

The lipid bilayer is solvated by CG nonpolar water molecules as we used previously.[4] The secondary conformation of a peptide in the peptide-DPPG bilayer system was employed as α-helix. The initial system of peptide self-assembly shown in **Figure S2A** contains different numbers of peptides in a disordered state. ($N_{melittin}$= 50, $N_{LDKA/G3/G4}$=120). The box size is 12 × 12 × 12 nm^3.

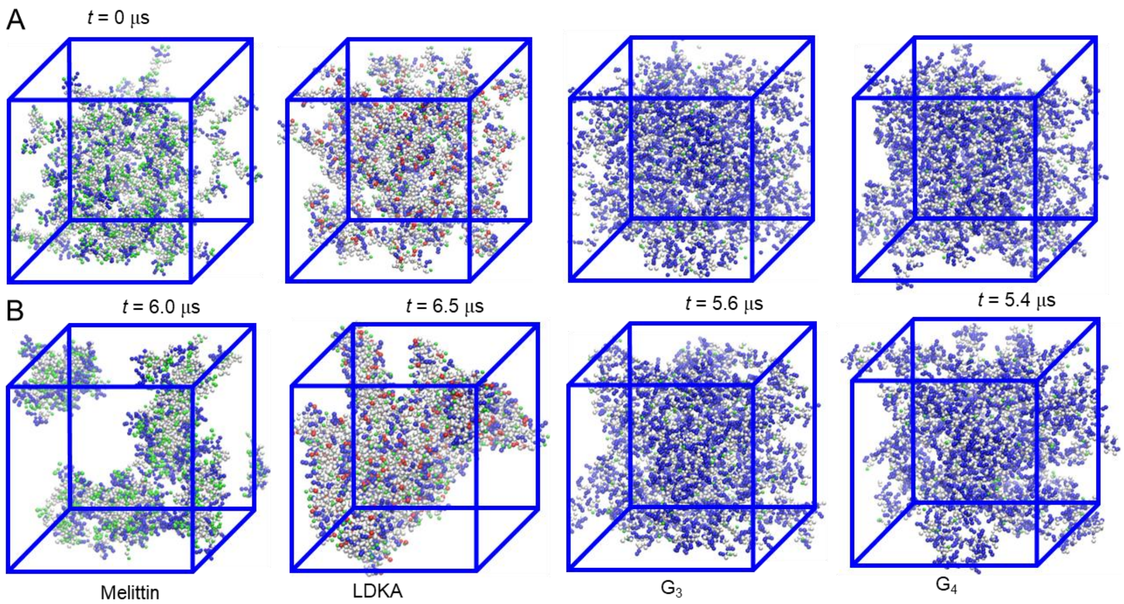

Figure S2. (A, B) The initial and final states of G_3, G_4 and LDKA (N = 120), and Melittin (N = 50), in neutral solution (100 mM NaCl solution) from CG-MD simulations after microseconds. The water environment in the box was removed to show clear peptide morphologies.

It is difficult to make reliable measurements of the size and shape of AMP nanoaggregates at concentrations above μM using light scattering techniques due to multiple scattering. MD simulations provide an effective means of revealing if self-assembly occurs and how the process proceeds to the final states. **Figure S2** show the initial and final states (after 5-6 μs) of AMP aggregation. The snapshot images reveal that only α-helix adopting LDKA molecules self-assemble into nanofibers with radii of 4 ~ 6 nm in the buffer. These nanofibers have a typical cylindrical structure with a hydrophobic core and charged outer surface, and they physically cross-link to form hydrogels. Like LDKA, Melittin also adopts an initial α-helical structure, but its nanoaggregates are small and diverse in size and shape and thus structurally disordered. From all-atom MD simulations, Liao *et al.*[17] have shown that Melittin monomers in aqueous solution can aggregate into the tetrameric state involving dimeric and trimeric intermediates. The formation of Melittin oligomers is clearly different from the ordered LDKA nanofibers. LDKA and Melittin bear distinctly different amphiphilic structures and the former favours self-assembly into ordered nanofibers, driven by a balance of hydrogen bonding, hydrophobic, hydrophilic and electrostatic interactions.[18] In contrast, G_3 and G_4 exist as random coils in neutral solution, with some of them forming oligomers due to their distinct sequences.

Typical AFM images from AMP solutions are shown in **Figure S3A**. Among the four AMPs, only LDKA self-assembles into nanofibers, whilst the other 3 AMPs aggregate into amorphous morphologies. Small LDKA nanoparticles can also be observed under AFM imaging. These alternatives concurrently expressed morphologies may indicate that the long nanofibers of LDKA are self-assembled from small nanoobjects. Thus, the MD simulation results of different peptide aggregate morphologies (**Figure S2D**) are in good agreement with the observations from AFM imaging.

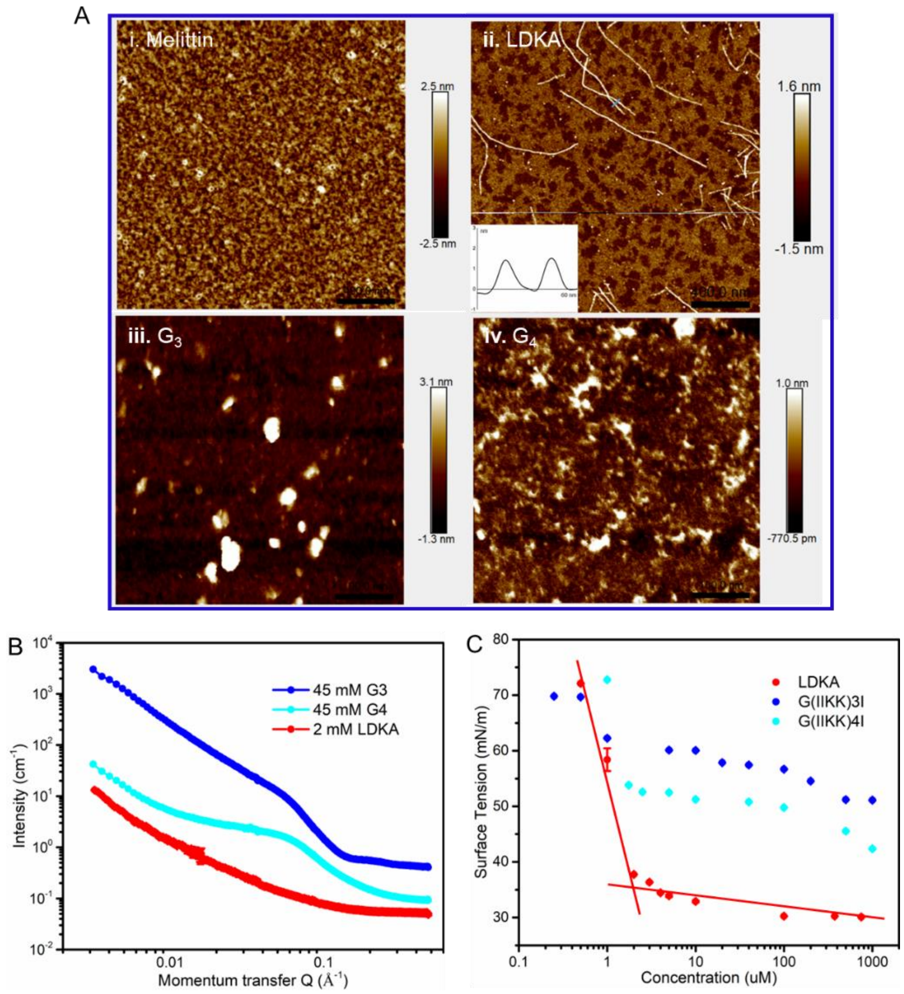

Figure S3. (A) AFM images of (i-iv) Melittin, LDKA, G_3 and G_4 self-assembled morphologies. (B) SANS profiles for the three designed AMPs (45 mM G_3/G_4 and 2 mM LDKA) in D_2O solution. (C) Surface tension changes of the three designed AMPs showing their different adsorption behaviour in the Tris buffer solution (pH = 7.4).

Typical self-assembled AMP nanostructures were further characterized by SANS and the scattering intensity profiles from the 3 designed AMPs from aqueous solutions in D_2O are shown in **Figure S3B**, with the concentrations of G_3/G_4 kept at 45 mM and of LDKA at 2 mM. SANS data analysis confirmed the long nanofibers from LDKA when its concentration was above its CAC (about 3 μM). The SANS profile can be fitted to the combined cylinder and lamellar models. The cylinder is characterized by a radius of 2.0 ± 0.2 nm with a polydispersity index of 0.25 and the length ranging from 500 nm to several μm. The size and shape of LDKA nanoaggregates from SANS are thus highly consistent with results from MD simulation and AFM studies. Our previous work[2] indicated that the CAC of G_4 was ~ 0.17 mM. G_4 can self-assemble and gel as its concentration increased to 25 mM. The SANS profiles obtained from G_3/G_4 solutions at the concentration of 45 mM indicate supramolecular assemblies that can be fitted with the cylinder+lamellar models, with the best-fit parameters listed in **Table S3**.

The four AMPs (LDKA, G_3, G_4 and Melittin) have different lengths and sequences and display different amounts of amphiphilicity. It is therefore useful to examine their surface adsorption and solution aggregation behaviour before assessing their antimicrobial actions and membrane lytic processes. The solutions used in these studies were prepared in Tris buffer at pH 7.4 containing 150 mM NaCl. AMP concentrations were varied from 1 to 1000 μM. A distinct observation was the gelling of LDKA under ambient temperature. Its solution also became turbid as its concentration rose, indicating its limited solubility. In contrast, the other 3 AMP solutions showed normal solution behaviour with no sign of drastic viscosity increase or turbidity. Interfacial adsorption and solution aggregation were measured at 20-23 °C using surface tension changes. These studies allowed the self-assembling ability of the AMPs to be assessed, relevant to their capacity to permeate membranes.

The three designed AMPs were all capable of decreasing the surface tension of the buffer solution. LDKA is most effective and can decrease surface tension to some 40 mN/m at a concentration of ~ 2 μM (**Figure S3C**). The fast reduction of surface tension at such a low concentration range reveals its exceedingly high surface adsorption capability. This feature is strongly associated with its low solubility and unique amphiphilic character. For G_4, however, increases in its concentration ranging from 1 to 1000 μM led to reduced surface tension changes compared with LDKA, but it was the 2nd most surface-active AMP studied. Over the concentration range from 1 to 100 μM, its surface tension drops from 55 to 50 mN/m; this is in the effective bactericidal concentration range. G_3 displays a concentration-dependent surface tension profile similar to G_4 and its surface tension values vary from 60 to 55 mN/m from 1 to 100 μM, showing weaker surface activity than G_4. Melittin decreases surface tension to ~ 35 mN/m at a concentration of 35 μM (0.1 mg/ml, data not shown), comparable to LDKA.[19]

6. SANS Fitting Parameters of AMP Self-assembly in Solution

Table S3. Model parameters from best fits to the measured SANS data from self-assembled G_3 and LDKA.

Peptide/ Concentration	**G_3/45 mM**	**LDKA/2 mM**
Fitting Model	Cylinder lamellar	Cylinder lamellar
Scale[a]	0.018	0.0012
Background ($\times 10^{-3}$ cm^{-1})	85±5	55±5
Scale ratio of A/B[b]	3±1	0.3±0.1
A_SLD_core ($\times 10^{-6}$ Å^{-2})	5±0.2	0.4±0.2
A_SLD_shell ($\times 10^{-6}$ Å^{-2})	5±0.2	5.0±0.5
A_radius (Å)	22±2	20±2
A_radius PDI[c]	0.25±0.05	0.25±0.05
A_thickness (Å)	8±1	7±3
A_length (Å)	2000	2000
B_length_tail (Å)	14±2	10±2
B_length_head (Å)	4±1	4±2
B_SLD ($\times 10^{-6}$ Å^{-2})	2.3±0.1	2±0.2
B_SLD_head	5.0±0.2	5.5±0.5

($\times10^{-6}$ Å^{-2})		
SLD Solvent ($\times10^{-6}$ Å^{-2})[d]	6.3±0.1	6.3±0.1

Note: Errors in SANS were estimated by the range of model parameters beyond which the SANS fits were noticeably different.

[a] Scale was the volume fraction of the self-assembly structure (including hydration) from the SANS model fit.

[b] Scale ratio of A/B was the ratio of volume fraction of two self-assembly structures cylinder and lamellar shapes from the SANS fitting model.

[c] PDI denotes polydispersity index of the cylinder radius.

[d] SLD of pure D_2O is 6.35×10^{-6} Å^{-2}. In our experiments, D_2O contained a small amount of H_2O due to sample mixing, leading to smaller SLD values for the solvents.

7. Antimicrobial and Biocompatibility Assays

Minimal inhibitory concentration (MIC) assays of different antimicrobials against various bacteria were carried out by broth microtiter dilution (BMD) according to the British Society for Antimicrobial Chemotherapy (BSAC) methodologies.[20] Breakpoints used to interpret MICs were based on published European Clinical Antimicrobial Susceptibility Testing (EUCAST) guideline.[21] Gram-negative *Escherichia coli* (*E. coli*, ATCC 25922) and Gram-positive *Staphylococcus aureus* (*S. aureus*, ATCC 6538) were obtained from the American Type Culture Collection (ATCC). Extended-spectrum beta-lactamase resistant *E. coli* (ESBL-*E. coli*) and meticillin-resistant *S. aureus* (MRSA) were clinically isolated strains. All bacteria were grown in Mueller Hinton broth (MHB).

Table S4. Bacterial MICs of different antimicrobials against *E. coli* and *S. aureus* and their respective antibiotic-resistance strains.

Components/Strains	*E. coli* [a]	*ESBL-E. coli*	*S. aureus*	*MRS aureus*/μM	Hemolysis EC$_{50}$/μM
G$_3$	8.0	8.0	3.5	3.1	> 1000
G$_4$	4.0	2.0	9.4	4.7	250
LDKA	23.4	80	6.3	12.5	250
Melittin	2.0	2.0	2.0	1.3	5.0
Ampicillin	6.0	> 1000	0.2	> 1000	> 1000
Tetracycline	4.0	4.0	0.8	0.5	> 1000
Minocycline	2.0	2.0	0.8	0.25	> 1000

[a]The concentration unit of antimicrobial in MIC assays is μM.

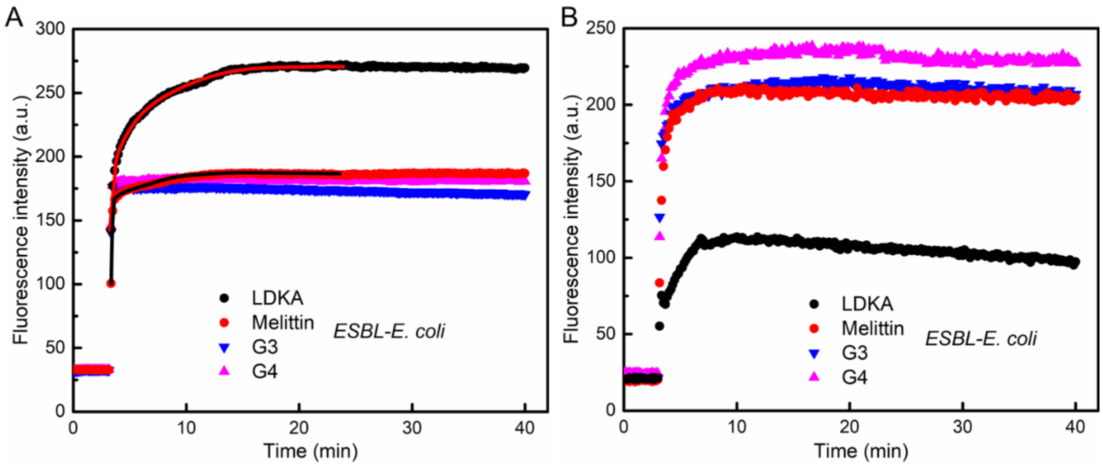

Figure S4. Permeability of outer membrane (A) and cytoplasmic membrane depolarization (B) by AMPs at 10 × MIC concentration for drug-resistant ESBL-*E. coli*.

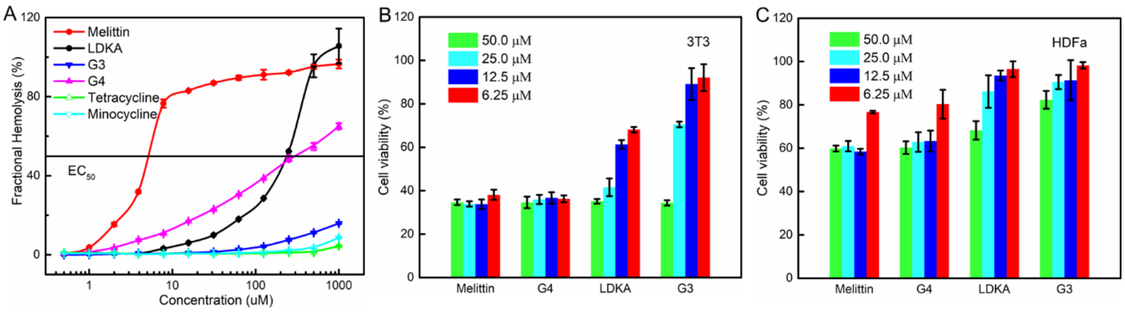

Figure S5. (A) Haemolysis profiles measured from exposure of AMPs and conventional antibiotics to human red blood cell (hRBC) at concentrations ranging from 0 to 1000 μM. Fractional haemolysis is shown as a function of peptide concentration. Cytotoxicity profiles measured from MTT assays from exposure of AMPs to 3T3 (B) and HDFa (C) at concentrations ranging from 6.25 to 50 μM.

8. AFM of Pure Liposome and Raman Spectroscopy of Liposomes with and without AMPs

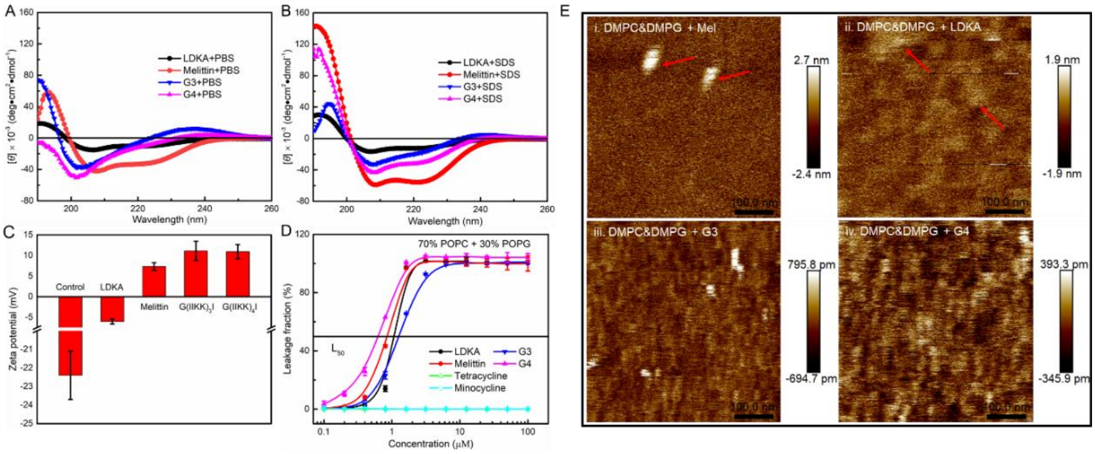

Figure S6. Molar ellipticity plotted versus wavelength to show secondary structures of Melittin, LDKA, G_3 and G_4 in (A) Tris buffer solution and (B) the buffer containing 25 mM SDS micelles. (C) Zeta potential of SUVs comprised of DMPC/DMPG (7/3, mol/mol) upon exposure to 10 μM AMPs. (D) Percentage of fluorescence leakage of CF-incorporated SUVs comprised of POPC/POPG (7/3, mol/mol) upon exposure to AMPs. (E) AFM images showing a variety of features in a DMPC/DMPG (7/3, mol/mol) bilayer incubated with AMPs.

AFM images of Si surface and Si wafer coated with DMPC&DMPG bilayer were shown in **Figure S7**, both of them are relatively smooth while the DMPC&DMPG bilayer presents more obvious roughness. The roughness (~ 3 nm) is mostly owed to the natural morphology of periodic wrinkles on lipid bilayer when coated on Si wafer. The AMP induced bilayer coated on the freshly cleaned Si wafer obeyed the following method: the pure bilayer was coated on the Si firstly, the extra solution on the Si was gently removed by N_2 gas, then a low concentration of AMP solution was added onto the coated bilayer, after ~1 min membrane binding, the AMP solution was gently removed. The samples would be ready for AFM measurements.

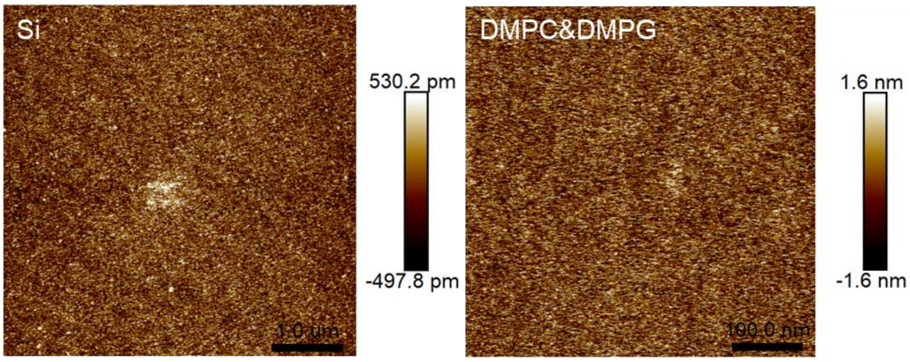

Figure S7. AFM images of Si wafer surface and DMPC&DMPG deposited on Si wafer. Their scale bars were 1.0 μM and 100 nm respectively.

Raman spectra have been used to investigate phospholipid acyl chain structure in vesicles under different conditions,[22] and its high sensitivity offers useful insight into structural disturbances within lipid membranes as a result of binding or association.[23] The binding of AMPs to the same DMPG/DMPG SUVs was employed in the Raman spectroscopy, the SUVs and AMPs were firstly mixed at a fixed ratio and fully reacted. About 80 μL mixed solution was dropped onto Si wafer, after solvent evaporation under 37 °C environment to make sure the samples were totally dried. Then, their Raman spectra characterizations were carried out. The range of the measured Raman shift was from 1250 to 3200 cm^{-1}.

The spectra in **Figure S8** were measured from DMPC/DMPG SUVs deposited onto a silicon wafer after solvent evaporation, comparing changes in peaks at ~1294 cm^{-1} and ~1437 cm^{-1} (**Figure S8A**) and 2800-2955 cm^{-1} (**Figure S8B**) before and after mixing with the AMPs with the molar ratio of 10 : 1. The peak at 1295 cm^{-1} is associated with the CH_2 twisting mode. Its broadening and shifting to the higher frequency is evident of acyl chain disturbances. The width of the peak further increased in both G_3 and G_4, indicating the decoupling of the acyl chains associated with the increased disorder in the membrane core. Similar situations also occurred from LDKA and Melittin binding, suggesting that they can disturb the membrane core like G_4.

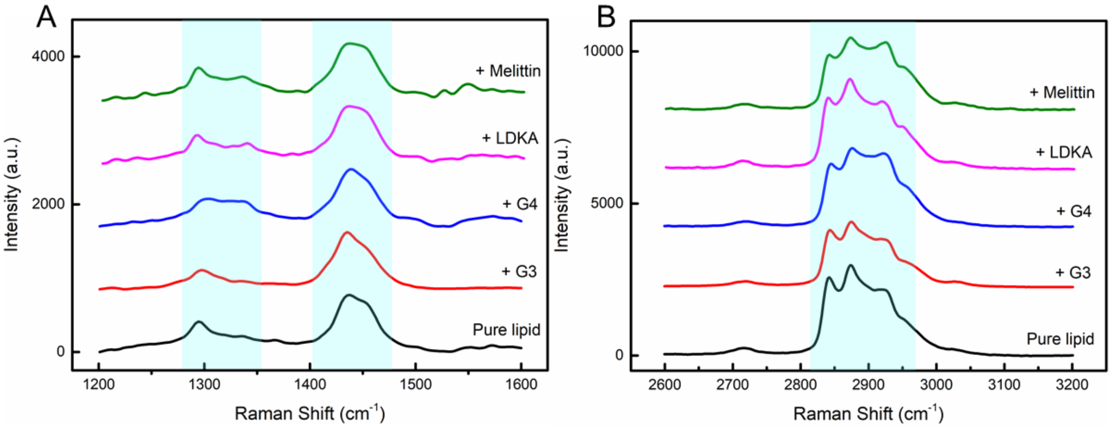

Figure S8. Variations of the Raman spectra of DMPC/DMPG SUVs before and after exposure to AMPs with a lipid/AMP molar ratio 10 : 1. All samples were deposited on silicon wafer and measured at 23 °C. The spectrum of full wavelength and assignment of the main Raman bands for SUVs in different groups shown in **Table S5**.

The CH_2 bending region is a unique indicator of lipid lattice order, this region contains the strongest signal coming from both methylene bending or scissoring at 1436 cm^{-1} and asymmetric methyl bending at 1455 cm^{-1}. The ratio I_{1436}/I_{1455} increases in the group of G_3 and G_4 (from 1.18 to 1.40 and 1.23), indicating that the process of cationic G_3/G_4 membrane binding improves the orderness of the lipid bilayer. While the wider peaks around 1436 cm^{-1} from LDKA and Melittin reflected the more disorder membrane states than both G_3 and G_4. This seems to be at conflict with the conclusion drawn from the CH_2 twisting mode, but actually reflects the complex process of disturbance of the bilayer caused by cationic AMPs.

The C-H stretching region around 2800-3000 cm^{-1} is characterized by three principal peaks: the peaks at 2844 and 2875 cm^{-1} are assigned to the symmetric and antisymmetric C-H stretching vibrations, respectively, and the 2934 cm^{-1} peak assigned in part to the terminal methyl symmetric stretching.[24] The ratio of the antisymmetric C-H stretching (2875 cm^{-1}) to the symmetric C-H stretching (2844 cm^{-1}) indicates lateral packing density of acyl chain in the DMPG/DMPC membrane and an increase in the peak intensity ratio reveals acyl chain rotational order. Here, the obvious increase of I_{2875}/I_{2844} ratio in G_4, LDKA and Melittin groups (increase from 1.16 to 1.24, 1.26 and

1.31) shows their corresponding higher packing density and more ordered acyl chains than G_3 under the fixed P/L ratio. This situation reflects that a thick adsorption layer of cationic AMPs onto a negatively charged membrane can also improve membrane order to a different degree. Other than this, the I_{2924}/I_{2844} peak intensity ratio is sensitive to intermolecular chain coupling, and the increase of the ratio in the group of G_4, LDKA and Melittin (from 0.84 to 1.16, 0.95 and 1.22) means that there is more freedom of motion and rotational disorder in the membrane.[23a, 25] Overall, the situations described above indicate the greater disturbances of the lipid tail region by G_4 and Melittin than the slightly disordered membranes induced by G_3 and LDKA.

Thus, Raman specstroscopy is highly effective at resolving structural features from the DMPC/DMPG model (mol/mol, 7/3) and the membrane mixed with AMPs, with the corresponding Raman shifts being highly consistent with previously reported values.[24, 25b, 26] Full band assignments are given in **Table S5**.

Table S5. Assignment of the main Raman bands for SUVs in different groups and the spectra are shown in **Figure S8**.

Raman shift (cm^{-1})	Assignments
1294-1303	CH_2 twist
1435-1438	CH_2/CH_3 scissoring
1647-1655	Amide I band
1733-1736	C-H stretching
2840-2844	CH_2 symmetric stretching
2873-2875	CH_2 antisymmetric stretching
2917-2923	CH_3 symmetric stretching
2950-2952	CH_3 asymmetric stretching

9. SANS Fitting Model of SUV with AMPs and NR Fitting Model of AMPs' Binding with Lipid Monolayer

Table S6. Model parameters from fits to the SANS data from LPS/POPC SUVs and AMPs' binding SUVs, similar fitting models were also employed in our previous work.[6, 27]

Sample	**1 mM hLPS/hPOPC**	**Sample**	**+ G3**	**+ G4**	**+ LDKA**	**+ Melittin**
			100 μM	100 μM	100 μM	100 μM
Fitting Model A[a]	**CMS[c]**	**Fitting Model B[b]**	**CMS_LP[d]**	**CMS_LP**	**CMS_LP**	**CMS_LP**
Background (×10^{-3} cm^{-1})	3.5±0.2	**Background (×10^{-3} cm^{-1})**	3.5±0.2	3.5±0.2	3.5±0.2	3.5±0.2
A_volume fraction (× 10^{-3})	2.5±0.2	**Scale_A**	1	1	1	1
A_core_SLD (× 10^{-6} Å^{-2})	6.0±0.1	**A_core_SLD (× 10^{-6} Å^{-2})**	6.0±0.1	5.8±0.1	6.0±0.1	5.0±0.1
A_solvent_SLD (× 10^{-6} Å^{-2})	6.3±0.1	**A_solvent_SLD (× 10^{-6} Å^{-2})**	6.2±0.1	6.2±0.1	6.2±0.1	6.2±0.1
A_radius (Å)	205±10	**A_radius (Å)**	185±10	230±10	200±10	200±10
A_radius PDI[e]	0.5±0.1	**A_radius PDI[c]**	0.5±0.1	0.5±0.1	0.5±0.1	0.5±0.1
A_layer1_thickness (Å)	15±1	**A_thickness (Å)**	35±2	36±2	35±2	30±2
A_layer 1_SLD (× 10^{-6} Å^{-2})	5.4±0.2	**A_shell_SLD (× 10^{-6} Å^{-2})**	3.5±0.2	3.7±0.2	3.2±0.2	3.7±0.2
A_layer 2_thickness (Å)	30±2	**A_thickness PDI[f]**	0±0.1	0.3±0.1	0±0.1	0.4±0.1
A_layer 2_SLD (×10^{-6} Å^{-2})	0.3±0.1	**Scale_B**	1.4±0.1	23±1	14±1	167±5
A_layer 3_thickness (Å)	15±1	**B_peak_pos (Å^{-1})**	0.1±0.005	0.11±0.005	0.03±0.005	0.098±0.005
A_layer 3_SLD (×10^{-6} Å^{-2})	5.4±0.2	**B_peak_hwhm (Å^{-1})**	0.01±0.001	0.005±0.001	0.015±0.001	0.005±0.001

[a] Model A is the core multilayer shell model model to represent pure lipid SUVs.

[b] Model B is a Lorentzian peak model (see in

http://www.sasview.org/sasview/user/models/model_functions.html#peaklorentzmodel).

[c]CMS denotes the core multilayer shell model and [d]CMS_LP denotes a Lorentzian peak model.

[e]PDI and [f]PDI denote polydispersity index of the vesicle radius and shell thickness, respectively.

Table S7. Model parameters from fits to the SANS data from POPC/POPG SUVs and AMPs' binding SUVs, similar fitting models were also employed in our previous work.[6, 27]

Sample	**1 mM hPOPC /POPG**	**+ G3/μM**			**+ G4/μM**			**+ LDKA/μM**		
		50	100	200	50	100	200	50	100	200
Fitting Model[a]	**CMS**[b]	**CMS**			**CMS**			**CMS**		
Background ($\times 10^{-3}\ cm^{-1}$)	14.5±0.5	14.5±0.5			14.5±0.5			14.5±0.5		
A_volume fraction ($\times 10^{-3}$)	2.5±0.2	2.0±0.2			2.0±0.2			2.5±0.2		3.5±0.5
A_core_SLD ($\times 10^{-6}$ Å^{-2})	6.3±0.1	6.1±0.1	6.1±0.1	6.0±0.1	6.2±0.1	6.1±0.1	6.3±0.1	6.1±0.1	6.2±0.1	6.3±0.1
A_solvent_SLD ($\times 10^{-6}$ Å^{-2})	6.3±0.1	6.3±0.1			6.3±0.1			6.3±0.1		
A_radius (Å)	180±10	180±10	190±10	190±10	180±10	180±10	185±10	270±10	290±10	460±25
A_radius PDI[c]	0.4±0.1	0.5±0.1	0.4±0.1	0.5±0.1	0.5±0.05	0.6±0.05	0.60±0.1	0.3±0.1	0.3±0.1	0.6±0.1
A_layer1_thickness (Å)	7±1	7±1	8±1	8±1	8±1	10±2	8±1	8±1	10±2	7±2
A_layer 1_SLD ($\times 10^{-6}$ Å^{-2})	3.8±0.2	3.1±0.2	3.3±0.2	4.2	3.8±0.2	2.8±0.2	2.8±0.2	4.0±0.2	4.0±0.2	4.5±0.2
A_layer 2_thickness (Å)	27±3	27±3	27±3	27±3	27±3	28±2	10±3	27±3	25±2	27±2
A_layer 2_SLD ($\times 10^{-6}$ Å^{-2})	-0.1±0.1	-0.1±0.1	0.2±0.1	-0.1±0.1	-0.1±0.1	0.1±0.1	4±0.2	-0.1±0.1	-0.1±0.1	-0.1±0.1
A_layer 3_thickness (Å)	7±1	7±1	7±1	7±1	7±1	7±1	27±2	7±1	7±1	7±1
A_layer 3_SLD ($\times 10^{-6}$ Å^{-2})	3.8±0.2	3.8±0.2	3.8±0.2	3.8±0.2	3.8±0.2	3.8±0.2	0.3±0.1	3.8±0.2	3.8±0.2	4.5±0.2

A_layer 4_thickness (Å)	7
A_layer 4_SLD ($\times 10^{-6}$ Å^{-2})	3.6±0.2

[a] Model A is the core multilayer shell model to represent SUVs.

[b] CMS denotes the core multilayer shell model.

[c] PDI denotes polydispersity index of the vesicle radius.

Table S7-1. Model parameters from fits to the SANS data from POPC/POPG SUVs and Melittin binding SUVs

Sample	**1 mM hPOPC/POPG**	**+ Melittin**	**Sample**	**+ Melittin**
		50 μM		100 μM
Fitting Model A[a]	**CMS[b]**	**CMS**	**Fitting Model B**	**CMS_LP**
Background ($\times 10^{-3}$ cm^{-1})	14.5±0.5	4.0±0.5	**Background ($\times 10^{-3}$ cm^{-1})**	3.5±0.2
A_volume fraction ($\times 10^{-3}$)	2.5±0.2	2.5±0.2	**Scale_A**	1
A_core_SLD ($\times 10^{-6}$ Å^{-2})	6.3±0.1	6.2±0.1	**A_core_SLD ($\times 10^{-6}$ Å^{-2})**	6.0±0.1
A_solvent_SLD ($\times 10^{-6}$ Å^{-2})	6.3±0.1	6.3±0.1	**A_solvent_SLD ($\times 10^{-6}$ Å^{-2})**	6.2±0.1
A_radius (Å)	180±10	250±10	**A_radius (Å)**	220±10
A_radius PDI[c]	0.4±0.1	0.4±0.1	**A_radius PDI**	0.5±0.1
A_layer1_thickness (Å)	7±1	20±2	**A_thickness (Å)**	35±2
A_layer 1_SLD ($\times 10^{-6}$ Å^{-2})	3.8±0.2	5.7±0.2	**A_shell_SLD ($\times 10^{-6}$ Å^{-2})**	3.5±0.2
A_layer 2_thickness (Å)	27±3	33	**A_thickness PDI[d]**	0±0.1
A_layer 2_SLD ($\times 10^{-6}$ Å^{-2})	-0.1±0.1	0.3±0.1	**Scale_B[e]**	105±5
A_layer 3_thickness (Å)	7±1	18±2	**B_peak_pos[f] (Å^{-1})**	0.066±0.005
A_layer 3_SLD ($\times 10^{-6}$ Å^{-2})	3.8±0.2	6.2±0.2	**B_peak_hwhm[g] (Å^{-1})**	0.024±0.001

[a,b,c] Of same meaning as in Table S6.

[d] PDI denotes polydispersity index of the bilayer thickness of vesicle.

[e-g] Denotes the specific parameters in a Lorentzian peak model (Fitting Model B) (http://www.sasview.org/sasview/user/models/model_functions.html#peaklorentzmodel)

Table S8. Best fit parameters obtained from analysis to NR profiles of the DPPG monolayer without and with exposure to AMPs, as reported in the previous work.[4, 6] τ is the layer thickness, φ is the volume fraction, Γ is the surface concentration. Tail, head, and peptide layers are denoted layers 1 – 3, representatively.

Layer	**T (Å)**	**φ_{lipid}**	**$\varphi_{peptide}$**	**$\varphi_{solvent}$**	**$\Gamma_{peptide}$ (μM/m²)**	**$\Gamma_{peptide}$ (mg/m²)**
DPPG						
Tail	18 ± 2	1.00 ± 0.05	-	-	-	-
Head	10 ± 1	0.59 ± 0.06	-	0.41 ± 0.04	-	-
DPPG + MLT						
Tail	18 ± 2	0.80 ± 0.08	0.15 ± 0.03	0.05 ± 0.03	0.12 ± 0.01	0.35 ± 0.03
Head	13 ± 1	0.36 ± 0.04	0.27 ± 0.03	0.37 ± 0.03	0.15 ± 0.02	0.45 ± 0.04
Peptide	29 ± 3	-	0.55 ± 0.06	0.45 ± 0.05	0.73 ± 0.07	2.06 ± 0.20
DPPG + LDKA						
Tail	20 ± 2	0.86 ± 0.08	0.05 ± 0.01	0.00 ± 0.00	0.08 ± 0.01	0.12 ± 0.01
Head	14 ± 1	0.40 ± 0.04	0.08 ± 0.01	0.52 ± 0.05	0.09 ± 0.01	0.14 ± 0.01
Peptide	21 ± 2	-	0.39 ± 0.04	0.61 ± 0.06	0.69 ± 0.07	1.01 ± 0.10
DPPG + G_3						
Tail	20 ± 2	0.76 ± 0.08	0.12 ± 0.01	0.06 ± 0.02	0.17 ± 0.02	0.28 ± 0.03
Head	14 ± 1	0.36 ± 0.04	0.16 ± 0.02	0.48 ± 0.05	0.16 ± 0.02	0.27 ± 0.03
Peptide	10 ± 1	-	0.35 ± 0.04	0.65 ± 0.07	0.25 ± 0.03	0.41 ± 0.04
DPPG + G_4						
Tail	20 ± 2	0.79 ± 0.08	0.13 ± 0.01	0.04 ± 0.02	0.15 ± 0.02	0.31 ± 0.03
Head	14 ± 1	0.37 ± 0.04	0.30 ± 0.02	0.33 ± 0.03	0.24 ± 0.02	0.50 ± 0.05
Peptide	11 ± 1	-	0.56 ± 0.05	0.44 ± 0.04	0.34 ± 0.03	0.73 ± 0.07

10. AMPs' Binding Behaviours onto DPPG Bilayers with P/L Changing, and Dye Leakage of AMPs Attacking Pure POPG SUVs.

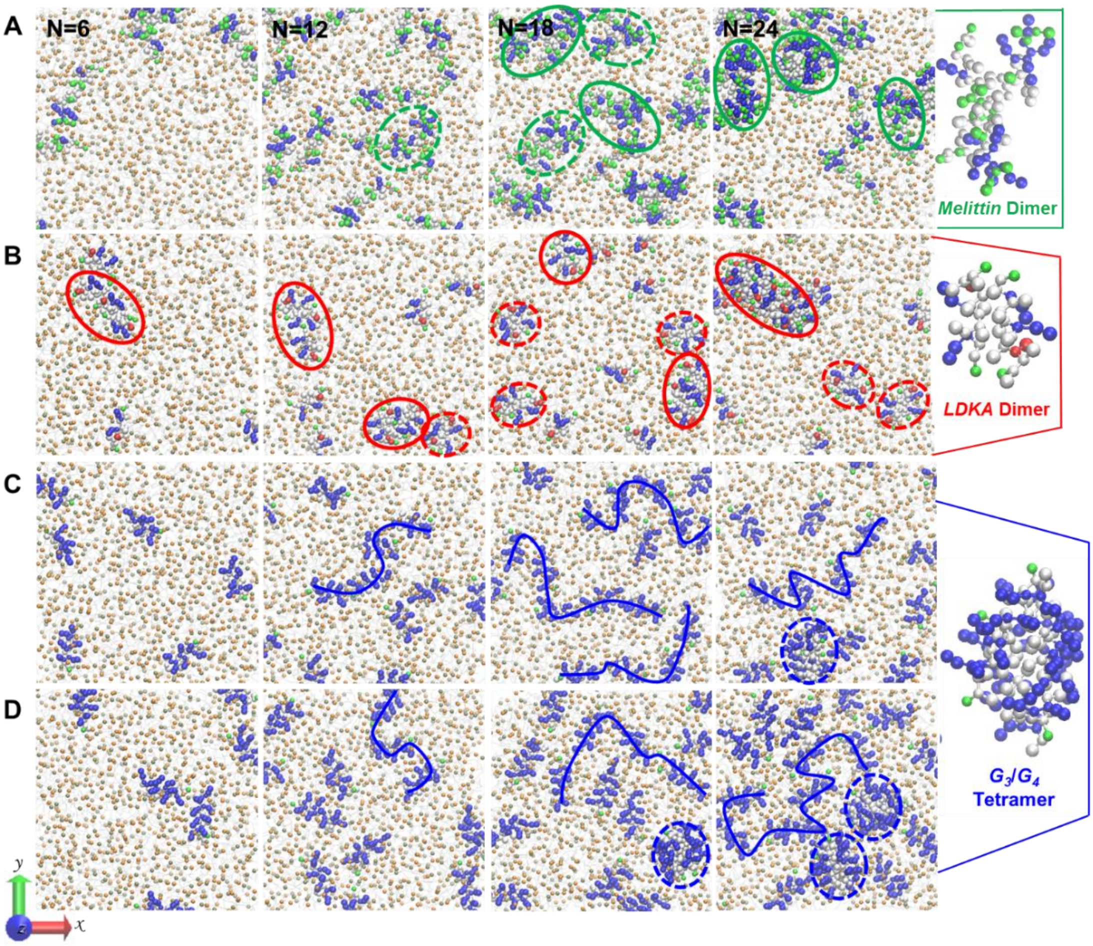

Figure S9. Top-views of (A) melittin, (B) LDKA, (C-D) G_3/G_4 changing with number of peptide (from N = 6, N = 12, N = 18 to N = 24) on DPPG bilayer. The simulation time of each peptide-lipid bilayer system is 1 *us*. The right part is their representative conformation of peptide oligomers, respectively.

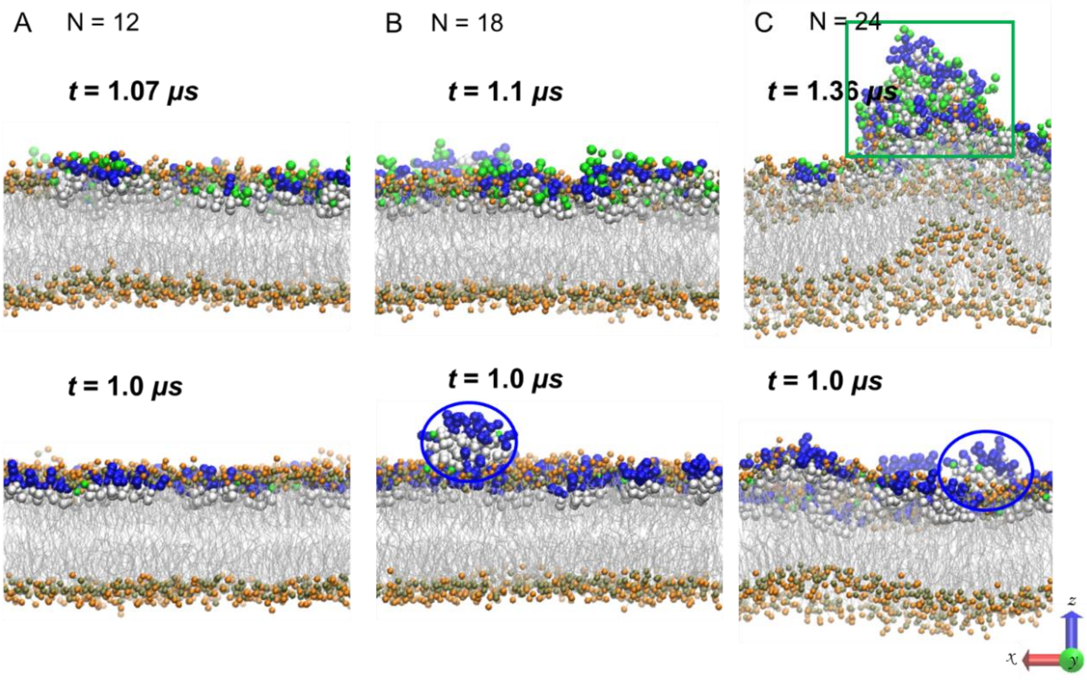

Figure S10. Melittin (upper part) and G_4 (lower part) of different numbers on DPPG bilayer after microsecond MD running, (A) N = 12, (B) N = 18 and (C) N = 24.

To clearly know the charge property of SUVs and the AMP induced SUVs leakage of different modes, fluorescence leakage of 100 % POPG SUVs was compared to 30% POPG SUVs. The results of leakage fraction of 100% POPG showed that the AMP concentration corresponding to 50% leakage and 100% leakage increased in different degrees, especially in the case of melittin, G_3 and G_4. This phenomenon indicated that AMPs' excessive binding or aggregating due to strong electrostatic adsorption onto membrane would be unfavoured to the fully leakage of SUVs. To have a clear comparison with our MD simulation results, the leakage fraction with AMP concentration changing was calculated to get an equivalent link with the P/L ratio. The leakage fraction started to decrease in the group of LDKA and melittin after a P/L ratio of 1/40, at a similar P/L ratio (≥ 1/44, equal to N ≥ 12) (**Figure S8**) in MD simulations obvious AMP clusters or aggregates have been formed onto membrane rather than in the monomer state. However, the leakage fraction decreased from P/L ratio of 1/10, which is consistent with the simulation results that the formation of G_3/G_4 intramembrane clusters demanded a higher P/L ratio (≥ 1/22 for G_3, ≥1/29 for G_4, equal to $N_{G3} \geq 24/N_{G4} \geq 18$) than in case of LDKA/melittin.

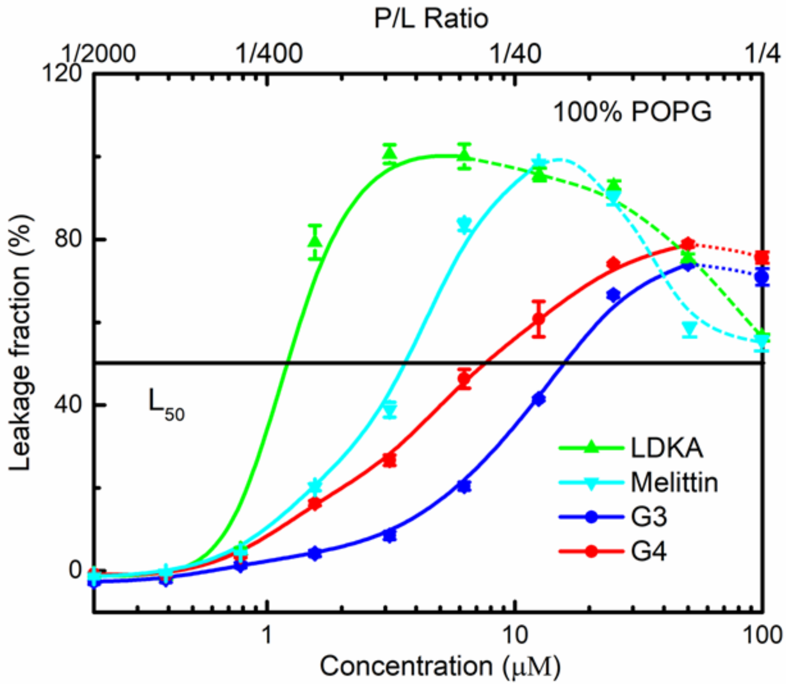

Figure S11. Fluorescence leakage fraction of 100% POPG SUVs upon exposure to AMPs, the bottom x-axis is absolute AMP concentration, the upper x-axis is the calculated molar P/L ratio.

11. References

[1] Haoning Gong, Jing Zhang, Xuzhi Hu, et al., *ACS Applied Materials & Interfaces* **2019**, *11*, 34609-34620.

[2] Meiwen Cao, Wenjing Zhao, Lei Wang, et al., *ACS Applied Materials & Interfaces* **2018**, *10*, 24937-24946.

[3] O. Arnold, J.C. Bilheux, J.M. Borreguero, et al., *Nuclear Instruments and Methods in Physics Research Section A* **2014**, *764*, 156-166.

[4] Haoning Gong, Mingrui Liao, Xuzhi Hu, et al., *ACS Applied Materials & Interfaces* **2020**, *12*, 44420-44432.

[5] aRaymond F Chen, Jay R Knutson, *Analytical Biochemistry* **1988**, *172*, 61-77; bFang Pan, Zongyi Li, Haoning Gong, et al., *Journal of Colloid and Interface Science* **2018**.

[6] Haoning Gong, Marc-Antoine Sani, Xuzhi Hu, et al., *ACS Applied Materials & Interfaces* **2020**, *12*, 55675-55687

[7] aDaniela Ciumac, Richard A Campbell, Luke A Clifton, et al., *ACS Omega* **2017**, *2*, 7482-7492; bDaniela Ciumac, Richard A Campbell, Hai Xu, et al., *Colloids Surf B Biointerfaces* **2017**, *150*, 308-316; cHaoning Gong, Mingrui Liao, Xuzhi Hu, et al., *ACS Appl Mater Interfaces* **2020**; dHaoning Gong, Marc-Antoine Sani, Xuzhi Hu, et al., *ACS Applied Materials & Interfaces* **2020**, *12*, 55675-55687.

[8] Andrew Nelson, *Journal of Applied Crystallography* **2006**, *39*, 273-276.

[9] William Humphrey, Andrew Dalke, Klaus Schulten, *Journal of Molecular Graphics* **1996**, *14*, 33-38.

[10] Haoning Gong, Xuzhi Hu, Mingrui Liao, et al., *ACS Applied Materials & Interfaces* **2021**, *13*, 16062-16074.

[11] Alex H. de Vries, Siewert J. Marrink, Alan E. Mark, *The Journal of Physical Chemistry B* **2004**, *108*, 750-760.

[12] aYifei Qi, Helgi I. Ingólfsson, Xi Cheng, et al., *Journal of Chemical Theory and Computation* **2015**, *11*, 4486-4494; bSunhwan Jo, Taehoon Kim, Vidyashankara G. Iyer, et al., *Journal of Computational Chemistry* **2008**, *29*, 1859-1865.

[13] Christian Sander, Wolfgang Kabsch, *Biopolymers* **1983**, *22*, 2577-2637.

[14] Carsten Kutzner, Berk Hess, David van der Spoel, Erik Lindahl, *Journal of Chemical Theory and Computation* **2008**, *4*, 435-447.

[15] aShuichi Nosé, *The Journal of Chemical Physics* **1984**, *81*, 511-519; bRahman A. J Parrinello M. R. A., *Journal of Applied Physics* **1982**, *52*, 7182-7190; cM. Klein, *Molecular Physics* **1983**, *50*, 1055-1076.

[16] Jochen S. Hub, Bert L. de Groot, David van der Spoel, *Journal of Chemical Theory and Computation* **2010**, *6*, 3713-3720.

[17] Myvizhi Esai Selvan, Chenyi Liao, Jun Zhao, Jonathan L. Slimovitch, Severin T. Schneebeli,, John C. Shelley Mee Shelley, Jianing Li, *The Journal of Physical Chemistry B* **2015**, *119*, 10390-10398.

[18] aCharles H. Chen, Charles G. Starr, Evan Troendle, et al., *Journal of the American Chemical Society* **2019**, *141*, 4839-4848; bCharles H. Starr Chen,

Charles G. Guha, Shantanu Wimley, William C. Ulmschneider, Martin B. Ulmschneider, Jakob P., *The Journal of Membrane Biology* **2021**, *254*, 75-96.

[19] S. C. Ebeling, S. M. Kelly, B. T. O'Kennedy, et al., *Biochimie* **1997**, *79*, 503-508.

[20] *Clinical Microbiology and Infection* **2000**, *6*, 509-515.

[21] D. F. J. Brown G. Kahlmeter, F. W. Goldstein, A. P. MacGowan, J. W. Mouton, I. Odenholt, A. Rodloff, C-J. Soussy, M. Steinbakk, F. Soriano, O.Stetsiouk, *Clinical Microbiology and Infection* **2006**, *12*, 501-503.

[22] aS Fowler Bush, Ralph G Adams, Ira W Levin, *Biochemistry* **1980**, *19*, 4429-4436; bK. Shirota, K. Yagi, T. Inaba, et al., *Biophysical Journal* **2016**, *111*, 999-1007; cL. Collard, F. Sinjab, I. Notingher, *Biophysical Journal* **2019**, *117*, 1589-1598; dA. A. Dmitriev, N. V. Surovtsev, *The Journal of Physical Chemistry. B* **2015**, *119*, 15613-15622.

[23] aJ. P. Kitt, D. A. Bryce, S. D. Minteer, et al., *Journal of the American Chemical Society* **2017**, *139*, 3851-3860; bDebanjan Bhowmik, Kaustubh R. Mote, Christina M.MacLaughlin, et al., *ACS Nano* **2015**, *9*, 9070–9077.

[24] Schultz Z. D., Levin I. W., *Annual Review of Analytical Chemistry* **2011**, *4*, 343-366.

[25] aOrendorff Christopher J., Ducey Michael W., Pemberton Jeanne E., *The Journal of Physical Chemistry A* **2002**, *106*, 6991-6998; bChristopher B. Fox, Rory H. Uibel, Joel M. Harris, *The Journal of Physical Chemistry B* **2007**, *111*, 11428-11436.

[26] Michel Pezolet Danielle Carrier, *Biophysical Journal* **1984**, *46*, 497-506.

[27] Jing Zhang, Haoning Gong, Mingrui Liao, et al., *Journal of Colloid and Interface Science* **2022**, *608*, 193-206.

Chapter 3 From Cell Wall to Cytoplasmic Membrane: Multiple Actions of Antimicrobial Peptides against Gram-positive Bacteria

Mingrui Liao,[1#] Haoning Gong,[1] Xuzhi Hu,[1] Ziwei Wang,[2] Xuebo Quan,[3] Zongyi Li,[1] Andrew J. McBain,[4] Jian Zhou,[5] Mario Campana,[6] and Jian R. Lu[1,*]

[1]Biological Physics Laboratory, Department of Physics and Astronomy, School of Natural Science, The University of Manchester, Oxford Road, Manchester M13 9PL, UK.

[2]National Graphene Institute, The University of Manchester, Oxford Road, Manchester M13 9PL, UK.

[3]Shenzhen Bay Laboratory, Institute of Systems and Physical Biology, Shenzhen, 518132, China

[4]Division of Pharmacy and Optometry, Faculty of Biology, Medicine and Health, The University of Manchester, Oxford Road, Manchester M13 9PL, UK.

[5]School of Chemistry and Chemical Engineering, Guangdong Provincial Key Laboratory for Green Chemical Product Technology, South China University of Technology, Guangzhou 510640, China.

[6]STFC ISIS Facility, Rutherford Appleton Laboratory, Didcot, OX11 0QX, UK.

[#]To whom as PhD candidate should be responsible to all the experiments and simulation work.

[*]To whom all correspondence should be made: J.lu@manchester.ac.uk

Abstract

A group of amphiphilic peptides based on the well-studied G_3 ($G(IIKK)_3I\text{-}NH_2$) has been designed to fight infections from Gram-positive bacteria including sensitive *S. aureus* and resistant MRSA, focusing on mechanistic processes. By conducting time-dependent killing experiments, we found that substitutions of II by WW (GWK), II by FF (GFK), and KK by RR (GIR) resulted in improved bactericidal efficiencies than G_3 (GIK) on both *S. aureus* and MRSA, with the order of GWK > GIR > GFK > GIK. Electronic microscopy imaging revealed structural disruptions of antimicrobial peptide (AMP) binding to bacterial cell walls. Fluorescence assays including AMP binding to anionic lipoteichoic acids (LTA) in cell-free and cell systems indicated concentration-dependent membrane destabilization associated with bacterial killing. Furthermore, AMP's binding to anionic plasma membrane via similar fluorescence assays was also investigated, producing membrane depolarization and leakage in different extents. Small angle neutron scattering (SANS) unravelled that AMPs can bind and overcame the LTA barrier and reached cytoplasmic membrane to cause leakage. The combined results from fluorescence assays and molecular dynamics (MD) simulations revealed that GWK and GIR can rigidify the membrane by increasing the values of Laurdan generalized polarization (GP) and decrease the diffusive efficiency of the anionic lipid membrane more significantly than GIK and GFK. The combined SANS and MD analyses pointed to the important role of intramembrane peptide nanoaggregates in antimicrobial actions. Clustering within the lipid membrane by AMP binding associated with hydrophobic mismatch and intramembrane nanostructuring caused fluidic and rigid areas, accelerating membrane disintegration, resulting in fast bacterial killing.

Keywords: **Fast antimicrobial activity; cell wall; AMP; LTA; cytoplasmic membrane; membrane depolarization; membrane fluidity change**

1. Introduction

Methicillin-resistant *Staphylococcus aureus* (MRSA) is widely known as superbug. Its frequent occurrence in serious nosocomial infections is threating the global health.[1] Superbugs like MRSA often show resistance to multiple antibiotics, and the great threat of multidrug resistance (MDR) together with the long cycle of new antibiotic development imposes an urgent demand for the development of new antimicrobial treatments.[2, 3] Different from the structure and composition of Gram-negative bacteria, the envelope of Gram-positive bacteria such as *Staphylococcus aureus* (*S. aureus*) is comprised of a thick outer cell wall and a negatively-charged cytoplasmic membrane. The cell wall is responsible for various roles in live bacteria, including provision of structural support, mediation of materials that are directly exposed to the cytoplasmic membrane and prevention of membrane lysis from changes of outer environment. The thick peptidoglycan layer is the main body of the cell wall, in which polyanionic teichoic acids are surrounded and linked with the cytoplasmic membrane via glycolipid anchors.

Antibiotics such as vancomycin and daptomycin are natural peptide derivatives. They target Gram-positive bacteria and impose their therapeutic actions by inhibiting the synthesis of cell wall components such as lipoteichoic acids (LTA) and causing structural changes of plasma membrane such as curvature, malfunctions of large membrane pores and aberrant recruitments of membrane proteins.[4-7] Other antimicrobial peptides (AMPs) may kill microbial species differently.[8] For example, a short peptide PTP-7 (sequence of FLGALFKALSKLL) can kill both sensitive and resistant Gram-positive bacteria indiscriminately, but is not effective against Gram-negative bacteria.[9] In contrast, Piscidin 1 (P1) and Piscidin 3 (P3), both naturally occurring, are efficacious against Gram-negative bacteria. P1 can kill bacteria within several min whilst it took about 1 h for P3. Both of them can penetrate through cell membranes and have further colocalization with nucleoids, but P1 is more membrane disruptive than P3 while P3 is much stronger in condensing DNA via charge driven interactions.[10, 11]

In addition to acting on the cell membrane, AMPs may also act on the cell wall, inhibit protein folding or enzyme activity, or even act intracellularly.[12, 13] Therefore, once an AMP has reached the cell wall, cell membrane, or its internal target, it is important to understand how it interacts with the specific targets of Gram-negative and Gram-positive bacteria.[14, 15] It is widely accepted that cationic AMPs are electrostatically driven to interact with cytoplasmic membrane, become inserted and in turn disrupt its structure. The cell wall of Gram-positive *S. aureus* contains the non-covalently linked LTAs with an average molecular weight of 6200 g/mol (with average 24 repeating unit of glycerolphosphate), of which 70% are substituted by D-alanine.[16, 17] The phosphate groups in each repeating unit of LTA impart rich net negative charges, which would attract oppositely charged compounds.[1] Natural cationic AMPs such as mellitin, cecropin and human cathelicidin (LL-37) show good affinity to LTA molecules, but may also exert effects on cytoplasmic membrane whilst imposing their antimicrobial actions.[1, 18-20] The components of microbial cell wall works as an electrostatic barrier in capturing AMPs, and hence prevents AMPs from direct interaction with the cytoplasmic membrane, leading to the decreased effective AMP concentration as a result of accumulation onto the cell wall. On the other hand, it has also been postulated that the binding and attraction of AMPs to LTA molecules can initiate the killing of bacteria by mediating the entry of the AMPs into the bacteria, that is, LTAs may work as polyanionic ladder to the entry of cationic AMPs into the cytoplasmic membrane from outside.[1]

Anionic lipids such as cardiolipin (CL), phosphatidylglycerol (PG) and lysyl-phosphatidylglycerol (LPG) in the cytoplasmic membrane constitute over 80% of the total lipids, and the ratio of CL to PG is about 2:3 (molar ratio).[21] Lipid domains are transient and play important roles in the functioning of the membrane.[22, 23] Revealing how AMP binding affects the lateral heterogeneity in the cellular processes is important for understanding how AMPs interact with bacterial membranes and kill bacteria. Through neutron scattering measurements from the contrast-matched membranes, Nickels *et. al* [24] found that distributions of lipids in the membrane of

Gram-positive *Bacillus subtilis were* non-uniform and the membranes were characterized by nanoscopic lateral features (smaller than 40 nm). Such domain formation or breakdown in the membrane upon AMP binding would impact membrane fluidity. Using fluorescence microscopy from a Gram-positive model organism *Bacillus subtilis*, Müller *et al*. found that daptomycin cannot cause discrete membrane pores or change membrane curvature, but can efficiently alter the overall membrane fluidity upon daptomycin binding and clustering.[6] The reduced mobility of lipid acyl chains indicated the enhanced rigidity of the membrane, which might prevent the binding of many peripheral membrane proteins to the plasma membrane.[6, 25]

It remains unclear how an AMP penetrates through a cell wall and causes subsequent clustering of the anionic lipids. Such knowledge would help us to learn how to balance different membrane actions in fast bacterial killing, *e.g.* LTA affinity, depolarization of cytoplasmic membrane, cell leakage and membrane rigidity. By focusing on understanding how AMPs interact with different membranes, we aim to address these issues by combining experimental approaches with computer simulations. We try to clarify the mechanistic processes between AMP's single membrane targeting and multiple biophysical effects in killing bacteria and understand how lipid clustering induced by cationic AMPs and subsequent hardening of the plasma membrane enhances potency against resistant Gram-positive bacteria.

2. Experiment methods

Information about the bacterial strains and descriptions of all the chemicals including various lipids, LTA, fluorescence probes are given in Supporting Information (**SI**).

2.1 Antimicrobial Evaluations of AMPs

The minimum inhibitory concentration (MIC) assays of *Staphylococcus aureus* (*S. aureus*, ATCC 6538) and methicillin-resistant *Staphylococcus aureus* (MRSA) against different AMPs were carried out by Tryptic Soy Broth (TSB) according to the British Society for Antimicrobial Chemotherapy (BSAC) methodologies.[26] Breakpoints used to interpret MICs were based on published European Clinical Antimicrobial

Susceptibility Testing (EUCAST) guidelines.[27]

2.2 Evaluations of Dynamic Bacterial Killing

Two bacterial strains *S. aureus* ATCC 6538 and MRSA were respectively inoculated in 10 mL of TSB at 37 °C for 18-24 h. All bacteria were grown to an optical density of $OD_{600} \approx 0.6$ for further use, and cell suspension was diluted to ~ 1.25×10^6 CFU ml^{-1} in pH 7.4 phosphate buffered saline (PBS) solution. Bacteria suspension was mixed with AMP at a selected concentration, and the bacteria samples were diluted and spread uniformly onto independent TSB agar plates over different time points. Untreated bacteria in PBS solution served as negative control. The colony-forming units (CFUs) were counted after overnight 37 ºC incubation. All the sample points were independently repeated three times in same settings.

2.3 BODIPY™-TR-cadaverine (BC) Displacement of LTA in both Cell Free and Cell Systems

Binding affinity to LTA from *S. aureus* was investigated in both cell free and *S. aureus* cell systems, by BC fluorescent displacement assays. Quenching of fluorescence was observed when probe BC bound to LTA, displacement of probe into the solution would lead to enhancement of its fluorescence emission. All the assays were performed in 96-well plates. Fluorescence intensity was monitored on a microplate reader (Varioskan LUX, Thermo Scientific, USA) using excitation and emission wavelengths of 580 nm and 620 nm, respectively.

For cell free assays, stock solutions of BC (10 μM) and LTA (20 μg/mL) were prepared by dissolution in Tris buffer (10 mM Tris + 150 mM NaCl, pH 7.4). Desired concentration of BC (final concentration 5 μM) and cell-free LTA (final concentration 10 μg/mL) were mixed. After 15 min, selected AMPs of different concentrations were mixed with BC-LTA mixture and kept for 30 min in the dark at room temperature. For experiments performed on *S. aureus* (ATCC 6538), desired concentration of BC and freshly washed Gram-positive bacteria cells (final $OD_{600} \approx 0.1$) were mixed. Mixture was kept for 30 min in the dark at room temperature until equilibration. After 30 min, concentrations of the selected compounds and mixture of BC (final concentration 5 μM) and cell suspension were added to the plate and kept for 30 min.[28]

2.4 Cytoplasmic Membrane Depolarization, AMP's Binding to Anionic Lipid and Laurdan-based Membrane Fluidity Measurements

Cytoplasmic membrane depolarization assays directly showed the kinetic membrane damage via fluorescence assays. Firstly, the log-phase *S. aureus* cells were collected by centrifugation at 4000 × g and washed with sterile PBS solution twice. The cell suspension was incubated with 2 μM $DiSC_3(5)$ at 37 °C in a dark environment for 1 hr until equilibration in HEPES buffer (10 mM HEPES + 5 mM Glucose + 100 mM KCl, pH 7.4). An aliquot of 100 μL of the cell suspension was placed in a 96-well plate, AMPs of selected concentration were added into the wells and recorded the fluorescence intensity continuously (excitation and emission wavelengths of 630 and 680 nm, respectively).[29]

10-N-nonyl acridine orange (NAO) is a fluorescence probe widely used to visualize CL and PG domains in bacterial membranes with emission peak when bound to anionic lipids. Self-quenching of NAO binding with small unilamellar vesicle (SUV) was titrated by NAO to determine the optimal probe concentration. The final NAO concentration for the assays was 10 μM. The increase of NAO fluorescence will indicate the ability of an AMP displacing NAO from its binding to anionic lipids in SUVs. Fluorescence measurements were recorded on 96-well plates after the addition of NAO-loaded SUVs in different AMP concentrations.[30] All the measurements were recorded at room temperature using a beforementioned microplate reader with excitation and emission wavelengths of 488 and 520 nm, respectively. Data were normalised based on fluorescence intensity in pure NAO solution wells (maximum fluorescence of NAO in solution, 100%) and peptide-free wells (minimum fluorescence of lipid-bound NAO, 0%).

Determination of membrane fluidity by 2-Dimethylamino-6-1auroylnaphthalene

(Laurdan) generalized polarization (GP) was performed as reported previously.[6, 31] *S. aureus* was grown in MHB supplemented with 1.25 mM $CaCl_2$ and 10% glucose at 37 °C. Cell suspension was diluted to a density of $OD_{600} \approx 0.2$ and stained with 10 μM Laurdan for 30 min. Then, cells were centrifuged and washed four times with PBS solution supplemented with 10% glucose for further use. For measurements in cell-free system, prepared POPG/CL SUVs (for method see **Section 2.6**) of selected concentration were mixed with Laurdan solution. 100 μL cell suspension ($OD_{600} \approx 0.2$) or SUV was added with different AMPs, Laurdan fluorescence intensities were recorded continuously at 460 ± 5 nm and 500 ± 5 nm upon excitation at 330 nm with a microplate reader previously used. Laurdan GP was calculated using the formula $GP = (I_{460}-I_{500})/(I_{460}+I_{500})$.[6]

2.5 Scanning Electron Microscopy (SEM) of Bacterial Cell Morphology

SEM was used to observe the morphological change of AMP-treated bacteria. After a similar method of harvesting mid-log phase bacteria in **Section 2.4**, bacteria of $\sim 10^8$ CFU ml^{-1} treated with AMPs at 4×MIC for 1 hr were collected by centrifugation and washed by PBS solution three times. Then, cell suspension was fixed with 2.5% glutaraldehyde in PBS solution at 5 ºC overnight. The bacteria were further rinsed with PBS solution three times to remove extra glutaraldehyde, and dehydrated through a series of ethanol-water solvent (ethanol volume of 30%, 50%, 70% and 100%) wash. The samples were dried in freezer drier and fixed on poly-lysine coated Si wafer, and coated with a thin gold layer prior to image under field emission SEM.

2.6 Circular Dichroism (CD) Spectra and Zeta Potential Measurements

CD measurements were carried out on a Chirascan Series Spectrometer at the room temperature of 20-22 °C, about 50 μL peptide solution at concentration of 0.5 mM was confined in a rectangular quartz cell. The light pass length is 1 mm, CD spectra were scanned with the range from 260 to 190 nm.

The potential change of POPG/CL SUVs (mimicking the plasma membrane model of Gram-positive bacteria) upon AMP binding was tested on the instrument of ZEN3600 Nano-ZS at room temperature (around 22 °C). Lipids POPG and CL (with a molar ratio of 6/4) were dissolved together in chloroform and evaporated overnight to obtain the dry phospholipid films. The lipid film was dissolved in Tris-NaCl buffer (pH 7.4) at 5 mg/mL, followed by a previously applied extrusion method to produce SUV solution.[32] AMP and SUVs were mixed in Tris-NaCl buffer (10 mM Tris, 50 mM NaCl, pH 7.4) at a final concentration of 50 μM and 0.1 mg/ml, respectively, and then injected into the capillary cell (type NO. DTS1060C). After 120 s equilibrating process, triplicate measurements were carried out at 20 ± 1 °C for each sample to reduce the random errors.

2.7 SUV Leakage

POPG/CL (with a molar ratio of 6/4) SUVs were prepared using the same approach as described previously with calcein loading.[32] The detailed procedure can be found in a previous publication.[33] The excitation wavelength and emission spectra were set to be 490 nm and scanned from 510 to 530 nm, respectively. The fluorescence intensity at the emission wavelength of 518 nm was calculated as representative leakage of the calcein-entrapped SUVs. The leakage percentage (%) for each sample was calculated with the following equation:

$$Leakage\ percentage\ (\%) = \frac{(I_{peptide} - I_{neg})}{(I_{pos} - I_{neg})} \times 100 \tag{1}$$

where I_{neg} and I_{pos} represent the negative and positive controls, respectively, which indicate the initial 0% SUV leakage before incubation with the selected compounds and the 100% SUV leakage after incubation with 0.2% (w/w) Triton X-100. $I_{peptide}$ is the fluorescence intensity of SUV after peptide addition. All measurements were carried out in 96-well plate at room temperature.

2.8 SANS of Lipid SUVs with AMP binding

SANS experiments were performed using the Larmor diffractometers at the ISIS Pulsed Neutron Source (Rutherford Appleton Laboratory, Didcot, UK), using the same experimental configuration as previously described.[34] LTA/POPC (a mass ratio of 1/9) and POPG/CL (a molar ratio of 6/4) SUVs were prepared in D_2O Tris buffer (10 mM Tris and 150 mM NaCl, pH 7.4) and then mixed with AMP solutions for SANS measurements. Samples were measured at 22 °C. The final SUV concentration was 1 mM, and the selected AMP concentrations in different systems. Each SANS measurement was performed once. Correction and azimuthal averaging of the measured SANS data were performed in the Mantid framework (www.mantidproject.org). Reduced SANS data were then fitted with a core multilayer shell model (http://www.sasview.org/sasview/user/models/model_functions.html#coremultishellmodel) using software SasView 4.2 (www.sasview.org).

2.9 CG-MD Simulation of Cytoplasmatic Membrane Interacting with AMPs

The coarse-grained (CG) model of the POPG/CL bilayer (with a molar ratio of 6/4) was created by CHARMM-GUI to study the binding of AMPs to the membrane within microseconds. [35, 36] The initial size of the simulation box is 13.35 × 13.35 × 35.0 nm^3 in the x, y and z directions, with each leaflet of the bilayer containing 200 lipid molecules under periodic boundary condition. The lipid bilayer is located at the middle part of the simulation box and dissolved by CG water molecules. In the systems containing AMPs, the ratio of peptide to lipid is fixed at 1:20 while counterions (Na^+ and Cl^-) were added for charge neutralisation and with a final concentration of 100 mM. Atomistic peptide’s mapping to corresponding CG models was transferred via Martinize script based on the force field of Martini 2.2.[37] Peptides with a typical alpha-helical conformation on negatively-charged membrane supported by evidence of CD measurements (**Figure S1**) were put above the bilayer with a distance of about 1.5 nm to reduce the effects of the initial states of peptide molecules on the final MD phenomena. Before investigating AMPs’ interaction with the lipid bilayer, the single lipid bilayer in solvent was simulated for enough long time (500 ns) to obtain a well-equilibrated state. All the CG simulations were performed on GROMACS 2016 and visualized via VMD 1.9.2.[38-40] The simulation details about conditions and parameters can be found from our previously published work.[32]

2.10 Neutron Reflection (NR) of Lipid Monolayers Interacting with AMPs

NR experiments of AMP binding with lipid monolayer were performed with the SURF reflectometer at the ISIS Pulsed Neutron Source (STFC Rutherford Appleton Laboratory, Didcot, UK) and the FIGARO reflectometer at the Institut Laue Langevin (Grenoble, France). Samples were scanned at SURF at 3 angles of incidence (0.35°, 0.65°, 1.5°) and at FIGARO at 2 angles of incidence (0.62°, 3.8°). These instruments all covered the effective momentum transfer range (Q-range) of 0.01 ~ 0.3 $Å^{-1}$ used in the NR data analysis. The details about procedures of lipid monolayer preparation, peptide injection and further data analysis of NR profiles of different isotopic contrasts can see in our previous descriptions.[32, 41, 42]

3. Results and discussions

3.1 Antimicrobial Activity of AMPs and Membrane Targeting Actions

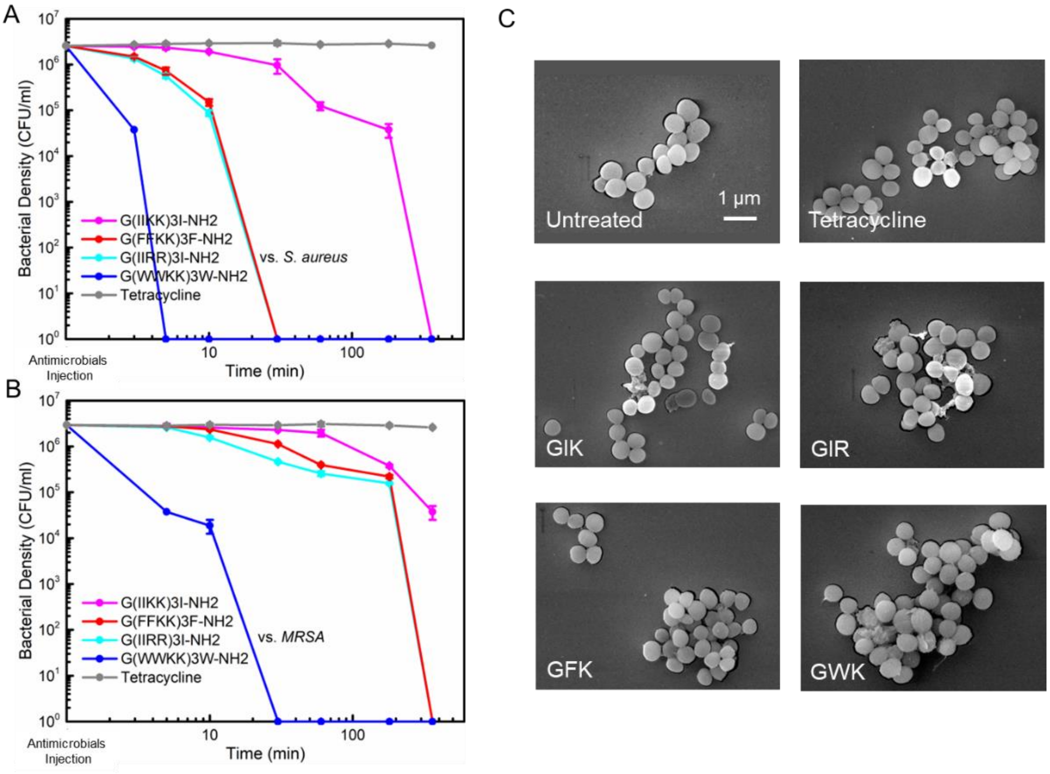

Figure 1. (A, B) Dynamic killing curves of four AMPs against *S. aureus* (ATCC 6538) and MRSA (clinical strain) at the concentration of 16 μM. (C) SEM images of the MRSA cell morphologies before and after interacting with AMPs and antibiotic tetracycline, the concentration used was 50 μM and the incubation time was 2 h. The scale bar corresponds to 1 μm.

In the series of the four AMPs used in this work, GIK (G(IIKK)$_3$I-NH$_2$, G$_3$) has been widely studied. Substitutions of II by WW, II by FF (GFK), and KK by RR (GIR) resulted in the three new ones, denoted as GWK, GFK and GIR, respectively. The four AMPs have the same net positive charge of 7. **Table S1** shows that the four AMPs have the retention times around 19 min from the rp-HPLC analysis, showing very similar hydrophobicity of them in spite of the substitutions of different amino acids. Furthermore, GIK, GFK and GIR adopt random coils in buffer solution, but GWK adopts a distinct α-helix conformation, suggesting its stronger amphiphilic balance associated with the π-π interaction between side chain Ws (**Figure S1**). In contrast, dissolution of the four AMPs into the micellar solution of SDS led to dominant feature of α-helix structure from all of them, consistent with the promotion of the secondary structure associated with electrostatic and hydrophobic interactions.

The MIC values are all around 3 μM. Tetracycline (TC) was used as controls, showing lower MICs against both the sensitive and resistant strains. From the results of dynamic killing of Gram-positive *S. aureus* and drug-resistant MRSA as shown in **Figure 1**, cell viability was affected after exposure to AMPs within minutes. All four peptides show time-dependent killing within the first 3 hr of exposure, but there are huge differences in their time-dependent killing rates, with GWK > GIR ≈ DFK > GIK. Even though antibiotic TC displayed a better antimicrobial activity in its lower MIC values (below 1 μM) against both Gram-positive strains than the AMPs (about 3 μM) (**Table S1**), it showed no time-dependent decline in cell viability over the testing time. Among all the AMPs tested, GWK showed the most efficient dynamic bacterial killing, achieving a complete killing of sensitive *S. aureus* strain within 5 min and that of resistant MRSA within 30 min. GIR and GFK showed similar time-dependent actions, but it took 30 min and several hours to kill the sensitive and resistant strains, respectively. The time-dependent killing of GIK followed the same sequence but the time taken for a complete killing was much longer.

The MRSA sample (clinical strain) was also used to assess morphological changes of the cells after their exposure to AMPs using SEM. In both GIR and GWK treatments, the cells appeared to have changed their shapes, with debris and inner contents released; surface morphological changes of the cells were more pronounced when treated with GIK or GFK. In contrast, cell surface morphology after incubation with TC showed no obvious change compared to the untreated group. This observation is consistent with the non-membrane related antibacterial action, i.e., an intracellular inhibition process.[43, 44] These results suggest that treatment of MRSA with AMP is associated with significant structural changes of the cell membranes when compared to the untreated cells with smooth cell envelope.[45]

3.2 AMP Binding with LTA in Cell Wall

The mechanistic process of AMP action with LTA from *S. aureus* was also examined using the BODIPY™-TR-cadaverine (BC) displacement assay. BC is an amphiphilic molecule showing good affinity to LTA and the binding leads to a self-quenching of fluorescence. The further binding of LTA with the addition of an exogenous compound leads to the BC displacement, and this process can be measured by enhanced fluorescence intensity. **Figure 2A** shows the fluorescence displacement of the cell free-LTA with increasing concentration of AMP. BC displacement of GIR from the cell-free LTA was treated as positive control. BC displacement from the cell free-LTA was induced by all four AMPs, and the difference among them would be the binding ability to LTA. The concentration of the 50% BC displacement for the AMPs followed an order as: GIR ≈ GFK (1.2 μM) > GIK (2.5 μM) > GWK.

To verify if AMPs also bind to the LTA at the surface of *S. aureus*, we reproduced the BC displacement assay on bacterial cells. **Figure 2B** shows the time evolution of BC fluorescence intensity, reflecting displacement from its binding to *S. aureus* by different AMPs. Displacement of the BC was observed from *S. aureus*, through enhancement of fluorescence occurred in the order of GIR ≈ GFK > GIK > GWK, which is the same as from the cell-free LTA system. Thus, GWK showed the lowest ability of LTA binding in both BC displacement assays indicated by its low fraction of fluorescence displacement. The effects of AMPs on BC fluorescence efficiency were examined. All AMPS can reduce BC fluorescence and GWK can decrease the fluorescence intensity of BC by 44% compared to the control group, the largest intensity reduction of the AMPs studied. (**Figure S2**)

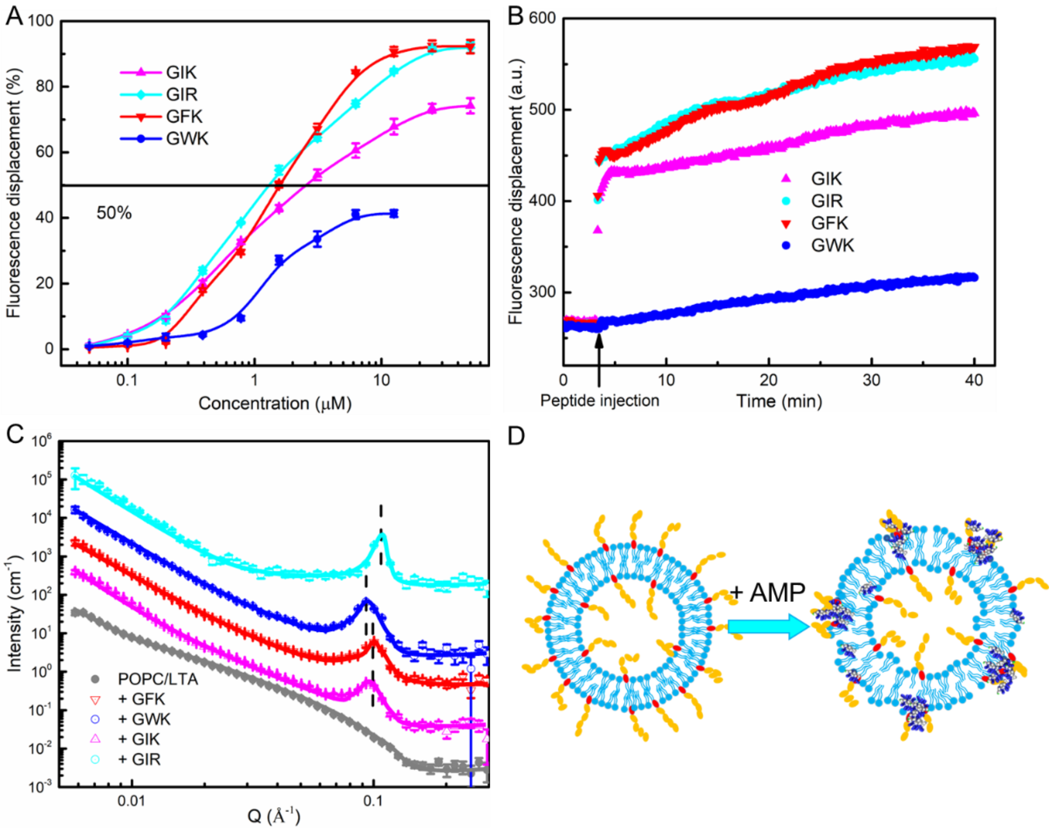

Figure 2. (A) Fluorescence assay of BODIPY™-TR-cadaverine (BC) (5 μM) displacement from cell free LTA (20 μg/mL) systems by increasing concentrations of AMPs. (B) Dynamic BC emission intensity as a reflection of AMP binding to LTA of *S. aureus* (cell system) at the concentration of 50 μM. (C) SANS profiles from POPC/LTA (w/w, 10/1) SUVs before and after interactions of GIK, GIR, GFK and GWK at the concentration of 100 μM in D_2O Tris buffer (10 mM Tris, 150 mM NaCl, pH 7.4), scattering intensity is plotted as a function of wave vector Q. (D) Schematic illustrations to show the intramembrane aggregates and lipid reorganization after AMP binding.

Complementary to the BC displacement from the measurements of AMP affinity with LTA, SANS experiments aiming for peptides' specific interaction with LTA containing SUVs were taken (**Figure 2C**). Different from membrane lipids, LTA can not form a stable monolayer at the air/liquid interface, but it formed micellar aggregates in aqueous solution.[46, 47] The micellar structure of the Staphylococcal LTA was characterized via X-ray scattering by Labischinski and Fischer *et al*. The results were analysed using a typical core-shell sphere model. The diameter of the entire sphere was 22 nm, and the hydrophobic core of the glycolipid anchor was 5 nm in diameter. It was surrounded by the thick shell of hydrophilic head group layer of 8.5 nm.[47, 48] In contrast, the structure of LTA/POPC SUV measured from SANS results is represented by a typical multiple-layer core-shell sphere. Upon binding of AMPs, the overall SUV nanostructures changed substantially, as indicated by the changes in the SANS profiles against the one measured from SUVs alone, consistent with the intensive intramembrane AMP attacks. The occurrence of the broad peaks in the SANS profiles indicated the structural transformation of the single bilayer into periodic multi-bilayer stacks. In detail, the broad peaks in the four AMPs reflected AMPs' effects on membrane phase-separation and formation of AMP-LTA nanoaggregates. All the broad peaks have characteristic Q-positions at around 0.1: 0.097 (GIK), 0.10 (GFK), 0.096 (GWK) and 0.106 (GIR) $Å^{-1}$, indicating the unit thickness of stacking bilayer around 60 Å (=2π/Q), and the central Q value of the peak intensity at the tested concentration follows: GIR > GWK > GFK ≈ GIK.

Roversi and Castanho *et al*. [49, 50] reported that AMP binding to LTA can reduce the effective peptide concentration on the inner membrane interface, but these side effects are slight on bacterial killing via the binding with cytoplasmic membrane. In relation to AMP's antimicrobial activity, there is lack of correlation between the degree of LTA neutralization and MIC values against Gram-positive bacteria.[51] Thus, these previous studies have provided some useful indications about how AMPs approach the cytoplasmic membrane after they have overcome the LTA barrier in the cell wall.

3.3 Effects of AMPs on Cytoplasmic Membrane: Structural Basis to Depolarization and Leakage

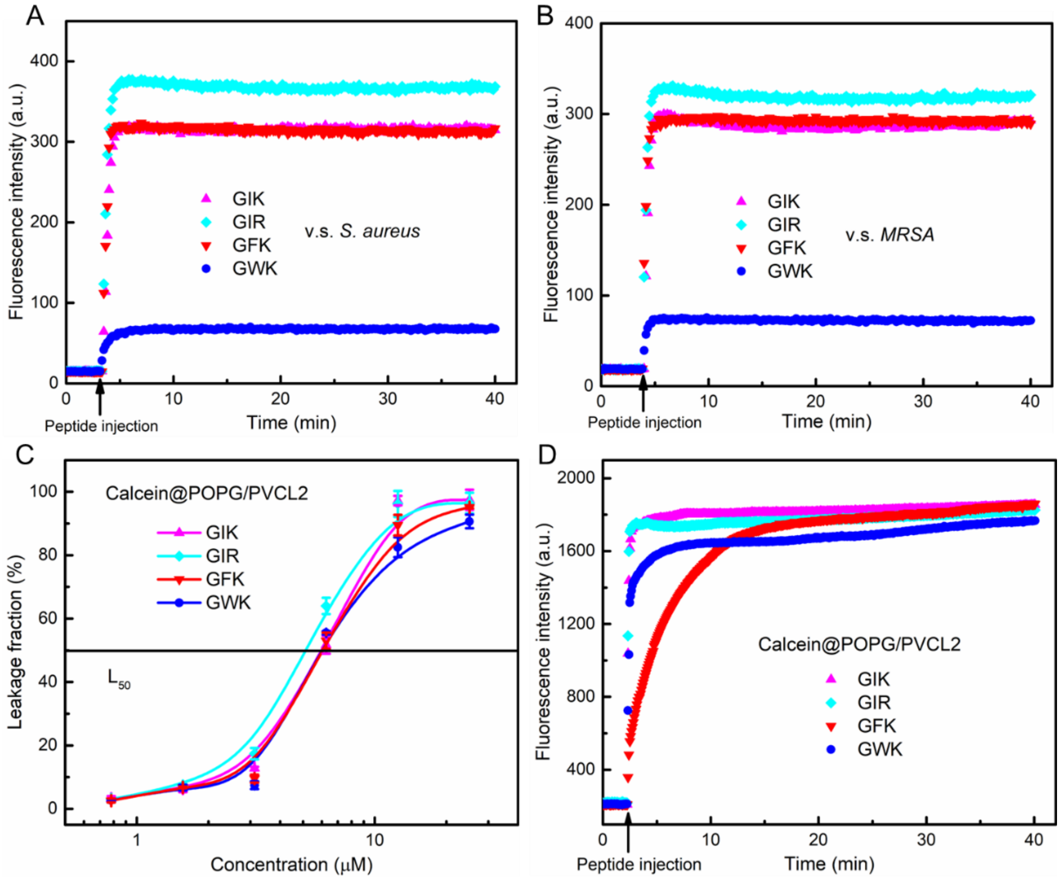

Figure 3. (A, B) DiSC$_3$(5) fluorescence changing with time as a reflection of membrane potential of *S. aureus* and MRSA incubated with 50 μM AMP individually. (C, D) Fluorescent dye leakage of POPG/CL (mimicking the cell membrane of *S. aureus*, with the molar ratio of 6/4) SUVs interacting with the AMPs of increasing concentrations, and corresponding the dynamic leakage of SUV by AMP at concentration of 16 μM.

The membrane potentials were reduced by >99% within 5 min of adding AMPs in both bacterial strains. (**Figures 3A&B**) The degree of membrane depolarization upon addition of GWK in the DiSC$_3$(5) assay is the lowest among all AMPs studied. This does not seem to be consistent with its fastest dynamic killing. However, binding of cationic AMPs onto the POPG/CL SUVs led to the potential changes from negative to positive, and GWK showed the highest positive gain. (**Figure S3**) Although the loss of viability following exposure to GWK appeared rapidly (**Figure 1A&B**), cell viability defined here is actually an ability of AMP-treated cells forming colonies on agar within 18-24 h after contact with the compounds. In case of daptomycin, an antibiotic targeting

Gram-positive bacteria, Silverman and Hobbs *et al*. found that membrane depolarization of *S. aureus* was gradual and intracellular biosynthesis procedure remained active for at least 30 min, but the cell viability declined rapidly under these conditions.[52, 53]

Other than previous evaluations of membrane depolarization-induced cell leakage, SUV model (POPG/CL, 6/4, mol/mol) mimicked the negatively-charged cytoplasmic membrane was built to assess AMP's physical disruptions on membrane and corresponding leakage efficacies. The results of SUV leakage fraction with increasing AMP concentration showed that the concentration of GIR corresponding to 50% SUV leakage (~ 5 μM) is the lowest among the four AMPs. (**Figure 3C**) In addition, the dynamic leakage of SUVs was measured to examine the efficacy of membrane disruptions by different AMPs at the concentration of 16 μM. GIK and GIR showed the fastest leakage equilibration within a few minutes and achieved the highest leakage fraction. While GWK showed the slightly decrease of leakage fraction, it was still better than GFK in leakage equilibration. (**Figure 3D**)

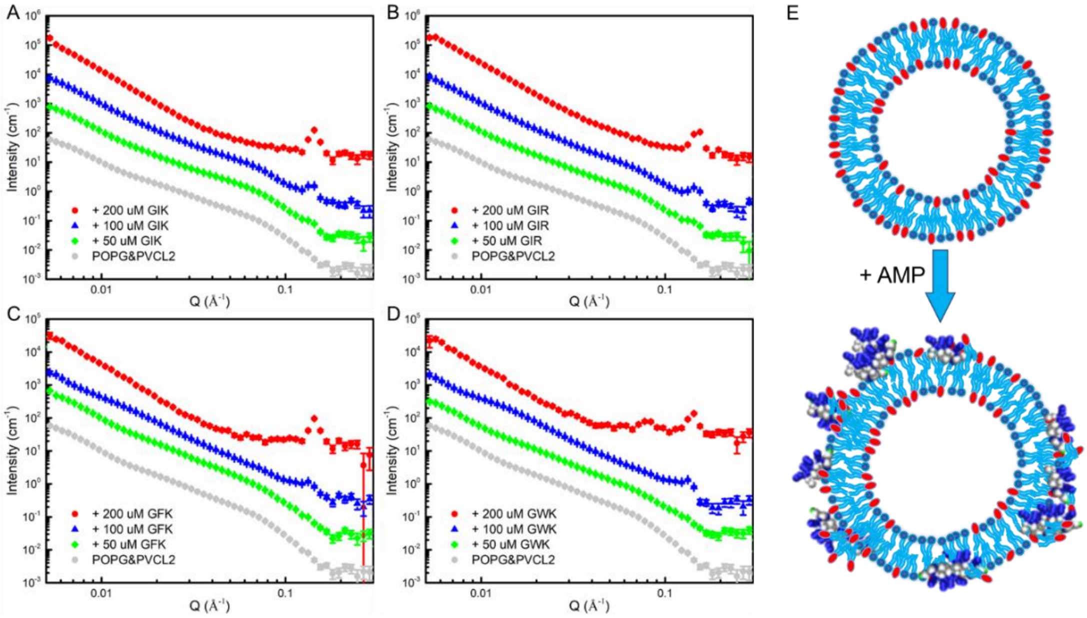

Figure 4. SANS profiles from POPG/CL (mol/mol, 6/4) SUVs before and after interactions with (A-D) GIK, GIR, GFK and GWK at concentrations of 50, 100 and 200 μM in D_2O Tris buffer (150 mM NaCl, 10 mM Tris, pH 7.4). The scattering

intensity is plotted as a function of wave vector Q. Detailed fitting models and parameters are given in **Table S3.** (E) The schematic graph on the right plane showed the peptide-lipid clusters and vesicle morphology change after AMP binding.

Based on the fully negatively-charged membrane of Gram-positive bacteria, PG and CL in *S. aureus* were the two main lipid components at a molar ratio of 58/42. POPG/CLSUVs (at the molar ratio of 6/4) were prepared to mimic the bacterial cell membrane in SANS experiments.[21, 54] POPG/CL SUVs before peptide addition shared a similar core-shell sphere as LTA/POPC SUV, with a radius of about 160 Å and membrane thickness of 41 Å, the thickness of the outer leaflet of the membrane increased with peptide addition from 8 Å to 10 Å (GIK), 12 Å (GIR and GFK) and 18 Å (GWK), respectively. The broad peaks occurred when peptide concentration was higher than 50 μM, indicating the substantial changes of the overall SUV nanostructures under the intensive AMP attacks. (**Figure 4A-D**) The two distinct features of the structural changes were the lipid clustering in membrane phase separation and the transformation of the single bilayer into periodic multi-bilayer stacks induced by cationic peptides. The overall size of the SUV increased from the radius of 160 Å to over 180 Å with the formation of the peptide-bilayer stacks at the peptide concentration of 100 μM, while the bilayer thickness decreased from 41 Å to about 30 Å. The radius and thickness changes may suggest that lipid clustering induced by peptide AMPs in specific areas contributed to the bilayer thinning which can be well linked to the interdigitating and condensing effects of the AMP molecules between the lipid lamellar stacks. The broad peaks had characteristic Q-positions at 0.138 (GIK), 0.15 (GIR), 0.13 (GFK) and 0.138 (GWK) Å^{-1}, indicating the thicknesses of the bilayer repeating unit around 45 Å ($=2\pi/Q$). With the peptide concentration further increased, the broad peak intensity in each SUV system was enhanced. This can be linked to the number of bilayers in the stacks. Interestingly, two obvious broad peaks at the Q-position of 0.08 and 0.142 occurred in GWK system, suggesting two different sizes of lipid-peptide nanoaggregates formed onto the SUV surfaces. Similar phenomenon can also be observed in the GFK system, indicating the specific roles of intermolecular π-π and cation-π interactions for aromatic residues in their mediations of the peptide-lipid stacking.

3.4 AMP Binding on Anionic Lipids and Effects on Membrane Fluidity

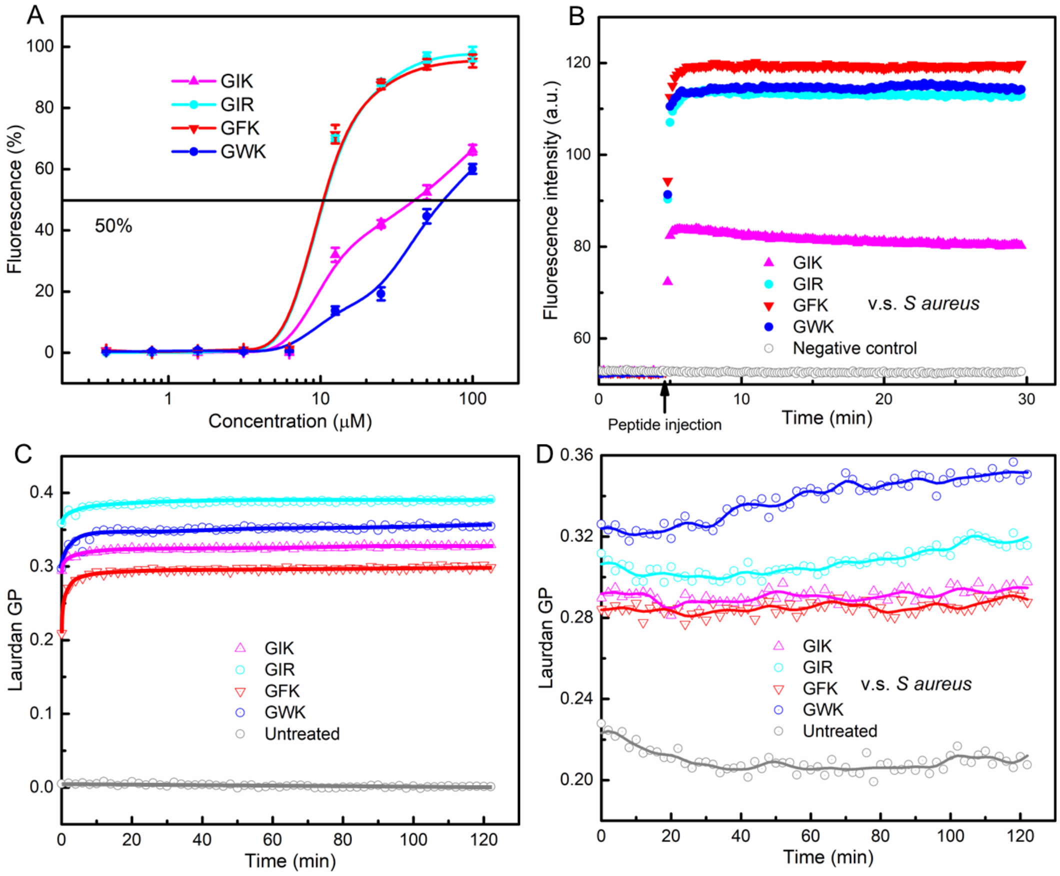

Figure 5. AMP binding with lipid POPG/CL SUVs and rigidify the cell membrane. (A, B) Binding of AMPs to the anionic lipids in POPG/CL SUVs (at the molar ratio of 60 to 40) and *in vitro* cell system of *S. aureus* (ATCC 6538), assessed by displacing the NAO dye from SUVs and cell membranes monitored through fluorescence increase. The fluorescence emission of NAO in cell systems after peptide addition (with the final concentration of 100 μM) was recorded at 530 ± 5 nm. (C, D) Spectroscopic measurements of membrane fluidity with Laurdan in both cell-free (POPG/CL SUVs) and cell (*S. aureus*) systems at the peptide concentration of 100 μM. Laurdan was excited at 330 nm and fluorescence emission was recorded at 460 ± 5 nm and 500 ± 5 nm.

NAO has been widely used to visualize the CL and PG domains in bacterial membranes through the specific Stokes shift of the emission peak when bound to anionic lipids. CL and PG-containing SUVs were prepared and labelled with NAO. With increasing concentrations of AMPs added, dose-dependent fluorescence increase was observed, indicating that NAO was displaced from the SUVs as a result of peptide binding to the negatively charged lipids (**Figure 5A**). The EC_{50}s (the peptide concentration required to induce 50% fluorescence displacement) of GIK and GWK are higher than the values of GIR/GFK, reflecting the more effective binding of GIR/GFK to the CL and PG lipid domains.[30] In parallel to the different aggregation behaviour of the AMPs onto the model SUV membrane, the affinity of NAO to the PG/CL lipids in *S. aureus* was also assessed. It was found that GIR, GFK and GWK showed the greater displacement of NAO than GIK.[56] Different from GIR, GFK and GIK in the slight enhancement of the fluorescence intensity of NAO, GWK influenced the NAO emission intensity in a dose-dependent way, and the molecular aggregates of GWK in solution (> 50 μM) can enhance the fluorescence intensity along with the red shift while the GWK monomers would decrease fluorescence intensity with its increasing concentration (≤ 25 μM). (**Figure S4**) Interestingly, the emission peak of NAO labelled *S. aureus* with GWK binding showed obvious red shift from ~ 528 nm to ~ 540 nm (**Figure S5**), which can be attributed by the intermolecular interactions between GWK and NAO molecules.

To examine how the clustering of the fluid lipids by AMPs affects the overall fluidity of the cell membrane, we used the membrane fluidity-sensitive dye Laurdan. This probe changes its fluorescence emission wavelength depending on the amount of water molecules between lipid head groups, thus providing a measure for lipid head group density and fatty acid chain flexibility.[31] As can be seen in **Figure 5C**, all four AMPs resulted in a rapid increase in Laurdan's general polarisation (GP) values with their binding to the SUVs, but to varying degrees, reflecting rapid membrane rigidification. The decrease in membrane fluidity occurs in less than 2 min, suggesting that it is a direct effect of AMP insertion into the bilayer rather than a intracellular adaptation. Similar phenomena were observed from the cell systems, in agreement with the data from the Laurdan fluorescence of SUV-Laurdan mixed systems. (**Figure 5D**) The GP value increased significantly (GWK > GIR > GIK ≈ GFK > Untreated), indicating a decreasing liquid-like state in the cytoplasmic membrane of *S. aureus*.[57]

3.5 MD Simulation of POPG/CL Membrane Binding with AMP

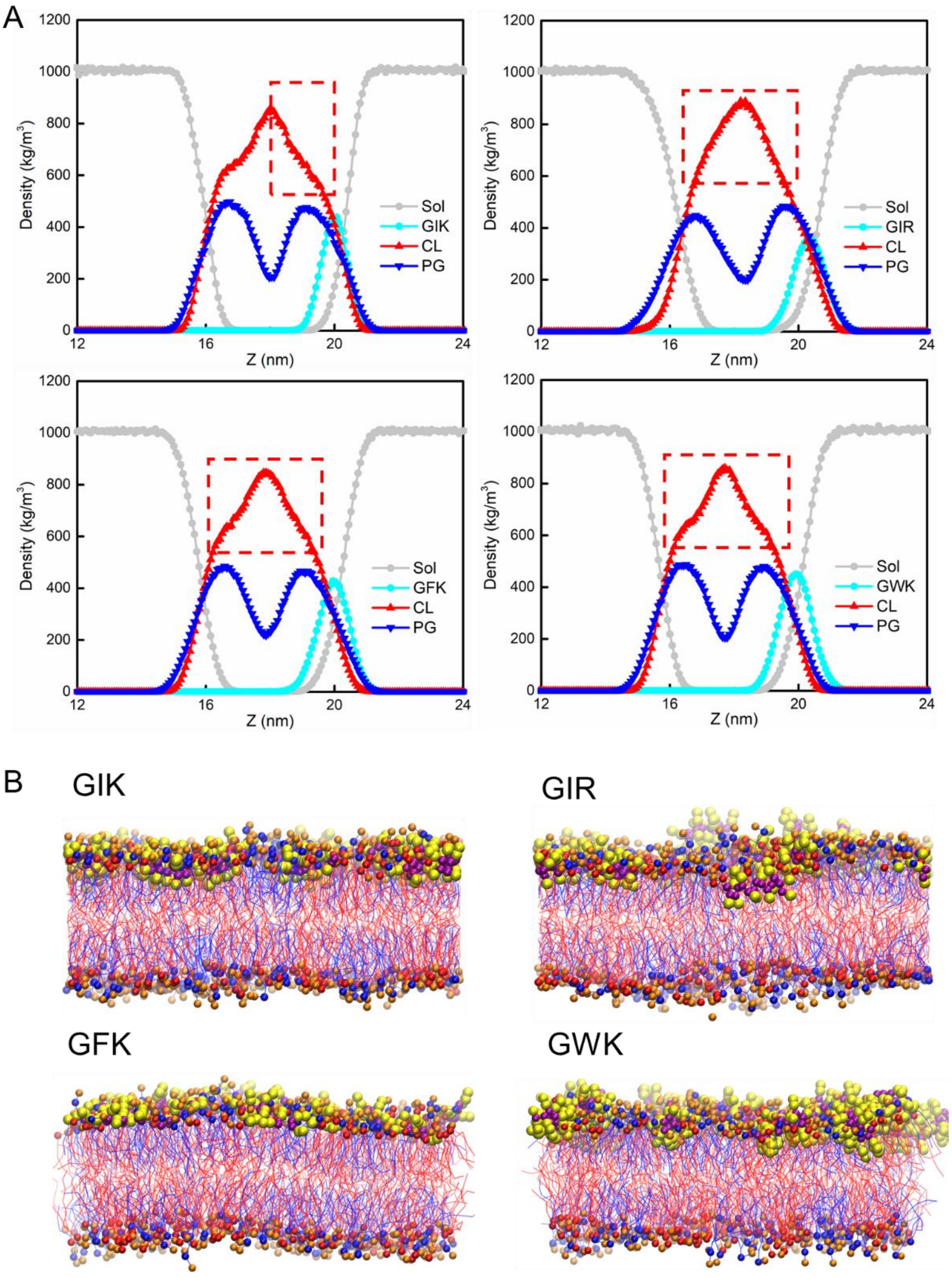

Figure 6. (A) Density distribution profiles of POPG/CL bilayers upon AMP binding (the graph of the lipid bilayer alone is given in **Figure S6** of **SI**). (B) The side-views of

the MD system after simulation time of 1 μs, the solvent environment was removed for a clear view. The molar ratio of AMP peptide to lipid in each simulation system was 1/20; blue and red lines represent lipid POPG and CL, respectively; blue and red beads denote the negatively-charged PO_4 groups in POPG and CL; orange beads denote all the glycerol groups in the membrane; yellow and purple beads represent the AMP molecules binding into the membrane.

From the profiles of density distributions of the bilayer system alone (**Figure S6**), the density curve of CL presents a typically symmetric peak featured with two shoulders below the main peak. However, the central PG density peak is opposite to the CL peak and is effectively negatively distributed and the two shoulders are shown as positive peaks. Thus, the middle main peak is distinctly lower than the two shoulders. The PG distribution is slightly wider than that of the CL distribution; and its entire thickness is about 5.5 nm. (**Figure S6**) Thus, the bilayer model depicts a clear CL distribution in the bilayer core region, with the PG lipids being distributed along the two sides. This structural character is consistent with the much stronger hydrophobicity of the CL lipids than the PG lipids.

Cationic AMPs strongly bind to the CL/PG membrane and disturb the symmetricity of the bilayer. AMP binding leads to lipid reorganization and asymmetric membrane conformation, even though all the AMPs are located at the middle region between the lipid head and tail parts of the outer membrane leaflet. (**Figure 6B**) The CL distribution curve in the case of GIR represents a progressive reorganization or destruction of the membrane. This is indicated by the total disappearance of the featured "shoulders" beneath the central peak. Other than this, the enhanced boundary gap between the curves of CL and PG distributions can result from the selective binding of GIR onto the CL microdomains. While in the other three AMPs, the decreased symmetricity of the membrane is also caused by AMP's destruction on the central CL domains.

The impacts of structural disruption and reorganisation of AMPs together with their enhancement of lipid phase separation and CL clustering can be verified by the altered

CL and PG distributions surrounding the AMP monomers and clusters, as evident in **Figure 6A-D**. From the radius distribution function (RDF) analysis of the phosphate groups (PO$_4$, the negatively-charged group in PG; and PO$_4$1/2, the two negatively-charged groups in CL) around the AMP molecules, the first peak intensity of PO$_4$1/2 is much stronger than that of PO$_4$ in systems of GIR and GWK. This result is consistent with the overview of peptide binding onto the outer leaflet membrane (represented by PO$_4$ in blue beads and PO$_4$1/2 in red beads); GIR and GWK tend to form more peptide clusters and oligomers than monomers in systems of GIK and GFK.

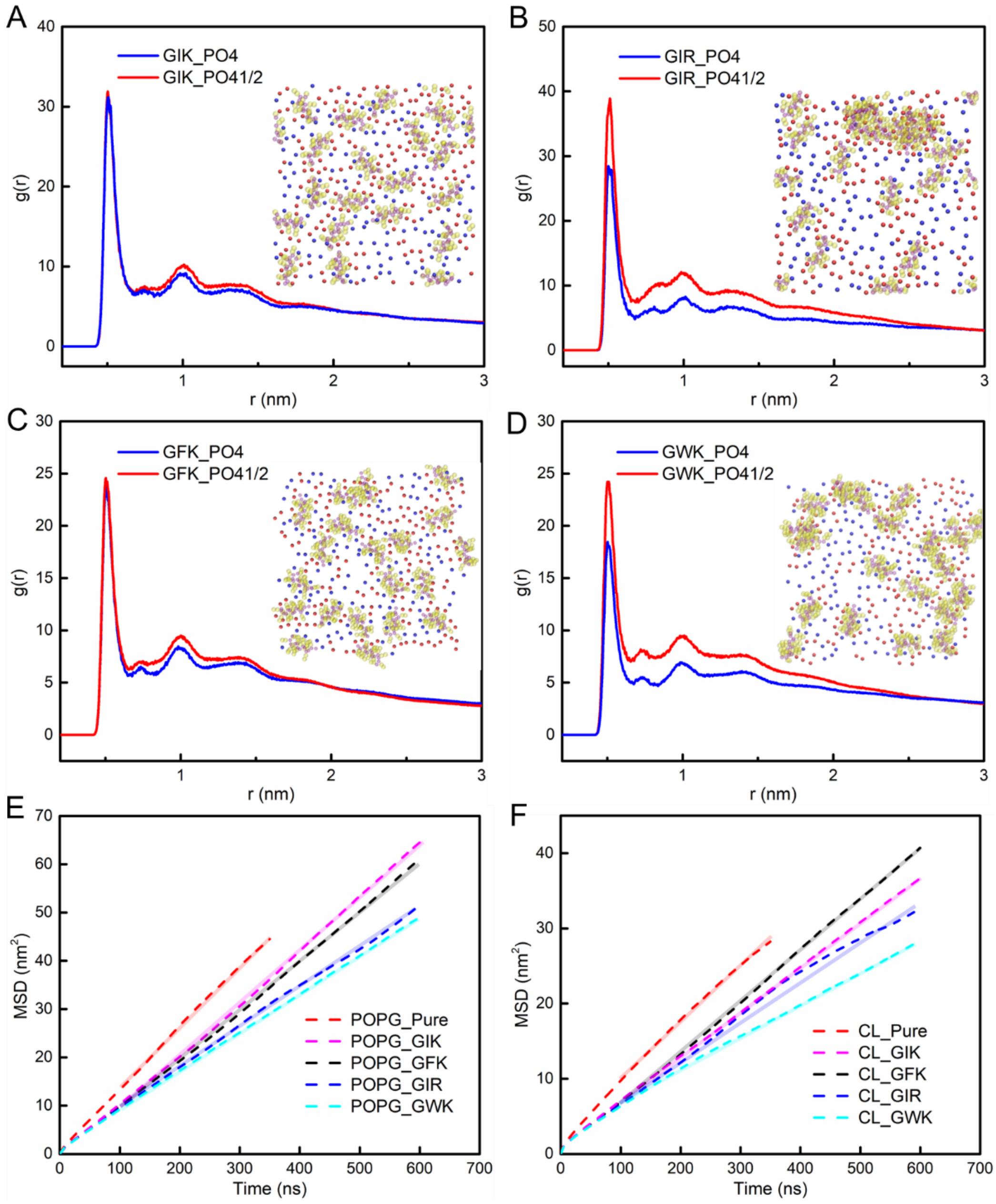

Figure 7. (A-D) RDFs of AMPs in coordination with the negatively-charged groups of PO_4 and $PO_41/2$ in POPG and CL, respectively. Inset pictures are the snapshots of PO_4 beads on the outer leaflet of membrane binding with AMP monomers/clusters; blue beads are PO_4 in POPG while red beads are $PO_41/2$ in CL. (E, F) Plots of mean square displacement (MSD) of POPG and CL in the lipid membrane before and after interacting with AMPs. The diffusion coefficients are extracted from the linear fits (within the range of 100-600 ns, as shown in transparent solid lines) according to **equation 1**.

It is well likely that the large CL and PG microdomains in bacterial cells break down into small clusters, leading to reduced membrane fluidity and changes in membrane phases. As a result, bacterial cells suffer from severe morphological defects, including increase in curvature and decrease in size.[55] These features are consistent with the increased membrane permeabilization. Here, we analyse the mean square displacements (MSDs) and lipid diffusion coefficients (D) before and after the addition of AMPs (**Figure 6E, F**) to evaluate the migration rates of lipid molecules in the membrane and further clarify the effects of binding and insertion of AMPs into the membrane on membrane fluidity. The equation of motion can be written as follows:

$$D_\alpha = \frac{1}{6N_\alpha} \lim_{i \to \infty} \frac{d}{dt} \sum_{i=1}^{N_\alpha} \{[r_i(t) - r_i(0)]^2\} \tag{2}$$

where D_α denotes the statistical average displacement of particles along a given direction within time *t*, *i.e.*, MSD, N_α denotes the number of diffusing atoms in the system, *t* denotes time and *r* denotes displacement. **Equation (2)** shows that Brownian motion must obey the rules of molecular thermal motion. The differential of the MSD to the time ratio (*i.e.*, the curve slope *a*) was also used to replace the differential approximation. Since the MSD value was already a mean value exceeding the number of diffusing atoms (N_α), equation (1) can be simplified as follows:

$$D = \frac{a}{6} \tag{3}$$

The data of simulation time from 100 ns to 600 ns with relative stability were selected for analysis. The MSD slope of the membrane without AMP was greater than that after the addition of AMP. Thus, the diffusion coefficients of both PG and CL were lower in the system with AMPs and the lipid molecules moved much slower in the *xy* plane. With addition of different AMPs, peptides became embedded as they bounded tightly with the head groups of the lipids and even inserted into the hydrophobic core of the membrane. The decrease in MSD was indicative of increased electrostatic and hydrophobic interaction between AMPs and lipids in the membrane, the reduced order of the MSD slopes follows: Pure bilayer > GIK > GFK > GIR > GWK (PG); Pure bilayer > GFK > GIK > GIR > GWK (CL). The corresponding values of the PG /CL diffusion coefficients in membrane systems with and without AMPs can be seen in **Table 1** and follow the same order as the MSD slopes.

Table 1. MSD slopes (K_{MSD}) and diffusion coefficients (D) of POPG and CL in lipid bilayers without and with AMP binding from MD simulations.

MD System	K_{MSD} (POPG)	K_{MSD} (CL)	$D_{POPG}/10^{-5}$ cm^2/s	$D_{CL}/10^{-5}$ cm^2/s
Bilayer alone	0.126	0.0745	0.0289	0.0176
+GIK	0.110	0.0593	0.0268	0.0143
+GIR	0.0825	0.0536	0.0208	0.0133
+GFK	0.103	0.0685	0.0255	0.0165
+GWK	0.0795	0.0430	0.0192	0.0110

3.6 Neutron Reflection (NR) Study of AMP Binding with DPPG Monolayer

To determine how AMP binds with anionic lipid membranes, a spread PG monolayer at the air/water interface was utilized to facilitate NR. The surface pressure each DPPG monolayer was compressed to the surface pressure of 28 mN/m to mimic the average resting membrane pressure. NR reflectivity measurements involved parallel runs under different H/D substitutions to lipid and water to enhance resolution in the determination of the layer thickness and composition. The reflectivity profiles measured for the determination of the spread DPPG monolayer structures and the best fits are shown in **Figure S7**. The DPPG monolayer was assumed to be comprised of two parts, the hydrophobic tail layer in air with a thickness of 18 ± 1 Å and the hydrophilic head layer submerged in water with a thickness of 10 ± 1 Å.[32]

In contrast to the uniform DPPG monolayer, AMP binding led to significant structural changes, and the exact changes were AMP dependent. **Figures 8A-D** show the reflectivity profiles under different isotopic contrasts and the best model fits, with the fitted scattering length density (SLD) data also shown. The concentrations of the AMPs used were fixed at 10 μM.

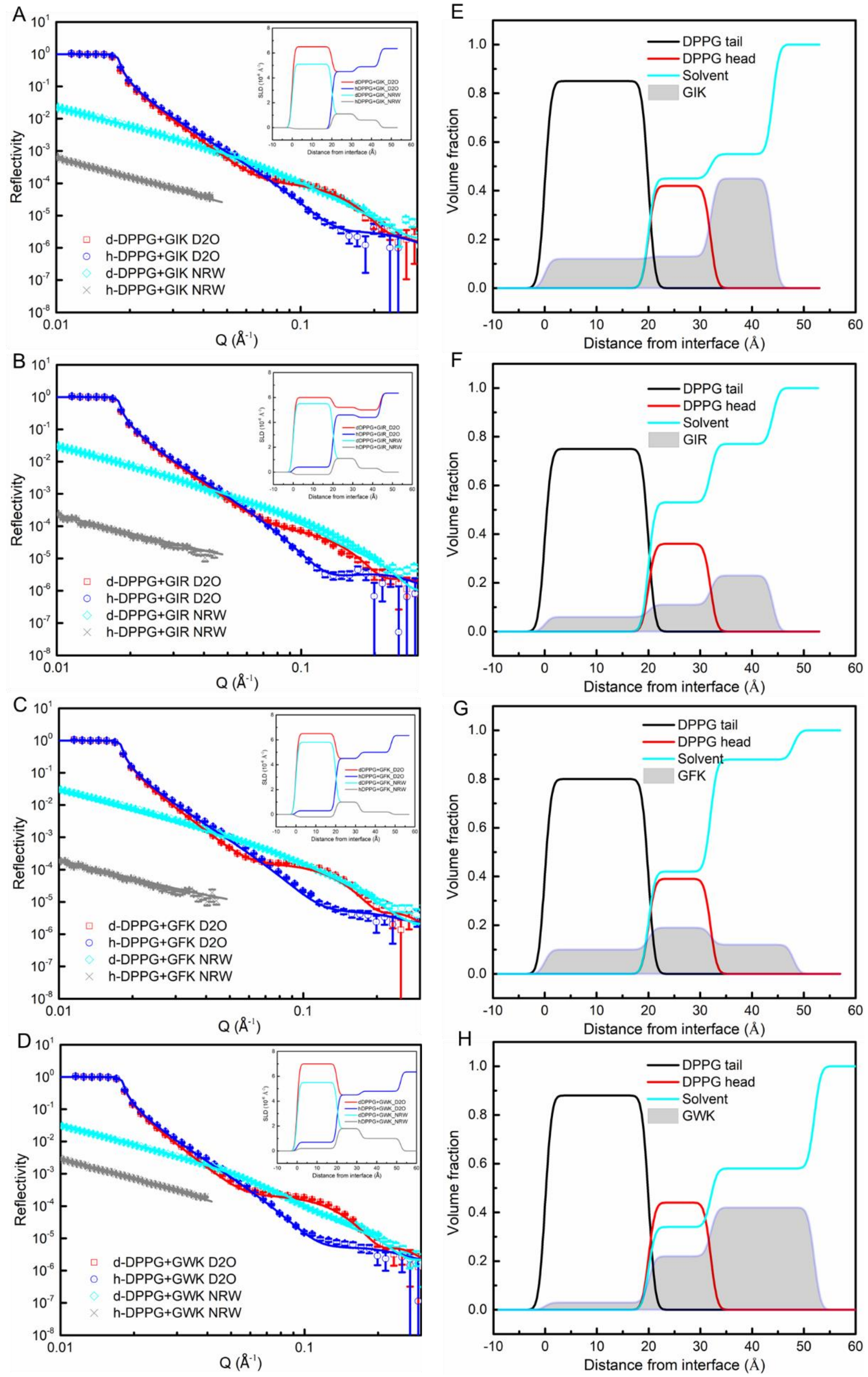

Figure 8. Neutron reflectivity profiles measured under different isotopic contrasts for each AMP binding to DPPG monolayers (at the concentration of 10 μM) and the

corresponding best fits. (A-D) Reflectivity after each AMP (GIK, GIR, GFK and GWK) binding with the DPPG monolayer is plotted against the perpendicular wave vector (*Q*). The scattered points are the measured data and the continuous curves are the best fits. The insets in (A-D) are the best model fitted SLD profiles under different contrasts. (E-H) Fractional volume distributions of the different components in systems of DPPG monolayer upon binding with AMPs. Lipid tails and heads are in black and red lines, respectively. Peptides are drawn in grey shadows, and solvent in light blue. The volume fraction distribution of DPPG without AMP and the corresponding NR profiles are shown in **Figure S7**. Best fitted parameters are given in **Table S8.**

Similar reflectivity curves were measured for binding of different AMPs against the lipid monolayer alone. All reflectivity profiles show normal monotonic delay but the profile from dDPPG in D_2O shows an obvious positive fringe around $Q \approx 0.07$. Data analysis to the measured NR reflectivity profiles from the parallel four isotopic contrasts revealed that AMP binding caused a thickening of the DPPG monolayer and the lipid dissolution, but to different extents. Among all the AMPs, GIR desorbed over 15% of the DPPG molecules from the monolayer and formed lipid-peptide aggregates with thickness of 27 Å under the head layer. While GIK bound onto the monolayer with a larger amount but showed no greater dissolution of lipid molecules than GIR. Its additional layer under the head region was about 15 Å. Differences in GIK and GIR binding can implicate different membrane-targeting antimicrobial efficacy and dynamic killing. GWK binding formed the protruding peptide-rich layer of 20 Å under the head layer. The peptide-rich layer can function as an AMP reservoir during the membrane-lytic process. GFK showed a similar behaviour to GWK. As a peptide containing aromatic residues, it can form intermolecular aggregates onto the DPPG monolayer via π-π, cation-π and hydrophobic interactions, but its peptide-rich layer in both thickness and volume fraction is inferior to the GWK system. However, GFK displayed further insertion into the tail region of the lipid monolayer than what was observed from GWK. The different membrane binding behaviour between GFK and GWK can also explain how different intramembrane peptide-clusters or aggregates formed by these AMPs lead to very different antimicrobial efficacy and efficiency.

4. Conclusion

The three new AMPs derived by substituting II by FF and WW and KK by RR in the widely studied G_3 (GIK) sequence did not alter their total charges or hydrophobicity as indicated by the rp-HPLC retention times, but these amphiphilic AMPs displayed very different efficacy and efficiency against Gram-positive bacteria including sensitive *S. aureus* and drug-resistant MRSA. This work demonstrated that the self-promoted binding and insertion of these AMPs to the LTA layer is driven by electrostatic interaction, but the subsequent hydrophobic interaction can differ, depending on the side chain features from the amino acids. AMPs can all approach cytoplasmic membrane, cause membrane depolarization and leakage and form intramembrane nanoaggregates. Both experiments and MD simulations provide useful evidence to relate the observed differences in antimicrobial actions to intramembrane aggregation, changes in membrane rigidity and phase separation. The four AMPs showed varying affinity to LTA in both cell-free and *S. aureus* systems and different extents of depolarization of cytoplasmic membrane. SANS experiments of peptide interaction with LTA SUVs revealed that GWK binds differently with LTA and such outer surface binding can obstruct GWK peptide penetration onto the plasma membrane leading to relatively weak membrane depolarization.

AMPs also showed strong binding with the anionic cytoplasmic membrane but again varied in different extents. Data from both cell and cell-free systems and MD simulations all pointed to the better effects of GIR and GWK associated with altered membrane rigidity and decreased diffusion efficiency than GIK and GFK. Furthermore, GWK and GIR can more easily form intramembrane peptide-lipid clusters and induce membrane phase separation. These multiple effects are well correlated with their antimicrobial efficacy and time-killing performance: GWK > GIR > GFK > GIK. Because these membrane targeting actions are fast and effective, the mechanistic processes help explain why AMPs are promising agents to fight bacterial resistance.

Associated Content

Supporting Information Available

The supporting information is available free of charge on the website, including materials information, CD, NR profiles and fitting models and parameters, MD simulation results, fluorescence emission spectroscopies, Zeta potential.

Author Information

Corresponding Authors

***E-mail: j.lu@manchester.ac.uk (J.R.L.).**

***Tel: 0044 161 200 3926**

ORCID

Mingrui Liao: 0000-0002-9481-4026

Haoning Gong: 0000-0003-1590-2042

Xuzhi Hu: 0000-0002-9246-7040

Xuebo Quan: 0000-0003-3738-9059

Thomas A. Waigh: 0000-0002-7084-559X

Jian Zhou: 0000-0002-3033-7785

Jian Ren Lu: 0000-0001-5648-3564

Conflicts of Interest

The authors declare no conflict of interest.

Acknowledges

Thank for the studentship supports from the University of Manchester joint with China Scholarship Council (UoM-CSC joint PhD program) to M.L., H.G. and Z.W., supports to H.G. and X.H. via an overseas research studentship funded by the UoM, research fund supports from Syngenta to X.H., and funding from the National Natural Science Foundation of China (No. 21908066) to X.Q. We appreciate Rehana Sung, Derren Heyes for their assistance of HPLC and CD. We acknowledge the beam time awarded from the ISIS neutron facility (RB 1920496 & 2210031 & 2210029). An allocation time from the Shared Computation Facility (SCF) at the UoM is gratefully acknowledged.

5. References

[1] Malanovic N, Lohner K. Gram-positive bacterial cell envelopes: The impact on the activity of antimicrobial peptides. Biochimica et Biophysica Acta (BBA) 2016;1858:936-46.
[2] Zhou M, Qian Y, Xie J, Zhang W, Jiang W, Xiao X, et al. Poly(2-Oxazoline)-based functional peptide mimics: Eradicating MRSA infections and persisters while alleviating antimicrobial resistance. Angewandte Chemie International Edition 2020;59:6412-9.
[3] Xiao X, Zhang S, Chen S, Qian Y, Xie J, Cong Z, et al. An alpha/beta chimeric peptide molecular brush for eradicating MRSA biofilms and persister cells to mitigate antimicrobial resistance. Biomaterials science 2020;8:6883-9.
[4] Pogliano J, Pogliano N, Silverman JA. Daptomycin-mediated reorganization of membrane architecture causes mislocalization of essential cell division proteins. Journal of Bacteriology 2012;194:4494-504.
[5] Pogliano J, Pogliano N, Silverman JA. Daptomycin-mediated reorganization of membrane architecture causes mislocalization of essential cell division proteins. Journal of Bacteriology 2012;194:4494-504.
[6] Muller A, Wenzel M, Strahl H, Grein F, Saaki TNV, Kohl B, et al. Daptomycin inhibits cell envelope synthesis by interfering with fluid membrane microdomains. Proceedings of the National Academy of Sciences of the United States of America 2016;113:E7077-E86.
[7] Silverman J, Perlmutter N, Shapiro H. Correlation of daptomycin bactericidal activity and membrane depolarization in Staphylococcus aureus. Antimicrobial agents and chemotherapy 2003;47:2538-44.
[8] Hurdle JG, O'Neill AJ, Chopra I, Lee RE. Targeting bacterial membrane function: an underexploited mechanism for treating persistent infections. Nature Reviews Microbiology 2010;9:62-75.
[9] Kharidia R, Liang JF. The activity of a small lytic peptide PTP-7 on Staphylococcus aureus biofilms. The Journal of Microbiology 2011;49:663.
[10] Hayden RM, Goldberg GK, Ferguson BM, Schoeneck MW, Libardo MD, Mayeux SE, et al. Complementary Effects of Host Defense Peptides Piscidin 1 and Piscidin 3 on DNA and Lipid Membranes: Biophysical Insights into Contrasting Biological Activities. The journal of physical chemistry B 2015;119:15235-46.
[11] Mihailescu M, Sorci M, Seckute J, Silin VI, Hammer J, Perrin BS, Jr., et al. Structure and Function in Antimicrobial Piscidins: Histidine Position, Directionality of Membrane Insertion, and pH-Dependent Permeabilization. Journal of the American Chemical Society 2019;141:9837-53.

[12] Lienkamp K, Kumar KN, Som A, Nusslein K, Tew GN. "Doubly selective" antimicrobial polymers: how do they differentiate between bacteria? Chemistry – A European Journal 2009;15:11710-4.

[13] Epand RF, Mowery BP, Lee SE, Stahl SS, Lehrer RI, Gellman SH, et al. Dual Mechanism of Bacterial Lethality for a Cationic Sequence-Random Copolymer that Mimics Host-Defense Antimicrobial Peptides. Journal of Molecular Biology 2008;379:38-50.

[14] Bechinger B, Gorr SU. Antimicrobial peptides: Mechanisms of action and resistance. Journal of dental research 2017;96:254-60.

[15] Brogden KA. Antimicrobial peptides: pore formers or metabolic inhibitors in bacteria? Nature Reviews Microbiology 2005;3:238-50.

[16] Fischer W. Physiology of lipoteichoic acids in bacteria. In: Rose AH, Tempest DW, editors. Advances in Microbial Physiology: Academic Press; 1988. p. 233-302.

[17] Fischer W, Rösel P. The alanine ester substitution of lipoteichoic acid (LTA) in Staphylococcus aureus. FEBS Letters 1980;119:224-6.

[18] Bucki R, Janmey PA. Interaction of the gelsolin-derived antibacterial PBP 10 peptide with lipid bilayers and cell membranes. Antimicrobial Agents Chemotherapy 2006;50:2932-40.

[19] Scott MG, Gold MR, Hancock REW. Interaction of cationic peptides with lipoteichoic acid and Gram-positive bacteria. Infection and Immunity 1999;67:6445-53.

[20] Freire JM, Gaspar D, Veiga AS, Castanho MA. Shifting gear in antimicrobial and anticancer peptides biophysical studies: from vesicles to cells. Journal of Peptide Science 2015;21:178-85.

[21] Epand RM, Epand RF. Bacterial membrane lipids in the action of antimicrobial agents. Journal of Peptide Science 2011;17:298-305.

[22] Lingwood D, Simons K. Lipid rafts as a membrane-organizing principle. Science 2010;327:46-50.

[23] Mukherjee S, Maxfield FR. Membrane domains. Annual review of cell and developmental biology 2004;20:839-66.

[24] Lopez D, Nickels JD, Chatterjee S, Stanley CB, Qian S, Cheng X, et al. The in vivo structure of biological membranes and evidence for lipid domains. PLOS Biology 2017;15:e2002214.

[25] McMahon HT, Gallop JL. Membrane curvature and mechanisms of dynamic cell membrane remodelling. Nature 2005;438:590-6.

[26] Determination of minimum inhibitory concentrations (MICs) of antibacterial agents by agar dilution. Clinical Microbiology and Infection 2000;6:509-15.

[27] Kahlmeter G, Brown DFJ, Goldstein FW, MacGowan AP, Mouton JW, Odenholt I, et al. European committee on antimicrobial susceptibility testing (EUCAST) technical notes on antimicrobial susceptibility testing. Clinical Microbiology and Infection 2006;12:501-3.

[28] Swain J, Khoury ME, Flament A, Dezanet C, Briée F, Smissen PVD, et al. Antimicrobial activity of amphiphilic neamine derivatives: Understanding the

mechanism of action on Gram-positive bacteria. BBA - Biomembranes 2019;1861:182998.

[29] Winkel JDt, Gray DA, Seistrup KH, Hamoen LW, Strahl H. Analysis of antimicrobial-triggered membrane depolarization usingvoltage sensitive dyes. Frontiers in Cell and Developmental Biology 2016;4:29.

[30] Sautrey G, El Khoury M, Dos Santos AG, Zimmermann L, Deleu M, Lins L, et al. Negatively charged lipids as a potential target for new amphiphilic aminoglycoside antibiotics. The Journal of biological chemistry 2016;291:13864-74.

[31] Parasassi T, Gratton E. Membrane lipid domains and dynamics as detected by Laurdan fluorescence. Journal of Fluorescence 1995;5:59-69.

[32] Gong H, Liao M, Hu X, Fa K, Phanphak S, Ciumac D, et al. Aggregated mmphiphilic antimicrobial peptides embedded in bacterial membranes. ACS applied materials & interfaces 2020;12:44420-32.

[33] Hu X, Carter J, Ge T, Liao M, Margaret Stephens A, McLnnes EF, et al. Impacts of chain and head lengths of nonionic alkyl ethoxylate surfactants on cytotoxicity to human corneal and skin cells in agri-spraying processes. Journal of colloid and interface science 2022.

[34] Gong H, Hu X, Liao M, Fa K, Ciumac D, Clifton LA, et al. Structural disruptions of the outer membranes of Gram-negative bacteria by rationally designed amphiphilic antimicrobial peptides. ACS applied materials & interfaces 2021;13:16062-74.

[35] Qi Y, Ingólfsson HI, Cheng X, Lee J, Marrink SJ, Im W. CHARMM-GUI Martini Maker for Coarse-Grained Simulations with the Martini Force Field. Journal of chemical theory and computation 2015;11:4486-94.

[36] Jo S, Kim T, Iyer VG, Im W. CHARMM-GUI: a web-based graphical user interface for CHARMM. J Comput Chem 2008;29:1859-65.

[37] Monticelli L, Kandasamy SK, Periole X, Larson RG, Tieleman DP, Marrink S-J. The MARTINI Coarse-Grained Force Field: Extension to Proteins. Journal of chemical theory and computation 2008;4:819-34.

[38] Humphrey W, Dalke A, Schulten K. VMD: Visual molecular dynamics. Journal of Molecular Graphics 1996;14:33-8.

[39] Berendsen HJC, van der Spoel D, van Drunen R. GROMACS: A message-passing parallel molecular dynamics implementation. Computer Physics Communications 1995;91:43-56.

[40] Pronk S, Páll S, Schulz R, Larsson P, Bjelkmar P, Apostolov R, et al. GROMACS 4.5: a high-throughput and highly parallel open source molecular simulation toolkit. Bioinformatics 2013;29:845-54.

[41] Gong H, Sani M-A, Hu X, Fa K, Hart JW, Liao M, et al. How do self-assembling antimicrobial lipopeptides kill bacteria? ACS applied materials & interfaces 2020;12:55675-87

[42] Fa K, Liu H, Gong H, Zhang L, Liao M, Hu X, et al. In-Membrane Nanostructuring of Cationic Amphiphiles Affects Their Antimicrobial Efficacy and Cytotoxicity: A Comparison Study between a De Novo Antimicrobial Lipopeptide and Traditional Biocides. Langmuir : the ACS journal of surfaces and colloids 2022;38:6623–37.

[43] Brodersen DE, Clemons WM, Carter AP, Morgan-Warren RJ, Wimberly BT, Ramakrishnan V. The structural basis for the action of the antibiotics tetracycline, pactamycin, and hygromycin B on the 30S ribosomal subunit. Cell 2000;103:1143-54.
[44] Guerra W, Silva-Caldeira PP, Terenzi H, Pereira-Maia EC. Impact of metal coordination on the antibiotic and non-antibiotic activities of tetracycline-based drugs. Coordination Chemistry Reviews 2016;327-328:188-99.
[45] Greber KE, Roch M, Rosato MA, Martinez MP, Rosato AE. Efficacy of newly generated short antimicrobial cationic lipopeptides against methicillin-resistant Staphylococcus aureus (MRSA). International Journal of Antimicrobial Agents 2020;55:105827.
[46] Gutberlet T, Markwitz S, Labischinski H, Bradaczek H. Monolayer investigations on the bacterial amphiphile lipoteichoic acid and on lipoteichoic acid/dipalmitoyl-phosphatidylglycerol mixtures. Makromolekulare Chemie Macromolecular Symposia 1991;46:283-7.
[47] Labischinski H, Naumann D, Fischer W. Small and medium-angle X-ray analysis of bacterial lipoteichoic acid phase structure. Eur J Biochem 1991;202:1269-74.
[48] Fischer W, Markwitz S, Labischinski H. Small-angle X-ray scattering analysis of pneumococcal lipoteichoic acid phase structure. Eur J Biochem 1997;244:913-7.
[49] Roversi D, Luca V, Aureli S, Park Y, Mangoni ML, Stella L. How Many Antimicrobial Peptide Molecules Kill a Bacterium? The Case of PMAP-23. ACS chemical biology 2014;9:2003-7.
[50] Melo MN, Ferre R, Castanho MARB. Antimicrobial peptides: linking partition, activity and high membrane-bound concentrations. Nature Reviews Microbiology 2009;7:245–50.
[51] Malanovic N, Leber R, Schmuck M, Kriechbaum M, Cordfunke RA, Drijfhout JW, et al. Phospholipid-driven differences determine the action of the synthetic antimicrobial peptide OP-145 on Gram-positive bacterial and mammalian membrane model systems. Biochimica et Biophysica Acta (BBA) 2015;1848:2437-47.
[52] Hobbs JK, Miller K, O'Neill AJ, Chopra I. Consequences of daptomycin-mediated membrane damage in Staphylococcus aureus. Journal of Antimicrobial Chemotherapy 2008;62:1003-8.
[53] Silverman JA, Perlmutter NG, Shapiro HM. Correlation of daptomycin bactericidal activity and membrane depolarization in Staphylococcus aureus. Antimicrobial agents and chemotherapy 2003;47:2538-44.
[54] Ciumac D, Gong H, Campbell RA, Campana M, Xu H, Lu JR. Structural elucidation upon binding of antimicrobial peptides into binary mixed lipid monolayers mimicking bacterial membranes. Journal of colloid and interface science 2021;598:193-205.
[55] El Khoury M, Swain J, Sautrey G, Zimmermann L, Van Der Smissen P, Decout JL, et al. Targeting bacterial cardiolipin enriched microdomains: An antimicrobial strategy used by amphiphilic aminoglycoside antibiotics. Scientific Reports 2017;7:10697.

[56] Rodriguez ME, Azizuddin K, Zhang P, Chiu S-m, Lam M, Kenney ME, et al. Targeting of mitochondria by 10-N-alkyl acridine orange analogues: Role of alkyl chain length in determining cellular uptake and localization. Mitochondrion 2008;8:237-46.

[57] Sautrey G, Zimmermann L, Deleu M, Delbar A, Machado LS, Jeannot K, et al. New amphiphilic neamine derivatives active against resistant Pseudomonas aeruginosa and their interactions with lipopolysaccharides. Antimicrobial agents and chemotherapy 2014;58:4420–30.

Supporting Information

From Cell Wall to Cytoplasmic Membrane: Multiple Actions of Antimicrobial Peptides against Gram-positive Bacteria

Mingrui Liao,[1#] Haoning Gong,[1] Xuzhi Hu,[1] Ziwei Wang,[2] Xuebo Quan,[3] Zongyi Li,[1] Andrew J. McBain,[4] Jian Zhou,[5] Mario Campana,[6] and Jian R. Lu[1,*]

[1] Biological Physics Laboratory, Department of Physics and Astronomy, School of Natural Science, The University of Manchester, Oxford Road, Manchester M13 9PL, UK.

[2] National Graphene Institute, The University of Manchester, Oxford Road, Manchester M13 9PL, UK.

[3] Shenzhen Bay Laboratory, Institute of Systems and Physical Biology, Shenzhen, 518132, China

[4] Division of Pharmacy and Optometry, Faculty of Biology, Medicine and Health, The University of Manchester, Oxford Road, Manchester M13 9PL, UK.

[5] School of Chemistry and Chemical Engineering, Guangdong Provincial Key Laboratory for Green Chemical Product Technology, South China University of Technology, Guangzhou 510640, China.

[6] STFC ISIS Facility, Rutherford Appleton Laboratory, Didcot, OX11 0QX, UK.

[#] To whom as PhD candidate should be responsible to all the experiments and simulation work.

[*] To whom all correspondence should be made: J.lu@manchester.ac.uk

1. Bacterial strains and materials

The following bacterial strains were purchased from ATCC: *Staphylococcus aureus* (*S. aureus* ATCC 6538), Meticillin-resistant *Staphylococcus aureus* (*MRSA*) were clinically isolated strains obtained from the Manchester Royal Infirmar. Antimicrobial peptides (AMPs) were synthesized by ChinaPeptides Co., Ltd. (Shanghai, China). Fluorescence probes N-phenyl-1-naph-thylamine (NPN), 3,3′-Dipropylthiadicarbocyanine iodide (DiSC$_3$(5)), Laurdan, Calcein and Calcein-AM, were supplied from Sigma-Aldrich. SYTO 9, BODIPY-TR-cadaverine (BC) and Nonyl Acridine Orange (NAO) was obtained from Thermo Fisher.

Lipids 1,2-dipalmitoyl-sn-glycero-3-[phosphor-rac-(3-lysyl(1-glycerol))] (sodium salt) (DPPG), acyl chain deuterated DPPG (d_{62}-DPPG), 1-palmitoyl-2-oleoyl-sn-glycero-3-phospho-(1′-rac-glycerol) (sodium salt) (POPG) and 1-palmitoyl-2-oleoyl-sn-glycero-3-phosphocholine (POPC), 1',3'-bis[1-palmitoyl-2-oleoyl-sn-glycero-3-phospho]-glycerol (sodium salt) (16:0-18:1 Cardiolipin) were obtained from Avanti Polar Lipids (Alabaster, USA). Hydrogenated lipoteichoic acid (LTA) extracted from *S. aureus* was purchased from Sigma-Aldrich.

Table S1. Antimicrobial activities of AMPs against Gram-positive bacteria and molecular information of the AMPs.

Peptide/antibiotic code	Peptide sequence	MIC/μM		Theoretical M_w/g·mol^{-1}	Measured M_w/g·mol^{-1}	Charge/e (pH = 7.4)	Retention time/min
		S. aureus	*MRSA*				
GWK	G(WWKK)$_3$W	3 ± 0.5	1.5 ± 0.5	2147.6	2150.0	+7	18.84
GFK	G(FFKK)$_3$F	3 ± 0.5	3 ± 0.5	1874.3	1876.0	+7	18.20
GIK	G(IIKK)$_3$I	3 ± 0.5	3 ± 0.5	1636.2	1638.0	+7	18.77
GIR	G(IIRR)$_3$I	1.5 ± 0.5	1.5 ± 0.5	1804.3	1806.0	+7	19.16
TC	Tetracycline	0.8 ± 0.2	0.6 ± 0.2	444.4	445.2	--	--

2. Fluorescence spectroscopy

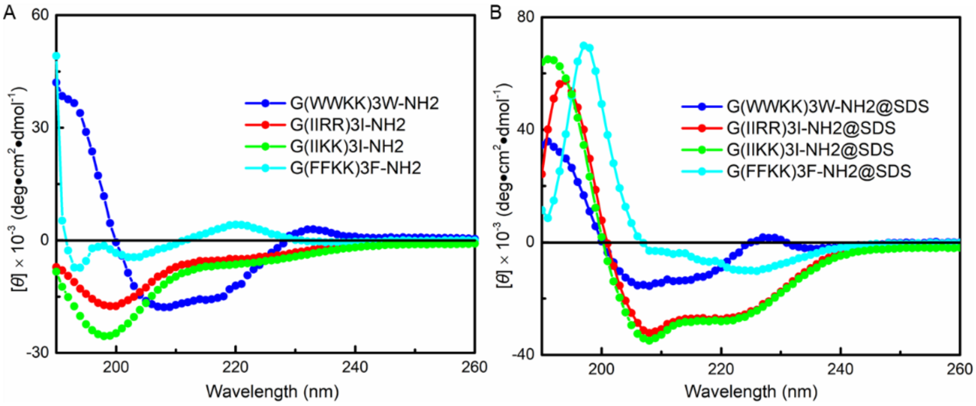

Figure S1. Secondary structural characterizations of the AMPs at the concentration of 0.5 mM in presence of (A) neutral PBS solution and (B) SDS solution (50 mM) mimicked negatively-charged environment.

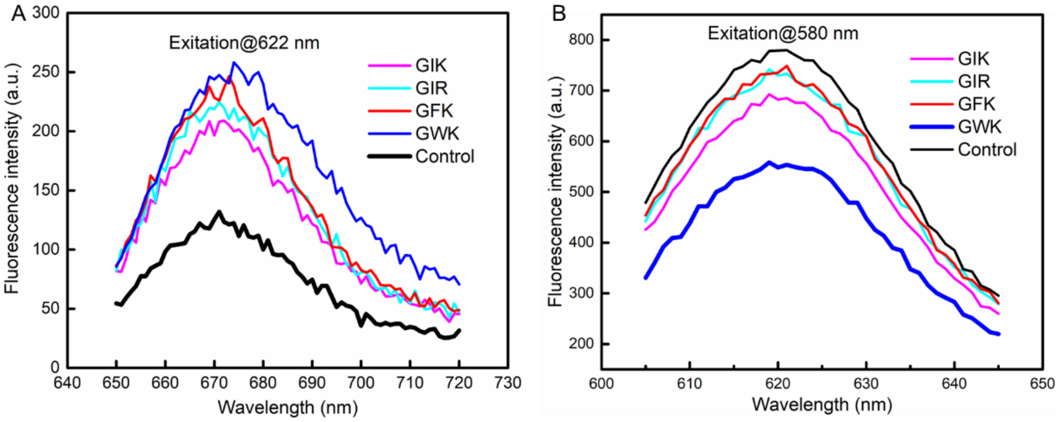

Figure S2. Emission spectroscopy of 50 μM AMPs at 10 μM (A) $DiSC_3(5)$ and (B) BODIPY™-TR-cadaverine (BC) fluorescence probes, respectively. The solution environment was pH 7.4 Tris buffer (150 mM NaCl, 10 mM Tris), all the measurements were carried out under room temperature.

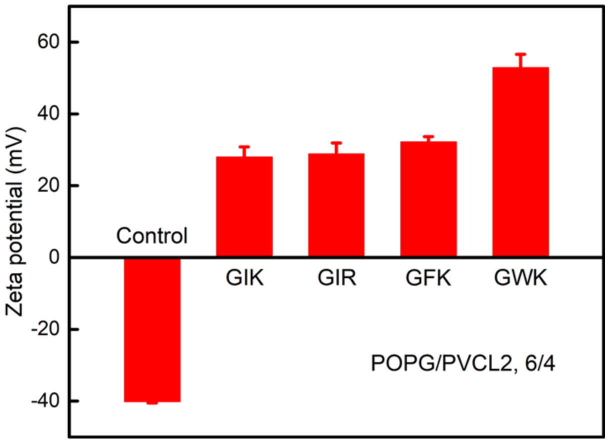

Figure S3. Zeta potential of 50 μM AMPs when bound to the POPG/CL SUVs.

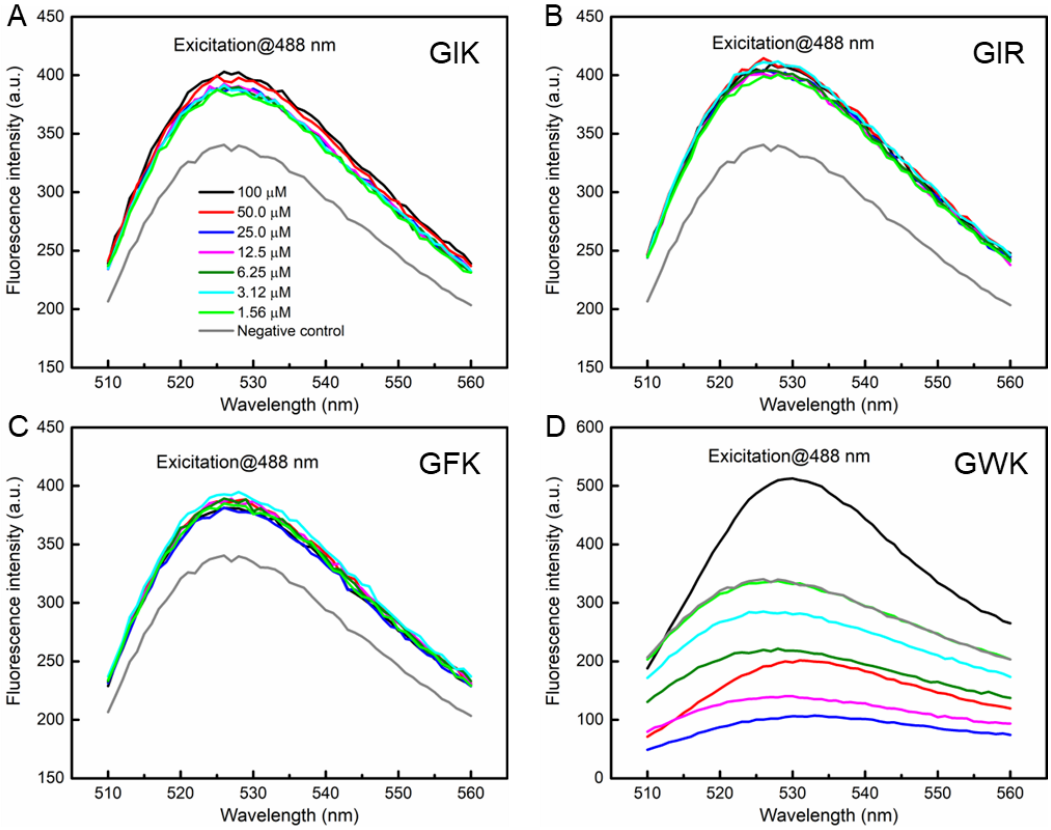

Figure S4. Emission spectroscopic intensities upon addition of AMPs on 10 μM NAO fluorescence probe, and the AMP peptide concentration ranging from 0 to 100 μM. The solution environment was pH 7.4 Tris buffer (150 mM NaCl, 10 mM Tris).

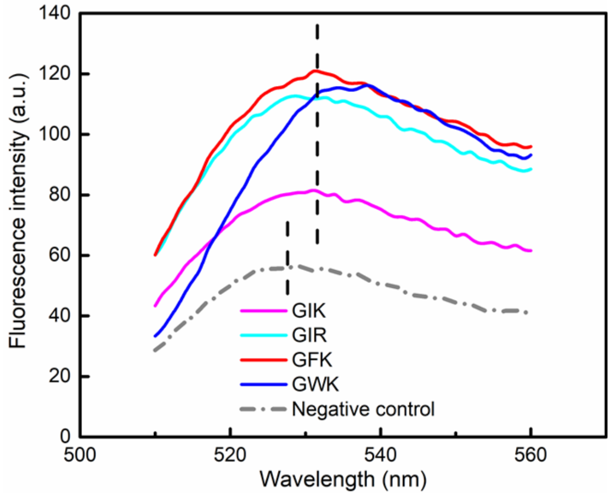

Figure S5. Emission spectroscopy of NAO labelled *S. aureus* mixed with AMP peptides at the concentration of 50 µM. The solution environment was pH 7.4 Tris buffer (150 mM NaCl, 10 mM Tris).

3. SANS Fitting Model of LTA/POPC and PVCL2/POPG SUVs with AMPs

Table S2. Structural parameters from best fits to the SANS data from LTA/POPC SUVs and after AMP binding at different concentrations. Similar fitting models were also employed in our previous work.[13, 14]

Sample	**1 mM hLTA/hPOPC**		**GIK**	**GIR**	**GFK**	**GWK**
			100 µM	100 µM	100 µM	100 µM
Fitting Model A	**CMS**	**Fitting Model B**	**CMS_LP**	**CMS_LP**	**CMS_LP**	**CMS_LP**
Background ($\times 10^{-3}$ cm^{-1})	2.5±0.2	**Background ($\times 10^{-3}$ cm^{-1})**	2.5±0.2	3.8±0.2	4.5±0.2	2.5±0.2
A_volume fraction ($\times 10^{-3}$)	3.6±0.2	**Volume fraction ($\times 10^{-3}$)**	3.2±0.2	3.6±0.2	3.4±0.2	3.2±0.2

A_core_SLD (× 10^{-6} Å^{-2})	6.0±0.1	**Scale_A**	3	0.25	1.5	1
A_solvent_SLD (× 10^{-6} Å^{-2})	6.3±0.1	**A_core_SLD (× 10^{-6} Å^{-2})**	5.9±0.1	5.8±0.1	5.9±0.1	5.9±0.1
A_radius (Å)	180±10	**A_solvent_SLD (× 10^{-6} Å^{-2})**	6.3±0.1	6.3±0.1	6.3±0.1	6.3±0.1
A_radius PDI^{c}	0.6±0.1	**A_radius (Å)**	200±10	200±10	200±10	200±10
A_layer1_thickness (Å)	8±1	**A_radius PDI**	0.5±0.1	0.5±0.1	0.5±0.1	0.5±0.1
A_layer1_SLD (× 10^{-6} Å^{-2})	3.5±0.2	**A_thickness (Å)**	48±2	48±2	48±2	48±2
A_layer2_thickness (Å)	25±2	**A_shell_SLD (× 10^{-6} Å^{-2})**	4.8±0.2	5.2±0.2	4.8±0.2	4.8±0.2
A_layer2_SLD (×10^{-6} Å^{-2})	0±0.1	**A_thickness PDI^{f}**	0±0.1	0±0.1	0±0.1	0±0.1
A_layer3_thickness (Å)	8±1	**Scale_B**	20	70	25	30
A_layer3_SLD (×10^{-6} Å^{-2})	3.5±0.2	**B_peak_pos (Å^{-1})**	0.097±0.001	0.106±0.001	0.1±0.001	0.096±0.001
A_layer4_thickness (Å)		**B_peak_hwhm (Å^{-1})**	0.008±0.001	0.002±0.001	0.008±0.001	0.006±0.001

A_layer 4_SLD ($\times 10^{-6}$ Å^{-2})	

Table S3. Structural parameters from best fits to the SANS data from PVCL2/POPG SUVs and after AMP binding at different concentrations. Similar fitting models were also employed in our previous work.[13, 14]

Sample	**1 mM hPVCL/hPOPG**	**GIK**	**GIR**	**GFK**	**GWK**
		50 µM	50 µM	50 µM	50 µM
Fitting Model	**CMS**	**CMS**	**CMS**	**CMS**	**CMS**
Background ($\times 10^{-3}$ cm^{-1})	2±0.2	2.8±0.2	2.8±0.2	2.8±0.2	2.8±0.2
A_volume fraction ($\times 10^{-3}$)	3.6±0.2	3.4±0.2	3.8±0.2	3.8±0.2	3.0±0.2
A_core_SLD ($\times 10^{-6}$ Å^{-2})	6.0±0.1	5.9±0.1	5.9±0.1	5.9±0.1	5.9±0.1
A_solvent_SLD ($\times 10^{-6}$ Å^{-2})	6.3±0.1	6.3±0.1	6.3±0.1	6.3±0.1	6.3±0.1
A_radius (Å)	160±10	150±10	150±10	150±10	150±10
A_radius PDI[c]	0.5±0.1	0.6±0.1	0.6±0.1	0.6±0.1	0.6±0.1
A_layer1_thickness (Å)	8±1	10±1	12±1	12±1	18±1

A_layer 1_SLD (×10^{-6} Å^{-2})	4.0±0.2	4.0±0.2	4.0±0.2	4.0±0.2	5.8±0.2
A_layer 2_thickness (Å)	25±2	25±2	25±2	25±2	26±2
A_layer 2_SLD (×10^{-6} Å^{-2})	0±0.1	-0.1±0.1	0.2±0.1	0.2±0.1	0.6±0.1
A_layer 3_thickness (Å)	8±1	8±1	8±1	8±1	8±1
A_layer 3_SLD (×10^{-6} Å^{-2})	4.0±0.2	4.0±0.2	4.0±0.2	4.0±0.2	4.8±0.2

Table below continued from **Table S3**

Sample	**GIK**		**GIR**		**GFK**		**GWK**		
	100 µM	200 µM	100 µM	200 µM	100 µM	200 µM	100 µM	200 µM	
Fitting Model	**CMS_LP**		**CMS_LP**		**CMS_LP**		**CMS_LP**	**Fitting Model**	**Sphere_LP**
Background (×10^{-3} cm^{-1})	3.0±0.2	4.0±0.2	3.0±0.2	3.5±0.2	2.8±0.2	3.5±0.2	3.0±0.2	**Background (×10^{-3} cm^{-1})**	3±0.2
Volume fraction (× 10^{-3})	3.0±0.2	2.4±0.2	3.0±0.2	2.4±0.2	3.4±0.2	2.4±0.2	3.0±0.2	**Scale**	2.4±0.2
Scale_A	15	1	18	1	8	0.18	12	**Scale_A**	25
A_core_SLD (×10^{-6} Å^{-2})	5.9±0.1	5.0±0.1	5.9±0.1	5.0±0.1	6.2±0.1	5.0±0.1	5.9±0.1	**A_SLD (×10^{-6} Å^{-2})**	3.6±0.1
A_solvent_SLD (×10^{-6} Å^{-2})	6.3±0.1	6.3±0.1	6.3±0.1	6.3±0.1	6.3±0.1	6.3±0.1	6.3±0.1	**A_solvent_SLD (×10^{-6} Å^{-2})**	6.3±0.1

A_radius (Å)	180±10	190±10	190±10	190±10	180±10	190±10	250±10	**B_radius (Å)**	200±10
A_radius PDI	0.6±0.1	0.6±0.1	0.6±0.1	0.6±0.1	0.6±0.1	0.6±0.1	0.6±0.1	**B_radius PDI**	0.9±0.1
A_thickness (Å)	30±2	42±2	30±2	46±2	30±2	46±2	30±2	**Scale_B**	700
A_shell_SLD (× 10^{-6} $Å^{-2}$)	4.8±0.2	4.4±0.2	4.8±0.2	3.6±0.2	4.8±0.2	3.6±0.2	4.8±0.2	**B_peak_pos ($Å^{-1}$)**	0.08±0.005
A_thickness PDI[f]	0±0.1	0±0.1	0±0.1	0±0.1	0.4±0.1	0±0.1	0±0.1	**B_peak_hwhm ($Å^{-1}$)**	**0.008±0.001**
Scale_B	6±1	21±1	6±1	21±1	4±1	21±1	6±1	**Scale_C**	4.5
B_peak_pos ($Å^{-1}$)	0.138±0.005	0.15±0.005	0.15±0.005	0.15±0.005	0.13±0.005	0.15±0.005	0.138±0.005	**C_peak_pos ($Å^{-1}$)**	0.142±0.002
B_peak_hwhm ($Å^{-1}$)	0.005±0.001	0.004±0.001	0.006±0.001	0.004±0.001	0.004±0.001	0.004±0.001	0.005±0.001	**C_peak_hwhm ($Å^{-1}$)**	**0.01±0.001**

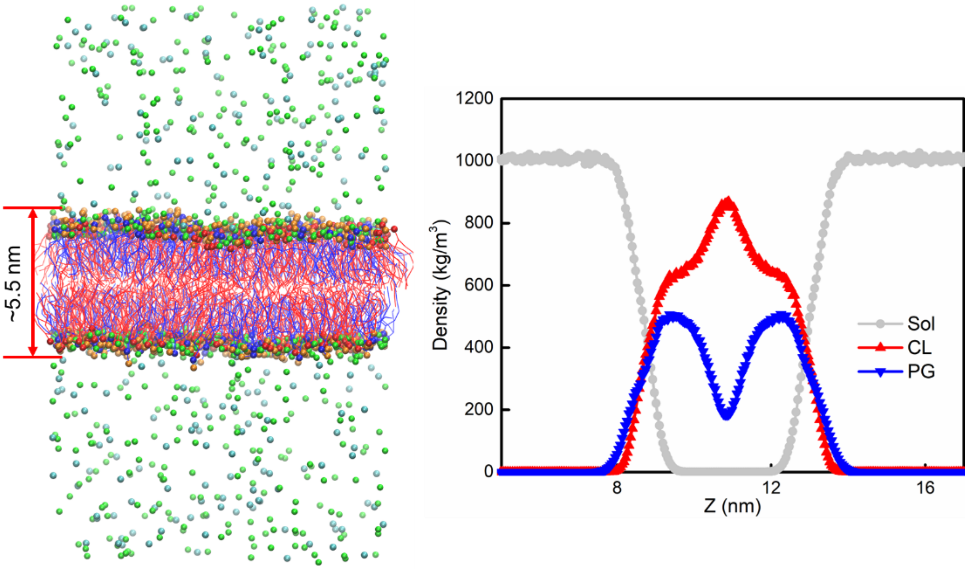

Figure S6. Snapshot of the POPG/PVCL2 bilayer (left) and the corresponding density distribution profiles (right).

4. NR Fitting Model of AMPs’ Binding with DPPG Monolayers

Table S1. Chemical formula, molecular volumes and weights of samples.

Components		**Formula**	**Molecular Volume (Å^3)**[c]	**Molecular Mass (Da)**[a]
DPPG[b]	Head group	$C_8H_{12}O_{10}P$	283	299
	Tail group	$C_{30}H_{62}$	865	422
GIK		$C_{80}H_{155}N_{21}O_{14}$	2444.6	1636.2
GIR		$C_{80}H_{155}N_{33}O_{14}$	2532.2	1845.3
GFK		$C_{101}H_{141}N_{21}O_{14}$	2137.3	1915.3
GWK		$C_{115}H_{148}N_{28}O_{14}$	2415.2	2188.5

[a] Molecular weights are calculated based on 100% hydrogenated samples.

[b] The DPPG tail group has 2 palmitic chains, and a phosphatidylglycerol (PG) head group. The molecular volumes and weights are kept the same as used previously.[1, 2]

[c] Molecular volumes and weights of peptides are estimated using the online calculators, e.g., (http://psldc.isis.rl.ac.uk/Psldc/) and (https://www.pepcalc.com/). Peptides were purchased from ChinaPeptides Co., Ltd. (Shanghai, China), and have been characterized as previously described.[3]

Table S2. Theoretical SLDs used in the NR fittings.

Components		**SLD**[a] **(10^{-6} Å^{-2})**	
		D_2O	NRW[b]
dDPPG	Head	3.27	2.59
	Tail	7.08	7.08
hDPPG	Head	3.27	2.59
	Tail	-0.38	-0.38
GIK[c]		1.97	0.95
GIR		2.84	1.40
GFK		3.15	1.98
GWK		3.64	2.33

[a] SLDs of peptides were calculated using the ISIS biomolecular SLD calculator (http://psldc.isis.rl.ac.uk/Psldc/).

[b] Null reflection water (NRW) is prepared by mixing 8% D_2O and 92% H_2O by volume.

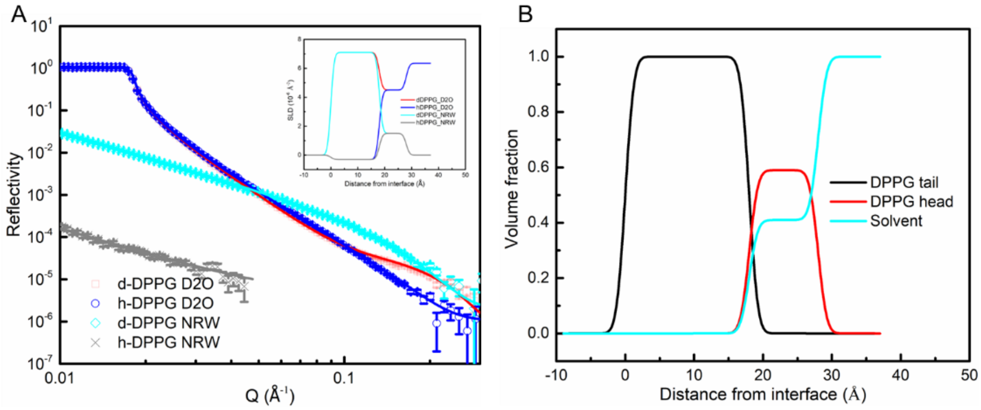

Figure S7. (A) NR reflectivity profiles measured under different H/D substitutions to lipid and water and the best fits, with the fitted scattering length density (SLD) profiles shown in the inset. (B) Volume fraction distributions of different regions of DPPG monolayer and water (solvent) determined at the air/water interface.

5. References

[1] Gong H, Sani M-A, Hu X, Fa K, Hart JW, Liao M, et al. How do self-assembling antimicrobial lipopeptides kill bacteria? ACS applied materials & interfaces 2020;12:55675-87

[2] Fa K, Liu H, Gong H, Zhang L, Liao M, Hu X, et al. In-Membrane Nanostructuring of Cationic Amphiphiles Affects Their Antimicrobial Efficacy and Cytotoxicity: A Comparison Study between a De Novo Antimicrobial Lipopeptide and Traditional Biocides. Langmuir : the ACS journal of surfaces and colloids 2022;38:6623–37.

[3] Gong H, Liao M, Hu X, Fa K, Phanphak S, Ciumac D, et al. Aggregated mmphiphilic antimicrobial peptides embedded in bacterial membranes. ACS applied materials & interfaces 2020;12:44420-32.

Chapter 4 Antimicrobial Synergy of Lipopeptides Paired with Conventional Antibiotics

Mingrui Liao,[1#] Haoning Gong,[1] Xuzhi Hu,[1] Ziwei Wang,[2] Lin Zhang,[1] Ke Fa,[1] Huayang Liu,[1] Andrew J. McBain[3] and Jian R. Lu[1,*]

[1]Biological Physics Laboratory, Department of Physics and Astronomy, School of Natural Science, The University of Manchester, Oxford Road, Manchester M13 9PL, UK.

[2]Department of Physics and Astronomy, School of Natural Science, The University of Manchester, Oxford Road, Manchester M13 9PL, UK.

[3]Division of Pharmacy and Optometry, Faculty of Biology, Medicine and Health, The University of Manchester, Oxford Road, Manchester M13 9PL, UK.

[#]To whom as PhD candidate should be responsible to all the experiments and simulation work.

*To whom all correspondence should be made: J.lu@manchester.ac.uk

Abstract

Antimicrobial resistance (AMR) is fast becoming a major global challenge in both hospital and community settings as many current antibiotics and treatment processes are under the threat of being rendered less effective or ineffective. Synergistic combination of an antibiotic and an aiding agent with a different set of properties provides an important but largely unexploited option to “repurpose” existing biomaterial’s space while addressing issues of potency, spectrum, toxicity and resistance in early stages of antimicrobial drug discovery. This work explores how to combine tetracycline/minocycline (TC/MC) with a broad-spectrum antimicrobial lipopeptide that has been designed to improve the efficiency of membrane targeting and intramembrane accumulation, thereby enhancing antimicrobial efficacy. Experimental measurements of fractional inhibition concentration index (FICI) were undertaken from binary antibiotic-lipopeptide combinations. Most FICI values were found to be lower than 0.5 against both Gram-positive and Gram-negative bacterial strains studied including 3 AMR strains, revealing strong synergetic effects via favorable membrane-lytic interactions. The antimicrobial actions of this type of binary combinations are featured by the fast time-killing and high TC/MC uptake, benefited from effective membrane-lytic disruptions by the lipopeptide. This study thus provides an important mechanistic understanding of the combined antibiotic-lipopeptide approach to improve the therapeutic potential of conventional antibiotics by illustrating how amphiphilic lipopeptide-antibiotic combinations interact with biological membranes, providing a promising alternative to combat AMR through rational design of lipopeptide as an aiding agent.

Keywords: Antimicrobial resistance, drug combination, enhanced potency, bacterial kill kinetics, hydrophobic interactions.

1. Introduction

Tetracycline (TC) and its derivatives are a group of broad-spectrum antibiotics that have been widely used to treat bacterial infections. TC has the characteristic tetracyclic structure and is treated as the parent compound for nomenclature purpose of the group. TC is also well-known in the treatment of rheumatoid arthritis and in the prevention of malaria.[1] Minocycline (MC), a semi-synthetic and replenished version of TC, has superseded TC because of its more potent antimicrobial activity. MC has also been used to treat acne vulgaris and several sexually transmitted diseases. Meanwhile, it has recently been reported that TC and MC can exert a variety of other biological actions, including anti-inflammatory and anti-apoptotic activities, inhibition of proteolysis, angiogenesis and tumor metastasis.[2] Furthermore, MC has shown other multifaceted activities, *e.g.*, targeting a number of debilitating neurological diseases.[3] These TC compounds have high binding affinity to ribosomal 30S subunit stabilized by the magnesium (Mg) salt bridge between the hydroxyl groups of TC/MC and the phosphate groups of rRNA, thereby inhibiting ribosome activity.[1, 4] Thus, through interacting with nucleic acids these tetracyclic molecules impose their biological interferences by forming hybrid nanostructures of tetracycline-nucleotide complexes.

As in the case of other antibiotics, misuse and overuse of tetracyclic antibiotics have also led to bacterial resistance, threatening human health and ecological balance. Discharged antibiotics pollute environment by interfering with the selection of bacterial community and shifting the competition between antibiotic-resistant and antibiotic-sensitive strains.[5] An effective way to reduce antibiotic resistance and pressure on the natural evolvement is to decrease their use, improve their efficiency and reduce their release into living environment.[6] Because of lack of new antibiotics into clinical use, many countries have adopted the pattern of the cyclical use of effective antibiotics and development of new treatments to combat multi-drug resistant pathogens.[7, 8] Rather than individual antibiotics, treatment by combining two or more drugs can be more efficient in fighting infections.[9-11] Combination therapy can not only improve the efficacy of known antibiotics, but also help repurpose other agents or biomaterials with different functions toward combating antimicrobial resistance.[12].

Natural antimicrobial peptides (AMPs) form an essential part of innate defense in multicellular species and have been explored as antimicrobial materials or potential drugs. Polymyxin and vancomycin are exemplar semi-synthetic AMPs that have been used alone or to supplement other antibiotics in clinical practice.[13-16] Although it has been thought that these AMPs are less likely to cause resistance and mutagenesis in the natural environment, resistant strains can be readily obtained in laboratory conditions under intensive selections.[17, 18] Drug resistance, including TC and Polymyxin resistance, presents an ever-increasing global public health threat that involves all major microbial pathogens and antimicrobial drugs.[19-22]

Combinatory AMP-antibiotic mixtures have been reported to be effective in treating multiple drug-resistant pathogens, where active components work coherently to synergize therapeutic outcome.[23, 24] These combined therapies appear as a promising approach due to the different modes of action of AMPs compared to commonly used antibiotics. In this regard, it is hypothesized that the permeabilization or physical disruption of the bacterial membrane by a compound allows the antibiotic to enter the bacteria more easily and achieve a higher accumulated concentration. The development of such new synergistic therapies requires further biophysical understanding of the interactions between antibiotic-peptide and bacterial membrane. A previous study by Ulvatne *et al.*[25] has revealed that lipopeptides with chain lengths shorter than the required minimum cannot synergize well with antibiotics against Gram-negative *E. coli* and that their combined effects would also become weak against Gram-positive *S. aureus*. The synergy between AMP and antibiotic is highly dependent on how AMPs interact with the bacterial membrane. For example, enhanced membrane permeability and formation of semi-transient membrane nanopores, or AMP acting as an antibiotic carrier, can lead to vastly different outcome. Meanwhile, increased permeability and disruption of the membranes by AMPs alone may not lead to synergic effects with antibiotic against Gram-negative bacteria.[26] The proton motive force (PMF) across membrane may affect the uptake of antibiotics, as Taber and Yamaguchi *et al*. reported that the uptake of kanamycin and tetracycline is specifically driven by transmembrane potential ($\Delta\psi$) and transmembrane pH gradient (ΔpH), respectively.[27, 28] AMP binding can dissipate $\Delta\psi$ and ΔpH and alter antibiotic uptake.

Similar studies involving Polymyxin E (Colistin) combined with antibiotics containing rich aromatic rings or hydrophobic tails such as teicoplanins, vancomycin and trimethoprim have also shown potential treatment modalities against multidrug-resistant bacteria.[29-32] These synergetic effects can largely be attributed to Colistin's interaction with LPS at the surface of the outer membrane, but there is again a lack of understanding of how the interactive processes lead to increased membrane permeability to hydrophobic antibiotic molecules in killing multidrug-resistant bacteria.[33-35]

While the membrane action of AMP is clear, the interaction between AMP and antibiotic in the role of synergy is largely unknown. Understanding how the membrane-lytic AMP collaborates with bacteriostatic antibiotics is the key to the synergistic action of the drug pair. The conjugates formed by linking the two drug molecules via a chemical bond may become more effective, but it can be difficult to ascertain the gain.[35] Recent studies have revealed several unexpected phenomena, indicating that our insights into how cells and organisms respond to drug combinations are still rudimentary.[5, 36-40] Ghaffar *et al.*[41] conjugated the antibiotic levofloxacin with the hydrophobic AMP indolicidin. Although the antimicrobial activity of the drug conjugate was still present, it was not improved compared to the substances alone. In comparison, the binary mixture of levofloxacin and indolicidin showed slightly improved antibacterial activity in comparison to levofloxacin and indolicidin alone, demonstrating that the covalent linkage diminished their activity.

This work aims to explore how to combine tetracycline or minocycline (TC, MC) with a broad-spectrum antimicrobial lipopeptide (denoted as C_8GIK and C_8GIR) that has been designed to improve antimicrobial efficacy and dynamic killing efficiency against Gram-positive, Gram-negative and resistant bacteria. Experimental measurements from binary antibiotic-lipopeptide combinations were presented in the form of fractional inhibition concentration index (FICI). The results revealed synergetic effects against all bacterial strains studied including 3 AMR strains. The antimicrobial actions from the binary mixtures are featured by the fast time-killing and high TC/MC uptake, benefited from the fast membrane-lytic disruptions of lipopeptides. This study thus provides an important mechanistic understanding of the combined antibiotic-lipopeptide approach to improve the therapeutic potential of conventional antibiotics by illustrating how amphiphilic lipopeptide-antibiotic combinations interact with biological membranes, providing a promising alternative to combat AMR.

2. Experiment methods

2.1 Circular dichroism

Circular dichroism (CD) spectra were measured using a Chirascan Series Spectrometer. Each sample was scanned at least three times to obtain a high signal-to-noise ratio. Quartz cell of 0.1 mm path length was used in the experiments. The CD spectra were scanned from 190 to 260 nm, with intervals of 1.0 nm and a 0.5 s response time (scan rate 60 nm/min). The AMP stock solutions were either diluted in Tris-HCl buffer (20 mM Tris, 150 mM NaCl, pH 7.2) or mixed with sodium dodecyl sulfate (SDS) solutions. The final concentrations of antimicrobials and SDS were fixed at 1 mM and 25 mM, respectively. All the CD measurements were carried out at 20 ± 1 °C. The CD signals were calculated in units of mean residual molar ellipticity from millidegrees.

2.2 Surface physical activities of lipopeptides and their binding behaviour on the air/liquid lipid monolayer

Surface physical activity of a lipopeptide is reflected by its ability to adsorb at the air/water interface, measured by surface tension change (mN/m^{-1}) using a Du Noüy ring method (Krüss K11 tensiometer). Typically, a maximum of 1 h was required for the surface tension to equilibrate and an equilibrium value was taken when the change within 5 min was no more than 0.3 $mN\cdot m^{-1}$.[42] Lipid monolayer was created at the air/water interface using a Langmuir trough (Nima Technology) as previously employed by Ciumac and Gong *et al*. [42, 43] and further described in Section 4 of **Supporting Information**, with the equilibrium pressure kept at 28 mN/m. The dynamic surface pressure was monitored for up to 2 h after each lipopeptide/antibiotic injection. All experiments were carried out at the room temperature of 20-22 °C.

2.3 Fluorescence spectroscopy, SUV leakage and Raman spectroscopy

The fluorescence spectra indicated the C_8GIK-MC interaction in the form of C_8GIK-Mg^{2+}-MC complexes, which decreased the fluorescence excitation and emission efficiency of MC. All the fluorescence experiments were measured by a microplate reader (Varioskan LUX). The excitation wavelength and emission spectra range were adjusted according to different fluorescence probes.

Lipid powder was dissolved in chloroform and underwent evaporation overnight to form a lipid film. Dry phospholipid film mixtures were dissolved in 40 mM calcein fluorescence solutions in Tris-HCl buffer (pH 7.4) at 5 mg/mL, followed by an extrusion method to produce calcein-loaded SUVs. A Sephadex G-50 gel at 60 g/L was prepared by dissolving G-50 powder in Tris-HCl buffer and placed into a chromatography column overnight. External fluorescence molecules not encapsulated by the SUVs was removed by passing the extruded SUV products through the G-50 gel column. The calcein-loaded SUVs moved faster in the gel after passing through the G-50 column where they can be collected. To take into account the different charge features of membrane surfaces, we used POPC/POPG (7/3, mol/mol), POPC/LPS (9/1, mol/mol) and POPG/PVCL2 (6/4, mol/mol) to mimic the inner/outer membrane of Gram-negative bacteria and cytoplasmic membrane of Gram-positive bacteria.

Membrane disruption was assessed by calculating the fractional leakage of calcein entrapped inside the SUVs. The calcein leakage was quantitatively determined by the increase in fluorescence emission in an aqueous environment, while the fluorescent signal resulting from the calcein entrapped inside SUVs at high concentrations was weak.[44] Antimicrobial solutions were prepared by a serial twofold dilution method.

Aliquots of 100 μL calcein-loaded SUVs at a concentration of ~ 0.1 mg/mL were mixed with 100 μL peptide solutions. Mixtures of SUV and peptide interacted for 30 min before measurements. The excitation wavelength was set to be 490 nm, and the emission spectra were scanned from 510 to 530 nm, with the emission at 518 nm being recorded as representative of the leakage intensity of the calcein. The total leakage for each sample was measured after the addition of 100 μL 0.2% (w/w) Triton X-100. All fluorescence measurements were carried out at 20 ± 1 °C. The leakage fraction (%) for each sample was calculated using the following equation:

$$Leakage\,fraction\ (\%) = \frac{(I_p - I_0)}{(I_t - I_0)} \times 100 \qquad (1)$$

where I_0 and I_t represent negative and positive controls, respectively, which indicate the initial zero fluorescence leakage before AMP addition and the 100% fluorescence after 0.2% (w/w) Triton X-100 addition. I_p is the fluorescence after peptide addition, L_{50} was determined as the peptide concentration at which 50% SUV leakage occurred. Dynamic fluorescence leakage under same conditions was measured at a fixed peptide concentration (when 100% leakage fraction) with time changing.

Raman spectra were recorded using HORIBA micro-Raman spectrometer equipped with a full optical microscope. Samples were focused through a 100× lens and irradiated by 532 nm laser (2.33 eV). Data were collected using 1200 lines/mm grating with a spectra resolution of 2.71 cm^{-1}. Laser power was kept between 1 mW to 8 mW, and integration time was 60 s. Spectra were collected and analyzed in LabSpec 6 software.

2.4 2D NMR NOESY

NMR spectra were recorded on a Bruker Avance III B400 spectrometer (5 mm BBO probe) operating at 400 MHz for ^1H NMR at 20 ℃. 2D NMR NOESY spectroscopy was used to locate the antibiotic molecules in the self-assembly of lipopeptides according to their intermolecular interactions.[45, 46]

2.5 Atomic force microscopy (AFM) and small angle neutron scattering (SANS)

10 µL of 2-day aged lipopeptide solution at 20 mM was diluted to 2 mM and deposited onto a freshly cleaved mica plate, followed by gentle water cleaning and N_2 drying. AFM measurements were performed using a Bruker multimode AFM and analyzed using the Nasoscope software as previously described.[47, 48] SANS experiments were performed on the SANS2D instrument at the ISIS Pulsed Neutron Source (STFC Rutherford Appleton Laboratory, Didcot, UK). The samples of lipopeptide mixed with antibiotic in the presence of Tris-HCl D_2O buffer were filled in 2 mm path-length quartz cells (Hellma GmbH, Type 120) and measured at 20 °C. To further explore the different binding modes with membrane between lipopeptides and antibiotics, the SANS experiments of lipopeptide/antibiotic interacting with Lyso-PG micelles were designed. The raw SANS data were reduced using the Mantid framework and corrected following the standard procedures for the instrument.[49] Least-squares fitting analysis to a core-shell ellipsoid model using the SasView software version 5.0 (www.sasview.org) was used to interpret the reduced data.

2.6 Antibacterial assays

The minimal inhibitory concentration (MIC) of an antibiotic, a peptide or their binary mixture against bacteria is defined as the lowest concentration at which visible bacterial growth is inhibited.[50] Briefly, 100 µL of suspended bacteria (2×10^6 CFU/mL in the TSB medium) was mixed with 100 µL of antibiotic or peptide solution with different concentrations in a sterile 96-well plate. After incubation for 24 h at 37 °C, the optical density at 600 nm (OD_{600}) of the plate was recorded using the Varioskan LUX microplate reader (Thermo Scientific, USA). The wells with bacteria but in the absence of antibiotic or peptide and without bacteria served as the positive control and negative control, respectively. The survival ratio was defined as following:

$$Survival\,percentage\ (\%) = \frac{(OD_{600,sample} - OD_{600,negative})}{(OD_{600,positive} - OD_{600,negative})} \times 100 \qquad (2)$$

Each data point presented was the average of at least three independent experiments.

To determine synergistic or antagonistic interaction of an antimicrobial agent, a fractional inhibition concentration index (FICI)[51] was calculated for each isoeffective combination in the microtiter plate with the following formula:

$$FICI = \frac{\text{MIC of drug A in combination}}{\text{MIC of drug A alone}} + \frac{\text{MIC of drug B in combination}}{\text{MIC of drug B alone}} \tag{3}$$

Of all isoeffective combinations, the combination with the lowest FICI value was considered to be optimal (FICI opt.). An FICI opt value ≤ 0.5 indicates synergy, 0.5 - 4 indicates additive or no interaction, and > 4 indicates antagonism. The study protocol consisted of two independent experiments for all combinations of lipopeptide and antibiotic tested. A combination was considered synergistic or antagonistic if the two independent experimental results fell into the same category (synergy or antagonism); otherwise, the combination was considered non-interacting.

2.7 Dynamic antimicrobial action, bacterial live/dead staining

The time-dependent killing of lipopeptides and antibiotics was also tested to evaluate their antimicrobial potency. Briefly speaking, bacteria were exposed to a given lipopeptide or antibiotic at a fixed concentration over different times. Following the protocol employed previously,[52] the bacterial suspension undergoing an overnight culture was diluted to 1.25×10^6 CFU/mL in a PBS buffer and then mixed with antibiotic/lipopeptide to reach a fixed concentration. Aliquots of the mixtures were diluted and transferred to Muller Hinton agar (MHA) media after specific time points of exposure and counted after overnight growth at 37.5 °C.

For fluorescent microscopic imaging, bacterial cells at log-phase were washed with Tris-HCl buffer (20 mM Tris + 150 mM NaCl + 20 mM glucose, pH 7.4) and diluted to $\sim 10^8$ CFU/mL. Then, bacteria of $\sim 10^8$ CFU/mL were treated without and with lipopeptide for 3 h. The suspensions were stained with 2 μM SYTO 9 and 1 μM PI for 30 min in the dark, ready for observing under fluorescence microscopy.

2.8 NPN uptake, membrane depolarization and TC uptake

The same method was used to collect and wash log-phase *E. coli* for measurements of both outer membrane permeability and inner membrane depolarization induced by lipopeptides. The cell suspension was incubated with 15 μM N-phenyl-1-naphthylamine (NPN) for NPN uptake by bacterial cells, and 2 μM 3,3′-Dipropylthiadicarbocyanine iodide (DiSC$_3$(5)) for about 15 min and 1 h, separately, in 37 °C dark environment. To make sure fluorescence intensity was steadily checked with plate reader (NPN: λ_{ex}= 350 nm, λ_{em}= 420 nm; DiSC$_3$(5): λ_{ex}= 622 nm, λ_{em}= 670 nm), fluorescence intensity was recorded continuously when lipopeptide was added into 96-well plate.

TC uptake was evaluated by monitoring its fluorescence increase when it entered the cell.[53] Cultures of *E. coli* 25922 in MHB were grown to OD_{600} = 0.6. Cells were washed with HEPES buffer (10 mM, pH 7.4) and collected at 3800 rpm for 5 min. Cell suspension with $OD_{600} \approx 0.1$ was mixed with 100 μM TC and 5 μM lipopeptides, and fluorescence intensity was continuously recorded with excitation wavelength of 405 nm and emission wavelength of 535 nm.

2.9 Hemolytic activity and MTT assays

Lipopeptides, antibiotics or their mixtures were dissolved in 10 mM PBS buffer at pH 7.4, and the antimicrobial solutions were serially diluted in 10 mM PBS buffer at the same pH. Human red blood cells (hRBC) were washed three times and diluted in PBS buffer. Then, 100 μL of hRBC suspension (~2%, v/v) was incubated with 100 μL of drug solution at 37 °C for 1 h. After incubation, the mixtures were centrifuged at 1000g for 10 min, and the supernatant (50 μL) was transferred to a new 96-well plate. The released hemoglobin was recorded by the absorbance of the supernatants at 576 nm with a previously used Varioskan LUX microplate reader. The percentage of haemolysis was obtained using the following formula [54]:

$$Haemolysis\ (\%) = \frac{(OD_{576nm}\ of\ treated\ sample - OD_{576nm}\ of\ negative\ control)}{(OD_{576nm}\ of\ positive\ sample - OD_{576nm}\ of\ negative\ control)} \quad (4)$$

where the positive control was hRBCs treated with 0.1% Triton X-100, and the negative control was an untreated hRBC suspension.

The *in vitro* toxicities of lipopeptides, antibiotics and their mixtures toward HDFa and

3T3 cells (Human Dermal Fibroblast, adult, ATCC PCS-201-012; Embryo Fibroblast, Mus musculus, ATCC CRL-1658) were measured by the 3-(4,5-Dimethylthiazol-2-yl)-2,5-diphenyltetrazolium bromide (MTT) assay. Briefly, MTT solution (10 μL, 5 mg/mL) was added to each well of 96-well plate after the co-incubation of cells (at a concentration of 1×10^5 cell/ml) and drugs for 24 h. Then, the samples were cultured for another 4 h. The supernatant was discarded, and 150 μL dimethyl sulfoxide (DMSO) was added to dissolve the formazane crystals. The optical density was read at 570 nm on a microplate reader. Wells without cells were used as blanks and wells without peptide were taken as negative controls.

2.10 Neutron reflection (NR)

NR measurements were undertaken to determine how antimicrobials interacted with lipid monolayer spread on surface of water. NR experiment was carried out on the SURF reflectometer at the ISIS Pulsed Neutron Source (STFC Rutherford Appleton Laboratory, Didcot, UK) using the same setups as previously described.[47, 52] Each NR profile was achieved by scanning the air/liquid interface at three incident angles of 0.35°, 0.65°, and 1.5°, which covered the Q-range of about 0.01-0.5 $Å^{-1}$. In this work, acyl chain deuterated DPPG (d_{62}-DPPG, denoted as dDPPG) was spread on the D_2O surface, followed by injection of hydrogenated antimicrobial (MC or C_8GIK). This approach facilitated the observation of low SLD peptide binding onto deuterated lipid monolayer under D_2O. NR model fitting was performed by a Motofit package.[55] Changes in scattering length density (SLD, ρ) and volume fractions (φ_i) of interfacial components perpendicular to the scanned air/liquid interface were described by a two-layer or a three-layer model with their respective thickness denoted as τ_i. The total volume fractions of different components in a given layer is equal to 1; *i.e.* $\sum_n \rho_n = 1$. The fitted volume fractions and theoretical SLDs of these interfacial components must follow: $\sum_n \rho_n \varphi_n = \rho_{fit}$. Physical constants such as SLDs and volumes for molecules involved can be found in **Table S1**.

2.11 Atomistic molecular dynamics (MD) simulations

In order to visualize the interactions between antibiotic/lipopeptide and bacterial membrane, MD studies of binding of single molecule on the model membrane was carried out via GROMACS 2018 with Charmm36 force field. The time step used was 2 *fs* and the neighbour list was updated every 10 steps. Lipopeptide *3D* structure model was set up by *Avogadro* software firstly, to generate peptide's topology via CGenFF online tool.[56, 57] Initially, POPC/POPG (7/3, mol/mol) and POPG/PVCL2 (6/4, mol/mol) bilayers containing 200 lipids were built using CHARMM-GUI[58, 59] at 310 K and 1 *atm*. Single lipopeptide or antibiotic was placed 1.5 nm above the outer leaflet of the lipid bilayer. After hundreds of nanosecond production MD, the trajectory of the last 5 ns was used in data analysis. Visualization of all MD trajectories and simulation results were realized *via* the visual molecular dynamics (*VMD*) program.[60]

3. Results and discussions

Like many other antibiotics, tetracyclic antibiotics such as TC and MC function by targeting the metabolic process to impose growth inhibition. This mode of action may turn out to be disadvantageous, *e.g.*, for microbes such as *Propionibacterium acnes* (*P. acne*) that undergo inherently slow metabolism under anaerobic environment (hours or longer) [61], and the slow inhibitory process can lead to resistance. In contrast, it typically takes minutes for a lipopeptide to cause structural disruptions to bacterial membrane and deactivate the bacteria, thereby reducing the risk of resistance development. These two different working mechanisms can be combined when tetracyclic drug and lipopeptide are used together. The following work has been undertaken to illustrate the antimicrobial performance of tetracyclic drugs and lipopeptides individually, followed by demonstrating their synergistic effects when used in binary mixtures, against both susceptible and resistant bacteria.

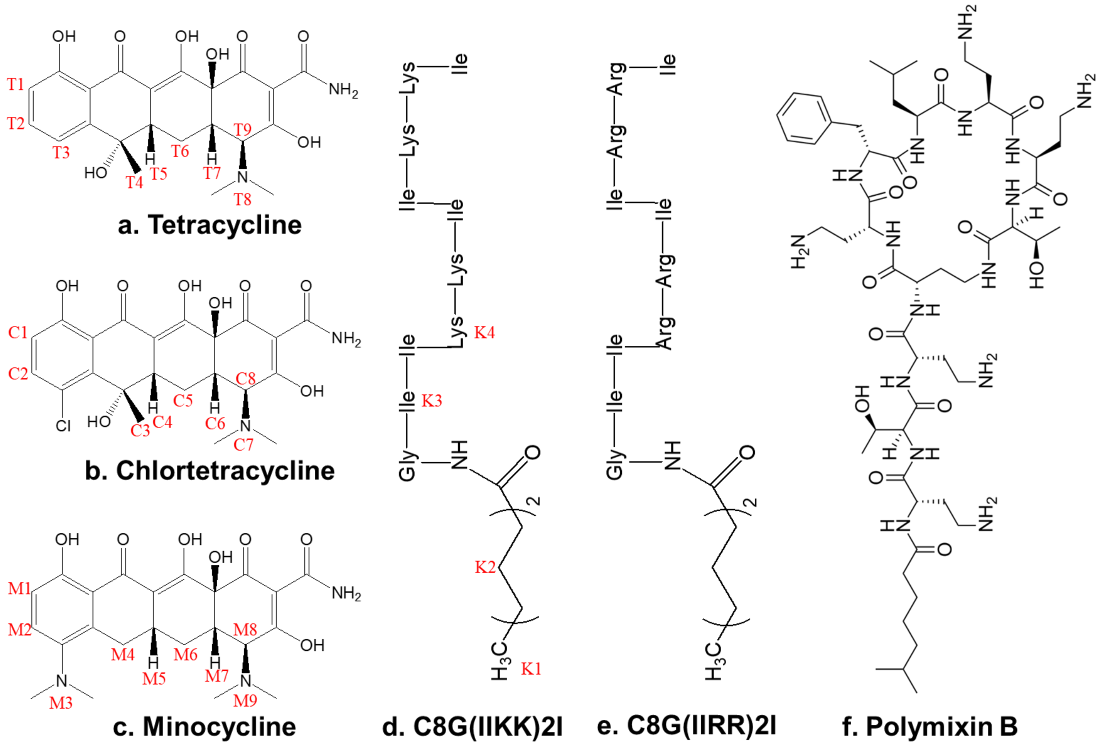

a. Tetracycline

b. Chlortetracycline

c. Minocycline

d. C8G(IIKK)2I

e. C8G(IIRR)2I

f. Polymixin B

Figure 1. Molecular structures of three antibiotics and 2 lipopeptides, (a-c) tetracycline (TC), chlortetracycline (CT), minocycline (MC), (e, f) lipopeptide $C_8G(IIKK)_2I$ (C_8GIK) and $C_8G(IIRR)_2I$ (C_8GIR) with specific hydrogens marked to aid the interpretation of the NMR spectra, and (f) lipopeptide antibiotic polymyxin B (PMB).

3.1 Antimicrobial activity

Molecular structures of three tetracyclic drugs (tetracycline, chlortetracycline (CT) and minocycline) together with three lipopeptides ($C_8G(IIKK)_2I$, $C_8G(IIRR)_2I$ and polymyxin B (PMB, control)) are shown in **Figure 1**. These two types of molecules have distinct structural characteristics. Their MICs against *Escherichia coli* (*E. coli*), extended spectrum *beta*-lactamase resistant ESBL-*E. coli*, tetracycline resistant TCR-*E. coli*, *Staphylococcus aureus* (*S. aureus*), methicillin-resistant *S. aureus (MRSA)* and anaerobic Gram-positive *Propionibacterium acnes* (*P. acne*) are given in **Table S3**. Most MICs obtained against the bacteria studied are within 2-15 µM. However, MICs from MC are consistently low and their MICs against *S. aureus*, *MRSA* and *P. acne* are below 2 µM. Some high MICs are observed, showing strain dependence on specific antibiotic or lipopeptide. The high MICs against *S. aureus* and resistant *MRSA* from

PMB are consistent with its selective potency against Gram-negative bacteria. Furthermore, TC and CT display high MICs against TCR-*E. coli*, as expected. Apart from these exceptions, MC and the two newly designed lipopeptides are highly effective against all bacteria studied, showing that just like MC, the two designed lipopeptides not only display broad spectrum efficacies against both Gram-positive and Gram-negative bacteria but also resistant strains.

3.2 Synergism of binary lipopeptide-antibiotic mixtures

MICs of binary mixtures of tetracyclic drug-lipopeptide with a molar ratio of 1/1 against different bacterial strains are shown in **Table S4**, covering the same bacterial strains as studied from individual antibiotics and lipopeptides. An important observation is the significant reduction of MICs for TCR-*E. coli* when binary TC-lipopeptide and CT-lipopeptide mixtures were used, showing a clear benefit from the lipopeptide.

Furthermore, the binary mixtures also alter some of the other MICs, with all the values now below 12.5 μM. In most cases, MICs from the binary mixtures are reduced compared to the use of individual antimicrobials, with values around 1 μM. These observations show that all binary combinations are effective against both Gram-negative and Gram-positive bacteria including the resistant strains.

To quantify the interaction of lipopeptide and antibiotic in a binary mixture, we have used **equation 3** to calculate the FICI values, with the results shown in heat maps for different binary pairs shown in **Figure 2**, covering the combinations of TC-C_8GIK, CT-C_8GIK, MC-C_8GIK, TC-C_8GIR, CT-C_8GIR and MC-C_8GIR against TCR-*E. coli* (**Figure 2A**), and the same combinations against *P. acne* (**Figure 2B**). All binary combinations are synergistic against TCR-*E. coli*, with FICI combination indices below 0.5. The same binary mixtures show similar efficacies against normal *E. coli* with most FICI values also below 0.5, but some of the values fall between 0.5 and 1 against ESBL-*E. coli*, indicating that the combined effects of the antibiotic-lipopeptide mixtures are largely of additive effect, with similar feature displayed from the binary tetracyclic-PMB mixtures. (**Figure S1**). However, the binary mixtures of MC-C_8GIK and MC-

C_8GIR achieve smaller FICI values, showing best antimicrobial efficacies. Similar changes were observed against Gram-positive *P. acne*, supporting the high efficacies covering the broad-spectrum activity of the tetracyclic compound-lipopeptide mixtures.

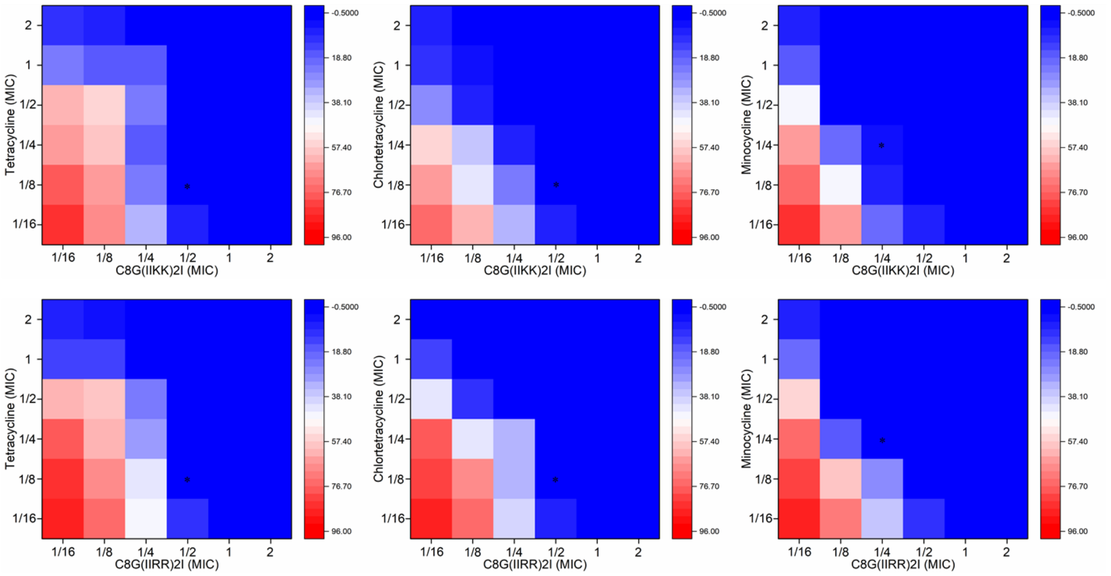
A. *TetR-E. coli*

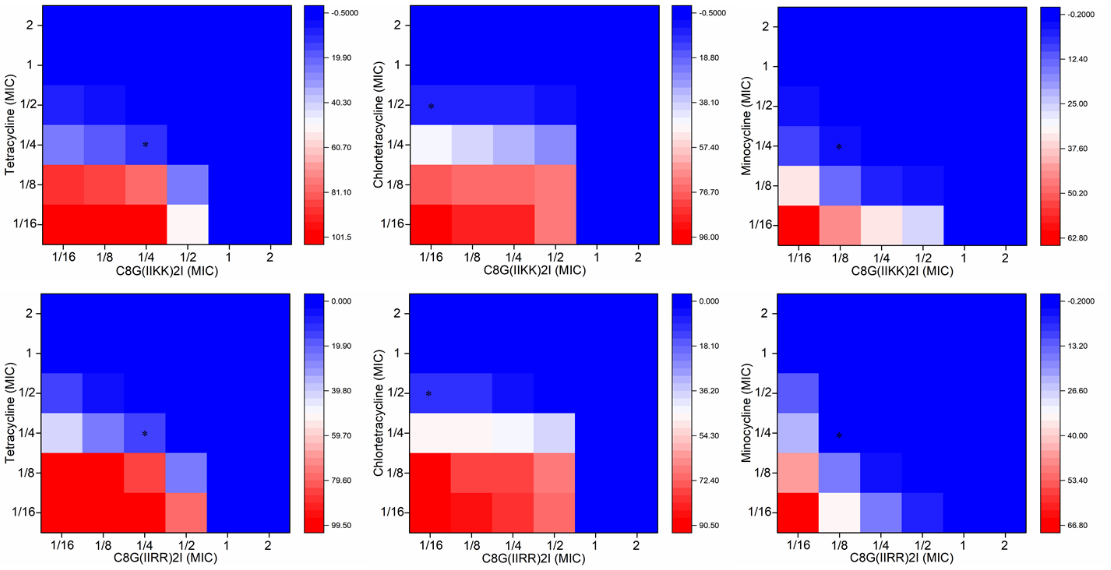
B. *P. acne 6919*

Figure 2. Heat maps show the antimicrobial activity of drug combination C_8GIK/C_8GIR-TC/CT/MC against (A) Gram-negative TCR-*E. coli* and (B) Gram-positive *P. acne* ATCC 6919. Synergy was evident as the FICI values are mostly below 0.5 from all binary mixtures against both bacterial strains.

Synergistic or additive effects as observed from the binary tetracyclic compound-lipopeptide mixtures are synonymous to the increased efficacies at reduced doses, demonstrating the benefits from different molecular characteristics and functions. Further studies must be undertaken to understand how these molecules work together to transverse different membranes.

3.3 Biocompatibility and dynamic killing of binary mixtures

Compared to conventional antibiotics, lipopeptides often show relatively high cytotoxicity to mammalian host cells. The cytotoxicity of lipopeptides, antibiotics and binary lipopeptide-antibiotic mixtures were tested using haemolytic assays (**Figure S2A**, after 1 h exposure) and MTT cell assays (**Figure S2B&C**, after 24 h exposure). Lipopeptides, tetracyclic drugs and their binary mixtures show little haemolysis below 100 μM (<5%). Given that most MICs are below 5 μM, there is a wide safety window for applying these antimicrobials individually or as binary mixtures. At concentrations up to 1000 μM, TC and its analogues have lowest haemolytic activity (< 10%), while C_8GIK and C_8GIR had EC_{50} values (50% haemolysis) at 700 and 900 μM, respectively. This trend fits to the general impression that lipopeptides show stronger haemolysis against human red blood cell (hRBCs) than conventional tetracyclic drugs and PMB at high concentrations. When the lipopeptides are combined with these antibiotics as binary mixtures (under the molar ratio of 4:1 for lipopeptide to antibiotic with the total molar concentrations kept the same as individual lipopeptides), the binary mixtures show substantially decreased haemolytic activities. Similar effect of concentration dependence is displayed from the viability of the mammalian cells against individual components (HDFa and 3T3 cells in **Figure S2B-D**) below 50 μM. At the two high concentrations of 62.5 and 125 μM, C_8GIR displays notably higher cytotoxicity. However, fluorescent staining images taken from HDFa cells exposed to individual (**Figure S2D**) and binary drug mixtures (**Figure S2E**, at 2× MIC) show that the cytocompatibility of the lipopeptide-antibiotic mixtures is visually better than the individual constituents under same concentrations.

Under *in vitro* antibacterial studies assessed for the effect of exposure time, lipopeptides exhibited faster antibacterial activities than the conventional tetracyclic drugs, as evident from data shown in **Figure S3** for tetracyclic drugs and in **Figure 3A-D** for lipopeptides alone or as binary mixtures (molar ratio of 1/1). C_8GIK and C_8GIR displayed much faster antimicrobial actions than PMB when exposed to *E. coli*, ESBL-*E. coli* and TCR-*E. coli* and Gram-positive *P. acne*. Over the first 2 h exposure, the three tetracyclic drugs show very little deactivations of *E. coli* and ESBL-*E. coli*. This trend of slow action is followed by PMB and PMB-MC mixture, showing a general lack of fast deactivation from the antibiotics. In contrast, fast deactivations of not only *E. coli* and ESBL-*E. coli* but also TCR-*E. coli* and Gram-positive *P. acne* are achieved by C_8GIK and C_8GIR, with C_8GIR imposing complete deactivation within 10 min and C_8GIK within 100 min, respectively. In all cases, binary mixing has not slowed down dynamic killing; in cases of application of C_8GIK-MC against ESBL-*E. coli* and C_8GIR-MC against TCR-*E. coli*, mixing sped up the dynamic killing processes.

Same trends were found against ESBL-*E. coli* and *MRSA* from another design antimicrobial peptide G_3.[52] It is perceived that fast deactivations of pathogenic bacteria may well benefit infection control in wound treatment where prolonged infection can cause further complications requiring surgical interventions such as debridement. Fast topical bacterial killing can also resolve infections from other opportunistic pathogens such as Gram-positive *P. acne* which is involved in acne vulgaris. When comparing the effects from tetracyclic compound, lipopeptide and their binary mixtures, the mixtures with MC show faster bactericidal action as well as lower MIC than the single components used alone. (**Figure 3D**)

Ejim and co-workers reported that synergistic effects in combinations of non-antibiotic-antibiotic with *in vitro* and *in vivo* activities exhibited against different bacterial pathogens, including multidrug-resistant isolates.[62] In their study, loperamide was assessed by outer-membrane permeability using an indicator NPN, which increased membrane permeability in *E. coli* and *P. aeruginosa*. Antimicrobial analysis of the loperamide-MC combination revealed that the addition of loperamide to various concentrations of MC reduced viable bacterial counts by 1-3 orders of magnitude. As tetracyclic drugs are known to preferentially inhibit the biosynthesis of envelope proteins, they concluded that loperamide acted by facilitating TC uptake, which then impaired protein synthesis.[62, 63] It has been widely thought that lipopeptides can quickly penetrate through the outer membrane and interact with the inner membrane of Gram-negative bacteria.[47, 64] Our lipopeptide-TC combination may well benefit from the same mechanism as the loperamide-TC mixture. The faster bacterial killing and lower antimicrobial MIC of the drug combination may arise from the easier internalization of the tetracyclic drug associated with the membrane disruptions caused by the lipopeptide.

Figure 3E shows the fluorescent images after staining of the bacterial cells with SYTO 9 and propidium iodide (PI) following incubation with different lipopeptides for 4 h. Strong green colour (live cells) was observed before treatment, but almost entirely red colour (dead cells) was shown after treatment with C_8GIK or C_8GIR. In contrast, there was still marked green fluorescence in *E. coli* treated with PMB. These observations further confirmed the faster bactericidal actions of C_8GIK and C_8GIR than PMB.

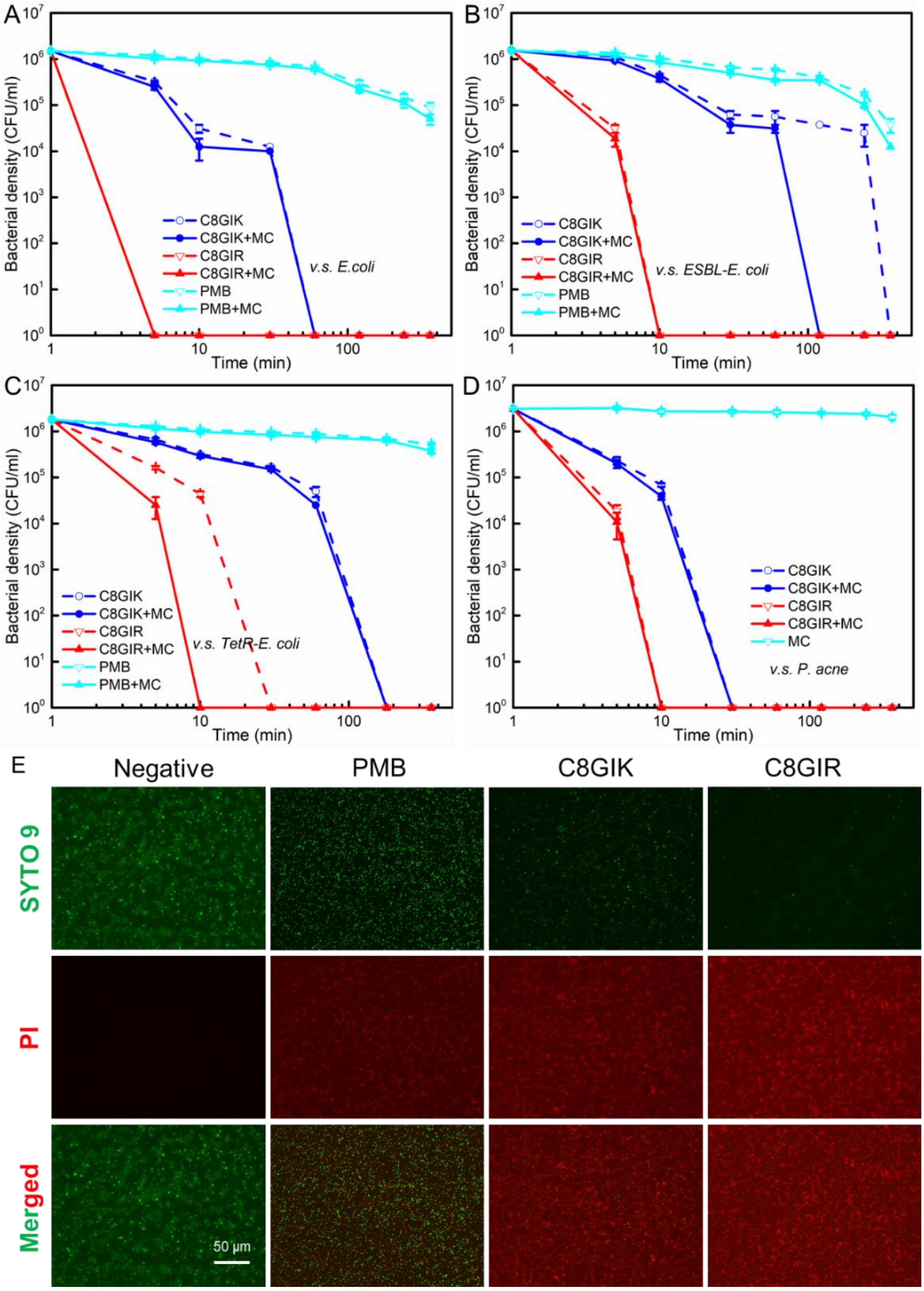

Figure 3. Dynamic killing actions of lipopeptides, antibiotics (2×MIC) and drug combinations (each at 2×MIC) against Gram-negative bacteria (A), *E. coli* 25922, (B) ESBL-*E. coli*, (C) TCR-*E. coli* and (D) Gram-positive *P. acne* ATCC 6919. (E) Fluorescent images of *E. coli* ATCC 25922 treated without and with different lipopeptides for 4 h after live/dead staining.

3.4 Bacterial membrane targeting and action mechanism of lipopeptide

The broad-spectrum antibacterial activities of our designed lipopeptides in contrast to the high potency of PMB against Gram-negative bacteria only inspire us to explore how their membrane-disrupting processes may differ, even though they share a common feature of membrane disruption.[47, 65-67] **Figure 4** shows bacterial membrane depolarizations from binding of the lipopeptides using NPN and $DiSC_3(5)$ as fluorescent indicators to outer and inner membrane models of Gram-negative bacteria, respectively, following the previously reported methods.[62, 68] **Figure 4A** show the two designed lipopeptides strongly interact with the outer membrane of *E. coli*, broadly consistent with the action of PMB. On the other hand, although PMB molecules can impose strong interaction with the outer membrane they cannot easily penetrate beyond the outer LPS bilayer. In contrast, lipopeptide C_8GIK can disrupt the outer membrane via insertion and intramembrane aggregation,[64, 69] leading to faster membrane depolorization and faster attainment to the equilibrium within 5 min. (**Figure 4A**) In the case of the inner membrane depolorization, C_8GIK and C_8GIR can again impose stronger and faster interaction whilst the impact from PMB is considerably weaker. (**Figure 4B**) Thus, C_8GIK and C_8GIR can impose intensive disruptions to both outer and inner membranes of Gram-negative bacteria, while PMB prefers to bind to the outer membrane and possibly becomes entrapped.

Against the weak interaction of PMB with the plasmatic membrane of *S. aureus*, C_8GIK and C_8GIR can again strongly depolorize the Gram-positive bacterial membrane. (**Figure 4C**) The different ability of membrane depolarization for the lipopeptides against *S. aureus* is consistent with their antimicrobial actions: PMB is selective against Gram-negative bacteria in terms of low MICs, while C_8GIK and C_8GIR show broad-spectrum efficacies against both Gram-positive and Gram-negative microbes. The weak ability of PMB to depolorize inner membranes may well contribute to its slow dynamic killing. Its abiity to transverse inner membranes may ultimately determine its MIC values.

In terms of chemical compound improving antibiotic uptake by bacterial cells, combination of membrane-targeting drug and antibiotic can enhance antimicrobial efficacy compared to individual ompounds. When synergized with TC, lipopeptides enhanced the uptake of TC by bacterial cells, the increase of TC fluorescence intensity in addition with lipopeptides supressed the control group at the initial stage, but the increasing tendency of TC uptake slow down in the former groups. (**Figure 4D**) Yamaguchi *et al*. suggested that the uptake of TC was specifically driven by ΔpH, consistent with the fact that the addition with lipopeptide only dissipated the membrane potential ($\Delta\psi$, reflecting on the increasing DiSC$_3$(5) fluorescence intensity in **Figure 4B**) but did not disrupt the transmembrane ΔpH (reflecting on the decreasing DiSC$_3$(5) fluorescence intensity).[28] PMB can improve TC uptake, but lipopeptides C$_8$GIK and C$_8$GIR deactivated bacterial cells in a relatively short time compared to PMB. Thus, C$_8$GIK and C$_8$GIR not only caused membrane damage and also dissipated the transmembrane potential of the proton motive force.

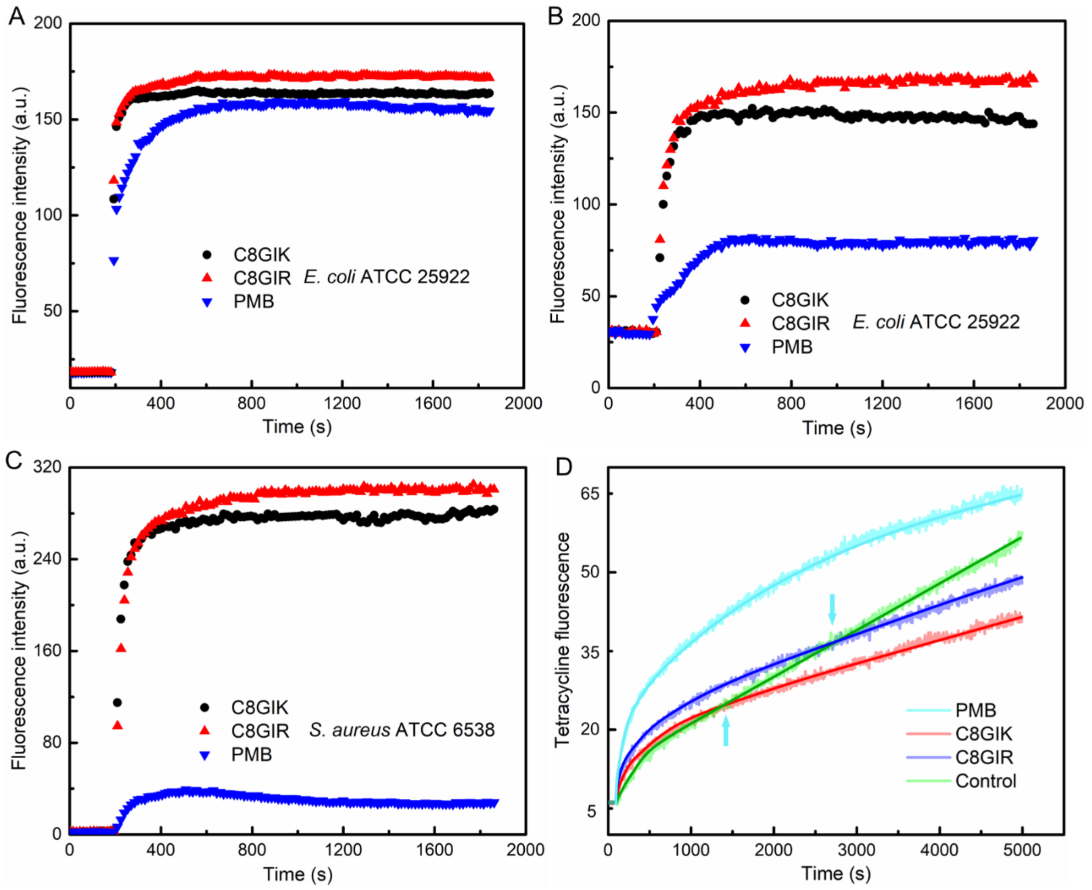

Figure 4. Antibacterial mechanism study of lipopeptides. Permeability change of outer membrane (A) and cytoplasmic membrane depolarization (B) by three lipopeptides at concentration of 100 µM against *E. coli* ATCC 25922 (outer and inner membranes) and (C) *S. aureus* ATCC 6538. (D) Lipopeptides enhance the uptake of TC in *E. coli*. Concentration of TC was 100 µM, and concentrations of lipopeptides were 5 µM.

To demonstrate possible differences in membrane permeation and leakage, flourenscent leakage of SUVs upon binding from the lipopeptides and MC was measured. Outer (POPC/LPS, 9/1, mol/mol) and inner (POPC/POPG, 7/3, mol/mol) membrane models of Gram-negative bacteria (**Figure 5A&B**) show little leakage when exposed to MC, but significant flourenscent leakage occurred upon binding of the two designed lipopeptides C_8GIK and C_8GIR above 10 µM. In contrast, PMB caused less time-dependent leakage upon binding to the outer mmbrane; very little leakage was observed upon its binding to the inner membrane either. Leakage from binding of the three lipoeptides to the POPG/PVCL2 SUVs mimicking the membrane of Gram-positive membrane also shows strong effects from the two designed lipopeptides and a relatively weak effect from PMB. (**Figure 5C**) These differences from binding of the liopeptides to SUVs are broadly consistent with the behaviour observed from their bactericidal actions to *E. coli* and *S. aureus*.

The amphiphilicity of the peptides is shown from their ability to reduce surface tension (**Figure S4A**). Up to 100 μM, the surface tension of PMB solution is almost constant at 70 mN/m, close to that of pure water. In contrast, C_8GIK and C_8GIR can bring the surface tension down to 40-50 mN/m, indicating far grreater surface physical activity. Upon binding to the DPPG monolayer kept at the constant surface pressure of 28 mN/m (**Figure S4B**), PMB binding can only lead to surface pressure rise by a few mN/m. In contrast, some 15 mN/m of pressure rise was observed from C_8GIK and C_8GIR binding, consistent with their better balanced amphiphilicity and greater surface activity. From neutron reflection, SANS and molecular dynamics simulations, Gong *et al*.[64] revealed the insertion of C_8GIK nanoaggregates into the middle of the outer membrane bilayer with its outer membrane leaflet comprised of LPS SUVs. Lack of amphiphilic balance implies weaker membrane binding ad structural disruptions from PMB. This is also well reflected in the transition of secondary structures where it can be seen from **Figure S5** that whilst PMB remained in non-ordered state, binding of C_8GIK and C_8GIR into the model bacterial membrane (micelles of sodium dodecyl suphate, SDS) promotes α-helix formation. These differences imply that PMB molecules may well become bound into outer bacterial membrane as monomers whilst membrane inserted nanoaggregates of the two designed lipopeptides are associated with membrane nanopores, causing different extent of membrane leakage.

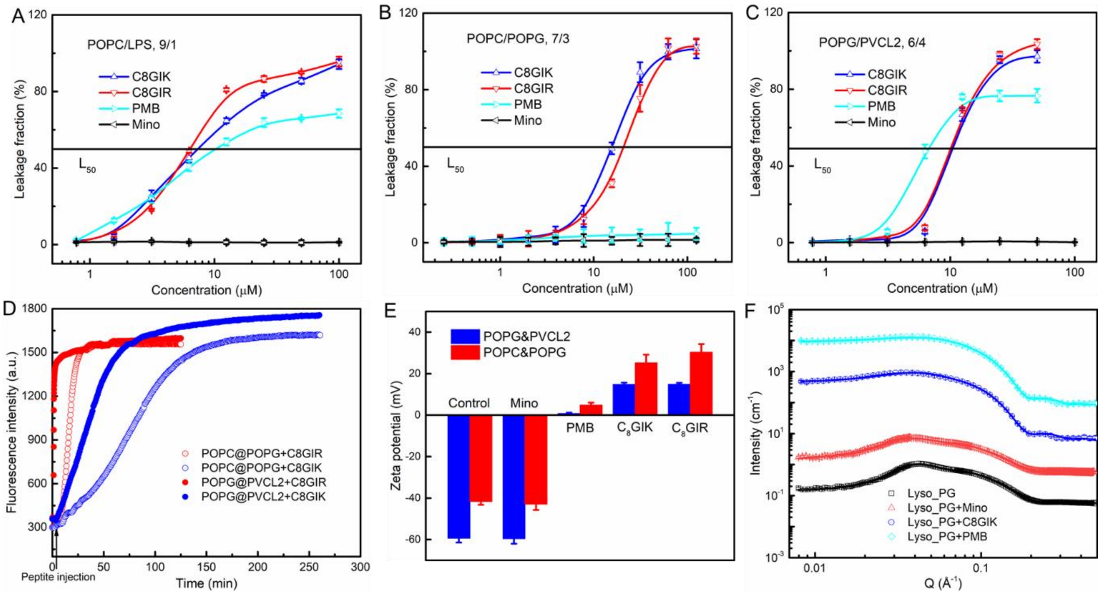

Figure 5. (A-C) Fluorescence leakage measured from binding of lipopeptides and MC to SUVs of POPC/LPS (9/1, mol/mol) and POPC/POPG (7/3, mol/mol) mimicking the outer and inner membranes of Gram-negative bacteria and POPG/PVCL2 (6/4, mol/mol) mimicking the membrane of Gram-positive bacteria. (D) Dynamic flourenscence leakage of POPC/POPG and POPG/PVCL2 with time changing, and (E) Their membrane potential affected by lipopeptides at a concentration of 50 μM. (F) SANS characterizations of lipopeptides interacting with lyso-PG micelles in D_2O PBS buffer (the molar ratio of antimicrobials to Lyso-PG is 1/10).

In the flourescent leakage of POPG/PVCL2 SUVs mimicking the membrane of Gram-positive membrane, C_8GIK and C_8GIR manifest better than PMB in both leakage efficacy and intensity. From the results of their dynamic leakage, C_8GIR is also more effective than C_8GIK (**Figure 5D**). Other than these, the changes of membrane potential affected by lipopeptide binding are also more profound. Because of their higher net charges and greater amphiphilic balance, C_8GIK/C_8GIR can change membrane potential greater than PMB after their membrane binding (**Figure 5E**).

To further explore how these antimicrobials interact with charged lipid membranes, Lyso-PG, a simpler version of charge lipids, was employed as a model to show the size change of the micelles before and after lipopeptide binding. (**Figure 5F**) Analysis to the SANS profiles revealed the spherical micelles formed by Lyso-PG based on the core-shell sphere model [46], with the inner core radius of 19 ± 1 Å and shell thickness of 6.0 ± 0.5 Å. Addition of MC had no impact on micelle size or charge state. However, exposure to the cationic lipopeptides led to the increase of the inner radius of the micelles to 22 ± 1 Å and the shell thickness of 8.0 ± 0.5 Å, with the total surface charges of the micelles being almost neutral. Furthermore, the polydispersity index (PDI) of the inner radius increased to 0.14, indicating a broder micellar size distribution after lipopeptide binding (**Table S5** in **SI**).

Raman spectra of lipopeptides interacting with SUVs of POPC/POPG and POPG/PVCL2 reveal that the binding of lipopeptides can affect the membrane packing order. (**Figure S7, Table S6**) The shoulder after the main peak ~ 1435 cm^{-1} becomes weaker in the POPC/POPG group while the shoulder still remains in the POPG/PVCL2 group. This region represents the CH_2 deformation, and the disappearance of the peak shoulder would mean the decreased acyl deformation of the lipid tails due to lipopeptide insertion. The POPC/POPG membrane integrity changed more significantly by lipopeptide binding and insertion. A more noticeable change from the two lipid models lies in the shift of the C-H stretching of region 2800-3000 cm^{-1} upon lipopeptide binding. Change in the ratio of the anti-symmetric C-H stretching (2883 cm^{-1}) to the symmetric C-H stretching (2847 cm^{-1}) in biomembrane is indicative of the lateral packing density of the acyl chains.[70] In both POPC/POPG and POPG/PVCL2 systems, the peak intensity around 2883 cm^{-1} decreased and broadened significantly with lipopeptide binding, indicating a decreased membrane orderness from the insertion of lipopeptide and the reduced CH_2 antisymmetric stretching.[70, 71]

Overall, the effectiveness of the three lipopeptides in causing the leakage of both outer and inner membranes of Gram-negative bacteria is supportive to their different bactericidal features and follows the order of C_8GIR > C_8GIK > PMB (**Figure 3**). The lack of leakage as shown in **Figures 5B&C** suggests that although PMB molecules can bind to the inner membrane they can’t cause effective structural damage and leakage. Membrane leakage and other related binding interactions also help explain why PMB is ineffective at deactivating Gram-positive bacteria.

3.5 Insight into the co-assembly between lipopeptide and MC

C_8GIK can self-assemble into nanofibers. AFM imaging revealed that the nanofibers have heights of 7.5 ± 1.5 nm and contour lengths beyond 5-10 μm. The SANS profiles of C_8GIK nanofibers with and without MC are broadly similar in shape but have some specific differences, indicating the subtle impact from MC binding. (**Figure 6A&B**) The best fits, using the elliptical cylinder model and shown as continuous lines, led to the minor radius of 6.5 ± 0.5 nm and the axial ratio of 1.8, with all best fit parameters given in **Table S7**. In the presence of MC, the C_8GIK nanofibers can be best fitted to the same model with similar structural parameters, except the radii of the nanofibers were 5.5 ± 0.5 nm. The corresponding SLD value of the fitted cylinders also decreased from 3.9 ± 0.2 to 2.5 ± 0.2. The reduced hydration degree suggested the increased organic content in the nanofibers as a result of mixing of MC because the SANS measurements involved all hydrogenous materials in D_2O.

The exact location of MC molecules in the C_8GIK nanofibers was studied by NOESY, with the NOESY spectra in the chemical shift range of 0-8 ppm being presented in **Figure S8A**. The NOESY spectra highlighting the interaction between C_8GIK and MC are presented in **Figure 6C**. The hydrogens present in MC were assigned as M1-M9; the hydrogens present in C_8GIK representing $-CH_2$ and $-CH_3$ (mainly located in lipopeptide tail and hydrophobic residue Ile) assigned as K1-K4 in SI Section 8. The chemical shifts of ~ 0.89 ppm and ~ 6.9 ppm correspond to the hydrogens of $-CH_3$ in Ile and M2 in MC. Their interactions were attributed to the head and tail parts of lipopeptide and benzene ring of MC, mainly driven by hydrophobic interactions among them.

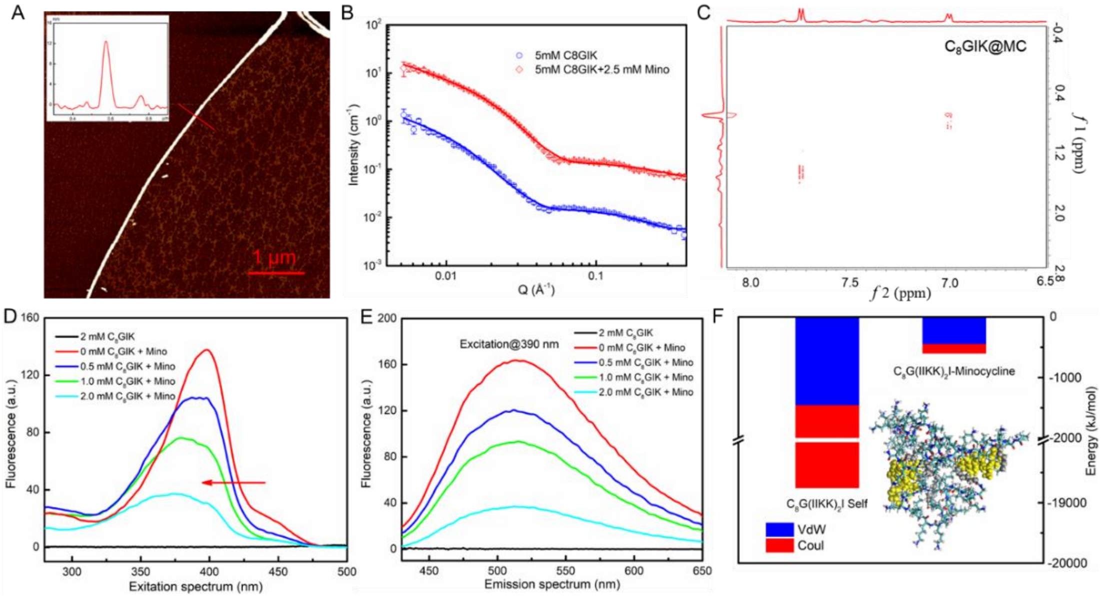

Figure 6. (A) AFM image of self-assembled C_8GIK nanofibers (with concentration of 6 mM in neutral buffer solution aged for 3 days). (B) SANS profiles of self-assembled lipopeptide (4 mM in neutral D_2O Tris buffer) without and with 1 mM MC. (C) NOESY spectra for 0.5 mM MC binding with 2 mM lipopeptide C_8GIK in D_2O. (D) Fluorescence excitation and (E) emission spectra for C_8GIK-Mg^{2+}-MC solutions, experiment conditions: different molar ratios of MC and C_8GIK were dissolved in 50 mM Mg^{2+} solution. (F) The intermolecular interaction energy of C_8GIK itself, and interaction energy between C_8GIK and MC, inset graph showed C_8GIK-MC binding conformation in the bulk solution via atomistic MD simulation of 300 ns; MC and C_8GIK molecules are shown in licorice style, MC is in yellow to distinguish from the lipopeptide, and hydrophobic lipopeptide tails are highlighted in grey beads.

The spectra shown in **Figure S8D&E** reveal that free MC solutions produce similarly enhanced fluorescence emission upon the addition of Mg^{2+}, indicating that fluorescence emission originated from the coordination of Mg^{2+} with MC. The fluorescence excitation and emission of MC-Mg^{2+} solutions were also strongly affected by the addition of C_8GIK. **Figure 6D** shows that as the concentration of C_8GIK increased from 0, 0.5, 1 to 2 mM, the excitation efficiency of the C_8GIK-Mg^{2+}-MC solution decreased significantly. A blue shift of the maximum-excitation wavelength ($\lambda_{exc.max}$) was also observed from $\lambda_{exc.max}$ ~ 400 nm for 0 mM C_8GIK to $\lambda_{exc.max}$ ~ 380 nm for 2 mM C_8GIK.

The emission spectra shown in **Figure 6E** also reveal a decreased fluorescence intensity of MC-Mg^{2+} solutions upon the addition of more C_8GIK. The fluorescence spectra indicated the C_8GIK-MC interaction in the form of C_8GIK-Mg^{2+}-MC complexes decreases the fluorescence excitation efficiency and fluorescence emission of MC.

To gain a more direct insight of structural features associated with the binding between amphiphilic C_8GIK and MC, atomistic MD simulations were carried out. From the snapshots of MD simulation for 300 ns, the MC molecules locate at both the hydrophobic tail region of the lipopeptide and hydrophobic residues of the lipopeptide head. Their binding energy arises from electrostatic and vdW (van der Waals) interactions where intermolecular vdW is the main contributor. (**Figure 6F)**

3.6 NR determination of binding of binary antimicrobial mixture onto DPPG monolayer

Each DPPG monolayer spread on the surface of water was confined at the initial surface pressure of 28 mN/m and its thickness and area per molecule were determined by NR. The DPPG monolayer was analysed using a two-layer model, a top tail layer in air and a head layer submerged in water.[47] The best fits led to the hydrophobic tail layer of 18±1 Å and the hydrophilic head layer of 10±1 Å. (**Figure S9**)

The binding behaviour of MC and C_8GIK at 10 μM on the DPPG monolayer was subsequently studied. Data analysis to the measured NR reflectivity profiles from three isotopic contrasts revealed weak perturbation of MC to the DPPG monolayer (**Figure 7A**), evident from SLD distributions in **Figure 7D**. MC binding led to slight disturbance to the monolayer, and can be treated as co-adsorption of MC at a volume fraction onto the lipid head layer (**Figure 7D**). In contrast, binding of C_8GIK significantly altered the structural feature of the DPPG monolayer, leading to 17% lipid dissolution and massive binding of lipopeptide. As shown in **Figure 7E**, a volume fraction of 0.10 of C_8GIK was co-adsorbed within the DPPG monolayer and an additional peptide layer with a volume fraction of 0.17 was adsorbed under the lipid head layer. When the concentration of MC or C_8GIK increased to 30 μM, the distribution and amount of binding of MC did not change much, compared to the data measured at 10 µM MC. (**Figures 7C, S9B**) However, the increased concentration of C_8GIK greatly enhanced its binding to the DPPG monolayer, with volume fractions of lipopeptide increased to 0.14 in the DPPG monolayer and 0.35 under the head layer. (**Figures 7C, S9C**) When MC and C_8GIK were combined together, the binary mixture preferred to aggregate across the entire DPPG monolayer, leading to the volume fraction of 0.10, 0.18, and 0.53 into the acyl chain, head, and under the head layer, respectively (**Figures 7C, F**). Given the strong tendency of self-assembly of the lipopeptide, it is most likely for the lipopeptide and MC to form in-membrane nanoaggregates, even though such co-assembly must also be mediated by their interactions with the lipid membrane.

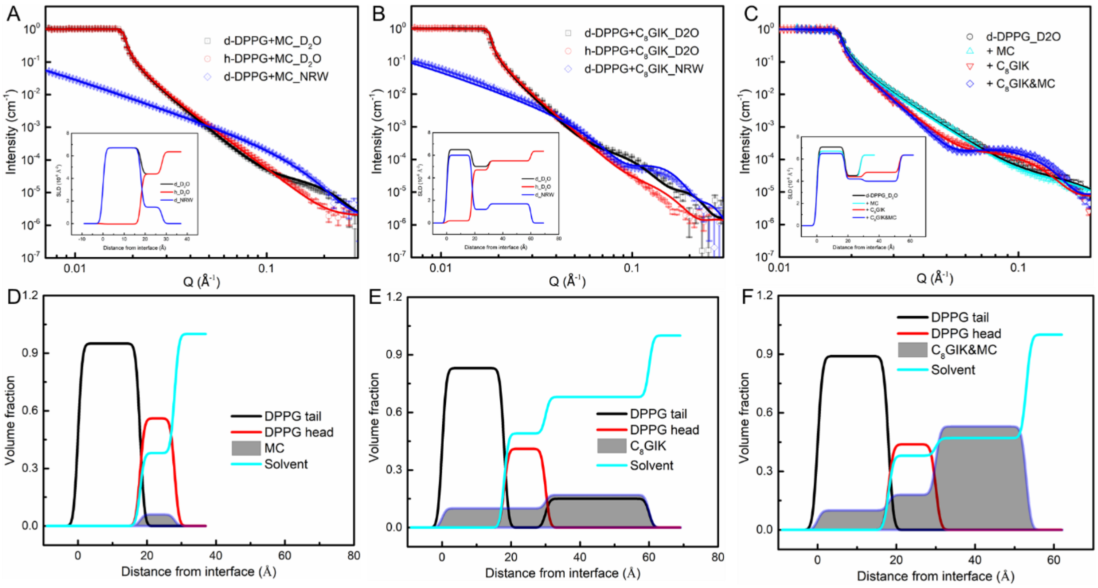

Figure 7. Neutron reflection data obtained from the DPPG monolayer before and after interaction with antimicrobials. (A, B) NR profiles (measured data and best fits) plotted as a function of momentum transfer (*Q*) measured after h-MC (10 µM) and h-C_8GIK (10 µM) binding to the DPPG monolayer under three different contrasts, (C) NR profiles measured before and after binding of h-MC (30 µM), h-C_8GIK (30 µM) and binary h-MC + h-C_8GIK (30 µM + 30 µM) mixture to the DPPG monolayer in D_2O subphase. The insets in (A-C) show the best fitted SLD profiles perpendicular to the interface (*z*-axis) under different isotopic contrasts and volume fraction distributions of the DPPG monolayer upon binding with antimicrobials in (D) MC (10 µM), (E) C_8GIK

(10 μM), and (F) MC (30 μM) + C_8GIK (30 μM). The volume fractions of DPPG without and with individual MC (30 μM) and C_8GIK (30 μM) corresponding to the NR profiles in (C) are shown in **Figure S9**. Volume fractions of antimicrobials are drawn in grey, lipid tails in black line, lipid heads in red line, and bulk solution in cyan. Detailed fitting parameters are listed in **Table S8**.

3.7 MD simulations of interactions between membrane and drug pair

Atomistic MD simulations of interactions between MC, C_8GIK and MC-C_8GIK pair with model bacterial membranes (POPC/POPG = 7/3 for Gram-negative inner membrane; POPG/PVCL2 = 6/4 for Gram-positive membrane) were undertaken. Both single antibiotic and lipopeptide can insert into the lipid bilayer within 300 ns. MC experienced a series of conformational changes when approaching the head region of the lipid membrane, and then became inserted into the hydrophobic core. The entire process was mainly driven by hydrophobic interaction between amphiphilic MC and hydrophobic lipid tail. (**Figure 8A**) Due to the strong electrostatic interaction between positively charged lipopeptide and negatively charged POPG, lipopeptide molecules approached the outer leaflet of the lipid membrane quickly. Along with the lipopeptide head embedded into the membrane, the hydrophobic tail was also drawn into it, via the concerted influence of both electrostatic and hydrophobic interactions over a period of 300 ns. (**Figure 8B**)

In contrast to the embedding of MC across the boundary between the tail region and head group region of the outer membrane leaflet, C_8GIK is distributed across the whole outer leaflet of the membrane. (**Figure 8A-B**) The more precise locations and distributions of these antimicrobials with respect to the POPC/POPG bilayer can be visualized from their mass density profiles (**Figure 8D-E**), where the peaks corresponding to the lipopeptide and MC partially overlap with the lipid phosphate distribution and even approach the hydrophobic core of the membrane, whilst the tail of the lipopeptide is ~10 Å closer to the center of the bilayer than its amino acid head group. Against simulations of PMB binding to the inner membrane of *E. coli* by

Berglund *et al.*[69], both lipopeptides were able to insert into the inner membrane, but the exact interactive processes and final membrane bound structures differ between them, broadly consistent to the different antimicrobial potency and efficiency in dynamic killing.

Individual MC and lipopeptide binding can alter membrane symmetry differently, with lipopeptide displaying a distinct feature of in-membrane conformational change. (**Figure 8D&E**) From the corresponding root mean square deviation (RMSD) analysis and the orientation changes in the process of C_8GIK insertion into the membrane, it was found that relatively flexible C_8GIK molecule shows more obvious conformation changes than MC with four conjugated rings. (**Figure 8G**) In the case of the MC-C_8GIK pair interacting with the POPC/POPG bilayer, MC binding with C_8GIK occurred in an early stage of the MD process (~ 50 ns) and they became inserted into lipid membrane together. At the final stage of simulation time, the MC-C_8GIK pair was embedded into the outer leaflet of the membrane. (**Figure 8C**) Compared with the individual MC and C_8GIK membrane systems, the density distribution of the MC-C_8GIK pair has the lowest ratio of overlapping area with the distribution of the lipid head layer. Upon binding from the antimicrobial drug pair, the membrane became more asymmetric than membranes upon binding from the antibiotic or lipopeptide alone. The asymmetry must be caused by the penetration of the antibiotic component into the acyl chain, with a substantial amount being also distributed across the head layer. (**Figure 8F**)

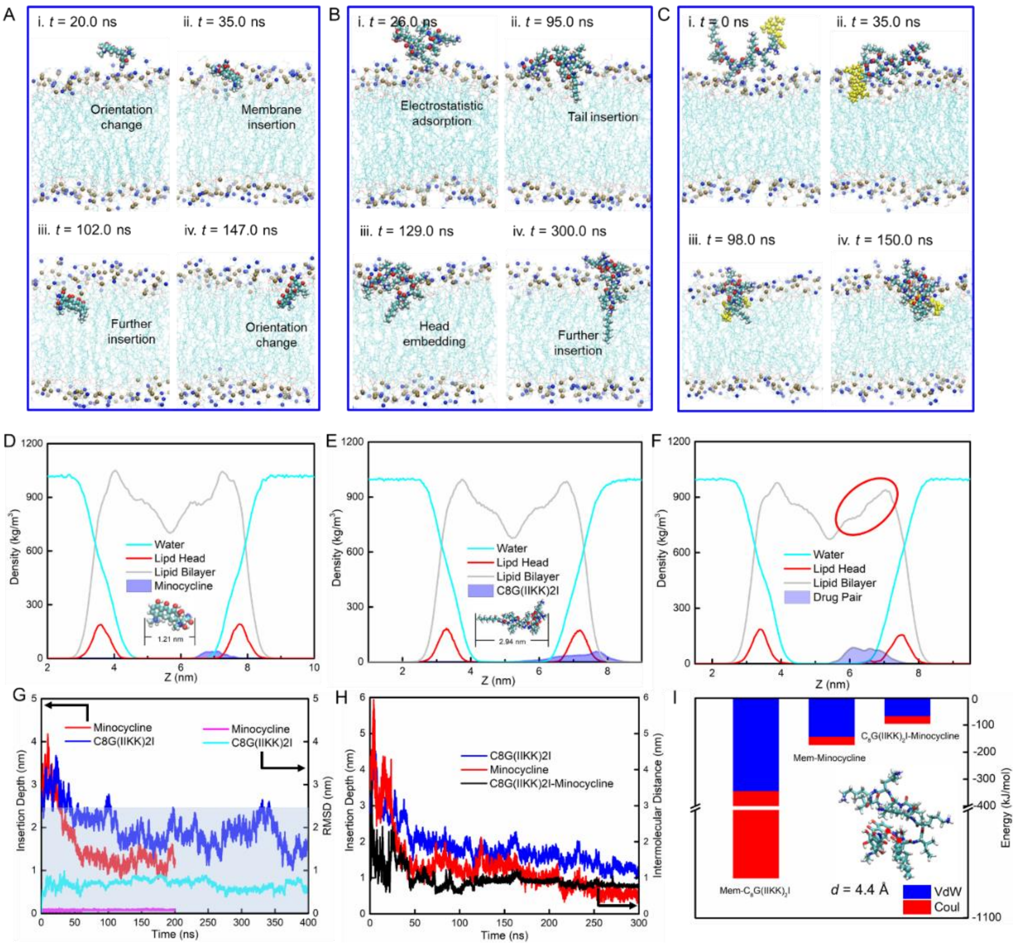

Figure 8. Atomistic molecular dynamics simulations of binding of MC, C_8GIK and their binary mixture to Gram-negative bacterial membrane (POPC/POPG = 7/3). (A-C) Snapshots of MC, C_8GIK and their drug pair inserting into lipid membrane with time, lipid molecules are shown in line style, heavy atoms (N and P) in the positively and negatively charged groups of the lipid bead are represented by blue and brown beads, while the antimicrobial molecules are shown in style of VDW (a visualization style). MC is coloured in yellow, all the solvent backgrounds are removed for a clear view. (D-F) Mass density profiles of main components in corresponding atomistic systems, solvent (light blue curve), lipid bilayer (grey curve), lipid head (red curve) and antimicrobial molecules (shadow). Time-dependent insertion of single MC (red line) and C_8GIK (blue line) into lipid bilayer (z axis distance between the mass center of lipid bilayer and antimicrobial), and their conformation changes (pink and light blue lines) in the lipid membrane characterized by root mean square deviation (RMSD) during the same time scale. (H) Insertion depth (z axis distance) of the paired MC (red

line) and C_8GIK (blue line) into lipid bilayer and their intermolecular distance (black line) change with time. (I) The interaction energy between antimicrobials and membrane, and interaction between lipopeptide and antibiotic. The inset graph shows the conformation of MC binding with C_8GIK when they were embedded in the lipid bilayer.

In terms of the molecular insertion depth into the membrane by MC and C_8GIK (the distance between the mass centre of the lipid membrane and antimicrobial molecules along the *z* axis), the antibiotic-lipopeptide pair had a more stable and quicker process of membrane insertion than the individual components. (**Figure 8G&H**) The nearly constant centroid distance between MC and C_8GIK (~ 10 Å after 50 ns MD run) reveals their relatively stable binding conformation. Their adjacent molecular groups are close within 4.4 Å. The fast insertion of C_8GIK in the binary mixture into the membrane was driven by the strong dispersion and hydrophobic interactions due to the opposite charges. We therefore calculated the interaction energy of the lipopeptide/antibiotic and the bilayer. (**Figure 8I**) Here, the interaction energy was defined as van der Waals (VdW) and electrostatic (Coul) interactions between lipopeptide/antibiotic and membrane, along with intermolecular interactions between the drug pair.

Based on totally different components between the inner membrane of Gram-negative bacteria and that of Gram-positive bacteria, and the different binding behaviour of both lipopeptide and MC, a simplified POPG/PVCL2 model mimicking the membrane of Gram-positive bacteria was set up following our previous work.[72] Different from the quick insertion of the lipopeptide's tail into the POPC/POPG membrane after binding onto the outer leaflet, the single lipopeptide did not show obvious tail insertion into the negatively charged POPG/PVCL2 bilayer but preferred to be wholly embedded into the membrane. (**Figure 8A**) In contrast, MC alone can hardly bind onto the POPG/PVCL2 membrane (**Figure S10**). The situation however changed when the MC-lipopeptide pair interacted with the POPG/PVCL2 bilayer, as the membrane defects or disorders caused by lipopeptide can facilitate MC insertion. This mode of action is different from the binding of the MC-lipopeptide pair with each other in the POPC/POPG bilayer where the stronger electrostatic interaction between lipopeptide and the POPG/PVCL2 bilayer may restrain lipopeptide's orientation change and subsequent membrane insertion.

From the simulation results of binding of multiple lipopeptides and antibiotics with the membrane, it can be observed that there is a clear layer-by-layer structuring of the lipopeptide-MC mixture. The MC molecules can easily approach the membrane along with the membrane binding from lipopeptide. The lipopeptide can penetrate through the head part of membrane, while the MC molecules intertwine and gradually become embedded with the lipopeptides. (**Figure S11C&F**) This situation would be consistent with our NR results, i.e., the mixture of lipopeptide with MC can affect the negatively charged DPPG monolayer greater than the individual lipopeptide. The thick lipopeptide-MC layer on the outer leaflet of the membrane further enhances the disorder and distortion of the whole membrane than the single components.

4. Conclusions

With more pathogenic bacteria becoming resistant, many of the most commonly used antibiotics are becoming less effective. Development of a lipopeptide for binary pairing with dual antimicrobial actions can open up an alternative to fight antibiotic resistance. This work reveals that the easy insertion of lipopeptide into bacterial membrane allows internalization of a tetracyclic antibiotic via the formation of antibiotic-lipopeptide pairing through hydrophobic interaction between TC/MC and lipopeptide whilst binding to the bacterial membrane. The lipopeptide works as bacterial membrane disruptor and antibiotic carrier. The antibiotic can then become dispersed into intracellular environment. Synergistic antibacterial activity is realized when the dual complexes of lipopeptide and TC/MC act on the bacterial membrane and intracellular environment. This work has demonstrated that combining the membrane penetrating and disrupting ability of lipopeptide with tetracyclic antibiotic is highly effective in combating both Gram-negative and Gram-negative bacteria including MDR and anaerobic pathogens. The combined experimental and MD simulation studies offer important mechanistic insights into structural basis underlying membrane-specific interactions, important for designing and fine-tuning lipopeptide to facilitate TC/MC across microbial membrane whilst being biocompatible to host cells. This work provides a strong basis for testing the synergistic antibiotic-lipopeptide combinations in animal models and a new approach for exploring new antibiotic-peptide pairs to improve the therapeutic potential of other conventional antibiotics aimed at different medical applications.

Associated Content

Supporting Information Available

The supporting information is available, including NR profiles and analysis, and MD simulation results containing changes of model lipid bilayers upon binding from different AMPs.

Author information

Corresponding Authors

***E-mail: j.lu@manchester.ac.uk (J.R.L.).**

***Tel: 0044 161 200 3926**

ORCID

Mingrui Liao: 0000-0002-9481-4026

Haoning Gong: 0000-0003-1590-2042

Xuzhi Hu: 0000-0002-9246-7040

Huayang Liu: 0000-0002-2390-5414

Lin Zhang: 0000-0003-2153-4856

Jian Ren Lu: 0000-0001-5648-3564

Conflicts of interest

The authors declare no conflict of interest.

Acknowledgements

We thank studentship support from the University of Manchester in joint with China Scholarship Council (UoM-CSC joint PhD program) to M.L., H.G., L.Z. and Z.W., support to X.H. via an overseas research studentship by UoM, research grants from

Syngenta to X.H., from STFC to K.F., and from Lonza to K.F. and H.L.. We acknowledge the neutron beam times awarded from the ISIS Neutron Facility (RB 1920459 & 1920496) and from the ILL Neutron Facility (DOI: 10.5291/ILL-DATA.9-13-730) with technical assistance from Simon Wood. Computing time allocated from the Shared Computation Facility (SCF) at UoM is gratefully acknowledged. This work has benefited from the funding of a Marie Curie Fellowship ITN grant (grant number 608184) under SNAL (small nano-objects for alteration of lipid bilayers), a Knowledge Transfer Partnership grant (KTP 12697) by Innovate UK and Syngenta, and a LINK grant (BB/S018492/1) by BBSRC and AstraZeneca. We are grateful to the help and support from Prof. Jian Zhou in setting up atomistic simulation modelling. We thank Derren Heyes for his assistance to CD measurements.

5. References

[1] Guerra W, Silva-Caldeira PP, Terenzi H, Pereira-Maia EC. Impact of metal coordination on the antibiotic and non-antibiotic activities of tetracycline-based drugs. Coordination Chemistry Reviews. 2016;327-328:188-99.

[2] Garrido-Mesa N, Zarzuelo A, Galvez J. Minocycline: far beyond an antibiotic. British journal of pharmacology. 2013;169:337-52.

[3] Zhang T, Nong J, Alzahrani N, Wang Z, Oh SW, Meier T, et al. Self-assembly of DNA-minocycline complexes by metal ions with controlled drug release. ACS applied materials & interfaces. 2019;11:29512-21.

[4] Brodersen DE, Clemons WM, Carter AP, Morgan-Warren RJ, Wimberly BT, Ramakrishnan V. The structural basis for the action of the antibiotics tetracycline, pactamycin, and hygromycin B on the 30S ribosomal subunit. Cell. 2000;103:1143-54.

[5] Palmer AC, Angelino E, Kishony R. Chemical decay of an antibiotic inverts selection for resistance. Nature Chemical Biology. 2010;6:105-7.

[6] Lin D, Duan P, Yang W, Huang X, Zhao Y, Wang C, et al. Facile fabrication of melamine sponge@covalent organic framework composite for enhanced degradation of tetracycline under visible light. Chemical engineering journal. 2022;430:132817.

[7] Coates A, Hu Y, Bax R, Page C. The future challenges facing the development of new antimicrobial drugs. Nature Reviews Drug Discovery. 2002;1:895-910.

[8] Farha MA, Brown ED. Unconventional screening approaches for antibiotic discovery. Annals of the New York Academy of Sciences. 2015;1354:54-66.

[9] Clardy J, Fischbach MA, Walsh CT. New antibiotics from bacterial natural products. Nature Biotechnology. 2006;24:1541-50.

[10] Fischbach MA, Walsh CT. Antibiotics for emerging pathogens. Science. 2009;325:1089-93.

[11] Wright GD. Opportunities for natural products in 21st century antibiotic discovery. Natural Product Reports. 2017;34:694-701.

[12] Cottarel G, Wierzbowski J. Combination drugs, an emerging option for antibacterial therapy. Trends Biotechnol. 2007;25:547-55.

[13] Bechinger B, Gorr SU. Antimicrobial peptides: Mechanisms of action and resistance. Journal of dental research. 2017;96:254-60.

[14] Carratala JV, Serna N, Villaverde A, Vazquez E, Ferrer-Miralles N. Nanostructured antimicrobial peptides: The last push towards clinics. Biotechnology advances. 2020;44:107603.

[15] Fjell CD, Hiss, Jan A., Hancock, Robert E. W. and Schneider, Gisbert. Designing antimicrobial peptides: form follows function. Nature Reviews Drug Discovery. 2011;11:37-51.

[16] Giuliani A, Pirri G, Nicoletto S. Antimicrobial peptides: an overview of a promising class of therapeutics. Open Life Sciences. 2007;2:1-33.

[17] Dobson AJ, Purves J, Rolff J. Increased survival of experimentally evolved antimicrobial peptide-resistant Staphylococcus aureus in an animal host. Evolutionary applications. 2014;7:905-12.

[18] Gabriel G Perron MZ, Graham Bell. Experimental evolution of resistance to an antimicrobial peptide. Proceedings of the Royal Society B: Biological Sciences. 2005;273:251-6.

[19] Levy SB, Marshall B. Antibacterial resistance worldwide: causes, challenges and responses. Nature Medicine Supplement. 2004;10:S122-S9.

[20] Jiang L, Hu X, Xu T, Zhang H, Sheng D, Yin D. Prevalence of antibiotic resistance genes and their relationship with antibiotics in the Huangpu River and the drinking water sources, Shanghai, China. Science of the Total Environment. 2013;458-460:267-72.

[21] Xiao YH, Giske CG, Wei ZQ, Shen P, Heddini A, Li LJ. Epidemiology and characteristics of antimicrobial resistance in China. Drug Resistance Updates. 2011;14:236-50.

[22] Qiao M, Ying GG, Singer AC, Zhu YG. Review of antibiotic resistance in China and its environment. Environment international. 2018;110:160-72.

[23] Fischbach M. Combination therapies for combating antimicrobial resistance. Current Opinion in Microbiology. 2011;14:519-23.

[24] Pizzolato-Cezar LR, Okuda-Shinagawa NM, Machini MT. Combinatory therapy antimicrobial peptide-antibiotic to minimize the ongoing rise of resistance. Frontiers in microbiology. 2019;10:1703.

[25] Hilde Ulvatne SK, Trine Stiberg, Øystein Rekdal and John S. Svendsen. Short antibacterial peptides and erythromycin act synergically against Escherichia coli. Journal of Antimicrobial Chemotherapy. 2001;48:203–8.

[26] He J, Starr CG, Wimley WC. A lack of synergy between membrane-permeabilizing cationic antimicrobial peptides and conventional antibiotics. Biochimica et Biophysica Acta (BBA) - Biomembranes. 2015;1848:8-15.

[27] Taber HW, Mueller JP, Miller PF, Arrow A. Bacterial uptake of aminoglycoside antibiotics. Microbiological Reviews. 1987;51:439-57.

[28] Yamaguchi A, Ohmori H, Kaneko-Ohdera M, Nomura T, Sawai T. Delta pH-dependent accumulation of tetracycline in Escherichia coli. Antimicrobial agents and chemotherapy. 1991;35:53-6.

[29] Claeys KC, Fiorvento, Anna D., Rybak, Michael J. A review of novel combinations of colistin and lipopeptide or glycopeptide antibiotics for the treatment of multidrug-resistant acinetobacter baumannii. Infectious Diseases and Therapy. 2014;3:69-81.

[30] Gordon NC, Png K, Wareham DW. Potent synergy and sustained bactericidal activity of a vancomycin-colistin combination versus multidrug-resistant strains of Acinetobacter baumannii. Antimicrobial agents and chemotherapy. 2010;54:5316-22.

[31] Wareham DW, Gordon NC, Hornsey M. In vitro activity of teicoplanin combined with colistin versus multidrug-resistant strains of Acinetobacter baumannii. Journal of Antimicrobial Chemotherapy. 2011;66:1047-51.

[32] Vidaillac C, Benichou L, Duval RE. In vitro synergy of colistin combinations against colistin-resistant Acinetobacter baumannii, Pseudomonas aeruginosa, and Klebsiella pneumoniae isolates. Antimicrobial agents and chemotherapy. 2012;56:4856-61.

[33] Zhang J, Chen YP, Miller KP, Ganewatta MS, Bam M, Yan Y, et al. Antimicrobial metallopolymers and their bioconjugates with conventional antibiotics against multidrug-resistant bacteria. Journal of the American Chemical Society. 2014;136:4873-6.

[34] Brezden A, Mohamed MF, Nepal M, Harwood JS, Kuriakose J, Seleem MN, et al. Dual targeting of intracellular pathogenic bacteria with a cleavable conjugate of kanamycin and an antibacterial cell-penetrating peptide. Journal of the American Chemical Society. 2016;138:10945-9.

[35] Rodriguez CA, Papanastasiou EA, Juba M, Bishop B. Covalent modification of a ten-residue cationic antimicrobial peptide with levofloxacin. Frontiers in Chemistry. 2014;2:71.

[36] Chait R, Craney A, Kishony R. Antibiotic interactions that select against resistance. Nature. 2007;446:668-71.

[37] Hegreness M, Shoresh N, Damian D, Hartl D, Kishony R. Accelerated evolution of resistance in multidrug environments. Proceedings of the National Academy of Sciences of the United States of America. 2008;105:13977-81.

[38] Michel JB, Yeh PJ, Chait R, Moellering RC, Jr., Kishony R. Drug interactions modulate the potential for evolution of resistance. Proceedings of the National Academy of Sciences of the United States of America. 2008;105:14918-23.

[39] Ocampo P, Lázár V, Papp B, Arnoldini M, Abel zur Wiesch P, Busa-Fekete R, et al. Antagonism between bacteriostatic and bactericidal antibiotics is prevalent. Antimicrobial agents and chemotherapy. 2014;58:4573–82.

[40] Yeh PJ, Hegreness MJ, Aiden AP, Kishony R. Drug interactions and the evolution of antibiotic resistance. Nature Reviews Microbiology. 2009;7:460-6.

[41] Abdul Ghaffar K, M. Hussein W, G. Khalil Z, J. Capon R, Skwarczynski M, Toth I. Levofloxacin and indolicidin for combination antimicrobial therapy. Current Drug Delivery. 2015;12:108-14.

[42] Gong H, Liao M, Hu X, Fa K, Phanphak S, Ciumac D, et al. Aggregated mmphiphilic antimicrobial peptides embedded in bacterial membranes. ACS applied materials & interfaces. 2020;12:44420-32.

[43] Ciumac D, Campbell RA, Xu H, Clifton LA, Hughes AV, Webster JRP, et al. Implications of lipid monolayer charge characteristics on their selective interactions with a short antimicrobial peptide. Colloids and Surfaces B: Biointerfaces. 2017;150:308-16.

[44] Katsu T, Imamura T, Komagoe K, Masuda K, Mizushima T. Simultaneous measurements of K+ and calcein release from liposomes and the determination of pore size formed in a membrane. Analytical Sciences. 2007;23:517-22.

[45] Hu X, Gong H, Li Z, Ruane S, Liu H, Pambou E, et al. What happens when pesticides are solubilized in nonionic surfactant micelles. Journal of colloid and interface science. 2019;541:175-82.

[46] Hu X, Gong H, Hollowell P, Liao M, Li Z, Ruane S, et al. What happens when pesticides are solubilised in binary ionic/zwitterionic-nonionic mixed micelles? Journal of colloid and interface science. 2021;586:190-9.

[47] Gong H, Sani M-A, Hu X, Fa K, Hart JW, Liao M, et al. How do self-assembling antimicrobial lipopeptides kill bacteria? ACS applied materials & interfaces. 2020;12:55675-87

[48] Wang M, Zhou P, Wang J, Zhao Y, Ma H, Lu JR, et al. Left or right: how does amino acid chirality affect the handedness of nanostructures self-assembled from short amphiphilic peptides? Journal of the American Chemical Society. 2017;139:4185-94.

[49] Arnold O, Bilheux JC, Borreguero JM, Buts A, Campbell SI, Chapon L, et al. Mantid—data analysis and visualization package for neutron scattering and μ SR experiments. Nuclear Instruments and Methods in Physics Research Section A. 2014;764:156-66.

[50] Determination of minimum inhibitory concentrations (MICs) of antibacterial agents by agar dilution. Clinical Microbiology and Infection. 2000;6:509-15.

[51] Doern CD. When does 2 plus 2 equal 5? A review of antimicrobial synergy testing. Journal of clinical microbiology. 2014;52:4124-8.

[52] Gong H, Liao M, Hu X, Fa K, Phanphak S, Ciumac D, et al. Aggregated Amphiphilic Antimicrobial Peptides Embedded in Bacterial Membranes. ACS Appl Mater Interfaces. 2020;12:44420-32.

[53] Dockter ME, Magnuson JA. Membrane phase transitions and the transport of chlortetracycline. Archives of Biochemistry and Biophysics. 1975;168:81-8.

[54] Lai Z, Tan P, Zhu Y, Shao C, Shan A, Li L. Highly stabilized alpha-Helical coiled coils kill Gram-negative bacteria by multicomplementary mechanisms under acidic condition. ACS applied materials & interfaces. 2019;11:22113-28.

[55] Nelson A. Co-refinement of multiple-contrast neutron/X-ray reflectivity data using MOTOFIT. Journal of Applied Crystallography. 2006;39:273-6.

[56] Vanommeslaeghe K, Hatcher E, Acharya C, Kundu S, Zhong S, Shim J, et al. CHARMM general force field: A force field for drug-like molecules compatible with the CHARMM all-atom additive biological force fields. Journal of Computational Chemistry. 2009:NA-NA.

[57] Yu W, He X, Vanommeslaeghe K, MacKerell AD. Extension of the CHARMM general force field to sulfonyl-containing compounds and its utility in biomolecular simulations. Journal of Computational Chemistry. 2012;33:2451-68.

[58] Qi Y, Ingólfsson HI, Cheng X, Lee J, Marrink SJ, Im W. CHARMM-GUI Martini maker for coarse-grained simulations with the Martini Force Field. Journal of chemical theory and computation. 2015;108:4486–94.

[59] Jo S, Kim T, Iyer VG, Im W. CHARMM-GUI: A web-based graphical user interface for CHARMM. Journal of Computational Chemistry. 2008;29:1859-65.

[60] Humphrey W, Dalke A, Schulten K. VMD: Visual molecular dynamics. Journal of Molecular Graphics. 1996;14:33-8.

[61] Stokes JM, Lopatkin AJ, Lobritz MA, Collins JJ. Bacterial metabolism and antibiotic efficacy. Cell metabolism. 2019;30:251-9.

[62] Ejim L, Farha MA, Falconer SB, Wildenhain J, Coombes BK, Tyers M, et al. Combinations of antibiotics and nonantibiotic drugs enhance antimicrobial efficacy. Nature Chemical Biology. 2011;7:348-50.

[63] Chopra I, Hacker K. Effects of tetracyclines on the production of extracellular proteins by members of the propionibacteriaceae. FEMS Microbiology Letters. 1989;60:21-4.

[64] Gong H, Hu X, Liao M, Fa K, Ciumac D, Clifton LA, et al. Structural disruptions of the outer membranes of Gram-negative bacteria by rationally designed amphiphilic antimicrobial peptides. ACS applied materials & interfaces. 2021;13:16062-74.

[65] Nasompag S, Dechsiri P, Hongsing N, Phonimdaeng P, Daduang S, Klaynongsruang S, et al. Effect of acyl chain length on therapeutic activity and mode of action of the CX-KYR-NH2 antimicrobial lipopeptide. Biochimica et Biophysica Acta (BBA). 2015;1848:2351-64.

[66] Khalid S, Piggot TJ, Samsudin F. Atomistic and coarse grain simulations of the cell envelope of Gram-negative bacteria: what have we learned? Accounts of Chemical Research. 2019;52:180-8.

[67] Deris ZZ, Swarbrick JD, Roberts KD, Azad MA, Akter J, Horne AS, et al. Probing the penetration of antimicrobial polymyxin lipopeptides into gram-negative bacteria. Bioconjug Chem. 2014;25:750-60.

[68] Helander IM, Mattila-Sandholm T. Fluorometric assessment of Gram-negative bacterial permeabilization. Journal of Applied Microbiology. 2000;88:213-9.

[69] Berglund NA, Piggot TJ, Jefferies D, Sessions RB, Bond PJ, Khalid S. Interaction of the antimicrobial peptide polymyxin B1 with both membranes of E. coli: a molecular dynamics study. PLoS computational biology. 2015;11:e1004180.

[70] Schultz ZD, Levin IW. Vibrational spectroscopy of biomembranes. Annual review of analytical chemistry. 2011;4:343-66.

[71] Orendorff CJ, Ducey MW, Pemberton JE. Quantitative correlation of Raman spectral indicators in determining conformational order in alkyl chains. The Journal of Physical Chemistry A. 2002;106:6991-8.

[72] Ciumac D, Gong H, Campbell RA, Campana M, Xu H, Lu JR. Structural elucidation upon binding of antimicrobial peptides into binary mixed lipid monolayers

mimicking bacterial membranes. Journal of colloid and interface science. 2021;598:193-205.

Supporting Information

Antimicrobial Synergy of Lipopeptides Paired with Conventional Antibiotics

Mingrui Liao,[1#] Haoning Gong,[1] Xuzhi Hu,[1] Ziwei Wang,[2] Ke Fa,[1] Andrew J. McBain[3] and Jian R. Lu[1,*]

[1]Biological Physics Laboratory, Department of Physics and Astronomy, School of Natural Science, The University of Manchester, Oxford Road, Manchester M13 9PL, UK.

[2]Department of Physics and Astronomy, School of Natural Science, The University of Manchester, Oxford Road, Manchester M13 9PL, UK.

[3]Division of Pharmacy and Optometry, Faculty of Biology, Medicine and Health, The University of Manchester, Oxford Road, Manchester M13 9PL, UK.

[#]To whom as PhD candidate should be responsible to all the experiments and simulation work.
*To whom all correspondence should be made: J.lu@manchester.ac.uk

1. Bacterial strains and materials

The following bacterial strains were purchased from ATCC: *Escherichia coli* (*E. coli*, ATCC 25922), *Staphylococcus aureus* (*S. aureus* ATCC 6538), *Propionibacterium acnes* (*P. acne*, ATCC 11827). ESBL-*E. coli* and tetracycline-resistant (TCR) *E. coli* were clinically isolated strains obtained from the Manchester Royal Infirmar. Polymixin B and all the tetracycline antibiotics were purchased from Sigma Aldrich, lipopeptides C8GIK and C8GIR were synthesized by ChinaPeptides Co., Ltd. (Shanghai, China). Fluorescence probes N-phenyl-1-naph-thylamine (NPN), 3,3′-Dipropylthiadicarbocyanine iodide (DiSC$_3$(5)), Calcein-AM, Propidium iodide (PI) were supplied from Sigma-Aldrich and SYTO 9 was obtained from Thermo Fisher.

Lipids 1,2-dipalmitoyl-sn-glycero-3-[phosphor-rac-(3-lysyl(1-glycerol))] (sodium salt) (DPPG), acyl chain deuterated DPPG (d$_{62}$-DPPG), 1-palmitoyl-2-oleoyl-sn-glycero-3-phospho-(1′-rac-glycerol) (sodium salt) (POPG) and 1-palmitoyl-2-oleoyl-sn-glycero-3-phosphocholine (POPC), 1',3'-bis[1-palmitoyl-2-oleoyl-sn-glycero-3-phospho]-glycerol (sodium salt) (16:0-18:1 Cardiolipin), 1-myristoyl-2-hydroxy-sn-glycero-3-phospho-(1'-rac-glycerol) (sodium salt) (14:0 Lyso-PG) were obtained from Avanti Polar Lipids (Alabaster, USA). Hydrogenated RcLPS product extracted from *E. coli* was purchased from Sigma-Aldrich.

2. Key physical parameters used in neutron experiments

Table S1. Theoretical SLDs of lipids and antimicrobials used in neutron data analysis.

Components		**SLD (10^{-6} Å^{-2})**	**Molecular Mass**	**Molecular Volume**
PBS Buffer		6.35	/	/
dDPPG[a]	Head	3.27	299	283
	Tail	7.08	484	865
C$_8$GIK[b]		1.91	1279.5	1849.8
Mino[b]		3.01	457.5	400.0

[a]SLDs, molecular masses, and volumes of the deuterated DPPG were given in our previous publication.[1]

[b]SLDs, molecular masses, and volumes of hydrogenated peptides in D_2O were calculated using an online SLD calculator (http://psldc.isis.rl.ac.uk/Psldc/).

3. Molecular information of lipopeptides and antibiotics, and their antimicrobial and biocompatible assays

Chemical Reagents. Hydrogenated phospholipids (h-DPPG, h-POPG, h-POPC) and hydrocarbon chain deuterated versions (d62-DPPG) were purchased from Avanti Polar Lipids (Alabaster, AL), hydrogenated rough C LPS (RcLPS or LPS in text) was extracted from the outer membrane of *E. coli* (J5 strain, ATCC 43745) using the method previously described.[2, 3] Two lipopeptides used, C_8GIK and C_8GIR, were obtained from Ind-Chem Co. Ltd. (Nanjing, China). Antibiotics polymyxin B and tetracyclines were purchased from Sigma-Aldrich, with purities (checked by HPLC) > 98%. These antimicrobials were identified by independent measurements of MS, and minimum inhibitory concentration (MIC) tests against bacteria as shown in **Table S2&S3**, and the results were compared to known values from previous batches. All materials were used without further purification unless otherwise stated.

Table S2. Molecular structures of lipopeptides and antibiotics with their basic properties.

Peptide denotation	Sequence/Molecular formula	Theoretical M_w/g·mol^{-1}	Measured M_w/g·mol^{-1}	Charge/e
PMB	$C_{56}H_{100}N_{16}O_{17}S$	1301.6	1302.6	+2
C_8GIK	$CH_3(CH_2)_6COG(IIKK)_2I$	1279.5	1278.4	+4
C_8GIR	$CH_3(CH_2)_6COG(IIRR)_2I$	1391.6	1392.8	+4
Tetracycline	$C_{22}H_{24}N_2O_8$	444.4	445.6	0
Chlortetracycline	$C_{22}H_{23}ClN_2O_8$	478.9	480.2	0
Minocycline	$C_{23}H_{27}N_3O_7$	457.5	456.3	0

The theoretical molecular weight of a lipopeptide was calculated by addition of all the individual amino acid residues and a fatty acid, followed by subtraction of H_2O.

Table S3. MICs of different antimicrobials against *E. coli* and *S. aureus* and their respective antibiotic-resistance strains.

Component/ Strains	***E. coli*/μM**	**ESBL *E. coli*/μM**	**TetR-*E. coli*/μM**	***S. aureus*/μM**	***MRSA*/μM**	***P. acne*/μM**
Tetracycline	4.0	4.0	100	0.8	0.5	4.0
Minocycline	2.0	2.0	3.0	0.8	0.25	1.0
Chlortetracycline	4.0	4.0	50.0	2.4	0.5	8.0
Polymixin B	1.0	1.5	6.0	31.3	62.5	--
C_8GIK	12.0	12.0	6.0	1.6	0.5	2.0
C_8GIR	12.0	12.0	12.0	2.4	0.5	2.0

Table S4. MICs of binary mixtures of tetracyclic compound-lipopeptide combinations against *E. coli*, *S. aureus* and their respective antibiotic-resistance strains and anaerobic bacterium *P. acne*.

Component (1:1)/ Strains	***E. coli*/μM**	**ESBL *E. coli*/μM**	**TetR-*E. coli*/μM**	***S. aureus*/μM**	***MRSA*/μM**	***P. acne*/μM**
C_8GIK+Tet	4.8	6	6	≤ 0.4	0.8	1.6
C_8GIK+Chlor	2.4	12.5	6	≤ 0.4	≤ 0.4	3.2
C_8GIK+Mino	1.6	2.4	3	≤ 0.4	≤ 0.4	0.8
C_8GIR+Tet	2.4	4.8	12.5	≤ 0.4	0.8	1.6
C_8GIR+Chlor	1.6	6	12.5	≤ 0.4	≤ 0.4	3.2
C_8GIR+Mino	1.6	2.4	6	≤ 0.4	≤ 0.4	1.0

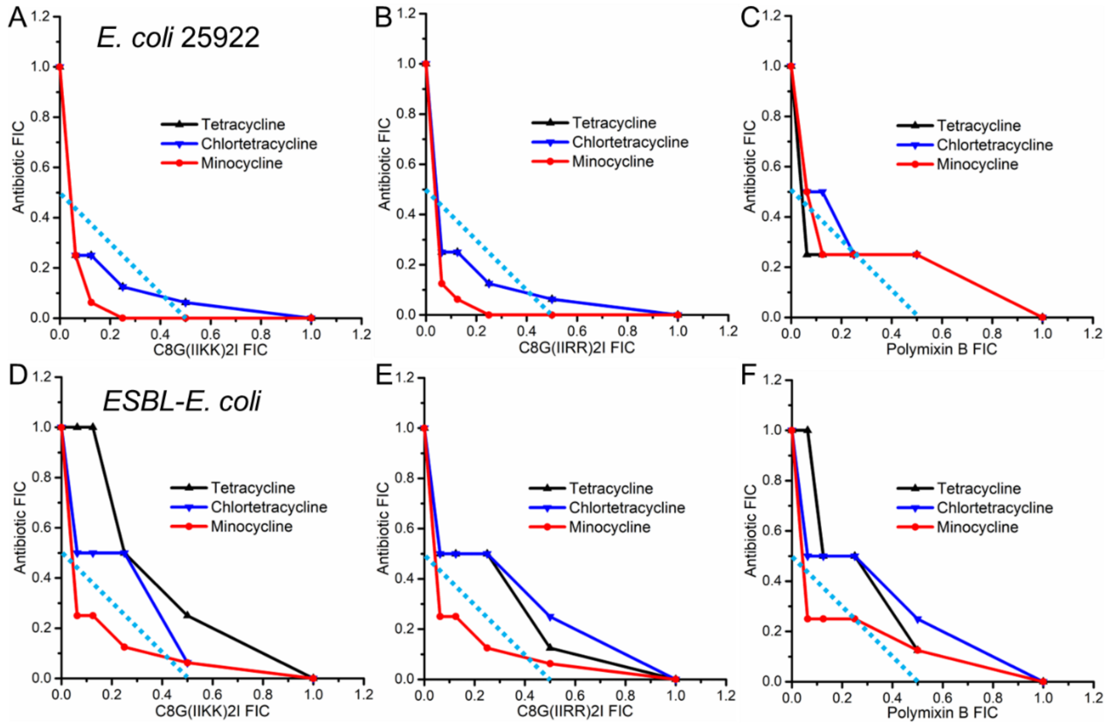

Figure S1. Drug pairs C_8GIK/C_8GIR/PMB-TC/CC/MC against Gram-negative (A-C) *E. coli* ATCC 25922 and (D-F) ESBL-*E. coli*.

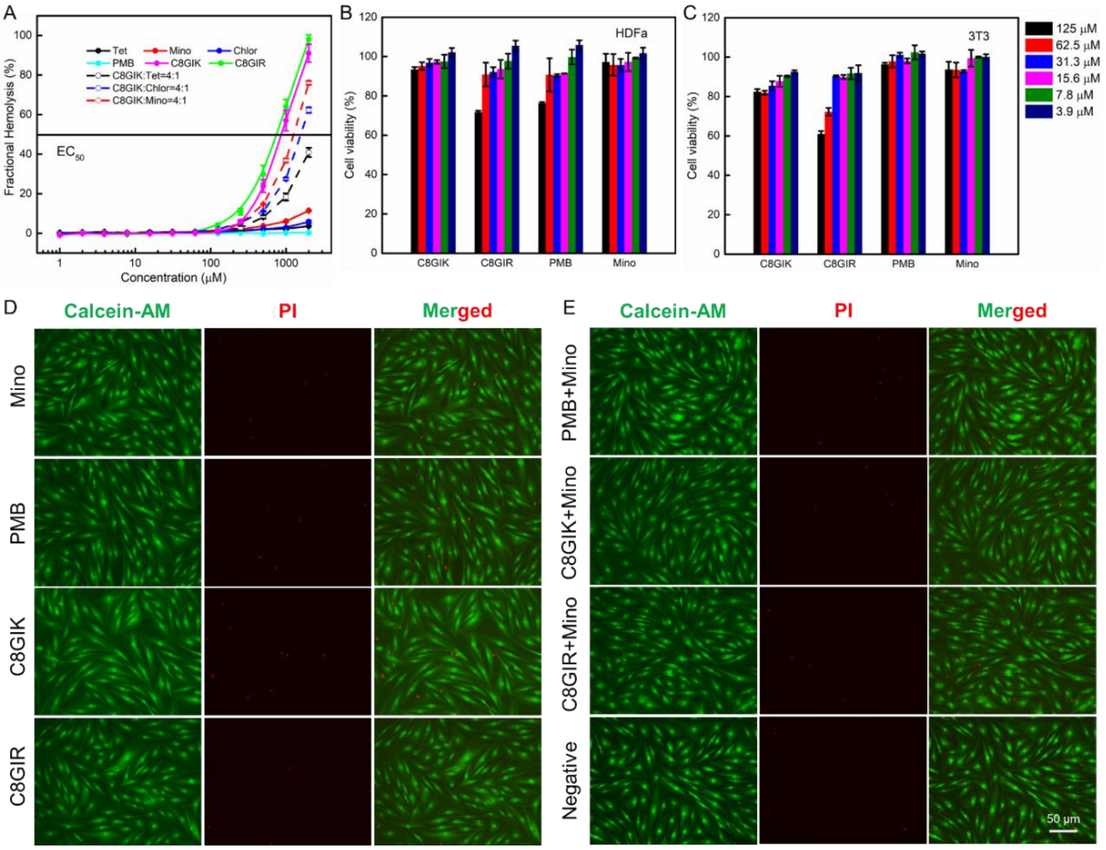

Figure S2. (A) Haemolysis assays of lipopeptides, antibiotics and C_8GIK-MC pairs in human red blood cells (hRBCs). (B-C) MTT assays of HDFa and 3T3 cells for three lipopeptides (C_8GIK, C_8GIR and PMB) and MC at different concentrations. (D, E) Live/dead staining images of HDFa directly in contact with different lipopeptides/antibiotic and lipopeptide-antibiotic pairs for 24 h (for individual drug with a concentration of 25 μM and 50 μM binary lipopeptides-antibiotic with molar ratio of 1:1). Scale bar is 50 μm. HDFa assays of the binary mixtures indicate the greater cytocompatibility than individual components under same concentrations.

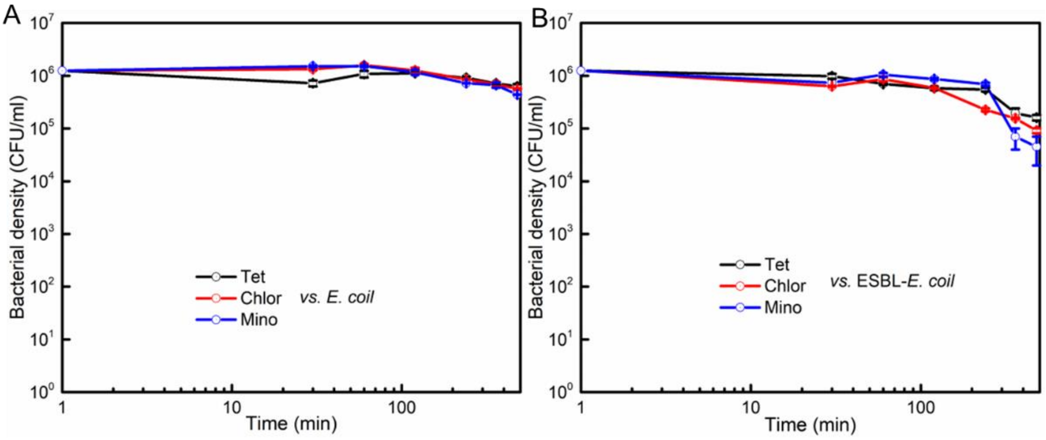

Figure S3. Dynamic killing performance of three tetracycline antibiotics (drug concentrations are 4× MIC) against Gram-negative (A) *E. coli* ATCC 25922, (B) drug-resistant ESBL-*E. coli.*

4. AMPs' structure and physical activity

Due to the surfactant property of different lipopeptides, the air-liquid adsorption of different lipopeptides in the bulk solution was measured. (**Figure S4A**) Both C_8GIK and C_8GIR tended to show air-liquid adsorption and decreased the surface pressure of water solution even at concentrations lower than 10 μM (from ~ 72 mN/m to ~ 50 mN/m), while PMB decreased the surface pressure rather weakly due to its good solubility in aqueous solution.

Following our previous studies,[4] DPPG was chosen as the outer leaflet of model negatively charged membrane. For simplicity, ~ 80 ml PBS buffer was added into the

Langmuir trough to form a positive liquid meniscus, followed by the gentle spreading of DPPG monolayer. DPPG monolayer achieved the initial surface pressure of 28 mN/m after compression with the trough barrier. Once the lipid monolayer became stabilized, ~ 2 ml antimicrobial stock solution was injected into the water subphase under the lipid monolayer to achieve a fixed concentration. The drug solution was uniformly spread underneath the lipid monolayer without disturbing it. This was achieved by inserting an “L-shape” stainless-steel needle of 15 cm in length underneath the Teflon barrier without disturbing the lipid monolayer. Surface pressure was continuously recorded upon lipopeptide injection. The dynamic changes in the surface pressure of the DPPG monolayer after peptide injection are shown in **Figure S4**. PMB at 10 μM led to a surface pressure increase of the DPPG monolayer by about 5 mN/m, while C_8GIK and C_8GIR had pressure rises up to 15 mN/m. In contrast, after MC interacting with DPPG monolayer, there was a slight initial surface pressure increase which then went back to the original level.

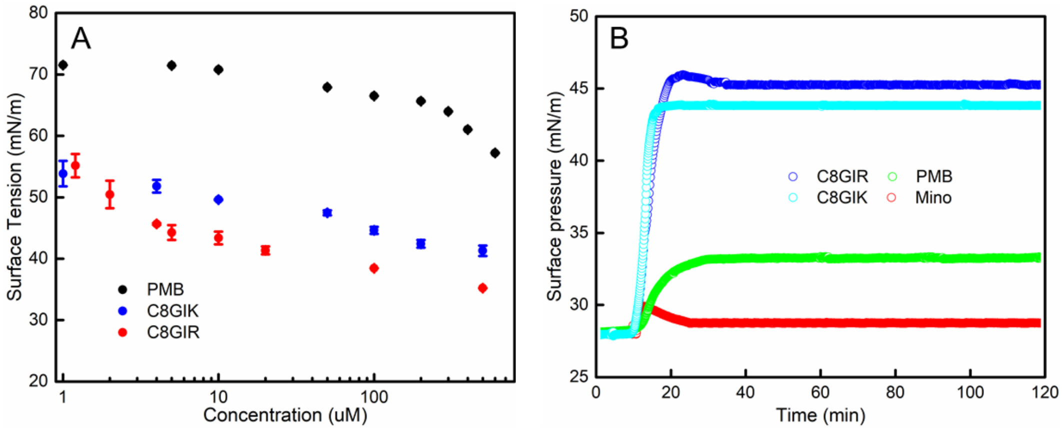

Figure S4. (A) Surface tension measurements of the three lipopeptides show their different adsorption behaviour in the PBS buffer solution. (B) Surface pressure changes from the spread DPPG monolayer upon injections of antibiotic and lipopeptides with final concentration of 10 μM.

Antimicrobial peptides/lipopeptides tend to change their secondary structures from random coils in electrically neutral environments to α-helices upon binding with anionic lipid membranes. This trend was observed with lipopeptides (C_8GIK, C_8GIR and PMB) based on changes in CD spectra (**Figure S5**). The CD characterizations of individual lipopeptides in buffer solution and in presence of SDS solution mimicked a negatively charged membrane environment.

To examine how the intermolecular binding between C_8GIK and tetracyclic drug (drug combination with a molar ratio of lipopeptide/antibiotic at 8/1) influences lipopeptide's secondary structure in PBS buffer and in SDS micelles was measured. (**Figure S5C&D**) C_8GIK retained to be non-ordered with and without tetracyclic compounds, but transition from non-ordered to α-helices occurred in negatively charged SDS micellar environment.

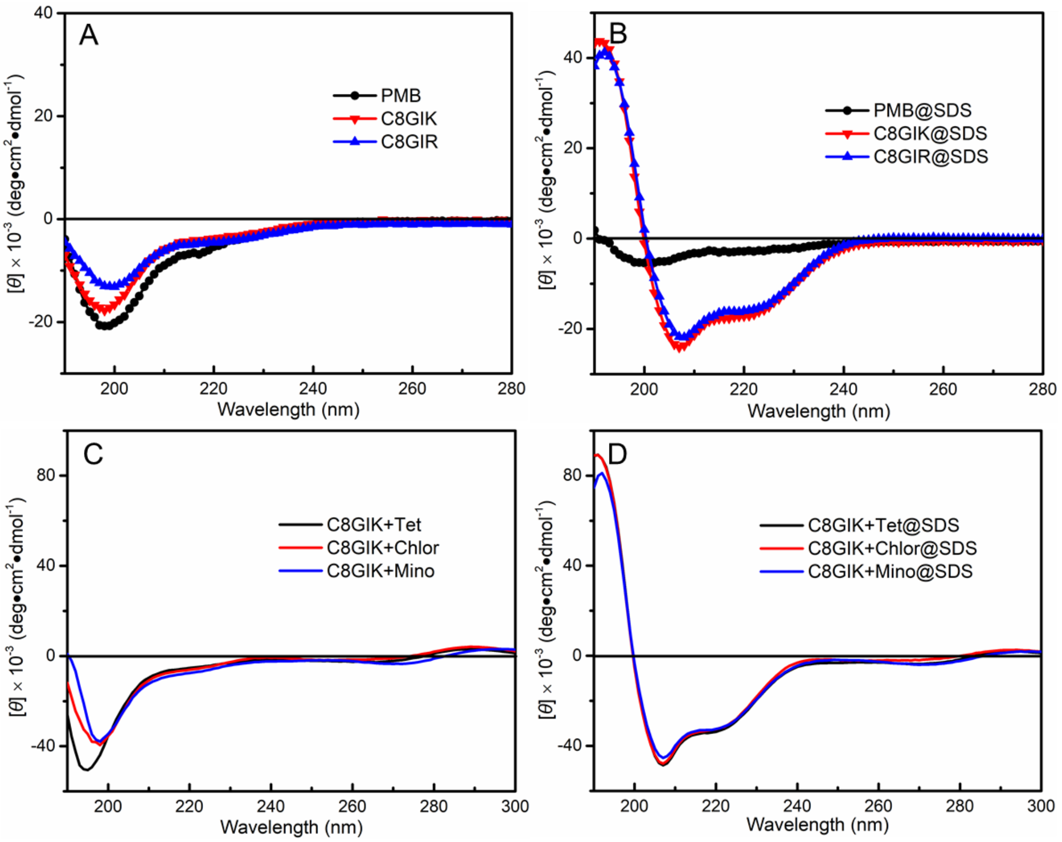

Figure S5. CD measurements of three lipopeptides ($C_8G(IIKK)_2I$, $C_8G(IIRR)_2I$, Polymixin B) in presence of both (A) PBS buffer solution and (B) 50 mM SDS solution. (C, D) Secondary conformation change of lipopeptide mixed with antibiotics in presence of PBS buffer and SDS micelles.

5. Kinetic leakage fraction of POPC/LPS SUVs with lipopeptides

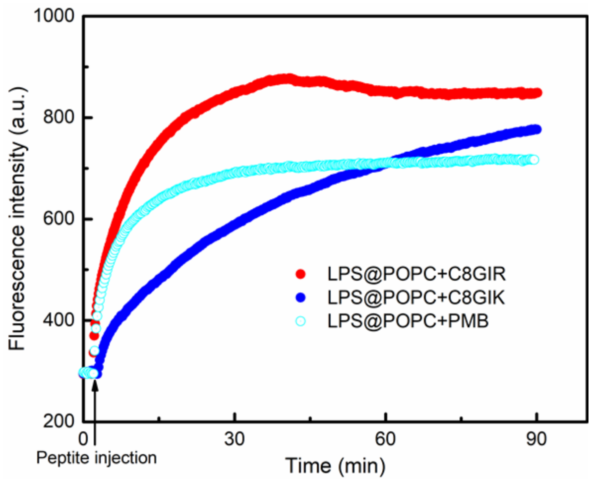

Figure S6. Kinetic fluorescence leakage of POPC/LPS SUVs mimicking the outer membrane of Gram-negative bacteria induced by 10 µM lipopeptides.

6. PG micelles with lipopeptides in SANS fit models

Table S5. Model parameters from fits to the SANS data of lipopeptides or antibiotic binding onto Lyso-PG micelles mimicking the negatively charged membrane environment.

Peptide/ Concentration	**Lyso-PG micelles/20 mM**	**+MC/2 mM**	**+C_8GIK /2 mM**	**+PMB /2 mM**
Fitting Model	core_shell_sphere	core_shell_sphere	core_shell_sphere	core_shell_sphere
Scale[a]	1	1	1	1
Background (×10^{-3} cm^{-1})	0.06±0.01	0.06±0.01	0.006±0.001	0.008±0.001
SLD_core (×10^{-6} Å^{-2})	-0.4±0.05	-0.4±0.05	-0.4±0.05	-0.4±0.05
SLD_shell (×10^{-6} Å^{-2})	5.0±0.1	5.0±0.1	5.0±0.1	5.0±0.1
Radius (Å)	19±1	19±1	22±1	21±1
Thickness (Å)[b]	6±0.5	6±0.5	7.5±0.5	8.0±0.5
Volume fraction	0.012±0.001	0.0075±0.001	0.0070±0.001	0.011±0.001
Charge	22±1	17±1	5±1	4±1
Distribution of radius	--	--	0.13±0.02	0.15±0.02

SLD Solvent ($\times 10^{-6}$ Å^{-2})[c]	6.35±0.1	6.35±0.1	6.35±0.1	6.35±0.1

Note: Errors in SANS were estimated by the range of model parameters beyond which the SANS fits were noticeably different.

[a] Scale was the volume fraction of the self-assembly structure (including hydration) from the SANS model fit.

[b] The shell thickness of core-shell sphere.

[c] SLD of pure D_2O is 6.35× 10^{-6} Å^{-2}. In our experiments, D_2O contained a small amount of H_2O due to sample mixing, leading to smaller SLD values for the solvents.

7. Raman spectrum of POPC/POPG with lipopeptides

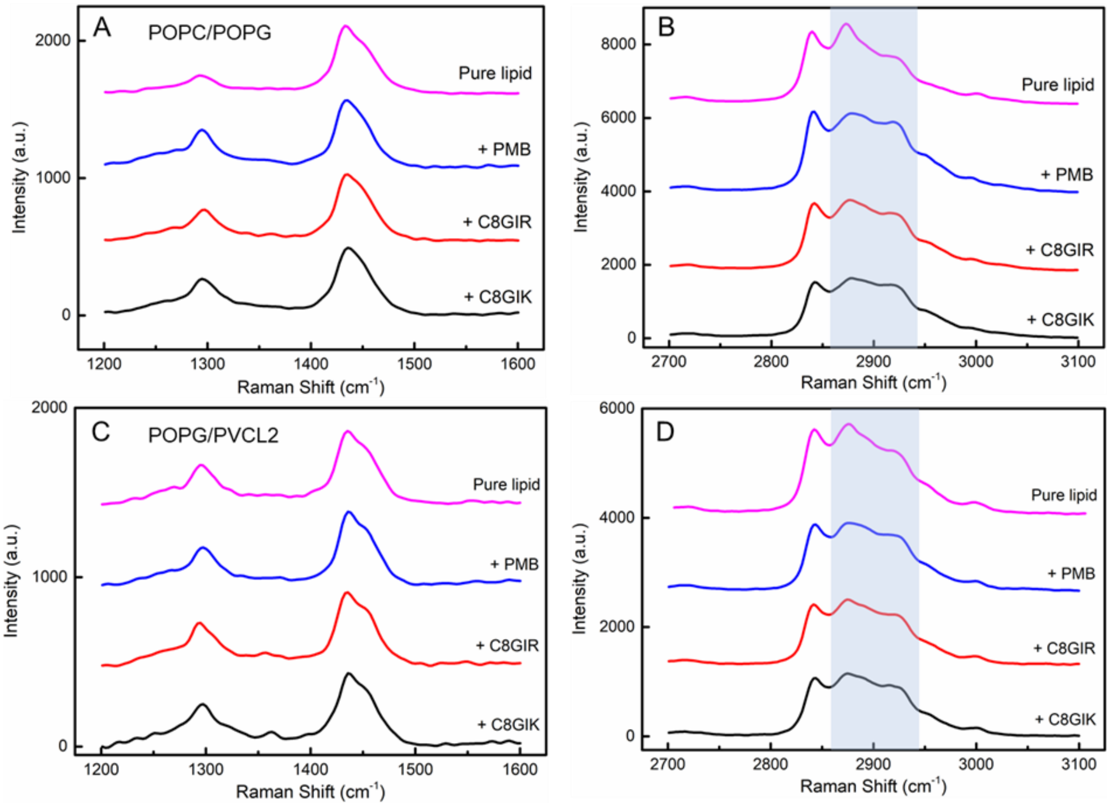

Figure S7. Raman spectra of (A-B) POPC/POPG and (C-D) POPG/PVCL2 SUVs interacting with three lipopeptides, respectively, with a molar ratio of lipopeptide to lipid 1/10.

Table S6. Assignment of the main Raman bands for SUVs in different groups shown in **Figure S3**.

Raman shift (cm^{-1})	Assignments
1294-1303	CH_2 twist
1435-1438	CH_2/CH_3 scissoring
1647-1655	Amide I band
1733-1736	C-H stretching
2840-2844	CH_2 symmetric stretching
2873-2875	CH_2 antisymmetric stretching
2917-2923	CH_3 symmetric stretching
2950-2952	CH_3 asymmetric stretching

8. Lipopeptide self-assembly and co-assembly with MC in SANS fit models

Table S7. Model parameters from fits to the SANS data from self-assembled C8GIK and co-assembled C_8GIK-Mino.

Peptide/ Concentration	**C_8GIK/4 mM**	**C_8GIK + MC/4 mM +1 mM**
Fitting Model	ECM[a]	ECM
$\varphi_{\text{self-assembled}}$ ($\times 10^{-4}$)[b]	1.1±0.1	1.1±0.1
φ_{all} ($\times 10^{-4}$)[c]	55.3	65.6
Self-assembled peptides (%)[d]	2±0.2	1.9±0.2
Minor_radius (Å)	65±5	55±5
Axial Ratio	1.8±0.2	1.8±0.2
Length (Å)	>1000	>1000

SLD_Cylinder ($\times10^{-6}$ Å^{-2})[e]	3.9±0.2	2.5±0.2
SLD Solvent ($\times10^{-6}$ Å^{-2})[f]	6.3±0.1	6.3±0.1

Note: Errors in SANS were estimated by the range of model parameters beyond which the SANS fits were noticeably different.

[a] ECM denotes the elliptical cylinder model. Errors in SANS were estimated by the range of model parameters beyond which the SANS fits were noticeably different.

[b] $\varphi_{\text{self-assembled}}$ was the volume fraction of the supramolecular nanofibrils (including hydration) from the SANS model fit.

[c] φ_{all} was the volume fraction of all dissolved peptide samples.

[d] Percentages of self-assembled peptides were calculated using $\varphi_{\text{self-assembled}}\times(1-\text{hydration})\ \varphi_{\text{all}}\times 100\%$.

[e] Nanofibers were composed of lipopeptide molecules and D_2O. Their SLD were estimated as 4× 10^{-6} Å^{-2} (i.e. 50% lipopeptide + 50% D_2O). More accurate SLD values can be obtained by optimising the simultaneous fits under multiple isotopic contrasts.

[f] The SLD of pure D_2O is 6.35× 10^{-6} Å^{-2}. In our experiments, D_2O may contain traces amounts of H_2O, leading to smaller SLD values.

9. NOESY spectrum and Fluorescence assays of C_8GIK-MC complex

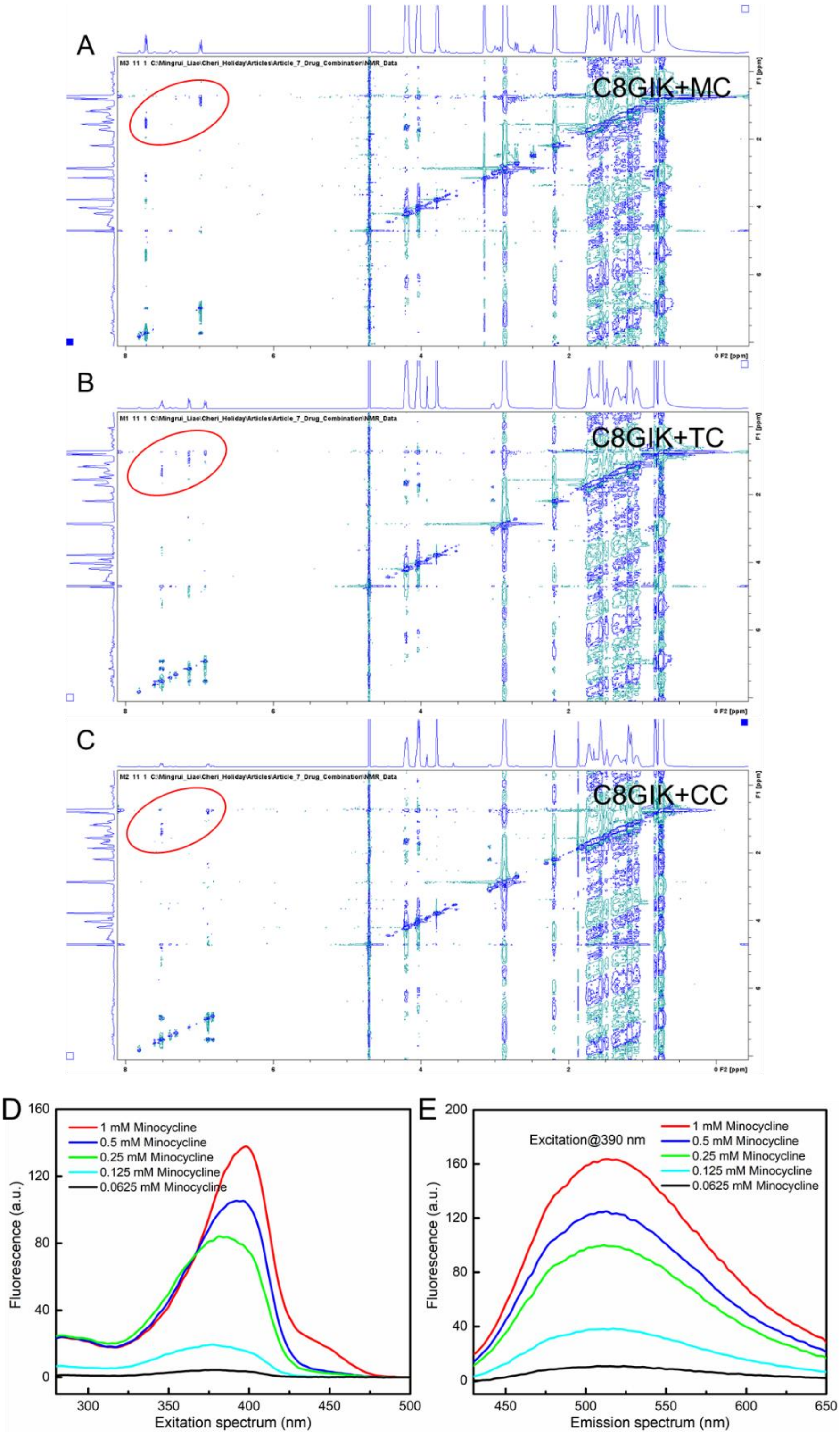

Figure S8. NOSEY spectrum of Fluorescence spectroscopy analysis. (A-C) NOESY spectra for MC/TC/CC with C_8GIK monomers and oligomers. Fluorescence excitation (D) and emission (E) spectra for free MC solutions. Experiment conditions:

Minocycline of concentration ranging from 0.0625 to 1 mM were mixed with 50 mM Mg^{2+} concentration. Fluorescence was measured by Skanlt plate reader (Thermofisher).

The hydrogens present in MC were assigned as M1: ~6.6 ppm, M2: ~6.9 ppm, M3: ~2.8 ppm, M4: 2.38 and 3.63 ppm, M5: ~2.88 ppm, M6: ~1.15 and 1.99 ppm, M7: ~3.1 ppm, M8: ~3.5 ppm and M9: ~2.43 ppm. The hydrogens present in C_8GIK representing $-CH_2$ and $-CH_3$ (mainly located in lipopeptide tail and hydrophobic residue Ile) were assigned as K1: ~0.86 ppm ($-CH_3$); K2: ~1.24 ppm, 1.27 ppm, 1.35 ppm, 1.69 ppm, 3.33 ppm ($-CH_2$); K3 (Ile): ~0.89 ppm ($-CH_3$), ~1.21 ppm ($-CH_2$), ~1.98 ppm (-CH) and ~4.23 ppm (-CH) and K4 (Lys): ~2.63 ppm, ~1.54 ppm, ~1.39 ppm, ~1.93 ppm ($-CH_2$), 4.36 ppm (-CH).

The hydrogens present in TC and CC were assigned as T1: ~7.10 ppm, T2: ~7.41 ppm, T3: ~7.31 ppm, T4: ~1.60 ppm, T5: ~2.72 ppm, T6: ~1.66 and 1.94 ppm, T7: ~3.09 ppm, T8: ~2.45 ppm and T9: ~3.46 ppm; C1: ~7.01 ppm, C2: ~7.48 ppm, C3: ~1.59 ppm, C4: 3.69 ppm, C5: ~2.12 and 2.89 ppm, C6: ~3.55 ppm, C7: ~2.44 ppm, C8: ~3.39 ppm. Similar molecular structure of TC and MC, the chemical shift reflecting TC-C_8GIK is also similar mainly between the hydrogen atoms directly linked with benzene ring and $-CH_3$ in lipopeptide.

The fluorescence excitation and emission of C_8GIK-MC solutions were strongly affected by the addition of Mg^{2+}. In **Figure S8**, as 50 mM Mg^{2+} was added with different concentrations of minocycline from 62.5 μM to 1 mM, the excitation efficiency of Mg^{2+}-MC increased significantly. A blue shift of the maximum-excitation wavelength ($\lambda_{exc.max}$) was also observed from $\lambda_{exc.max}$ ~ 370 nm for 62.5 μM minocycline to $\lambda_{exc.max}$ ~ 400 nm for 1 mM minocycline. The emission spectrum also showed an increased fluorescence intensity of Mg^{2+}-MC solutions by adding more MC.

10. Parameters in NR monolayer fit models

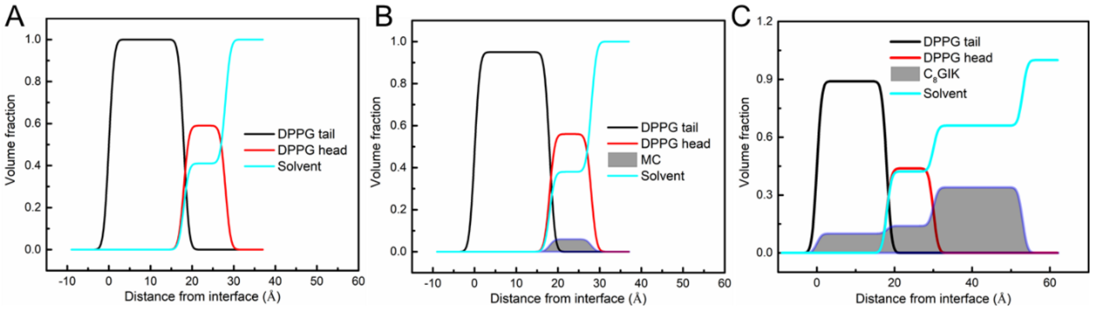

Figure S9. The volume fractions of individual DPPG monolayer, and binding with 30 μM MC (a higher concentration than the previously used 10 μM, to see the situation of concentration-depending binding) and 30 μM C_8GIK (to have a comparison to binding situation of 10 μM C_8GIK) corresponding to the NR profiles in **Figure 7C**.

Table S8. Best model fitting parameters of NR from the DPPG monolayer without and with additions of lipopeptides. τ is the layer thickness, φ is the volume fraction, Γ is the surface concentration. Tail, head, and peptide layers are layers 1-3, representatively.

Layer	**τ (Å)**	φ_{lipid}	φ_{peptide}	φ_{solvent}	Γ_{lipid} **(μMol/m²)**	$\Gamma_{\text{peptide/antibiotic}}$ **(μMol/m²)**
DPPG						
Tail	18 ± 2	1.00 ± 0.05	-	-	3.46±0.35	-
Head	10 ± 1	0.59 ± 0.06	-	0.41 ± 0.04	3.46±0.35	-
DPPG + 10 μM C_8GIK						
Tail	18 ± 2	0.83 ± 0.05	0.10 ± 0.01		2.87±0.30	0.16±0.02
Head	12 ± 1	0.41 ± 0.04	0.10 ± 0.01	0.49 ± 0.05	2.87±0.30	0.11±0.01
Peptide	30 ± 2	0.15 ± 0.02	0.17 ± 0.02	0.83 ± 0.08	0.86±0.10	0.46±0.05
DPPG + 30 μM C_8GIK						
Tail	18 ± 2	0.85 ± 0.05	0.10 ± 0.01		2.93±0.30	0.16±0.02
Head	12 ± 1	0.41 ± 0.04	0.14 ± 0.02	0.45 ± 0.05	2.93±0.30	0.15±0.02
Peptide	23 ± 2		0.34 ± 0.05	0.66 ± 0.06		0.70±0.07
DPPG + 10 μM MC						
Tail	18 ± 2	0.95 ± 0.05			3.28±0.35	

Head	10 ± 1	0.56 ± 0.06	0.06 ± 0.01	0.38 ± 0.04	3.28±0.35	0.20±0.03
			DPPG + 30 μM MC			
Tail	18 ± 2	0.95 ± 0.05			3.28±0.35	
Head	10 ± 1	0.56 ± 0.06	0.06 ± 0.01	0.38 ± 0.04	3.28±0.35	0.20±0.03
			DPPG + 30 μM C_8GIK& 30 μM MC			
Tail	18 ± 2	0.89 ± 0.05	0.10 ± 0.01		3.08±0.30	0.16±0.02
Head	12 ± 1	0.44 ± 0.04	0.18 ± 0.02	0.38 ± 0.04	3.08±0.30	0.19±0.02
Peptide &MC	23 ± 2		0.53 ± 0.05	0.47 ± 0.05		1.09±0.10

11. MD simulation of MC with POPG/PVCL2 membrane

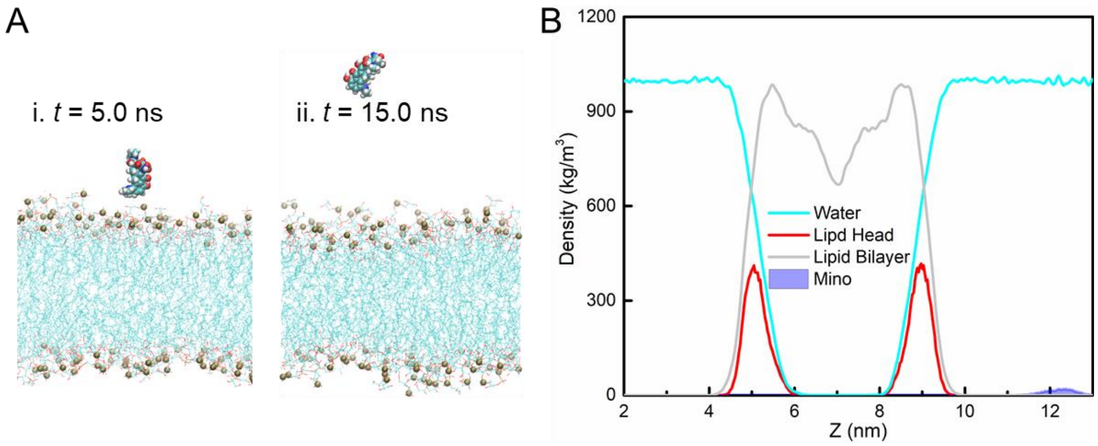

Figure S10. Atomistic MD simulation of Minocycline binding behaviour on POPG/PVCL2 bilayer mimicked plasmatic membrane of Gram-positive bacteria.

Minocycline molecule can hardly approach onto fully negatively charged membrane (POPG/PVCL2), it shows random dispersion above the membrane, from the molecular distribution profile of the system, the membrane orderness and symmetricity are keeping well and not disturbed by the single antibiotic.

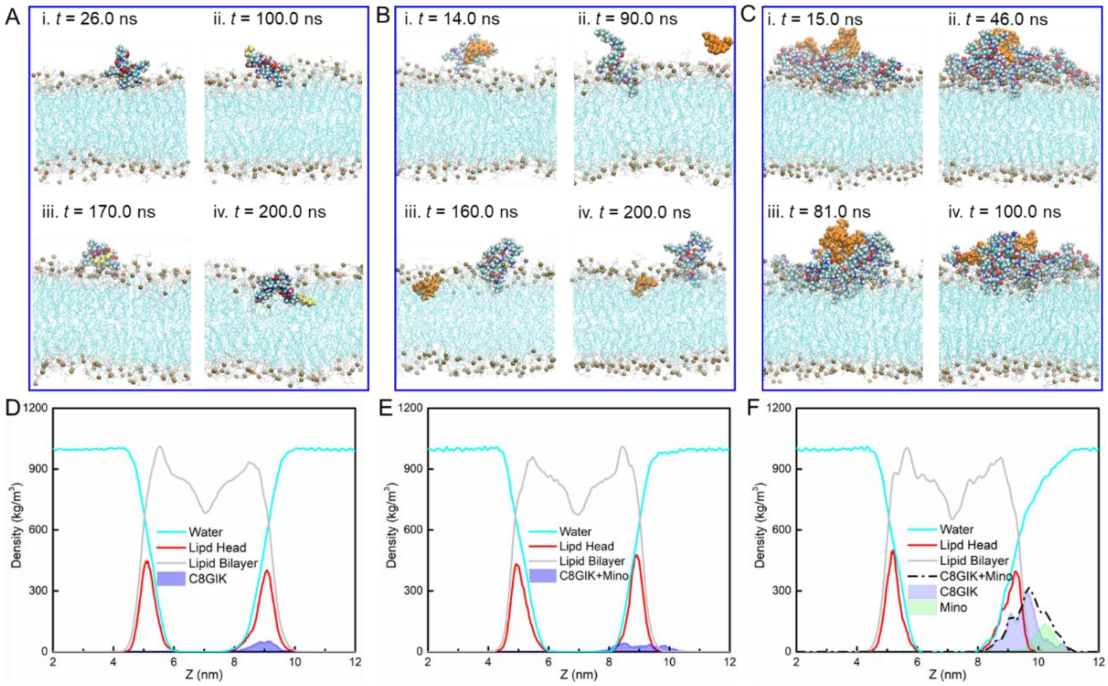

Figure S11. Atomistic molecular dynamics simulation of (A) single lipopeptide C_8GIK, (B, C) lipopeptide-antibiotic combination interacting with mimicking Gram-positive bacterial membrane (POPG/PVCL2, mol/mol, 6/4). (D-F) Mass Density profiles of main components in corresponding atomistic systems, solvent (light blue curve), lipid bilayer (gray curve), lipid head (red curve) and antimicrobial molecules.

12. References

[1] Gong H, Sani M-A, Hu X, Fa K, Hart JW, Liao M, et al. How do self-assembling antimicrobial lipopeptides kill bacteria? ACS applied materials & interfaces. 2020;12:55675-87

[2] Le Brun AP, Clifton LA, Halbert CE, Lin B, Meron M, Holden PJ, et al. Structural characterization of a model gram-negative bacterial surface using lipopolysaccharides from rough strains of Escherichia coli. Biomacromolecules. 2013;14:2014-22.

[3] Gong H, Hu X, Liao M, Fa K, Ciumac D, Clifton LA, et al. Structural disruptions of the outer membranes of Gram-negative bacteria by rationally designed amphiphilic antimicrobial peptides. ACS applied materials & interfaces. 2021;13:16062-74.

[4] Gong H, Liao M, Hu X, Fa K, Phanphak S, Ciumac D, et al. Aggregated mmphiphilic antimicrobial peptides embedded in bacterial membranes. ACS applied materials & interfaces. 2020;12:44420-32.

Chapter 5 Combination of pH-responsive AMP hydrogel and conventional antibiotic against Gram-negative bacteria

Mingrui Liao,[1#] Haoning Gong,[1] Xuebo Quan,[2] Xuzhi Hu,[1] Huayang Liu,[1] Zongyi Li,[1] Andrew J. McBain,[3] and Jian R. Lu[1,*]

[1]Biological Physics Laboratory, Department of Physics and Astronomy, School of Natural Science, The University of Manchester, Oxford Road, Manchester M13 9PL, UK.

[2]Shenzhen Bay Laboratory, Institute of Systems and Physical Biology, Shenzhen, 518132, China

[3]Division of Pharmacy and Optometry, Faculty of Biology, Medicine and Health, The University of Manchester, Oxford Road, Manchester M13 9PL, UK.

[#]To whom as PhD candidate should be responsible to all the experiments and simulation work.

[*]To whom all correspondence should be made: J.lu@manchester.ac.uk.

Abstract

Background

Clinical treatments of gastric infections using antibiotics suffer from the undesired killing of commensal bacteria and development of drug resistance. It is desirable to develop pH-responsive antimicrobial peptides that kill pathogenic bacteria such as *Helicobacter Pylori* (*H. pylori*) and resistant *Escherichia coli* (*E. coli*) under acidic condition with minimal toxicity to commensal bacteria whilst not raising the concern of drug resistance.

Experiments

Using a combined approach of cell assays, molecular dynamics (MD) simulations and membrane models facilitating biophysical and biochemical measurements including small angle neutron scattering (SANS), we have characterized the pH-responsive physiochemical properties and antimicrobial performance of two amphiphilic antimicrobial peptides (AMPs), GIIKDIIKDIIKDI and GIIKKIIDDIIKKI (denoted as 3D and 2D, respectively), that were designed by selective substitutions of cationic residues of Lys (K) in the extensively studied AMP G(IIKK)$_3$I with anionic residue Asp (D).

Findings

Whilst 2D kept non-ordered coils across the entire pH range studied, 3D displayed a range of secondary structures when pH was shifted from basic to acidic, with distinct self-assembly into nanofibers and hydrogels in aqueous environment. Further experimental and modeling studies revealed that the AMPs interacted differently with the inner and outer membranes of Gram-negative bacteria in a pH-responsive manner and that the structural features characterized by membrane leakage and intramembrane nanoaggregates revealed from fluorescence spectroscopy and SANS were well linked to antimicrobial actions. Different antimicrobial efficacies of 2D and 3D were underlined by the interplay between their ability to bind to the outer membrane lipid LPS (lipopolysaccharide), outer membrane permeability change and inner membrane

depolarization and leakage. Furthermore, AMP’s binding with the inner membrane under acidic condition caused both the dissipation of membrane potential ($\Delta\psi$) and the continuous dissipation of transmembrane ΔpH, with $\Delta\psi$ and ΔpH being the key components of the proton motive force (PMF). Combinations of antibiotic (Minocycline) with the pH-responsive AMP generated the synergistic effects against Gram-negative bacteria only under acidic condition. These features are crucial to target applications gastric infections, anti-acne and wound healing.

1. Introduction

Membrane permeabilization of cationic antimicrobial peptides (AMPs) can be exploited in a variety of clinical applications by rebalancing their selective responses to the lipid bilayer barriers.[1-2] AMPs can be designed to function in response to pH as a specific trigger because the pH of the wound environment plays an important role in wound healing.[3-4] For example, the healing phase of burns and acute wounds is associated with a temporary physiological acidosis.[4] However, the pH of the wound environment can vary drastically, depending on the type of wounds and the stage of the healing process. The wounds arising from diabetic foot ulcers and pressure ulcers represent a global health issue affecting millions of people.[5] Effective treatment of ulcers and prevention of them from reaching a chronic stage would significantly reduce patient suffering and the economic burden.[6]

Many studies have shown that an acidic environment helps wound healing by controlling wound infection, increasing antimicrobial activity, altering protease activity, releasing oxygen, reducing toxicity of bacterial end products and enhancing epithelization and angiogenesis.[7] Thus, it is important to develop pH-responsive drug delivery systems to enhance therapeutic specificity and accelerate wound healing. However, pH change can influence the efficacies of both conventional antibiotics and AMPs in infected wounds. *In vitro* observations have shown, for example, that the activity of a glycopeptide antibiotic oritavancin to vancomycin-resistant *E. faecium* decreases significantly in an acidic environment compared to neutral and alkaline conditions.[8] In contrast, several studies of pH-responsive polymers or nanoparticles for antimicrobial applications have demonstrated favourable antimicrobial efficacies *in vivo*.[9-11] Xie *et al.* have recently developed a polymer-based Ag nanoparticle clusters that displayed uniform pH-responsiveness and that can reassemble into non-uniform Ag nanoparticles in the acidic microenvironment of bacterial infections. This strategy helped target the living bacteria and secure the sustainable release of Ag^+ nanoclusters.[12] As a combination, pH-responsive polymer-drug conjugates can dramatically increase antimicrobial efficacy by benefiting from the strong synergy between the antibiotics and the pH-responsive polymer system.[13]

In general, hydrogels can maintain a moist environment and achieve the controlled release of bioactive molecules. These constitute the prerequisites for the design of modern wound dressings. Among various antimicrobial systems, responsive hydrogels have received significant attention due to their potential to respond to external triggers such as pH.[14-15] Hydrogels containing ionizable groups such as chitosan tend to display pH-responsive swelling or shrinking in acidic or neutral solution, due to the protonated or unprotonated effects of the amine groups, respectively.[16-17]

Many pH-responsive AMPs, including natural and artificially designed peptides, are potential antibiotics, and their antimicrobial mode of action is based on the permeabilization of microbial membranes. Their amphiphilicity hinges on changes to net charges and amphiphilic conformation switches that are primarily associated with the protonation of histidine, aspartic acid and glutamic acid residues as environmental pH is lowered. A number of pH-responsive AMPs and antimicrobial proteins have been studied, including kappacins, LL-37, histatins and lactoferrin, along with a number of their derivatives,[18-21] with primary therapeutic application aimed at wound healing where infections are often caused by bacterial and fungal biofilms. In general, these applications involve topical administration, such as the use of mouth washes, cream formulations and hydrogel delivery systems.[22]

On the other hand, many potent AMPs suffer from the dilemma of low potency, poor targeting and haemolytic activity, resulting in weak efficacy against pathogens and poor biocompatibility to host cells. Work by Zhang *et al.*[23] has demonstrated how to reduce the adverse effects and improve the antibacterial targeting of their AMPs by surface functionalization. The authors reported a pH-responsive surface coating platform of 2,3-dimethylmaleic anhydride (DMA) that was linked via ethylenediamine (EDA) linker. Melittin (MLT) was then attached to the surface by electrostatic interaction. Under an acidic infection environment, the β-carboxylic acid amides between DMA and EDA were fractured, resulting in MLT release. This functionalization strategy not only achieves pH-responsive release for the targeted antibacterial therapy, but also minimizes the adverse effect of MLT in biomedical applications.[10]

Peptide based antimicrobial hydrogels gather the advantages of both self-assembled hydrogel network and antimicrobial activity of an AMP, providing the prospect of loading with small functional molecules.[24-25] Here we report the design of an AMP hydrogel with pH-responsiveness and co-assembly with a traditional antibiotic, aiming for infection control and wound healing under acidic microenvironment, thereby illustrating the membrane-targeting mechanism underlying pH-responsive antimicrobial activity.

2. Experiment methods

Essential information of the bacterial strains and chemicals used in this study is provided below. Further sample descriptions are given in **Section 1** of **Supporting Information (SI)**.

2.1 Minimum Inhibitory Concentrations (MICs), Dynamic Killing and Drug Combination Evaluations

Antimicrobial assays. *Escherichia coli* (*E. coli*, ATCC 25922) and *Helicobacter pylori* (*H. pylori*, ATCC 700392) were purchased from ATCC, ESBL-*E. coli* were clinically isolated strains obtained from the Manchester Royal Infirmary. Their MICs against different antimicrobials were carried out by microdilution in Muller Hinton Broth (MHB) following the assay protocol by the British Society for Antimicrobial Chemotherapy.[26] All the tests and incubations of *H. pylori* were carried out under anaerobic conditions. Breakpoints used to interpret the MICs were based on the European Clinical Antimicrobial Susceptibility Testing (EUCAST) guideline.[27]

Bacterial dynamic killing. The time-dependent killing of the AMPs and conventional antibiotics was tested to evaluate their antimicrobial efficiency. In brief, bacteria were exposed to a given antimicrobial compound at a selected concentration over different exposure times. Following the protocol employed previously,[28] the bacterial suspension after overnight culture was diluted to 1.25×10^6 CFU/mL in a PBS buffer (pH 7.4 or 5.5) and then mixed with an AMP or antibiotic at the fixed concentration. Aliquots of the mixtures were diluted and transferred to the MHB agar plate after specific time points of exposure and counted after overnight growth at 37.5 °C.

FICI determination. FICs (fraction inhibition concentrations) were evaluated by setting up a chequerboard with 6 concentrations of each antibiotic and the test AMP. At least 2 replicates were done for each combination and the means used for calculation. The MIC for each drug was the lowest concentration that led to no bacterial cell growth. The FIC for drug A was calculated in the presence of drug B for a well showing no growth, divided by the MIC for drug A. The FICI (fraction inhibition concentration index) is the lowest FIC sum of both drug A and B.

2.2 Cell Biocompatibility Assays

Haemolysis assay. AMPs were dissolved in 10 mM PBS buffer at pH 7.4 or 5.5, and the antimicrobial solutions were serially diluted in 10 mM PBS buffer at the same pH. Human red blood cells (hRBC) were diluted in PBS buffer. Then, 100 μL of hRBC suspension (~2%, v/v) was incubated with 100 μL of drug solution at 37 °C for 1 h. After incubation, the mixtures were centrifuged at 1000g for 10 min, and the supernatant (50 μL) was transferred to a new 96-well plate. The released hemoglobin was recorded by the absorbance of the supernatants at 576 nm with a previously used Varioskan LUX microplate reader. The percentage of haemolysis was obtained using the following equation[29]:

$$Haemolysis\ (\%) = \frac{(OD_{576nm}\ of\ treated\ sample - OD_{576nm}\ of\ negative\ control)}{(OD_{576nm}\ of\ positive\ sample - OD_{576nm}\ of\ negative\ control)} \quad (1)$$

where the positive control was hRBCs treated with 0.1% Triton X-100, and the negative control was an untreated hRBC suspension.

MTT assays. The *in vitro* cytotoxicity of AMPs toward HDFa and NIH-3T3 cells (Human Dermal Fibroblast, adult, ATCC PCS-201-012; Embryo Fibroblast, Mus musculus, ATCC CRL-1658) were measured by the 3-(4,5-Dimethylthiazol-2-yl)-2,5-diphenyltetrazolium bromide (MTT) assay. Briefly, MTT solution (10 μL, 5 mg/mL) was added to each well of 96-well plate after the co-incubation of cells (at a concentration of 1 × 10^5 cell/mL) and drugs under different concentrations for 24 h. Then, the samples were cultured for another 4 h. The supernatant was discarded, and 150 μL dimethyl sulfoxide was added to dissolve the formazan crystals. The optical density was read at 570 nm on a microplate reader. Wells without cells were used as blanks and wells without AMP were taken as negative controls.

Fluorescence imaging of cell samples. Cytotoxicity of AMPs was evaluated on NIH-3T3 cells by staining with Calcein-AM/PI. Briefly, 3T3 cells were first incubated overnight in 96-well plates in an incubator (37 °C) under 5% CO_2, then exposed to 100 μL AMP solution at a selected concentration. After removing the supernatant, 3T3 cells were co-stained with Calcein-AM/PI for 20 min and then observed under fluorescence microscopy.

2.3 Evaluation of NPN Uptake and Cytoplasmic Membrane Depolarization Effects

The single colony of *E. coli* (ATCC 25922) was inoculated in 8 ml MHB medium and incubated overnight at 37 °C, shaking at 150 rpm/min. The log-phase bacteria were collected by centrifugation at 4000 × g and washed with sterile HEPES buffer (5 mM HEPES, 20 mM glucose, pH 7.4) twice. The cell suspension was diluted to $OD_{600} \approx 0.1$ in pH 7.4 HEPES buffer and incubated with 10 μM NPN at 37 ℃ in dark place for 1 h untill equilibration. Then, 100 μL bacterial suspension was mixed with AMP at a selected concentration, and fluorescence intensity was recorded continuously with excitation and emission wavelength of 350 and 420 nm, respectively.

Similarly, cytoplasmic membrane depolarization assays directly showed the dynamic membrane damage via fluorescence emission. Log-phase *E. coli* (ATCC 25922) cell suspension was incubated with 2 μM $DiSC_3(5)$ at 37 ℃ in a dark place for 1 h untill the good stability of the fluorescence intensity. An aliquot of 100 μL of the cell suspension was placed in a 96-well plate, AMPs of a chosen concentration was added into the columns and the fluorescence intensity recorded continuously with excitation and emission wavelengths of $\lambda_{ex}/\lambda_{em}$ = 622/670 nm.[30]

2.4 BODIPY-TR-cadaverine (BC) Displacement from LPS in Cell-free and Cell Systems

AMP binding to the lipid A region of LPS was determined using the BC displacement assay, in which the BC probe bound to the cell-free LPS is self-quenched but fluoresces when released in solution.[31] Stock solutions of BC (2 mM) and LPS (2 mg/mL) from *E. coli* were prepared by dissolution in Tris buffer (10 mM Tris + 150 mM NaCl, pH 7.4), separately. The above two stock solutions were diluted together in 10 ml Tris buffer to reach final concentrations of 20 μM and 20 μg/mL, respectively, and kept in the dark at room temperature for stability. 100 μL AMP in Tris buffer and 100 μL of the LPS-probe mixture were added to the 96-well plates. After 1h incubation in the dark at room temperature until equilibration, and fluorescence emission was measured on a microplate reader with excitation wavelength of 580 nm and emission wavelength of 620 ± 20 nm, respectively. EC_{50} is the midpoint of the curve corresponding to the half displacement of the probe.[32]

In the BC displacement of the cell system, *E. coli* cells of log-phase were washed with Tris buffer twice and diluted to $OD_{600} \approx 0.1$, and then incubated in presence of 20 μM BC solution in the dark for equilibration. After that, bacterial cell suspension was added with AMP at a selected concentration, fluorescence change would be recorded continuously with excitation wavelength of 580 nm and emission wavelength of 620 nm, respectively. The measurements for peptides' interference with the emission of BC was carried out for following the analysis. All the assays were performed in 96-well plates.

2.5 NAO Assays and Leakage of SUVs

Lipid POPC and POPG (with a molar ratio of 7/3) were dissolved together in chloroform, and the solvent was evaporated overnight to obtain dry phospholipid films. Then lipid films were dissolved in the Tris buffer (pH 7.4) at 5 mg/mL and followed by a previously used extrusion method to produce uniform SUVs with a diameter of around 50 nm.[33] To identify the roles of PG in peptide-induced membrane depolarization, a cationic fluorescent probe 10-N-nonyl acridine orange (NAO) known to bind to negatively charged lipids was used to reveal peptides' affinity to anionic lipid domains. SUVs solution (2 mM in Tris buffer) was diluted and mixed with NAO stock solution (2 mM in ethanol) with a final concentration of 10 μM (SUVs) and 4 μM (NAO), respectively. Peptides of gradient concentration were added to NAO-loaded SUVs in 96-well plate and followed by a 15 min stabilization at room temperature. The fluorescence intensity was recorded at room temperature on a previously used microplate reader with excitation and emission wavelengths of 488 and 520 nm, respectively. The data were normalized based on the fluorescence intensity in SUV-free wells (maximum fluorescence of NAO in solution, 100%) and peptide-free wells (minimum fluorescence of lipid-bound NAO, 0%).

For the dye-entrapped SUVs preparation, lipid films were dissolved in 40 mM calcein solutions in Tris buffer (pH 7.4) at 5 mg/mL, followed by a same extrusion method to produce calcein-loaded SUVs. After removing the extra dye outside the SUVs via a column chromatography filled with Sephadex G50 Gel (0.1g/mL). An appropriate SUVs concentration was selected for further measurements of membrane disruption activity by calculating the fraction of calcein leakage of the SUVs induced by peptides. Leakage of calcein was quantitatively determined by the increase in fluorescence emission in aqueous environments resulting from the decrease in self-quenching. Antimicrobial solutions were prepared by a serial twofold dilution method. Mixtures of SUVs and AMPs were kept in the dark for 30 min interaction and measured by a previously used microplate reader (Varioskan LUX). All the measurements were in 96-well plates with excitation wavelength of 490 nm and emission spectra scanning from 510 to 530 nm, and the emission peak at 518 nm was selected as representative leakage intensity of the calcein-loaded SUVs. The leakage percentage (%) for each compound was calculated as follow:

$$\textit{Leakage fraction}\ (\%) = \frac{(I_{sample} - I_{neg})}{(I_{pos} - I_{neg})} \times 100 \tag{2}$$

where I_{neg} and I_{pos} are the negative and positive controls, respectively, indicating the initial zero calcein leakage before the addition of AMPs and the 100% fluorescence after the addition of 0.2% (w/w) Triton X-100. I_{sample} is the fluorescence intensity after peptide addition.

2.6 Circular Dichroism (CD) Spectroscopy, Thioflavin T (ThT) Titration and Atomic Force Microscopy (AFM)

To explore the secondary structures of AMPs under different pH conditions and in the state of hydrogel, CD spectra were recorded on a Chirascan Series Spectrometer at room temperature. The sample solution was contained in a rectangular quartz cell with a light pass length of 1 mm under a constant flow of nitrogen gas. The wavelength was obtained from 260 to 190 nm with a step of 1 nm, the sample concentration was diluted to 0.5 mM for measurement.

ThT titration was specifically used to characterize the β-sheet conformation of a self-assembled peptide. The fluorescence spectra of the samples were recorded on a previously used microplate reader with an excitation wavelength of 420 nm and emission wavelength from 450 nm to 650 nm, respectively. A ThT stock solution was prepared and added to the peptide solution of different concentrations, and the final concentration of ThT was at 50 μM. The mixture solution was incubated at room temperature for 2 h equilibration for the following fluorescence test.

To further characterize the self-assembled morphological structures of a peptide AMP, AFM imaging was carried out on a Bruker Dimension 3100 instrument (Karlsruhe, Germany) in tapping mode in air. The samples were dropped onto a fresh mica wafer surface for AFM imaging and dried under atmospheric conditions.

2.7 MD Simulations

Peptide Self-assembly in Bulk Solution. To investigate the self-assembly behaviour of peptide 3D in bulk solution by MD simulation, the peptide number in each simulation system was fixed and solvated with 100 mM NaCl solution. According to the secondary conformation of the peptide in neutral/acidic solution, 3D was constructed with random coil conformation and different protonation states. The peptide solution systems used periodic boundary conditions and had a MD simulation time of ten microseconds after energy minimisation and pre-equilibration.

Force Field and MD Parameters. MD self-assembly processes were carried out at a coarse-grained (CG) molecular level using the MARTINI force field.[34] The standard cut-offs for the MARTINI force field were used for non-bonded interactions; a cut-off of 1.1 nm was used for van der Waals (vdW) interactions, and the Coulomb potential was shifted to zero between 0 and 1.1 nm with a relative dielectric constant of 15 to account for non-polarizable water. The time step used was 20 fs and the neighbour list was updated every 10 steps.[35-36] All peptide 3D structure models were set up by Avogadro software firstly to generate peptides' topologies, and the Martinize (v.2.6) script was used. The peptide structures were also used for secondary structure assignment, employing the Define Secondary Structure of Proteins (DSSP) program.[37] All simulations were run by the Gromacs 2016 package,[38] and every simulation system initially experienced energy minimization for removing close molecular contacts. Thereafter, MD runs for the peptide-bilayer system were carried out in the constant-*NPT* ensemble at ~ 310 K using the Berendsen (equilibration run) and Nosé-Hoover (production run) thermostats with a time constant of 2 ps, representing physiological temperature as successfully employed previously in the MARTINI model, with pressure bath of 1 bar controlled by Berendsen (equilibration run) and Parrinello-Rahman barostat (production run) with time constants of 6 and 12 ps, respectively.[39-41] The compressibility of the systems was set at 3×10^{-4} bar^{-1} in both lateral and normal directions to ensure a tensionless lipid bilayer. While in the peptide-solution system, there is no pressure loaded on water box after an equilibration run.

2.8 SANS of Peptide Self-assembly and Lipid SUVs with AMPs

All the SANS experiments were performed on the LARMOR diffractometer at the ISIS Pulsed Neutron Source (Rutherford Appleton Laboratory, Didcot, UK) and the D11 diffractometer at the ILL (Grenoble, France), using the same experimental configuration as previously described.[42] Prepared POPC/POPG (a molar ratio of 7/3) and LPS/POPC (a molar ratio of 1/9) SUVs were diluted in D_2O Tris buffer (10 mM Tris + 150 mM NaCl, pH 7.4) and then mixed with AMP stock solutions for SANS measurements. The final SUV concentration was 1 mM, and AMP concentrations were 0.05, 0.1, and 0.2 mM. All the samples were measured at 22 °C and performed once. Correction and azimuthal averaging of the as-measured SANS data were performed in the Mantid framework (www.mantidproject.org). Reduced SANS data were then fit with a core multilayer shell model (http://www.sasview.org/sasview/user/models/model_functions.html#coremultishellmodel) using the SasView 5.0 software (www.sasview.org).

2.9 Fluorescence Spectra of AMP-MC Drug Pair Interaction

Fluorescence spectroscopy analysis including fluorescence excitation and emission spectra for peptide hydrogel 3D-Mg^{2+}-MC (minocycline) solutions and free Mg^{2+}-MC solutions was carried out. The molar ratio of MC to 3D was at 1:1 in presence of 50 mM Mg^{2+} solution. Fluorescence excitation and emission were measured in 96-well plates by a microplate reader used previously. The fluorescence excitation and emission of MC-Mg^{2+} solutions under both acidic and neutral conditions were strongly affected by the addition of peptide 3D. The wavelength of excitation spectroscopy was from 320 nm to 500 nm, and excitation/emission wavelength of emission spectroscopy was 400 nm/450 ~ 650 nm.

3. Results and discussions

3.1 Self-assembly of pH-responsive Peptides

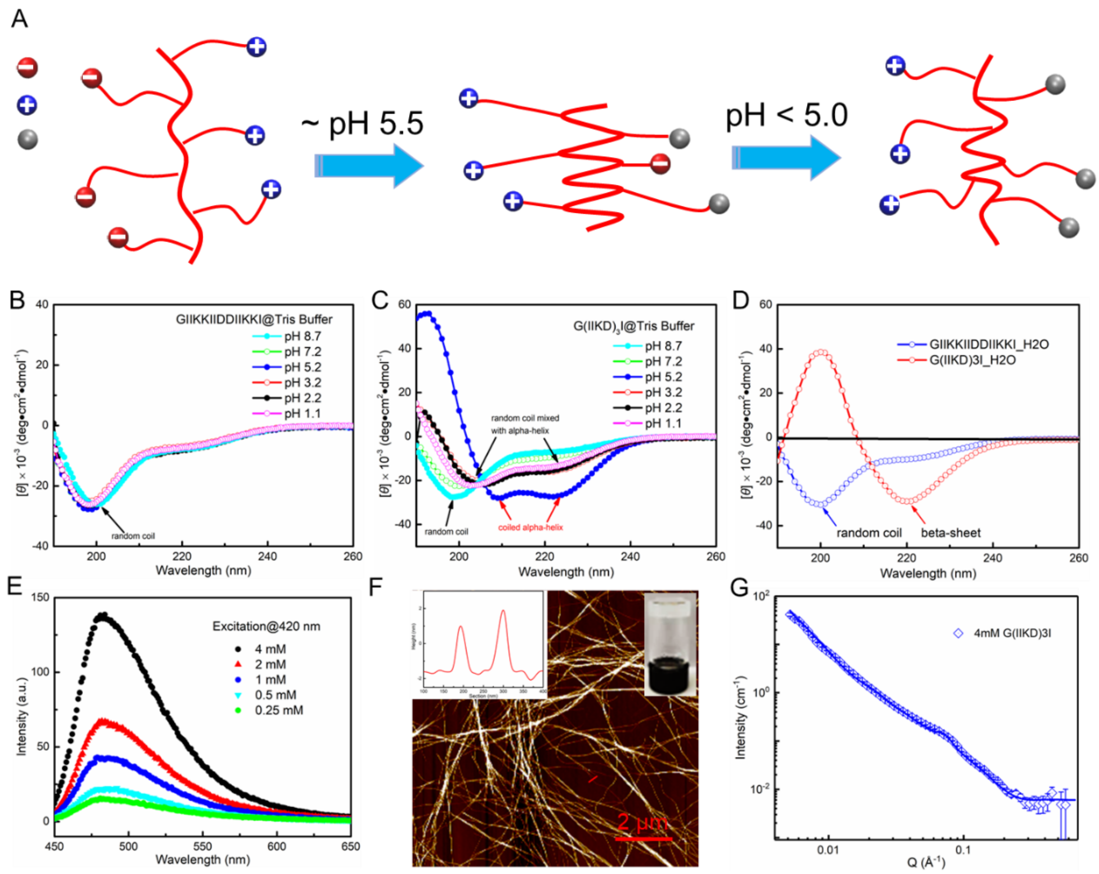

Figure 1. Secondary structural conformation and self-assembly of AMPs in aqueous environment. (A) Schematic illustrations of the pH-responsive conformation transitions of G(IIKD)$_3$I (3D), showing its adoption of the random coiled conformation at the physiological pH to impart low toxicity while transforming to the helical conformation under acidic condition to induce potent antimicrobial activity. The blue balls represent cationic groups, the red balls represent anionic groups (-COO$^-$), and the grey balls represent neutral groups (-COOH). (B, C) CD spectra of GIIKKIIDDIIKKI (2D) and 3D (500 μM) at pH values adjusted from 8.7 to 1.1 in Tris buffer (10 mM Tris + 150 mM NaCl). (D) The secondary structures of 3D self-assembled hydrogels and 2D (both peptides are at a concentration of 3 mM) in the neutral Tris buffer solution. Structural characterizations of the 3D self-assembly in the neutral aqueous solution by (E) ThT titration, (F) AFM image of self-assembled 3D nanofibers in the gel state (scale bar is 2 μm), the inset graphs were the local depth profile marked by the red line (left) and peptide’s macroscopic hydrogel state (right), and (G) SANS of 4 mM 3D self-assembled in neutral D$_2$O solution showing a typical lamellar morphology.

AMPs of GIIKKIIDDIIKKI (2D) and G(IIKD)$_3$I (3D) contain Asp (D) and Lys (K) residues and their charged states are pH dependent. Their molecular conformations in the aqueous solution must also be pH responsive. Figure 1A depicts the possible structural conformations that can be adopted by 3D as the solution pH goes down from physiological to the acidic condition due to the diminishing charges of the D residues. As its concentration increases, each peptide may adopt a different conformation due to increased intermolecular interactions. Changes in the secondary structure of the 2D and 3D peptides with pH in the solution form (at a concentration of 0.5 mM) were investigated by circular dichroism (CD) and the results are shown in **Figures 1B&C**. 2D adopted random coils over the entire pH range from 8.7 to 1.1, while 3D adjusted its secondary conformation with the decreasing charge state of D (pKa ~ 3.9). At pH $\geq$ 7.2, the carboxyl groups exhibited strong negative charges. 3D adopted random coils due to the intermolecular electrostatic interaction between the negatively charged carboxyl groups and the positively charged amine groups of the K residues. In contrast, as pH is shifted to acidic, carboxyl groups become partially protonated, 3D adopted the helical conformation, evident from the double minima at 208 and 222 nm, showing the direct impact from the depleted side-chain charge interactions. At pH ~ 5.2, 3D showed a standard coiled α-helical structure supported by strong positive signal around 195 nm. (**Figure 1B**) Further pH reduction led to the coexistence of random coils and α-helical conformations. Similar pH-responsive secondary conformation changes were also observed from antimicrobial polypeptides bearing randomly distributed negatively charged glutamic acid and positively charged synthetic residues.[43]

SDS micelles were used as a negatively charged membrane model to test conformational transitions. Both 2D and 3D adopted α-helical conformations when bound to the SDS micelles and this structural transition was independent of pH, showing that electrostatic interactions between peptides and SDS micelles favoured the conformational transition, typical of amphiphilic peptides. (**Figure S2A&B**)

Different from random coils or α-helix of 3D under the solution state (at concentration of 0.5 mM), 3D self-assembled hydrogel at the concentration of 3 mM presented a typical β-sheet indicated by a strong negative signal between 210 and 220 nm in the CD spectrum. (**Figure 1D**) With the increase in concentration, the non-ordered 3D in neutral solution underwent rapid self-assembly and transformed into β-sheet rich fibrils. In the neutral solution environment (pH ~ 7.0), the hydrophobic collapse of the Ile residues offered strong propensity to hold the peptide molecules together, while the side chains of the oppositely charged Asp and Lys residues significantly improved the intermolecular electrostatic attraction and hydrogen bonds. These interactions together directed the linear 3D to the extended β-sheet conformation, with the charged/hydrophilic Asp/Lys and hydrophobic Ile segregated on the opposite sides of the peptide backbone.[44-45] The periodic distribution of Asp and Lys residues in 3D tended to bury the Ile residues by forming a bilayer structure along the lateral direction to diminish the contact of Ile with water. This feature is well supported by the MD simulations to be shown later.

The β-sheet conformation of 3D in hydrogel state would be disrupted in presence of negatively charged SDS micelles. Instead, α-helical conformation can be promoted, a structural feature supported by the positive and negative signals at 195 nm and 208 nm, respectively. (**Figure S2C**) In contrast, exposure of 2D at low and high concentrations of 0.5 and 3 mM to the SDS micelles in the neutral Tris buffer transformed from random coils into perfect α-helix conformation, (**Figures 1D&S2**), showing no obvious self-assembling behaviour with increasing peptide concentration.

The β-sheet conformation in 3D hydrogel can also be confirmed by thioflavin T (ThT) titration experiments as shown in **Figure 1E**. ThT is a fluorescence probe that specifically binds with the amyloid-like β-sheet structure, resulting in enhanced fluorescence emission. The emission intensity of ThT around 480 nm increases with the concentration of 3D, suggesting the association of the solubilized ThT with the β-sheet in 3D self-assembled hydrogel.[46-47]

AFM imaging (**Figure 1F**) provided the direct evidence of the long nanofibrils formed from the self-assembly of 3D in solution, with thickness of 3.5 ± 0.5 nm, width of 50-80 nm and length of several μm (inset graph). Self-assembled nanofibrils collapsed onto the substrate surface can well be deformed. To further unravel the *in-situ* structure of the 3D nanofibrils in solution environment, specifically their diameters, SANS measurements were undertaken. Analysis to the SANS profile measured from the 3D hydrogel in D_2O buffer revealed the typical lamellar structure of the self-assembled morphology, with the thickness of the lamellae about 3.2 ± 0.1 nm. (**Figure 1G**) Other fitted parameters are given in **Table S2**.

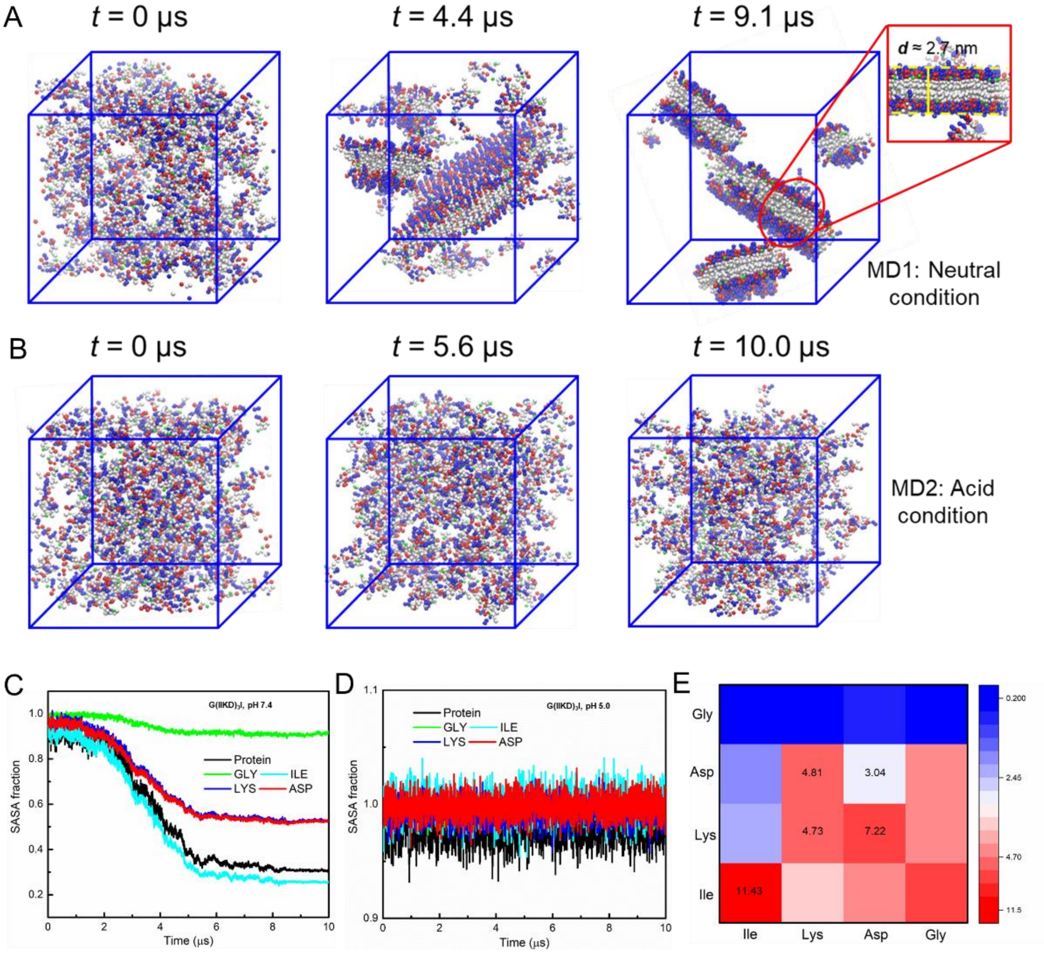

Figure 2. Self-assembly pathway of 3D at fully deprotonated and protonated states, which corresponds to the neutral (pH 5.5 – 9.0) and acidic pH (pH 1.5) values. (A, B) Self-assembly process of 3D represented by snapshots at three different time points under neutral and acidic conditions. (C, D) The solvent accessible surface area (SASA) fractions of the whole peptide and constituent residues (Gly, Ile, Lys, and Asp) as a function of simulation time under neutral (C) and acidic (D) conditions. (E) Contact numbers of different group pairs calculated using the last 1.0 μs simulation data in self-

assembly under neutral condition.

In order to decipher the mechanistic process underlying the experimentally observed formation of the 3D hydrogels, we conducted two individual 10 μs coarse-grained MD simulations on a system consisting of 200 3D molecules in neutral (Asp in fully deprotonated state) and extremely acidic (Asp in fully protonated state) aqueous solutions. The concentration of 3D in our simulations was 98 mM. This is much higher than that used in the experiments, but increasing concentration helps to accelerate the simulated aggregation process and save computational resources.[48-50] Initially, 200 3D molecules were randomly dispersed in the simulation box in both simulations. (**Figures 2A&B**) Under MD simulations of the peptide self-assembly at neutral condition, 3D molecules self-assembled into small lamellar clusters within 5 μs. After a further 4 μs, some small clusters fused into big ordered lamellar sheets, consistent with the decrease of the number of clusters and increase of the size of the lamellar sheets. The growth of the small aggregates into fewer but larger sheets took some 9 μs in the simulation time scale. However, stacking of single lamellar into multiple lamellar sheets did not occur. A single lamellar layer of 3D is about 2.7 nm thick from MD simulations, consistent with the SANS and AFM measurements.

A totally different scenario was observed in the MD simulations of the peptide self-assembly under acidic condition (**Figure 2B**) where the 3D molecules did not appear to self-assemble. A 3D molecule is composed of four types of amino acid: Gly (G), Ile (I), Lys (K), and D. To unravel the different roles of these four side chain groups during hydrogel formation, we calculated the fractions of their solvent accessible surface area (SASA) with respect to the SASA values in the initial randomly dispersed state. It can be seen from **Figure 2C** that the SASA fractions of three groups (I, K and D) rapidly dropped within the first 5.0 μs and then slowly decreased to their equilibrium values. However, G followed a slow and then further delayed SASA decline process. This can arise from G to be located at the edge of the lamellar sheet with little change in its solvent access. In contrast, the SASA fractions of all the residue types under acidic condition changed little within time. At the end of the simulation time, the SASA fraction values of hydrophobic I and charged K and D groups in MD runs under neutral and acid conditions were 0.26/1.0 (Ile), 0.53/1.0 (Lys) and 0.52/1.0 (D), respectively, lower than those of G (0.91/1.0). (**Figures 2C&D**) The SASA fractions of the K and D groups were comparable and much higher than that of I. These results demonstrate that the I groups are favourable to be buried inside the aggregates and form the hydrophobic cores within the hydrogels, while the K, D and G residues prefer to be exposed to the aqueous solution. **Figure 2E** shows that the I-I group pair had the highest contact number (11.43) within the radius of 0.674 nm, probably because they are the nearest neighbours in the sequence, indicative of the strongest interaction between them. The contact number between D and K groups ranked second (7.22/4.81). These results indicate that the interactions of I-I groups and K-D groups play important roles in hydrogel formation.

3.2 Antimicrobial Activities of Peptides

Table 1. MICs of antimicrobial peptides 2D and 3D and antibiotics against Gram-negative bacteria under acidic and neutral environments.

Bacterial Strains /Peptide	***E. coli*** **(ATCC 25922)/μM**		**ESBL *E. coli*/μM**		***H. pylori*/μM**	
	pH 7.4	pH 5.5	pH 7.4	pH 5.5	pH 7.4	pH 5.5
G(IIKD)$_3$I (3D)	62.5	31.3	93.8	31.3	> 100	22.9
GIIKKIIDDIIKKI (2D)	7.8	3.9	7.8	5.9	> 100	31.5
Tetracycline (TC)	4.6	2.3	4.6	2.3	2.3	3.1
Ampicillin	6.0	4.6	>500	> 500	--	--

Table 1 lists the minimum inhibitory concentrations (MICs) of the two designed AMPs against Gram-negative bacteria including *E. coli*, resistant ESBL-*E. coli* and *H. pylori* at pH 5.5 and 7, showing much higher MICs at pH 7.4. The antimicrobial activity of 2D is comparable to Tetracycline (TC) against both susceptible and resistant *E. coli* strains at the acidic pH. However, both 2D and 3D show superior antimicrobial

activities to ampicillin, as its MICs against ESBL-*E. coli* tend to be over 500 μM under both pH conditions.

Figures 3A&B show dynamic killing of the two AMPs against Gram-negative *E. coli*. 2D showed little response to pH but the dynamic killing was strongly time dependent. After 3 h exposure, ~70% of *E. coli* were killed, and no active cells can be detected after 6 h. In contrast, 3D displayed a strong pH dependence in its dynamic killing, with little antimicrobial effect under neutral condition. However, its dynamic killing at pH 5.5 closely followed those of the 2D profiles. These results show that the pH-responsive conformational changes also affect how 3D molecules attack bacterial membranes and their killing efficiency. The time dependent effects are broadly similar between susceptible and resistant ESBL strains, showing that the dynamic killing based on membrane disruption is not influenced by antibiotic resistance.

For comparison, dynamic killing from two other cationic AMPs was also assessed under same conditions. Both $G(IIKK)_3I$ and Polymixin B (denoted as GIK and PMB) displayed fast dynamic killing against *E. coli* and ESBL-*E. coli* at the concentration of 20 μM under neutral pH. (**Figures 3C&D**) However, little dynamic killing was observed over the same period of incubation under acidic condition. In contrast, the dynamic killing of TC was not much affected by pH change, consistent with its inhibitory action against the intracellular target.[51] Again, the main features of time dependent killing between susceptible and resistant strains remain the same for both TC and AMPs.

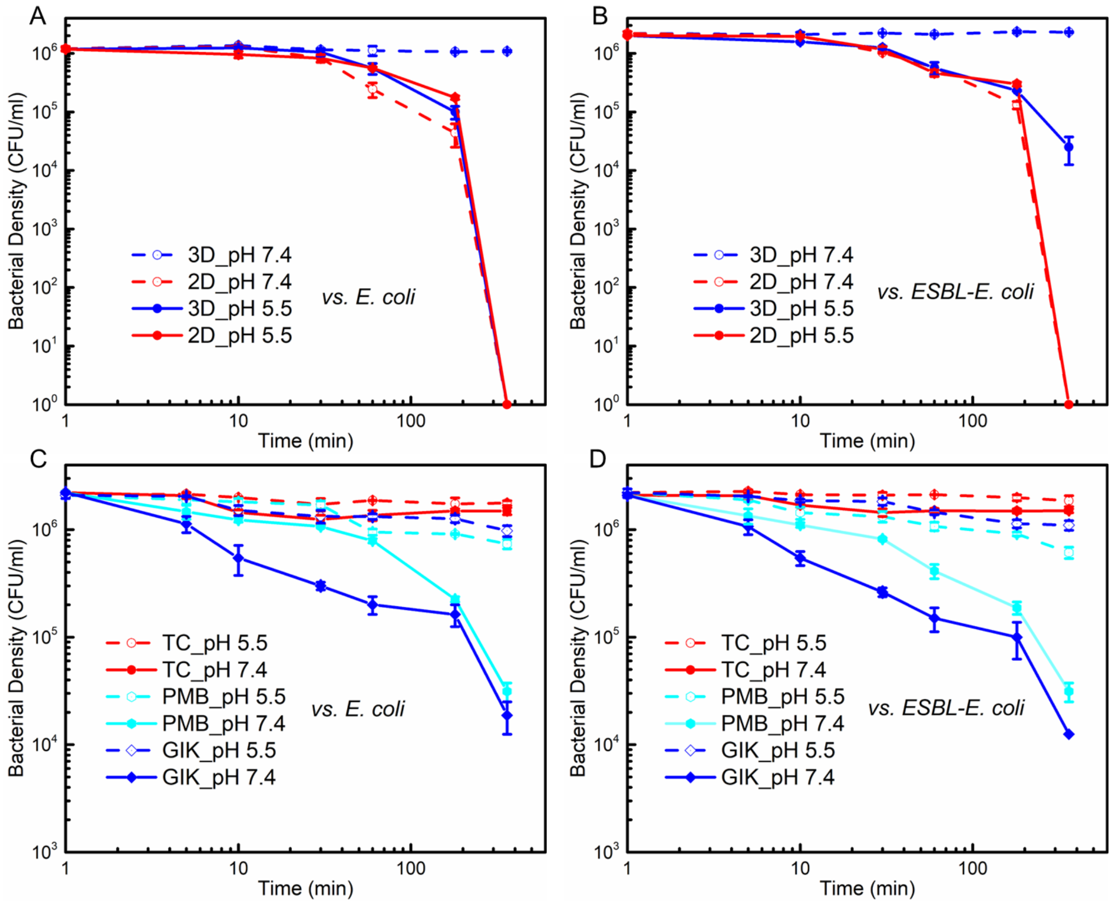

Figure 3. Dynamic killing of 2D and 3D against Gram-negative (A) *E. coli* (ATCC 25922) and (B) ESBL-*E. coli* (clinical strain) at concentration of 80 μM in presence of both acidic (PBS buffer, pH 5.5) and neutral (PBS buffer, pH 7.4) environments. (C, D) Dynamic killing of antibiotic TC, lipopeptide antibiotic PMB and peptide GIK as controls (with concentration of 20 μM) under pH 5.5 and 7.4. The bacterial density change in CFU/mL (Y-axis) is plotted against exposure time in minute (in log-log scale).

3.3 Cytocompatibility of Peptides

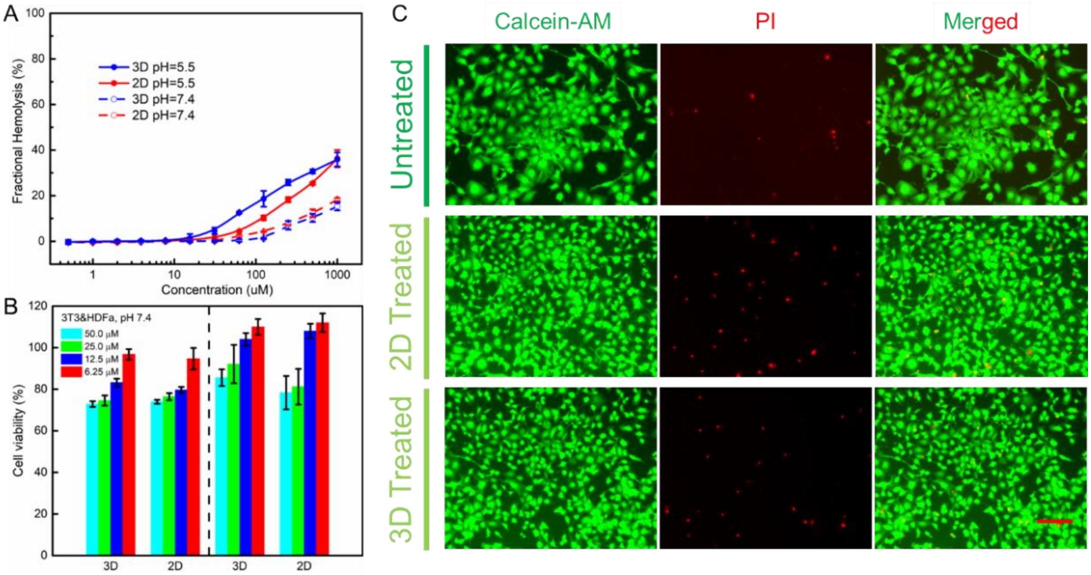

Figure 4. (A) Haemolysis evaluation of AMPs at pH 5.5 and 7.4, (B) NIH-3T3 mouse embryo fibroblast cells (left part) and HDFa cells (right part) for 24 h incubation at different AMP concentrations at pH 7.4. (C) Calcein-AM/propidium iodide (PI) staining of 3T3 cells after exposed to 50 μM 2D and 3D AMPs for 24 h. Scale bar, 50 μm.

Both 2D and 3D show slight haemolytic activity to human red blood cells and mild cytotoxicity to mammalian cells 3T3 and HDFa (**Figures 4A&B**). The fractions of the haemolyzed red blood cells from 2D and 3D treated groups (concentrations as high as 100 μM) increased from ~ 4.5% to 18% only, suggesting the high biosafety of the peptides. At the AMP concentration of 50 μM, some 80% HDFa cells were still viable. Furthermore, Calcein-AM/PI staining of 3T3 cells showed no obvious inhibition of growth after 1 day of incubation of the 3T3 cells with 50 μM AMPs (**Figure 4C**). These results indicate that these AMPs are safe and promising candidates when used alone or in combination with antibiotics.

3.4 FICI Determination of Drug Combination and Mode of Membrane Disruption

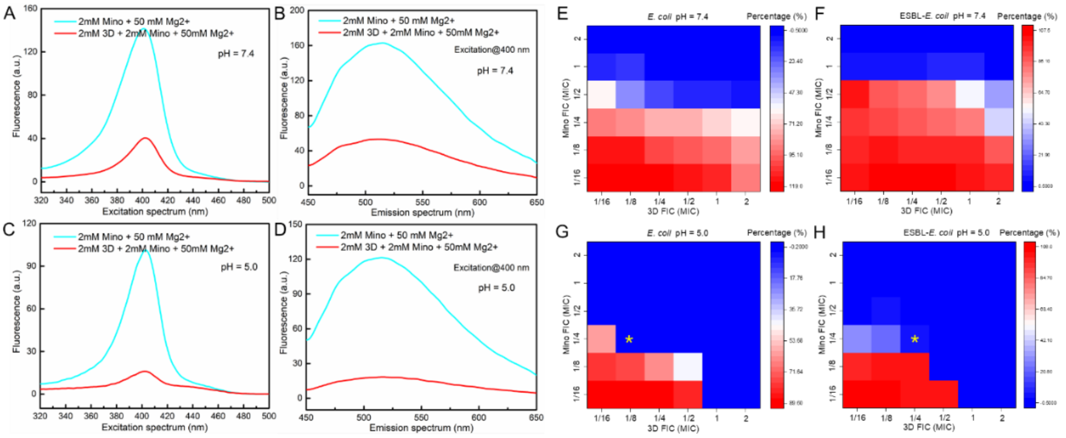

Figure 5. (A-D) Fluorescence excitation and emission spectra for AMP-MC drug pairs of 3D-MC complexes at the molar ratio of 1/1 being dissolved in 50 mM Mg^{2+} solution at pH 5.0 and 7.4. (E-H) Heat maps show the antimicrobial activities of the drug pairs against Gram-negative *E. coli* and ESBL-*E. coli* under acidic and neutral Tris buffers (10 mM Tris + 150 mM NaCl). The star points show the fractional inhibitory concentration index (FICI) in synergetic drug pairs.

As an amphiphilic AMP, 3D at the concentrations below 2 mM prefers to form lamellar structure under neutral pH condition. Its co-assembly with antibiotic Minocycline (denoted as MC) was studied by fluorescence spectroscopy. The fluorescence excitation and emission of the MC-Mg^{2+} solutions were strongly affected by the addition of 3D under neutral or acidic conditions. (**Figures 5A-D)** The fluorescence spectra indicated that strong 3D-MC interactions in the form of 3D-Mg^{2+}-MC complexes decreased the fluorescence excitation efficiency and fluorescence emission of MC. The 3D-MC complexes displayed a strong synergetic effect against Gram-negative *E. coli* and ESBL-*E. coli* under acidic condition (FICI is lower than 1/2) but an antagonistic effect under neutral condition. (**Figures 5E-H&S4**) Here, the combinations with the lowest FICI value that shows a bacterial inhibition over 90% are considered to be optimal. These combinations are marked with star points in Figures 5G&H.

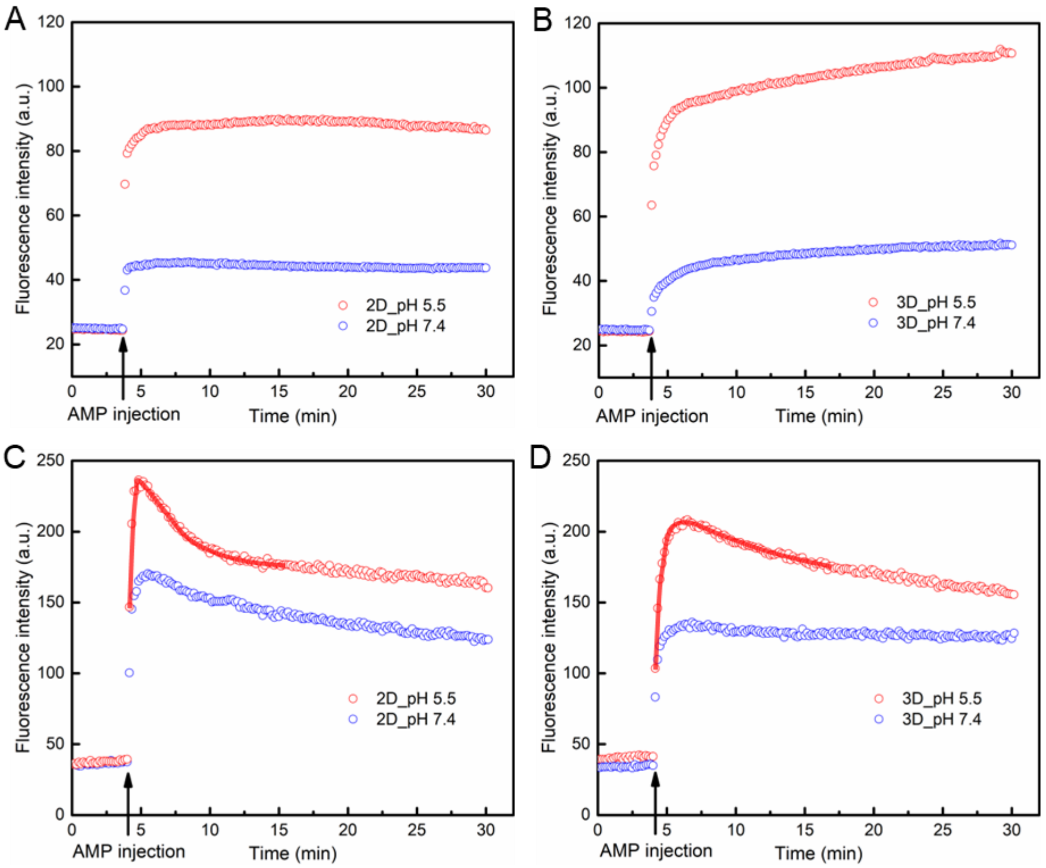

Figure 6. (A, B) Permeability change of outer membrane measured by fluorescence leakage of 1-N-phenylnaphthylamine (NPN) produced by pH-responsive binding of 2D and 3D at the concentration of 100 µM in *E. coli* under pH 5.5 and 7.4 (Tris buffer). (C, D) Cytoplasmic membrane depolarization (inner membrane) caused by pH-responsive 2D and 3D binding at the concentration of 100 µM against *E. coli* and the process was probed by the decaying fluorescence of the dye $DiSC_3(5)$.

The bactericidal actions associated with pH-responsive 2D and 3D binding to Gram-negative *E. coli* (ATCC 25922) were explored by permeability changes of the outer membrane as well as depolarization changes of the inner membrane. From the NPN uptake induced by 3D and 2D binding and indicated by fluorescence intensity, pH decrease favoured the change of membrane permeability of 3D, but it took longer time for 3D to equilibrate than 2D at both pH conditions, indicating that 2D can induce membrane deactivation more rapidly in contrast to 3D, consistent with the MICs showing better antimicrobial efficacy of 2D than 3D in both pH conditions.

In undertaking the fluorescence-based probing of membrane depolarization, bacteria were mixed with the dye DiSC$_3$(5), which was then accumulated in the cytoplasmic membrane in response to membrane potential change ($\Delta\psi$) and which then became self-quenched. When $\Delta\psi$ was disrupted upon peptide exposure, the dye was released into the medium, resulting in an increase in fluorescence. Greater inner membrane depolarization caused larger dye leakage via the dissipation of the membrane potential upon the exposure of 2D and 3D, and the fluorescence intensity of the quasi-equilibrium state under acidic condition was much stronger than neutral condition for both AMPs. Apart from its role as an indicator of membrane depolarisation, DiSC$_3$(5) can also inform the loss of the other component of the proton motive force (PMF), the transmembrane ΔpH, through the observed decrease in fluorescence. When the pH gradient is lost, bacterial cells compensate by increasing $\Delta\psi$ to keep the PMF constant. This increased membrane potential further concentrates the DiSC$_3$(5) dye in the membrane, so that high local concentration can lead to a decrease in fluorescence intensity due to further quenching. Although 2D led to a sharp increase of the DiSC$_3$(5) intensity and reached the peak value within 1 min, the further decrease of the fluorescence intensity was indicative of the disruption of ΔpH across the cell membrane. The partially protonated 2D and 3D molecules can be electroneutral antiporter for H^+ and K^+ causing a decrease in fluorescence as they selectively dissipate ΔpH. (**Figures 6C&D**) Because the membrane potential (ψ) and the transmembrane pH gradient (the difference between the intracellular and extracellular pH) are interdependent and constitute the two components of PMF, a shift in the extracellular pH to basic condition can lead to a decrease in the pH gradient across the membrane and a greater compensatory component in $\Delta\psi$ and a greater share of PMF. In contrast, a shift to acidic condition can lead to an increase in ΔpH across the membrane, resulting in a compensatory fall in $\Delta\psi$, such that the ΔpH component would enhance in PMF.[52] The ΔpH disruption incurred in 2D was more obvious than in 3D under neutral pH, consistent with the fact that 3D possesses better pH-responsive membrane-targeting than 2D.

3.5 BC Displacement, NAO Assays, Leakage and SANS of SUVs after AMP Binding

BC (BODIPY™-TR-cadaverine) displacement of the cell-free LPS system was carried out to examine if the peptides had any affinity to bind to LPS. Binding of AMP peptides to the LPS membrane can induce a dose-dependent displacement of the BC probe. After incubation with LPS, 2D and 3D incurred distinct BC displacements from LPS binding at pH 5.5. In contrast, little changes were observed at pH 7.4, indicating minimal affinity of the AMPs to LPS (**Figure. 7A**). From the peptide concentration corresponding to the 50% BC displacement, 2D and 3D showed very low concentrations (~ 2.5 μM) at pH 5.5, while the concentrations of 50% displacement increased sharply at pH 7.4 (> 50 μM). In BC displacements from the outer LPS membranes in cell systems, the efficacies of the fluorescence displacements by these two peptides under acidic condition were again much more significant than those obtained under neutral condition, consistent with the low capacities of AM binding to the lipid A region of LPS on the outer cell membrane under the physiological pH.

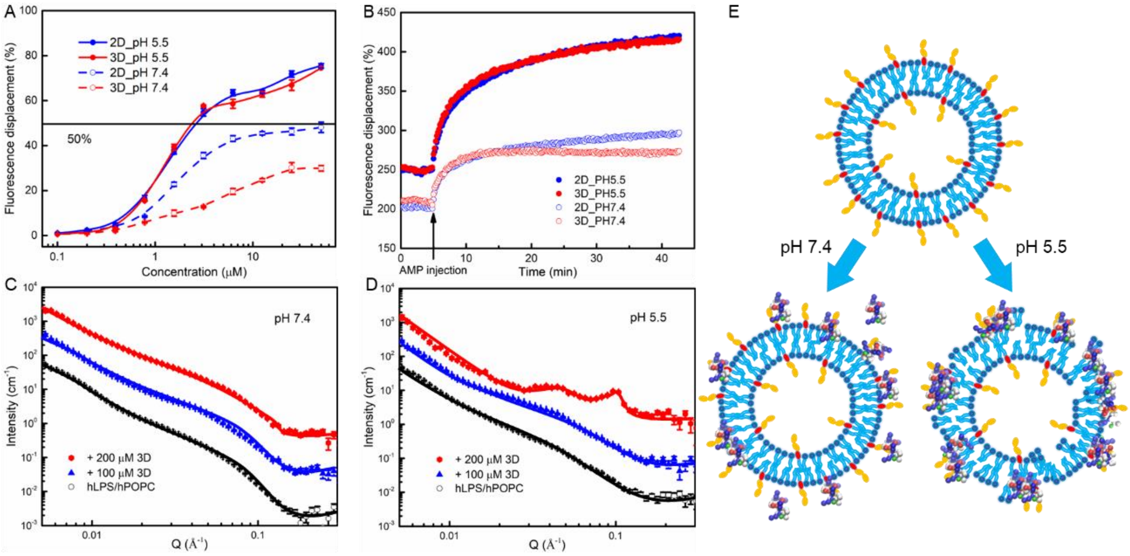

Figure 7. (A) AMP binding to LPS in cell free and cell systems. (A) Fluorescence displacements in fluorescence assays of BODIPY™-TR-cadaverine (BC) (5 μM) to show concentration-dependent binding of 2D and 3D to LPS molecules (20 μg/mL)

from cell-free systems at pH 5.5 and 7.4; (B) Dynamic BC fluorescence changes to show the time-dependent binding of 2D and 3D to the outer LPS membrane of *E. coli* (ATCC 25922) at the AMP concentration of 50 μM. (C, D) SANS scattering intensity profiles, measured as a function of momentum transfer (Q), from POPC/LPS (mol/mol, 9/1) SUVs, without and with AMP 3D at concentrations of 100 and 200 μM in D_2O Tris buffer at pH 7.4 (C) and 5.5 (D), with the parallel SANS results of AMP 2D shown in **Figure S3**. (E) Schematic illustrations to show the selective formation of intramembrane peptide-lipid aggregates under different pH environments. All the measurements were carried out in both pH 5.5 and 7.4 (10 mM Tris + 150 mM NaCl).

To further explore how 2D and 3D interact with outer LPS membrane, a SUV model of POPC/LPS was built for the SANS study. (**Figures 7C&D**) SANS analysis results indicated that the POPC/LPS SUVs alone adopted a typical spherical structure under both neutral and acidic conditions, with radius around 200 Å. The membrane bilayer was fitted into a symmetrical 3 layers, with the middle acyl chain layer of 30 Å and each of the two outer head layers of 17 Å. Data analysed from the SANS profiles obtained from SUVs mixed with 2D and 3D under neutral condition suggest little size changes but how SLD changes and hence peptide binding. (**Figures 7C&S4A**) Upon binding of 2D and 3D at pH 5.5, however, the overall SUV nanostructures changed and the extent of the changes increased with increasing peptide concentration, consistent with intensified AMP attacking. The most distinct structural change was the transformation of the single bilayer into periodic multi-bilayer stacks, supported by the broad peaks in their corresponding SANS profiles (**Figures 7D&S3B**). The occurrence of the broad peaks from both AMPs under acidic condition suggested structural disruptions to the bilayer and fusion of small membrane stacks associated with the formation of AMP-LPS nanoaggregates. The broad peaks have characteristic Q-position at 0.1 $Å^{-1}$ from 3D binding at 200 μM and 0.095 $Å^{-1}$ from 2D binding at 200 μM, respectively, indicating the repeating bilayer unit thicknesses around 60 Å (= $2\pi/Q$). The size for 3D at Q-position of 0.04 $Å^{-1}$ would be much larger, again resulting from the structural damage. The broad peak intensity is related to the number of repeating bilayer units in the stack. These bilayer stacks were clearly formed when the SUVs were exposed to the concentrations of 2D and 3D at 100 and 200 µM under acidic condition, with peak intensities at Q-positions of 0.01 and 0.02 Å^{-1} for 3D, much stronger than the Q-position of 0.008 Å^{-1} for 2D, indicating more intensive interactions with 3D. (**Table S3**) The larger aggregates and more intensive interactions of 3D with LPS can be attributed to its better amphiphilically balanced structure than 2D upon interaction with the LPS SUVs.

SUVs consisting of POPC/POPG lipids (7/3, mol/mol) were used to simulate the inner membrane of Gram-negative bacteria and assess how leakage can be caused by peptide binding under pH 7.4 and 5.5. As indicated previous, the fluorescence intensity of NAO was dependent on the concentration of the lipid in the membrane. a decrease in NAO concentration was observed upon peptide binding to the SUVs under acidic condition (**Figure 8A**). In the presence of 3D, the EC$_{50}$ values of pH 5.5 (~ 55 µM) was lower than EC$_{50}$ values for SUVs of pH 7.4 (> 100 µM), while the fluorescence curves of 2D at pH 7.4 and 5.5 were nearly identical, indicating better pH-responsiveness of 3D in binding to the PG membrane.

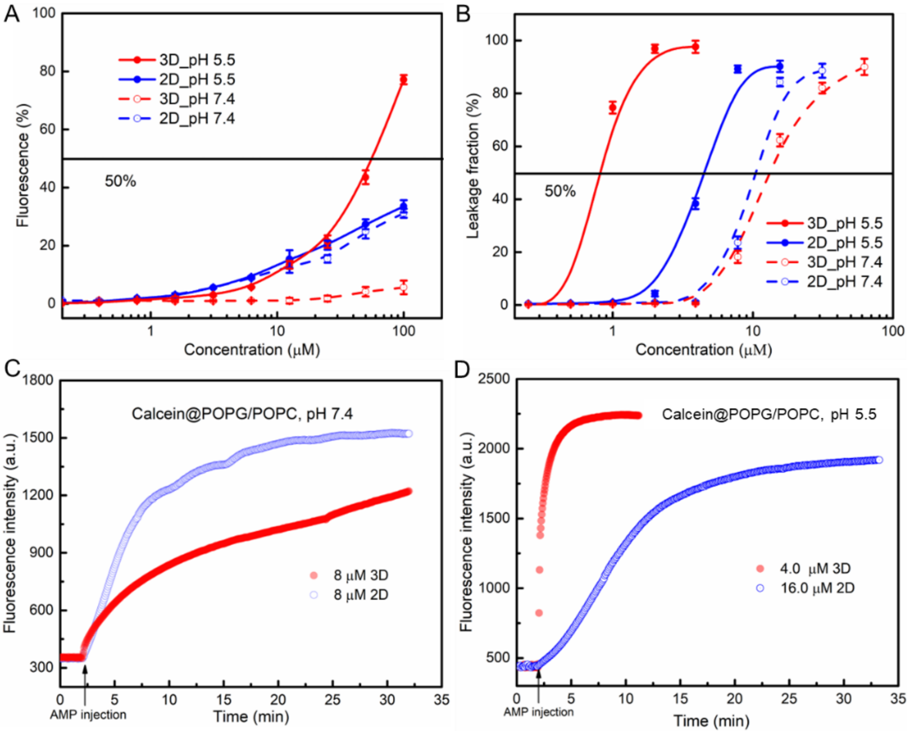

Figure 8. NAO and calcein assays to detect fluorescence displacement and leakage

upon peptide binding to anionic PG in POPG/POPC SUVs (3/7, mol/mol), respectively. (A) NAO displacement from anionic lipids in SUV induced by 2D and 3D at pH 5.5 and 7.4, indicating by the fluorescence intensity change with increasing peptide concentration**.** (B) Leakage fraction of calcein-loaded SUVs increases with increasing concentration of 2D and 3D at pH 5.5 and 7.4. (C, D) Fluorescence intensity increases from dynamic dye leakage of calcein encapsulated in POPG/POPC SUVs upon 2D and 3D binding at the fixed concentration and pH as specified.

Similar SUVs loaded with calcein probe were also prepared to test the membrane leakage induced by 2D and 3D under acidic and neutral conditions. After incubation, 3D induced great dye leakage from the SUVs at pH 5.5 while minimal dye leakage occurred at pH 7.4 (**Figure 8B**). In contrast, the difference in leakage between pH7.4 and 5.5 in 2D was relatively small. Overall, 3D under acidic environment can bind with anionic PG more effectively and lead to greater leakage fraction and faster leakage dynamics than 2D. These results demonstrated that even through the alpha-helix structures of 2D and 3D triggered by the negatively charged microenvironment were similar from the CD spectral analysis, different peptide sequences implicated different interactions with the bacterial membranes with different antimicrobial efficacy and efficiency under acidic condition. (**Figures S1&S2**) 3D clearly adopted superior amphiphilic structure to 2D and was advantageous in its intramembrane aggregation and structural disrupt leading to more effective antimicrobial actions at acidic condition.

In terms of dynamic leakage in presence of selected peptide concentrations (**Figures 8C&D**), the leakage efficiencies of both 3D and 2D at pH 5.5 are greater than those at pH 7.4, confirming the impact from the enhanced positive net-charges of the peptides that favoured their membrane binding and disruption. These results suggest that 2D and 3D peptides must adopt better amphiphilic conformations under acidic condition that can cause a higher level of fluorescence leakage and a faster membrane leakage.

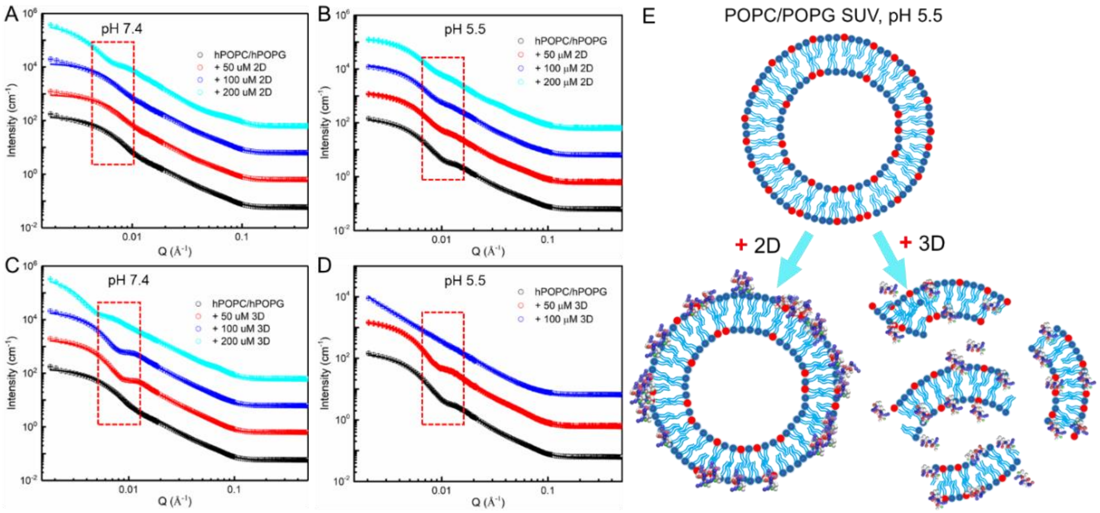

Figure 9. SANS profiles plotted as a function of Q, measured from POPC/POPG (mol/mol, 7/3) SUVs interacting with 2D (A, B) and 3D (C, D) at concentrations of 0, 50, 100 and 200 μM in D_2O Tris buffer (10 mM Tris + 150 mM NaCl, pH 5.5 and 7.4). (E) Schematic illustrations to depict how 2D and 3D binding forms different intramembrane AMP-lipid nanoaggregates in acidic environment.

Leakage of dyes from SUVs must result from structural disruptions of the membrane upon AMP binding. Small local structural disruptions can cause permeability change, but larger structural disruptions can cause fragmentations of local lipid bilayers and form peptide-lipid nanoaggregates fused with the main membrane bilayer fragments. Because SUVs of POPC/POPG mimic the inner membrane of Gram-negative bacteria and facilitates the binding with 2D and 3D, SANS measurements have also been undertaken to characterize the morphological structures of the SUVs, followed by the assessment of AMP binding under different AMP concentrations and pH changes in D_2O buffer. (**Figure 9**) Data analysis revealed that the SUVs can be well modelled by a core-shell sphere model (CSM), with the best fitted membrane thickness of 42 ± 2 Å and a sphere radius of 200 ± 10 Å. (**Table S5&S6**)

All SANS profiles of SUV-peptide systems under neutral condition can be modelled as core-shell sphere with a single lipid bilayer encapsulation. Binding of 2D over the low concentration range caused little change in the SUV radius or bilayer thickness, but an increase in concentration to 200 μM led to the obvious thickening of the outer head layer and radius increase from 200 ± 10 to 350 ± 10 Å. The size expansion must be related to membrane breakdown and fusion, consistent with the previous observation from similar SUV systems. (**Figure 9A**) Similar membrane fusion between individual SUVs occurred at lower peptide concentrations of 3D. Increase in SUV radius occurred from 200 ± 10 Å to 300 ± 10 Å at the concentration as low as 50 μM, (**Table S5**), indicating that 3D favoured the membrane fusion of the individual SUVs than that of 2D. This is evident from the broad SANS feature around 0.01 A^{-1} and the sharp increasing intensity in the lowest Q region over the high peptide concentration range. (**Figure 9C**)

Under acidic condition, the SANS profiles with addition of the 2D peptide can still be fitted from the core multilayer shell (CMS) model but with a slightly radius increase to the SUVs. (**Figure 9B**). In contrast, the distinct feature from addition of 3D under acidic condition is the membrane fusion of individual SUVs, even under low 3D concentrations, with the results clearly indicating the transfer of lysed membrane fragments from the collapse of SUVs into the lipid-peptide lamellar stacks. (**Figure 9D**) The schematic illustration in **Figure 9E** shows the typical membrane breakdown and morphological changes upon 2D and 3D binding with SUVs in acidic condition. The more disruptive membrane behaviour of 3D than 2D at acidic condition than at neutral pH as revealed from SANS data provides direct structural support to their more potent efficacy and efficiency as observed from cell assays, confirming that membrane leakage associated with the formation of intramembrane nanoaggregates is critical to the design of more potent and selective AMPs.

4. Conclusions

We designed two D and K-containing AMPs and developed the AMP-antibiotic pair as a therapeutic combination to target gastric Gram-negative bacterial infections based on the selective pH-responsiveness. Much of the work on AMPs was focused on their targeting on outer or inner membranes and membrane interaction. AMPs can be potent antimicrobials through their environmental responsiveness, self-assembly behaviour and pairing with conventional antibiotic.[53] The 3D AMP displayed pH-responsive antimicrobial activity and efficiency through different binding and interactions at molecular and cellular levels, resulting in altered permeability of the outer membrane, different dissipation of transmembrane Δψ and ΔpH for the inner membrane. These physiochemical property changes were linked to different membrane leakage, fusion, stacking and formation of intramembrane nanoaggregates. The differential pH-responsiveness between 2D and 3D can be attributed to the above factors and be reflected in their antimicrobial activities, which is also dependent on their individual amphiphilic structures and following intramembrane aggregation behaviour. Both 3D and 2D are designed to be pH-sensitive and greatly outperform the therapy of single antibiotic under acidic condition against Gram-negative *E. coli* and *H. pylori* including antibiotic-resistant strains. On the other hand, the two peptides show minimal cytotoxicity against mammalian cells, good compatibility and pH-dependent synergistic effect with antibiotic in the treatment of Gram-negative bacteria. The novel pH-responsive AMP hydrogel designed in this study can play a role of antibiotic nanocarriers and would be a promising candidate for site-specific pH-triggering antimicrobial performance.

Associated content

Supporting Information Available

The supporting information is available free of charge on the website, including materials used in all the experiments, CD measurements, FICI assays, parameters and fitting models in SANS studies.

Author information

Corresponding Authors

***E-mail: j.lu@manchester.ac.uk (J.R.L.).**

***Tel: 0044 161 200 3926**

ORCID

Mingrui Liao: 0000-0002-9481-4026

Haoning Gong: 0000-0003-1590-2042

Xuzhi Hu: 0000-0002-9246-7040

Huayang Liu: 0000-0002-2390-5414

Lin Zhang: 0000-0003-2153-4856

Jian Ren Lu: 0000-0001-5648-3564

Conflicts of interest

The authors declare no conflict of interest.

Acknowledgements

Thanks for the studentship supports from the University of Manchester joint with China Scholarship Council (UoM-CSC joint PhD program) to M.L. and H.G., supports to H.G. and X.H. via an overseas research studentship funded by the UoM, research fund supports from Syngenta to X.H., from Lonza to H.L. We appreciate Derren Heyes for his assistance of CD. We acknowledge the beam time awarded from the ISIS neutron facility (RB 1920459 & 2210031 & 2210218). We also acknowledge the beam time awarded from the ILL neutron facility (DOI: 10.5291/ILL-DATA.9-13-730) and technical assistance by Simon Wood. An allocation time from the Shared Computation Facility (SCF) at the UoM is gratefully acknowledged. Thanks for Prof. Jian Zhou's

help and suggestion on atomistic simulation modellings setup.

5. References

1. A. E. M. Hari Leontiadou, Siewert J. Marrink, Antimicrobial Peptides in Action. *J Am Chem Soc* **2006,** *128* (37), 12156-12161.

2. B. Bechinger; S. U. Gorr, Antimicrobial peptides: Mechanisms of action and resistance. *J Dent Res* **2017,** *96* (3), 254-260.

3. E. M. Jones; C. A. Cochrane; S. L. Percival, The Effect of pH on the Extracellular Matrix and Biofilms. *Adv Wound Care (New Rochelle)* **2015,** *4* (7), 431-439.

4. L. A. Schneider; A. Korber; S. Grabbe; J. Dissemond, Influence of pH on wound-healing: a new perspective for wound-therapy? *Arch Dermatol Res* **2007,** *298* (9), 413-420.

5. P. R. Cavanagh; B. A. Lipsky; A. W. Bradbury; G. Botek, Treatment for diabetic foot ulcers. *The Lancet* **2005,** *366* (9498), 1725-1735.

6. N. Ninan; A. Forget; V. P. Shastri; N. H. Voelcker; A. Blencowe, Antibacterial and Anti-Inflammatory pH-Responsive Tannic Acid-Carboxylated Agarose Composite Hydrogels for Wound Healing. *ACS Appl Mater Interfaces* **2016,** *8* (42), 28511-28521.

7. B. S. Nagoba; N. M. Suryawanshi; B. Wadher; S. Selkar, Acidic environment and wound healing: a review. *Wounds* **2015,** *27* (1), 5-11.

8. R.-C. Mercier; C. Stumpo; M. J. Rybak, Effect of growth phase and pH on the in vitro activity of a new glycopeptide, oritavancin (LY333328), against Staphylococcus aureus and Enterococcus faecium. *Journal of Antimicrobial Chemotherapy* **2002,** *50* (1), 19-24.

9. S. Kang; G. H. Park; S. Kim; J. Kim; Y. Choi; Y. Huang; Y. Lee; T. H. Choi, In Vitro and In Vivo Antimicrobial Activity of Antibiotic-Conjugated Carriers with Rapid pH-Responsive Release Kinetics. *Adv Healthc Mater* **2019,** *8* (14), e1900247.

10. X. Lv; J. Zhang; y. dongliang; J. Shao; W. Wang; Q. Zhang; X.-C. Dong, Recent Advances in pH-Responsive nanomaterials for anti-infective therapy. *Journal of Materials Chemistry B* **2020**.

11. H. Y. Yang; Y. Li; D. S. Lee, Recent Advances of pH-Induced Charge-Convertible Polymer-Mediated Inorganic Nanoparticles for Biomedical Applications. *Macromol Rapid Commun* **2020**, e2000106.

12. X. Xie; T. Sun; J. Xue; Z. Miao; X. Yan; W. Fang; Q. Li; R. Tang; Y. Lu; L. Tang; Z. Zha; T. He, Ag Nanoparticles Cluster with pH-Triggered Reassembly in Targeting Antimicrobial Applications. *Advanced Functional Materials* **2020,** *30* (17), 2000511.

13. M. Ye; Y. Zhao; Y. Wang; N. Yodsanit; R. Xie; S. Gong, pH-Responsive Polymer–Drug Conjugate: An Effective Strategy to Combat the Antimicrobial Resistance. *Advanced Functional Materials* **2020,** *30* (39), 2002655.

14. S. Nitta; S. Kaketani; H. Iwamoto, Development of chitosan-nanofiber-based hydrogels exhibiting high mechanical strength and pH-responsive controlled release. *European Polymer Journal* **2015,** *67*, 50-56.

15. M. Madaghiele; C. Demitri; A. Sannino; L. Ambrosio, Polymeric hydrogels for burn wound care: Advanced skin wound dressings and regenerative templates. *Burns & Trauma* **2014,** *2* (4), 2321-3868.143616.

16. Z. Hou; Y. V. Shankar; Y. Liu; F. Ding; J. L. Subramanion; V. Ravikumar; R. Zamudio-Vazquez; D. Keogh; H. Lim; M. Y. F. Tay; S. Bhattacharjya; S. A. Rice; J. Shi; H. Duan; X. W. Liu; Y. Mu; N. S. Tan; K. C. Tam; K. Pethe; M. B. Chan-Park, Nanoparticles of Short Cationic Peptidopolysaccharide Self-Assembled by Hydrogen Bonding with Antibacterial Effect against Multidrug-Resistant Bacteria. *ACS Appl Mater Interfaces* **2017,** *9* (44), 38288-38303.

17. S. Das; U. Subuddhi, Cyclodextrin Mediated Controlled Release of Naproxen from pH-Sensitive Chitosan/Poly(Vinyl Alcohol) Hydrogels for Colon Targeted Delivery. *Industrial & Engineering Chemistry Research* **2013,** *52* (39), 14192-14200.

18. B. Lopez-Garcia; P. H. Lee; K. Yamasaki; R. L. Gallo, Anti-fungal activity of cathelicidins and their potential role in Candida albicans skin infection. *J Invest Dermatol* **2005,** *125* (1), 108-115.

19. A. B. Mochon; H. Liu, The antimicrobial peptide histatin-5 causes a spatially restricted disruption on the Candida albicans surface, allowing rapid entry of the peptide into the cytoplasm. *PLoS Pathog* **2008,** *4* (10), e1000190.

20. L. Kacprzyk; V. Rydengard; M. Morgelin; M. Davoudi; M. Pasupuleti; M. Malmsten; A. Schmidtchen, Antimicrobial activity of histidine-rich peptides is dependent on acidic conditions. *Biochim Biophys Acta* **2007,** *1768* (11), 2667-2680.

21. M. Viejo-Diaz; M. T. Andres; J. F. Fierro, Modulation of in vitro fungicidal activity of human lactoferrin against Candida albicans by extracellular cation concentration and target cell metabolic activity. *Antimicrob Agents Chemother* **2004,** *48* (4), 1242-1248.

22. E. Malik; S. R. Dennison; F. Harris; D. A. Phoenix, pH Dependent Antimicrobial Peptides and Proteins, Their Mechanisms of Action and Potential as Therapeutic Agents. *Pharmaceuticals (Basel)* **2016,** *9* (4).

23. J. Zhang; W. Zhu; B. Xin; S. Lin; L. Jin; H. Wang, Development of an antibacterial surface with a self-defensive and pH-responsive function. *Biomater Sci* **2019,** *7* (9), 3795-3800.

24. J. Wang; X. Y. Chen; Y. Zhao; Y. Yang; W. Wang; C. Wu; B. Yang; Z. Zhang; L. Zhang; Y. Liu; X. Du; W. Li; L. Qiu; P. Jiang; X. Z. Mou; Y. Q. Li, pH-Switchable Antimicrobial Nanofiber Networks of Hydrogel Eradicate Biofilm and Rescue Stalled Healing in Chronic Wounds. *ACS Nano* **2019,** *13* (10), 11686-11697.

25. X. Hu; M. Liao; H. Gong; L. Zhang; H. Cox; T. A. Waigh; J. R. Lu, Recent Advances in Short Peptide Self-assembly: from Rational Design to Novel Applications. *Current Opinion in Colloid & Interface Science* **2020,** *45*, 1-13.

26. Determination of minimum inhibitory concentrations (MICs) of antibacterial agents by agar dilution. *Clinical Microbiology and Infection* **2000,** *6* (9), 509-515.

27. G. Kahlmeter; D. F. J. Brown; F. W. Goldstein; A. P. MacGowan; J. W. Mouton; I. Odenholt; A. Rodloff; C. J. Soussy; M. Steinbakk; F. Soriano; O.Stetsiouk, European committee on antimicrobial susceptibility testing (EUCAST) technical notes on antimicrobial susceptibility testing. *Clinical Microbiology and Infection* **2006,** *12* (6), 501-503.

28. H. Gong; M. Liao; X. Hu; K. Fa; S. Phanphak; D. Ciumac; P. Hollowell; K. Shen; L. A. Clifton; M. Campana; J. R. P. Webster; G. Fragneto; T. A. Waigh; A. J. McBain; J. R. Lu, Aggregated Amphiphilic Antimicrobial Peptides Embedded in Bacterial

Membranes. *ACS Appl Mater Interfaces* **2020,** *12* (40), 44420-44432.

29. Z. Lai; P. Tan; Y. Zhu; C. Shao; A. Shan; L. Li, Highly stabilized alpha-Helical coiled coils kill Gram-negative bacteria by multicomplementary mechanisms under acidic condition. *ACS Appl Mater Interfaces* **2019,** *11* (25), 22113-22128.

30. J. D. t. Winkel; D. A. Gray; K. H. Seistrup; L. W. Hamoen; H. Strahl, Analysis of antimicrobial-triggered membrane depolarization usingvoltage sensitive dyes. *Frontiers in Cell and Developmental Biology* **2016,** *4*, 29.

31. S. J. Wood; K. A. Miller; S. A. David, Anti-Endotoxin Agents. 1. Development of a Fluorescent Probe Displacement Method Optimized for the Rapid Identification of Lipopolysaccharide-Binding Agents. *Combinatorial Chemistry & High Throughput Screening* **2004,** *7* (3), 239-249.

32. G. Sautrey; L. Zimmermann; M. Deleu; A. Delbar; L. S. Machado; K. Jeannot; F. V. Bambeke; J. M. Buyck; J.-L. Decout; M.-P. Mingeot-Leclercq, New amphiphilic neamine derivatives active against resistant Pseudomonas aeruginosa and their interactions with lipopolysaccharides. *Antimicrob Agents Chemother* **2014,** *58*, 4420–4430.

33. H. Gong; M. Liao; X. Hu; K. Fa; S. Phanphak; D. Ciumac; P. Hollowell; K. Shen; L. A. Clifton; M. Campana; J. R. P. Webster; G. Fragneto; T. A. Waigh; A. J. McBain; J. R. Lu, Aggregated mmphiphilic antimicrobial peptides embedded in bacterial membranes. *ACS Appl Mater Interfaces* **2020,** *12* (40), 44420-44432.

34. A. H. d. V. Siewert J. Marrink, Alan E. Mark, Coarse Grained Model for Semiquantitative Lipid Simulations. *The Journal of Physical Chemistry B* **2004,** *108* (2), 750-760.

35. Y. Qi; H. I. Ingólfsson; X. Cheng; J. Lee; S. J. Marrink; W. Im, CHARMM-GUI Martini maker for coarse-grained simulations with the Martini Force Field. *J Chem Theory Comput* **2015,** *108* (2), 4486–4494.

36. S. Jo; T. Kim; V. G. Iyer; W. Im, CHARMM-GUI: A web-based graphical user interface for CHARMM. *Journal of Computational Chemistry* **2008,** *29* (11), 1859-1865.

37. C. S. Wolfgang Kabsch, Dictionary of Protein Secondary Structure. *Biopolymers* **1983,** *22*, 2577-2637.

38. C. K. Berk Hess, David van der Spoel, Erik Lindahl, GROMACS 4: Algorithms for Highly Efficient, Load-Balanced, and Scalable Molecular Simulation. *J Chem Theory Comput* **2008,** *4*, 435-447.

39. S. Nosé, A Unified Formulation of the Constant Temperature Molecular Dynamics Methods. *J Chem Phys* **1984,** *81* (1), 511-519.

40. R. A. J. Parrinello M. R. A., Polymorphic Transitions in Single Crystals: A New Molecular Dynamics Method. *Journal of Applied Physics* **1982,** *52*, 7182-7190.

41. M. Klein, Constant Pressure Molecular Dynamics for Molecular Systems. *Molecular Physics* **1983,** *50* (5), 1055-1076.

42. H. Gong; X. Hu; M. Liao; K. Fa; D. Ciumac; L. A. Clifton; M.-A. Sani; S. M. King; A. Maestro; F. Separovic; T. A. Waigh; H. Xu; A. J. McBain; J. R. Lu, Structural disruptions of the outer membranes of Gram-negative bacteria by rationally designed amphiphilic antimicrobial peptides. *ACS Appl Mater Interfaces* **2021,** *13* (14), 16062-

16074.

43. M. Xiong; Y. Bao; X. Xu; H. Wang; Z. Han; Z. Wang; Y. Liu; S. Huang; Z. Song; J. Chen; R. M. Peek, Jr.; L. Yin; L. F. Chen; J. Cheng, Selective killing of Helicobacter pylori with pH-responsive helix-coil conformation transitionable antimicrobial polypeptides. *Proc Natl Acad Sci USA* **2017,** *114* (48), 12675-12680.

44. A. S. Veiga; C. Sinthuvanich; D. Gaspar; H. G. Franquelim; M. A. Castanho; J. P. Schneider, Arginine-rich self-assembling peptides as potent antibacterial gels. *Biomaterials* **2012,** *33* (35), 8907-8916.

45. V. Madison; J. Schellman, Optical activity of polypeptides and proteins. *Biopolymers* **1972,** *11* (5), 1041-1076.

46. Y. Zhao; J. Wang; L. Deng; P. Zhou; S. Wang; Y. Wang; H. Xu; J. R. Lu, Tuning the self-assembly of short peptides via sequence variations. *Langmuir* **2013,** *29* (44), 13457-13464.

47. Z. Ma; X. Liu; J. Nie; H. Zhao; W. Li, Nano-antimicrobial peptides based on constitutional isomerism-dictated self-assembly. *Biomacromolecules* **2022,** *23* (3), 1302–1313.

48. Y. M. Abul-Haija; G. G. Scott; J. K. Sahoo; T. Tuttle; R. V. Ulijn, Cooperative, ion-sensitive co-assembly of tripeptide hydrogels. *Chem Commun (Camb)* **2017,** *53* (69), 9562-9565.

49. P. W. Frederix; G. G. Scott; Y. M. Abul-Haija; D. Kalafatovic; C. G. Pappas; N. Javid; N. T. Hunt; R. V. Ulijn; T. Tuttle, Exploring the sequence space for (tri-)peptide self-assembly to design and discover new hydrogels. *Nat Chem* **2015,** *7* (1), 30-37.

50. C. Guo; Y. Luo; R. Zhou; G. Wei, Probing the Self-Assembly Mechanism of Diphenylalanine-Based Peptide Nanovesicles and Nanotubes. *ACS Nano* **2012,** *6* (5), 3907-3918.

51. A. Yamaguchi; H. Ohmori; M. Kaneko-Ohdera; T. Nomura; T. Sawai, Delta pH-dependent accumulation of tetracycline in Escherichia coli. *Antimicrob Agents Chemother* **1991,** *35* (1), 53-56.

52. I. R. Booth, Regulation of cytoplasmic pH in bacteria. *Microbiological reviews* **1985,** *49* (4), 359-378.

53. S. Malekkhaiat Häffner; M. Malmsten, Influence of self-assembly on the performance of antimicrobial peptides. *Current Opinion in Colloid & Interface Science* **2018,** *38*, 56-79.

Supporting information

Combination of pH-responsive AMP hydrogel and conventional antibiotic in treatment of Gram-negative bacteria

Mingrui Liao,[1#] Haoning Gong,[1] Xuebo Quan,[2] Xuzhi Hu,[1] Huayang Liu,[1] Zongyi Li,[1] Andrew J. McBain,[3] and Jian R. Lu[1,*]

[1]Biological Physics Laboratory, Department of Physics and Astronomy, School of Natural Science, The University of Manchester, Oxford Road, Manchester M13 9PL, UK.

[2]Shenzhen Bay Laboratory, Institute of Systems and Physical Biology, Shenzhen, 518132, China

[3]Division of Pharmacy and Optometry, Faculty of Biology, Medicine and Health, The University of Manchester, Oxford Road, Manchester M13 9PL, UK.

[#]To whom as PhD candidate should be responsible to all the experiments and simulation work.

[*]To whom all correspondence should be made: J.lu@manchester.ac.uk.

1. Bacterial strains and materials

The following bacterial strains were purchased from ATCC: *Escherichia coli* (*E. coli*, ATCC 25922) and ESBL-*E. coli*. Polymixin B and tetracycline antibiotics were purchased from Sigma Aldrich. Peptides were synthesized by ChinaPeptides Co., Ltd. (Shanghai, China) and the purity was over 98%. Fluorescence probes Calcein, 3-(4,5-Dimethylthiazol-2-yl)-2,5-diphenyltetrazolium bromide (MTT), N-phenyl-1-naphthylamine (NPN), 3,3′-Dipropylthiadicarbocyanine iodide (DiSC$_3$(5)) and Calcein-AM were supplied from Sigma-Aldrich, BODIPY-TR-cadaverine (BC), Nonyl Acridine Orange (NAO) and SYTO 9 were obtained from Thermo Fisher.

Lipids 1-palmitoyl-2-oleoyl-sn-glycero-3-phospho-(1′-rac-glycerol) (sodium salt) (POPG) and 1-palmitoyl-2-oleoyl-sn-glycero-3-phosphocholine (POPC) were obtained from Avanti Polar Lipids (Alabaster, USA). Hydrogenated RcLPS product extracted from *E. coli* was purchased from Sigma-Aldrich.

2. Peptides' structural information

Table S1. Physical chemistry properties of the designed peptides.

Peptide denotation	Sequence	Theoretical M_w/g·mol^{-1}	Measured M_w/g·mol^{-1}	Retention time/min
3D	G(IIKD)3I	1596.9	1598.0	25.9
2D	GIIKKIIDDIIKKI	1610.0	1611.0	23.5

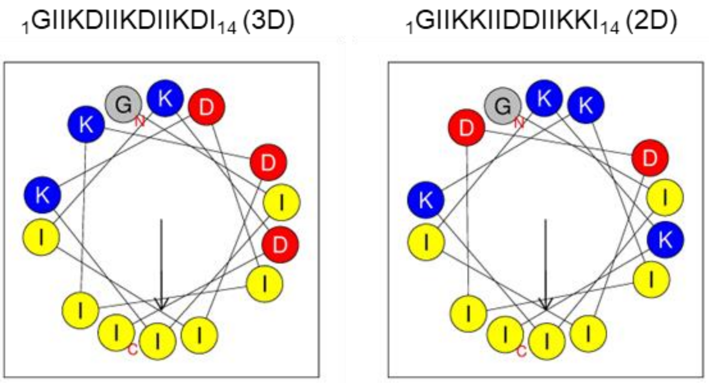

$_1$GIIKDIIKDIIKDI$_{14}$ (3D)

$_1$GIIKKIIDDIIKKI$_{14}$ (2D)

Figure S1. Screenshots of the wheel projection for 3D and 2D peptides.

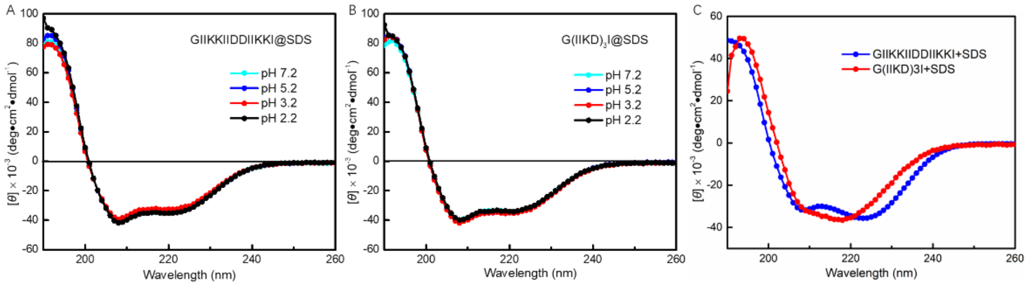

Figure S2. Secondary structures of (A) 2D and (B) 3D at the peptide concentration of 0.5 mM in 50 mM SDS micelles (Tris buffer, 10 mM Tris + 150 mM NaCl) under different pH values. (C) Secondary structures of 2D and 3D at the high concentration of 3 mM in presence of 50 mM SDS solutions.

3. Fitting models and parameters in SANS measurements

Table S2. Structural parameters from best fits to the measured SANS data from self-assembled 3D at neutral condition.

Peptide	**3D**
Concentration	**4 mM**
Fitting Model	Lamellar_hg
Scale[a]	0.01
Background (×10^{-3} cm^{-1})	5±0.5
A_Length_tail (Å)	8±1
A_Length_head (Å)	8±1
A_SLD (× 10^{-6} Å^{-2})	2.8±0.2
A_head_SLD (× 10^{-6} Å^{-2})	6.2±0.1
A_solvent_SLD[b] **(× 10^{-6} Å^{-2})**	6.3±0.1

Note: Errors in SANS were estimated by the range of the parameters beyond which the SANS fits were noticeably different.

[a] Scale was the volume fraction of the self-assembled structure (including hydration) from the SANS model fit.

[b] SLD of pure D_2O is 6.35× 10^{-6} Å^{-2}. In our experiments, D_2O contained a small amount of H_2O due to sample mixing, leading to smaller SLD values for the solvents.

Table S3. Structural parameters from best fits to the SANS data measured from LPS/POPC SUVs and SUVs after AMP binding at pH 7.4. The results are similar to those from our previous work.[1-2]

Sample	**1 mM hLPS/hPOPC**	**+ 3D/pH 7.4**		**+ 2D/pH 7.4**		
		100 µM	200 µM	100 µM	200 µM	
Fitting Model A[a]	**CMS**[c]	**CMS**	**CMS**	**CMS**	**Fitting Model B**[b]	**CMS_LP**[d]
Background (×10^{-3} cm^{-1})	2.0±0.2	4±0.2	4.5±0.2	4±0.2	**Background (×10^{-3} cm^{-1})**	3.5±0.2
A_volume fraction (× 10^{-3})	3.8±0.2	2.4±0.2	2.0±0.2	2.3±0.2	**Scale_A**	5
A_core_SLD (× 10^{-6} Å^{-2})	5.7±0.1	5.9±0.1	5.9±0.1	5.9±0.1	**A_core_SLD (× 10^{-6} Å^{-2})**	6.1±0.1
A_solvent_SLD (× 10^{-6} Å^{-2})	6.3±0.1	6.3±0.1	6.3±0.1	6.3±0.1	**A_solvent_SLD (× 10^{-6} Å^{-2})**	6.3±0.1
A_radius (Å)	200±10	200±10	200±10	185±10	**A_radius (Å)**	190±10
A_radius PDI[e]	0.5±0.1	0.6±0.1	0.6±0.1	0.5±0.1	**A_radius PDI**	0.5±0.1
A_layer1_thickness (Å)	17±1	20±2	28±2	20±2	**A_thickness (Å)**	38±2
A_layer1_SLD (× 10^{-6} Å^{-2})	5.5±0.2	5.6±0.2	6.1±0.2	5.6±0.2	**A_shell_SLD (× 10^{-6} Å^{-2})**	4.0±0.2
A_layer2_thickness (Å)	30±2	33±2	37±2	33±2	**A_thickness PDI**[f]	0±0.1
A_layer2_SLD (×10^{-6} Å^{-2})	0.5±0.1	0±0.1	0±0.1	0±0.1	**Scale_B**	65
A_layer3_thickness (Å)	17±2	17±2	17±2	17±2	**B_peak_pos (Å^{-1})**	0.034±0.005

A_layer 3_SLD ($\times 10^{-6}$ Å^{-2})	5.5±0.2	5.8±0.2	5.8±0.2	5.8±0.2	**B_peak_hwhm (Å^{-1})**	0.018±0.001

[a] Model A is the core multilayer shell model to represent pure lipid SUVs.

[b] Model B is a Lorentzian peak model (see in http://www.sasview.org/sasview/user/models/model_functions.html#peaklorentzmodel).

[c] CMS denotes the core multilayer shell model and [d] CMS_LP denotes a Lorentzian peak model.

[e] PDI denotes polydispersity index of the vesicle radius.

Table S4. Structural parameters from best fits to the SANS data measured from LPS/POPC SUVs and SUVs after AMP binding at pH 5.5. Similar results were obtained in our previous work.[1-2]

Sample	**1 mM hLPS/hPOPC**	**+ 3D/pH 5.5**				**+ 2D/pH 5.5**	
		100 µM		200 µM		100 µM	200 µM
Fitting Model A[a]	**CMS[d]**	**Fitting Model B[b]**	**CMS_LP[e]**	**Fitting Model C[c]**	**Sphere_LP[f]**	**CMS_LP**	**CMS_LP**
Background ($\times 10^{-3}$ cm^{-1})	8.0±0.2	**Background ($\times 10^{-3}$ cm^{-1})**	8±0.2	**Background ($\times 10^{-3}$ cm^{-1})**	8±0.2	8±0.2	8±0.2
A_volume fraction ($\times 10^{-3}$)	3.0±0.2	**Scale_A**	5	**Scale**	7	5	5
A_core_SLD ($\times 10^{-6}$ Å^{-2})	5.7±0.1	**A_core_SLD ($\times 10^{-6}$ Å^{-2})**	6.1±0.1	**Scale_A**	1.8	6.1±0.1	6.1±0.1
A_solvent_SLD ($\times 10^{-6}$ Å^{-2})	6.3±0.1	**A_solvent_SLD ($\times 10^{-6}$ Å^{-2})**	6.2±0.1	**A_SLD ($\times 10^{-6}$ Å^{-2})**	3.2±0.1	6.3±0.1	6.3±0.1
A_radius (Å)	200±10	**A_radius (Å)**	210±10	**A_solvent_SLD**	6.3±0.1	190±10	190±10

				(× 10^{-6} Å^{-2})			
A_radius PDI[g]	0.5±0.1	**A_radius PDI**	0.6±0.1	**B_radius (Å)**	200±10	0.6±0.1	0.6±0.1
A_layer1_thickness (Å)	18±2	**A_thickness (Å)**	38±2	**B_radius PDI**	1.0±0.1	38±2	38±2
A_layer1_SLD (× 10^{-6} Å^{-2})	5.8±0.2	**A_shell_SLD (× 10^{-6} Å^{-2})**	4.0±0.2	**Scale_B**	800	4.0±0.2	4.0±0.2
A_layer2_thickness (Å)	30±2	**A_thickness PDI[f]**	0±0.1	**B_peak_pos (Å^{-1})**	0.1±0.005	0±0.1	0±0.1
A_layer2_SLD (×10^{-6} Å^{-2})	0.8±0.1	**Scale_B**	60	**B_peak_hwhm (Å^{-1})**	**0.01±0.001**	25	15
A_layer3_thickness (Å)	18±2	**B_peak_pos (Å^{-1})**	0.034±0.005	**Scale_C**	7	0.038±0.005	0.095±0.005
A_layer3_SLD (×10^{-6} Å^{-2})	5.5±0.2	**B_peak_hwhm (Å^{-1})**	0.017±0.001	**C_peak_pos (Å^{-1})**	0.04±0.005	0.018±0.001	**0.008±0.001**
				C_peak_hwhm (Å^{-1})	**0.02±0.001**		

[a] Model A is the core multilayer shell model to represent pure lipid SUVs.

[b] Model B is a Lorentzian peak model based on CMS model (see in http://www.sasview.org/sasview/user/models/model_functions.html#peaklorentzmodel).

[c] Model C is also a Lorentzian peak model based on sphere model.

[d] CMS denotes the core multilayer shell model, [e] CMS_LP and [f] Sphere_LP denote a Lorentzian peak model.

[g] PDI denotes polydispersity index of the vesicle radius.

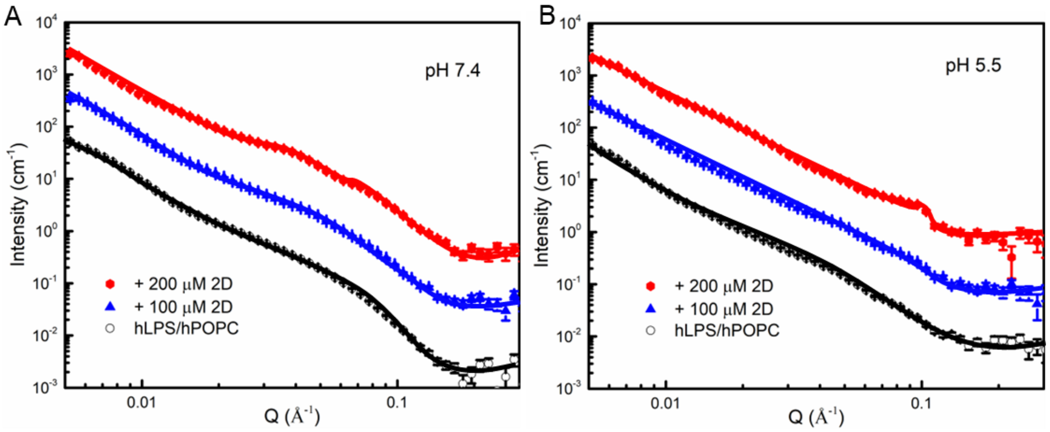

Figure S3. SANS of 1 mM LPS/POPC SUVs interacting with 2D at pH 7.4 (A) and 5.5 (B) D_2O Tris buffer (10 mM Tris + 150 mM NaCl).

Table S5. Structural parameters obtained from best fits to the SANS data measured from POPC/POPG SUVs and SUVs after AMP binding at pH 7.4. Similar results were obtained in our previous work.[1-2]

Sample	**1 mM hPOPC/POPG**	**+ 3D/pH 7.4**			**+ 2D/pH 7.4**		
		50	100	200	50	100	200
Fitting Model[a]	**CMS[b]**	**CMS**	**CMS**	**CMS**	**CMS**	**CMS**	**CMS**
A_volume fraction (× 10^{-3})	3.4±0.2	3.8±0.2	3.6±0.2	4.0±0.2	3.1±0.2	3.4±0.2	4.2±0.2
Background (×10^{-3} cm^{-1})	60±2	60±2	60±2	60±2	60±2	60±2	60±2
A_core_SLD (× 10^{-6} Å^{-2})	6.0±0.1	6.0±0.1	6.0±0.1	6.0±0.1	6.0±0.1	6.0±0.1	6.2±0.1
A_solvent_SLD (× 10^{-6} Å^{-2})	6.2±0.1	6.2±0.1	6.2±0.1	6.2±0.1	6.2±0.1	6.2±0.1	6.2±0.1
A_radius (Å)	200±10	300±10	340±10	400±10	200±10	200±10	350±10
A_radius PDI[c]	0.5±0.1	0.3±0.05	0.28±0.05	0.6±0.1	0.5±0.1	0.5±0.1	0.5±0.1
A_layer1_thickness (Å)	8±1	8±1	8±1	20±1	8±1	8±1	20±1

A_layer 1_SLD (× 10^{-6} Å^{-2})	4.0±0.2	3.8±0.2	3.6±0.2	5.0±0.2	4.0±0.2	4.0±0.2	4.8±0.2
A_layer 2_thickness (Å)	25±3	25±3	25±3	7±1	25±3	25±3	7±1
A_layer 2_SLD (×10^{-6} Å^{-2})	0±0.1	0±0.1	0±0.1	4.5±0.1	0±0.1	0±0.1	4.5±0.1
A_layer 3_thickness (Å)	8±1	8±1	8±1	25±1	8±1	8±1	25±1
A_layer 3_SLD (×10^{-6} Å^{-2})	4.0±0.2	3.8±0.2	3.6±0.2	0±0.1	4.0±0.2	4.0±0.2	0±0.1
A_layer 4_thickness (Å)				12±1			12±1
A_layer 4_SLD (×10^{-6} Å^{-2})				3.8±0.1			3.8±0.1

[a] Model A is the core multilayer shell model to represent SUVs.

[b] CMS denotes the core multilayer shell model.

[c] PDI denotes polydispersity index of the vesicle radius.

Table S6. Structural parameters from best fits to the SANS data measured from POPC/POPG SUVs and SUVs after AMP binding at pH 5.5. Similar results were obtained in our previous work.[1-2]

Sample	**1 mM hPOPC/POPG**	**+ 3D (μM)/pH 5.5**			**+ 2D (μM)/pH 5.5**		
		50	100		50	100	200
Fitting Model A[a]	**CMS[b]**	**CMS**	**Fitting Model B[c]**	**LM_hg[d]**	**CMS**	**CMS**	**CMS**
A_volume fraction (× 10^{-3})	60±5	60±5	**A_volume fraction (× 10^{-3})**	65±5	60±5	60±5	60±5
Background (×10^{-3} cm^{-1})	3.4±0.2	3.4±0.2	**Background (×10^{-3} cm^{-1})**	3.6±0.2	3.4±0.2	3.4±0.2	3.3±0.2

A_core_SLD (× 10^{-6} Å^{-2})	6.0±0.1	6.0±0.1	**A_Length_tail (Å)**	20±2	6.0±0.1	6.0±0.1	6.0±0.1?
A_solvent_SLD (× 10^{-6} Å^{-2})	6.2±0.1	6.2±0.1	**A_Length_head (Å)**	8±1	6.2±0.1	6.2±0.1	6.2±0.1?
A_radius (Å)	225±10	265±10	**A_SLD (× 10^{-6} Å^{-2})**	4.2±0.2	225±10	235±10	235±10
A_radius PDI[e]	0.45±0.1	0.40±0.1	**A_head_SLD (× 10^{-6} Å^{-2})**	5.7±0.2	0.45±0.1	0.45±0.1	0.45±0.1
A_layer1_thickness (Å)	8±1	8±1	**A_solvent_SLD (× 10^{-6} Å^{-2})**	6.2±0.1	8±1	8±1	7±1
A_layer 1_SLD (× 10^{-6} Å^{-2})	4.2±0.2	4.2±0.2			4.2±0.2	4.2±0.2	4.2±0.2
A_layer 2_thickness (Å)	24±2	24±2			24±2	24±2	24±2
A_layer 2_SLD (×10^{-6} Å^{-2})	0±0.1	0±0.1			0±0.1	-0.1±0.1	-0.2±0.1
A_layer 3_thickness (Å)	8±1	8±1			8±1	8±1	7±1
A_layer 3_SLD (×10^{-6} Å^{-2})	4.2±0.2	4.2±0.2			4.2±0.2	4.2±0.2	4.2±0.2

[a] Model A is the core multilayer shell model to represent SUVs.

[b] CMS denotes the core multilayer shell model.

[c] Model B is the lamellar model to represent SUVs after disrupted by AMPs.

[d] LM_hg denotes the lamellar model.

[e] PDI denotes polydispersity index of the vesicle radius.

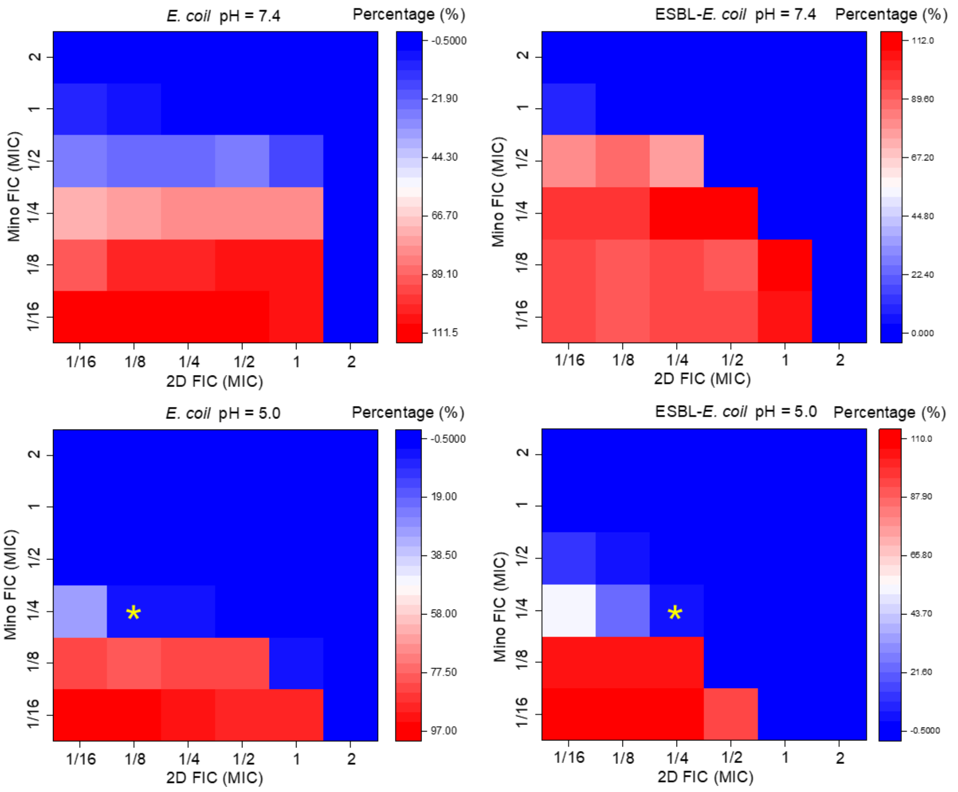

Figure S4. FICI of 2D-antibiotic combination. Heat maps show the antimicrobial activities of drug combination 2D-MC against Gram-negative bacteria at acidic and neutral Tris buffers (10 mM Tris + 150 mM NaCl). The star points show the fractional inhibitory concentration index (FICI) in synergetic drug combinations.

4. References

1. H. Gong; M.-A. Sani; X. Hu; K. Fa; J. W. Hart; M. Liao; P. Hollowell; J. Carter; L. A. Clifton; M. Campana; P. Li; S. M. King; J. R. P. Webster; A. Maestro; S. Zhu; F. Separovic; T. A. Waigh; H. Xu; A. J. McBain; J. R. Lu, How do Self-Assembling Antimicrobial Lipopeptides Kill Bacteria? *ACS Appl Mater Interfaces* **2020,** *12* (50), 55675-55687.
2. J. Zhang; H. Gong; M. Liao; Z. Li; R. Schweins; J. Penny; J. R. Lu, How do terminal modifications of short designed IIKK peptide amphiphiles affect their antifungal activity and biocompatibility? *J Colloid Interface Sci* **2022,** *608*, 193-206.

Chapter 6 Conclusions and future work

1. Conclusions

During the PhD project, AMPs' behaviours in the bulk solution and their link with peptides' action modes on the membrane were studied. Four representative peptides (G_3, G_4, LDKA and Melittin) were selected, the specific interaction modes between AMPs (of different hydrophobicity and self-assembly behaviours) and bacterial membrane models were explored by both computational simulations and experiments. The antimicrobial efficacy of AMPs is highly related to their self-assembly behaviour and is validated by a combination of MD simulations and experiments. In peptide's antimicrobial activity against Gram-negative bacteria, the AMP's disruption on bacterial outer membrane (OM) and inner membrane (IM) should be combined, this part of work was dependent on both steered molecular dynamics simulations and production MD simulations, combined with neutron scattering/reflection and some experiments based on liposome models. In detail, the formation of the peptide nanoaggregates on bacterial OM had a major impact on the efficiency of OM permeability and the level of AMPs that is available to attack bacterial IM. LDKA clusters can be prevented from approaching bacterial IM by bacterial OM, once approaching the bacterial IM, LDKA can disrupt the IM integrity by forming AMP-lipid nanoaggregates and cause membrane defects. The other three AMPs can disrupt the OM effectively, especially G_3 and G_4, forming smaller aggregates. In contrast, Melittin was more effective at becoming inserted into the charged IMs. This work showed that the "carpet model" was not the most efficient way to form nanopores and cause leakage. Potent antimicrobial activities must be associated with the intramembrane nano-aggregation as a more effective mode of action.

To further improve the antimicrobial activity of peptide especially in terms of fast bacterial killing and restricting the drug-resistance against Gram-positive bacteria, polar charged residue Arg (R) and aromatic residue Trp (W) and Phe (F) were introduced into the widely studied sequence $G(IIKK)_3I$ (denoted as GIK) and replaced

Lys (K) and Ile (I), respectively, namely G(IIRR)$_3$I, G(WWKK)$_3$W and G(FFKK)$_3$F (denoted as GIR, GWK and GFK). From the results of antimicrobial activity against Gram-positive bacteria, four amphiphilic AMPs displayed very different efficacy and efficiency against sensitive *S. aureus* and drug-resistant MRSA. It was found that the self-promoted binding and insertion of these AMPs to the LTA layer is driven by electrostatic interaction, and followed with AMPs approaching cytoplasmic membrane, causing membrane depolarization and leakage and forming intramembrane nanoaggregates. Both experiments and MD simulations provide useful evidence to relate the observed differences in antimicrobial actions to intramembrane aggregation, changes in membrane rigidity and phase separation. Data from both cell and cell-free systems and MD simulations all pointed to the better effects of GIR and GWK associated with altered membrane rigidity and decreased diffusion efficiency than GIK and GFK. Furthermore, GWK and GIR can more easily form intramembrane peptide-lipid clusters and induce membrane phase separation. These multiple effects are well correlated with their antimicrobial efficacy and time-killing performance: GWK > GIR > GFK > GIK. Because these membrane targeting actions are fast and effective, the mechanistic processes help explain why AMPs are promising agents to fight bacterial resistance.

To pave the way for the clinical application of AMP and alleviate the production of antibiotic resistance, a combined therapy involved with novel antimicrobial lipopeptides and conventional antibiotics was proposed and investigated. In system of lipopeptide combined with tetracycline antibiotics, all the drug pairs show synergistic or additional effects against Gram-negative bacteria including sensitive and drug-resistant strains. The work of lipopeptide-antibiotic combinations revealed that the easy insertion of lipopeptide into bacterial membrane allowed internalization of a tetracyclic antibiotic via the formation of antibiotic-lipopeptide pairing through hydrophobic interaction between tetracycline (TC) or minocycline (MC) and lipopeptide whilst binding to the bacterial membrane. This work has demonstrated that combining the membrane penetrating and disrupting ability of lipopeptide with tetracyclic antibiotic is highly effective in combating both Gram-negative and Gram-negative bacteria including MDR and anaerobic pathogens. The combined experimental and MD simulation studies offer important mechanistic insights into structural basis underlying membrane-specific interactions, important for designing and fine-tuning lipopeptide to facilitate TC/MC across microbial membrane whilst being biocompatible to host cells.

To respond to the dilemma of chronic wound infection and healing, pH-responsive peptide hydrogel based on GIK was specifically designed for the acidic microenvironment of acute wound in initial phase. Two D and K-containing AMPs (denoted as 2D and 3D) were designed and paired with antibiotic as a therapeutic combination to target gastric Gram-negative bacterial infections based on pH-responsiveness. 3D displayed pH-responsive antimicrobial activity and efficiency through different binding and interactions at molecular and cellular levels, resulting in altered permeability of the OM, different dissipation of transmembrane $\Delta\psi$ and ΔpH for the IM. The novel pH-responsive AMP hydrogel designed in this study can play a role of antibiotic nanocarriers and would be a promising candidate for site-specific pH-triggering antimicrobial performance.

2. Future work

The membrane targeting of both cationic AMPs and lipopeptides has been well studied, including membrane permeability change, membrane depolarization, and the relation between dual disruption of both outer and inner membrane and kinetic death of bacteria. However, the effects of membrane reorganization/disruption on membrane function and related dysfunction of membrane proteins are largely unknown. On the other way, peptides’ function can be designed aiming for the disturbance of membrane fluidity or membrane protein.

Importance of lipid domains. In the long period, the role of lipid domains in cytoplasmic membrane is important for membrane functionality such as signal transduction, and the function of various transmembrane proteins.[1] The incorporation of membrane proteins into lipid domains is of significant role to affect domain organization and cause domain segregation. In most cases, transmembrane proteins are located out of the lipid rafts to avoid perturbing the organization of the domains.[2] In contrast, some membrane proteins preferred to locate on the lipid domains, for the reason of anchoring into the membranes via the lipid anchor incorporating into well-organized domains or specifically binding with lipid enriched in the rafts.[3, 4] On the other hand, boundary lipids surrounding with membrane proteins showed a rapid exchanging behaviour and played important role in promoting association with different types of lipid organizations.

In the proposed mechanism of daptomycin's antimicrobial activity against Gram-positive bacteria, it had been confirmed that daptomycin binding with lipid molecules would decrease membrane fluidity and hence lead to the aberrant localization of peripheral membrane proteins onto membrane.[5] Upon the binding of peptide onto membrane, the bacterial cells are still in live state in some cases, how the effects of intramembrane peptide on membrane domains and continuous dysfunction of various membrane proteins still need to be explored. The complexities in this process are key to understand the peptides' targeting interaction other than membrane, and the antimicrobial activity of peptide-antibiotic combination for synergetic effects due to the cellular uptake of antibiotic would be related to some specific membrane proteins.

The targets of AMP other than membrane in antimicrobial or antibiofilm activity. Differences among peptides and differences among bacterial surfaces and cytoplasmic membranes are just a few of the variables that determine the extent of AMP-induced bacterial killing. Even though the formation of transmembrane channels or pores and extensive membrane disruption are widely accepted to lead to the cell lysis, designing AMPs based on their membrane activities alone would bring little effects in treating specific subset of microbe.[6, 7] Increasing speculations and evidence indicated that they are not the only killing mechanisms and AMPs had other intracellular targets, such as inhibiting DNA/RNA/protein (pleurocidin, dermaseptin and indolicidin),[8, 9] cell wall (mersacidin)[10] synthesis and enzymatic activity (drosocin and apidaecin),[11] activating autolysin[12]. With regard to AMPs' antibiofilm activity, some strategies other than improving AMPs' penetration into biofilm matrix can be employed, lactoferrin as a human external secretion can block biofilm development by opportunistic *Pseudomonas aeruginosa* via changing surface motility of bacterial cells and hence inhibiting the formation of cell clusters and biofilm.[13]

Challenges for AMPs in combating intracellular bacteria. Bacteria can reside within mammalian cells such as macrophage, giving rise to recurrent infections and increasing the difficulties in treatment. It had been confirmed by some studies that most of conventional antibiotics (such as daptomycin, vancomycin, rifampicin and linezolid) are compromised in treating intracellular *S. aureus in vitro* and *in vivo*.[14-16] *S. aureus* can invade various non-phagocytic cell types, and intracellular *S. aureus* in tissues can be associated with chronic or recurring infections including recurrent rhinosinusitis[17], osteomyelitis[18] and pulmonary infections[19].

Intracellular bacteria impose a higher complexity in their treatments, because many antibiotics are incapable to penetrate through membrane of mammalian cell, and can be exported out by the host cells showing a low capacity of drug loading. To overcome the barrier of eukaryotic cells and solve the difficulties of intracellular drug delivery to achieve the effective accommodation of antimicrobials, the AMPs and AMP-antibiotic conjugations designed for the treatment of intracellular pathogens are urgent for alleviating the current dilemma.

3. References

[1] Mukherjee S, Maxfield FR. Membrane domains. Annual review of cell and developmental biology 2004;20:839-66.
[2] Kai Simons EI. Functional rafts in cell membranes. Nature 1997;387.
[3] Deschenes RJ, Resh MD, Broach JR. Acylation and prenylation of proteins. Current Opinion in Cell Biology 1990;2:1108-13.
[4] Anderson RGW, Jacobson K. A Role for Lipid Shells in Targeting Proteins to Caveolae, Rafts, and Other Lipid Domains. Science 2002;296:1821-5.
[5] Muller A, Wenzel M, Strahl H, Grein F, Saaki TNV, Kohl B, et al. Daptomycin inhibits cell envelope synthesis by interfering with fluid membrane microdomains. Proceedings of the National Academy of Sciences of the United States of America 2016;113:E7077-E86.
[6] Brogden KA. Antimicrobial peptides: pore formers or metabolic inhibitors in bacteria? Nature Reviews Microbiology 2005;3:238-50.

[7] Otvos L. Antibacterial peptides and proteins with multiple cellular targets. Journal of Peptide Science 2005;11:697-706.

[8] Patrzykat A, Friedrich Carol L, Zhang L, Mendoza V, Hancock Robert EW. Sublethal Concentrations of Pleurocidin-Derived Antimicrobial Peptides Inhibit Macromolecular Synthesis in Escherichia coli. Antimicrobial agents and chemotherapy 2002;46:605-14.

[9] Subbalakshmi C, Sitaram N. Mechanism of antimicrobial action of indolicidin. FEMS Microbiology Letters 1998;160:91-6.

[10] Brötz H, Bierbaum G, Leopold K, Reynolds Peter E, Sahl H-G. The Lantibiotic Mersacidin Inhibits Peptidoglycan Synthesis by Targeting Lipid II. Antimicrobial agents and chemotherapy 1998;42:154-60.

[11] Otvos L, O I, Rogers ME, Consolvo PJ, Condie BA, Lovas S, et al. Interaction between Heat Shock Proteins and Antimicrobial Peptides. Biochemistry 2000;39:14150-9.

[12] Bierbaum G, Sahl HG. Autolytic system of Staphylococcus simulans 22: influence of cationic peptides on activity of N-acetylmuramoyl-L-alanine amidase. Journal of Bacteriology 1987;169:5452-8.

[13] Singh PK, Parsek MR, Greenberg EP, Welsh MJ. A component of innate immunity prevents bacterial biofilm development. Nature 2002;417:552-5.

[14] Lehar SM, Pillow T, Xu M, Staben L, Kajihara KK, Vandlen R, et al. Novel antibody-antibiotic conjugate eliminates intracellular S. aureus. Nature 2015;527:323-8.

[15] Barcia-Macay M, Seral C, Mingeot-Leclercq M-P, Tulkens Paul M, Van Bambeke F. Pharmacodynamic Evaluation of the Intracellular Activities of Antibiotics against Staphylococcus aureus in a Model of THP-1 Macrophages. Antimicrobial agents and chemotherapy 2006;50:841-51.

[16] Sandberg A, Hessler JH, Skov RL, Blom J, Frimodt-Moller N. Intracellular activity of antibiotics against Staphylococcus aureus in a mouse peritonitis model. Antimicrobial agents and chemotherapy 2009;53:1874-83.

[17] Clement S, Vaudaux P, Francois P, Schrenzel J, Huggler E, Kampf S, et al. Evidence of an Intracellular Reservoir in the Nasal Mucosa of Patients with Recurrent Staphylococcus aureus Rhinosinusitis. J Infect Dis 2005;192:1023-8.

[18] Bosse MJ, Gruber HE, Ramp WK. Internalization of Bacteria by Osteoblasts in a Patient with Recurrent, Long-Term Osteomyelitis: A Case Report. JBJS 2005;87.

[19] Jarry TM, Memmi G, Cheung AL. The expression of alpha-haemolysin is required for Staphylococcus aureus phagosomal escape after internalization in CFT-1 cells. Cellular Microbiology 2008;10:1801-14.